Lecture Notes in Bioengineering

Hermann Nirschl
Karsten Keller *Editors*

Upscaling of Bio-Nano-Processes

Selective Bioseparation by Magnetic Particles

Springer

Lecture Notes in Bioengineering

More information about this series at http://www.springer.com/series/11564

Hermann Nirschl · Karsten Keller
Editors

Upscaling of Bio-Nano-Processes

Selective Bioseparation by Magnetic Particles

Springer

Editors
Hermann Nirschl
Institute of Mechanical Process
Engineering and Mechanics
Karlsruhe Institute of Technology
Karlsruhe
Germany

Karsten Keller
DuPont
Wilmington
DE
USA

ISSN 2195-271X
ISBN 978-3-662-43898-5
DOI 10.1007/978-3-662-43899-2

ISSN 2195-2728 (electronic)
ISBN 978-3-662-43899-2 (eBook)

Library of Congress Control Number: 2014945953

Springer Heidelberg New York Dordrecht London

Printed on acid-free paper

Springer is part of Springer Science+Business Media (www.springer.com)

Preface

Despite ongoing progress in nano- and biomaterial sciences, large-scale bioprocessing of nanoparticles remains a great challenge, especially because of the difficulties in removing unwanted elements during processing in food, pharmaceutical, and feed industry at production level. While conventional processing requires a multitude of steps, a new approach was investigated based on the selective separation of proteins by adsorption to functionalized particles and selective separation by magnetic forces.

This book originated in a project called MagPro^{2}LIFE, which was funded by the EU in the seventh Framework Program and conducted from July 2009 to June 2013, and united many experts in the field to create a platform technology. It based on the results of the preceding project NanoBioMag, which laid the basics for the upscale of the process. The aim of the book is to collect the knowledge gathered during the project for use or for further research in the area. It provides a summary of the current state and the latest developments and achievements in the project. Topics include the synthesis of particles and their functionalization by different methods, the development of magnetic separation technology, and the application for In-Situ separation and downstream processing.

Karlsruhe, April 2014 Hermann Nirschl

Acknowledgments

We acknowledge the EU for funding our research in the seventh framework program in the project MagPro^{2}LIFE.

Special thanks to Koen Denoo for the excellent management of the project. Without his sophisticated management skills the project would never have been a success. Also we want to thank Dr. Johannes Lindner for his patience to bring together all the different contributions to this format.

Contents

About the Editors

Prof. Dr.-Ing. Hermann Nirschl is head of chair of process machinery at the Institute of Mechanical Process Engineering and Mechanics at the Karlsruhe Institute of Technology, focusing on process machinery in solid liquid separation, blending, nanoscaled particle structures and numerical simulation.

Dr. Karsten Keller is an Engineering Fellow of the Discovery Research group at Solae LLC (JV of DuPont) and has over 20 years of process engineering experience. He is developing novel processes for protein and new product opportunities from the lab-scale to commercial production and is the author of over 70 publications on subjects of separation, modeling, particle technology, biotechnology and nanotechnology. He is the inventor of 8 patents worldwide.

Contributors

Alexander Scholz Institute of Process Engineering in Life Sciences, Karlsruhe Institute of Technology, Karlsruhe, Germany

Rodica Alexandrescu National Institute for Laser, Plasma and Radiation Physics, Bucharest, Romania

Victor Alvan Amasifuen Institute of Mechanical Process Engineering and Mechanics (MVM), Karlsruhe Institute of Technology, Karlsruhe, Germany

Johann Bauer Merck KGaA, Darmstadt, Germany

Martin Cerff Institute of Process Engineering in Life Sciences, Karlsruhe Institute of Technology, Karlsruhe, Germany

Izabell Craciunescu National Institute for Research and Development of Isotopic and Molecular Technologies, Cluj-Napoca, Romania

Niels Dalgaard Mechanical Process Engineering and Mechanics, Karlsruhe Institute of Technology, Karlsruhe, Germany; DuPont Nutritional Biosciences Aps, Brabrand, Denmark

Helen Engel LinkedIn Corporation, Mountain View, CA, USA

Johannes Feller Mechanical Process Engineering and Mechanics, Karlsruhe Institute of Technology, Karlsruhe, Germany

Matthias Franzreb Institute of Functional Interfaces (IFG), Karlsruhe Institute of Technology, Eggenstein-Leopoldshafen, Germany

Gunnar Grim Mechanical Process Engineering and Mechanics, Karlsruhe Institute of Technology, Karlsruhe, Germany

Timothy John Hobley Technical University of Denmark, Lyngby, Denmark

Karl Holschuh Merck KGaA, Darmstadt, Germany

Sebastian Holzapfel LinkedIn Corporation, Mountain View, CA, USA

Karsten Keller DuPont, Wilmington, DE 19980, USA

Valéry Tchanque Kemtchou Bergakademie Freiberg, Institut für Mechanische Verfahrenstechnik und Aufbereitungstechnik, Freiberg, Germany

Johannes Lindner Institute of Mechanical Process Engineering and Mechanics, Karlsruhe Institute of Technology, Karlsruhe, Germany

Katharina Menzel Institute of Mechanical Process Engineering and Mechanics, Karlsruhe Institute of Technology, Karlsruhe, Germany

Ion Morjan National Institute for Laser, Plasma and Radiation Physics, Bucharest, Romania

Alexandrina Nan National Institute for Research and Development of Isotopic and Molecular Technologies, Cluj-Napoca, Romania

Christian Fiil Nielsen Mechanical Process Engineering and Mechanics, Karlsruhe Institute of Technology, Karlsruhe, Germany; DuPont Nutritional Biosciences Aps, Brabrand, Denmark

Hermann Nirschl Institute of Mechanical Process Engineering and Mechanics, Karlsruhe Institute of Technology, 76131 Karlsruhe, Germany

Anja Paulus Institute of Functional Interfaces (IFG), Karlsruhe Institute of Technology, Eggenstein-Leopoldshafen, Germany

Urs Alexander Peuker Bergakademie Freiberg, Institut für Mechanische Verfahrenstechnik und Aufbereitungstechnik, Freiberg, Germany

Clemens Posten Institute of Process Engineering in Life Sciences, Karlsruhe Institute of Technology, Karlsruhe, Germany

Susanne Rasmussen DuPont Nutritional Biosciences Aps, Brabrand, Denmark

Elisabeth Rondeau LinkedIn Corporation, Mountain View, CA, USA

Maria Schäfer Bergakademie Freiberg, Institut für Mechanische Verfahrenstechnik und Aufbereitungstechnik, Freiberg, Germany

Vlad-Mircea Socoliuc Romanian Academy-Timisoara Branch, Center for Fundamental and Advanced Technical Research, Timisoara, Romania

Wickie Sondergaard Romanian Academy-Timisoara Branch, Center for Fundamental and Advanced Technical Research, Timisoara, Romania

Rodica Turcu National Institute for Research and Development of Isotopic and Molecular Technologies, Cluj-Napoca, Romania

Ladislau Vékás Romanian Academy-Timisoara Branch, Center for Fundamental and Advanced Technical Research, Timisoara, Romania

Erich J. Windhab LinkedIn Corporation, Mountain View, CA, USA

Abbreviations

AEX	Anion Exchanger
AMTPS	Aqueous Micellar Two-Phase Systems
ATPS	Aqueous Two-Phase Separation
ATRP	Atom Transfer Radical Polymerization
BBI	Bowman-Birk-Inhibitor
BET	Brunauer-Emmet-Teller
CEX	Cation EXchanger
CFD	Computational Fluid Dynamics
CI	Chymotrypsin Inhibition
CIP	Cleaning In Place
CME	Continuous Magnetic Extraction
DLS	Dynamic Light Scattering
EBA	Expanded Bed Adsorption
FEM	Finite Element Modeling
HGMS	High Gradient Magnetic Separation
HGMF	High Gradient Magnetic Filtration
ISMS	In-Situ Magnetic Separation
ISPR	In-Situ Product Removal
LCA	Life Cycle Assessment
LCST	Lower Critical Solution Temperature
LD	Laser Diffraction
MANACO	Magnetic Nano Composites
MANDHALA	Magnetic Arrangement for Novel Discrete Halbach Layout
MEC	Magnetically Enhanced Centrifugation
MEP	Magnetic Extraction Phases
MF	Magnetic Fluid
MNP	Magnetic Nano Particle
NAMPEX	Nano Membrane Pore Extruder
NanoMags	Magnetic Nanoparticles
NMR	Nuclear Magnetic Resonance
NPC	Nanoparticles Clusters

NTU	Nephelometric Turbidity Unit
PBA	Packed Bed Adsorption
ROMER	Rotating Membrane Reactor
SANS	Small Angle Neutron Scattering
SDS-PAGE	Sodium Dodecyl Sulfate Poly Acrylamid-Gel Electrophoresis
SEM	Scanning Electron Microscopy
SIP	Sterilization In Place
SMEP	Smart Magnetic Extraction Phases
SOP	Standard Operating Procedure
SLS	Static Light Scattering
SolPro	Solution Process
TEM	Transmission Electron Micrograph
UF	Ultrafiltration
XPS	X-ray Photoelectron Spectroscopy
XRD	X-Ray Diffraction

Keywords

Selective protein separation · Magnetic particles · Scaling up processes · Superparamagnetic nanoparticles · High gradient magnetic separation · Magnetically enhanced centrifugation · Laser pyrolysis · Magnetic microgels · Vesicles by rotating membrane pore extrusion · Spray drying · Halbach magnet based HGMS · Continuous magnetic extraction · In-Situ magnetic separation

Chapter 1
Introduction

Hermann Nirschl

Biologically-derived materials represent one of the most important sources of new technology food and pharmaceutical products due to their precisely controlled structure, biofunctional properties and potential for inexpensive and sustainable production. Recent advances in a variety of areas of biotechnology, from systems biology to bioreactor technology, have made large-scale production of sophisticated new biomolecular materials possible. However, the costs of producing these exciting new materials can be prohibitive due to separation processing, which typically constitute 80 % of the total cost of production. Bioseparation technology used in industry today is based on principles first discovered over 70 years ago and improvements are needed at all stages of processing, i.e. from pre-treatment of raw materials prior to fermentation, the fermentative product itself, and during subsequent purification and modification to yield the final product.

Functional magnetic (nano)particle composites have the potential to enhance the physical and chemical properties of bioseparation processes, i.e. (nano)particles have extremely high surface areas, rapid binding kinetics and unique physical and chemical properties. However, handling them in complex and demanding bioprocesses where profits can be marginal for 'low-value, high-throughput' products is a great challenge. Such particles with magnetic properties might enable significant improvements in productivity, economic feasibility, sustainability and product quality and its control. However, implementation of functional magnetic particles as adsorbents in the bioprocessing industry requires the synergistic interplay of a host of components. The two major barriers to implementing magnetic nanoparticles and composites are the safe and effective large-scale manufacturing of appropriately functionalised superparamagnetic particles, and the lack of large-scale process technology to separate these particles from

H. Nirschl (✉)
Institute of Mechanical Process Engineering and Mechanics, Karlsruhe Institute of Technology, 76131 Karlsruhe, Germany
e-mail: hermann.nirschl@kit.edu

H. Nirschl and K. Keller (eds.), *Upscaling of Bio-Nano-Processes*,
Lecture Notes in Bioengineering, DOI 10.1007/978-3-662-43899-2_1

the production streams. For this technology to be accepted in industry, it must be safe, capable of scaling to high production rates, reliable, robust and inexpensive.

The goal of the EU funded MagPro^{2}Life project was to address these barriers and demonstrate the use of functional magnetic (nano)particle separation at pilot-scale on biotech pilot lines. The potential impact of selective magnetic separation is significant but adoption by the biotechnology industry hinges on successful initial demonstrations of complete technologies. Therefore, the main objective of the MagPro^{2}Life project is to scale-up innovative nanotechnology-based processes to pilot-line-scale and demonstrate the feasibility of this technology.

The MagPro^{2}Life project was based on a series of focused objectives:

- development of scalable magnetic particle production technologies;
- development of scalable surface functionalization technologies;
- develop large-scale processing technologies that can be used with the adsorbents produced;
- and integrate the previous three objectives to demonstrate that this technology can be implemented for safe, industrial scale bioseparation.

The project produced several magnetic nanoparticle separation technologies that can be applied to bioseparation in the industry, i.e. low-value, low-concentration products to high-value, high-concentration products. This was demonstrated in pilot-scale separation of a set of model biomolecular products.

MagPro^{2}Life was motivated by the fact that magnetic process technology can significantly improve the value chain in industrial production for emerging biotechnological and pharmaceutical markets. Major European companies and SMEs are expected to benefit from pilot line demonstrations of the new magnetic processes.

1.1 State-of-the-Art

The most commonly used industrial methods of biomolecular separation are based on filtration, centrifugation and fixed-bed chromatography. Filtration and centrifugation are most often used for low-resolution removal of solids, frequently combined with precipitation. Chromatography is a proven separation technology that is highly versatile. Biomolecules are purified using reversed phase chromatography utilising hydrophobic interactions. Ion exchange chromatography uses ionic interaction between the support surface and charged groups of the peptide. Gel permeation chromatography separates molecules primarily on the basis of size exclusion. However, fixed-bed chromatography has significant drawbacks when implemented on an industrial scale, i.e. discontinuous operation, intolerance to suspended solids and expensive capital and operating costs. For example in the case of ion exchange chromatography concentrated acids and brines are required

to elute the product and regenerate the separation media. Elution solutions in biotechnology also frequently contain substances to increase elution efficiency that have to be removed by additional separation steps. This results in the need for large volumes of sterile water from which large amounts of industrial waste is generated.

Thus, current bioseparation technologies have low process yields, high costs and require large numbers of discrete unit operations in series (e.g. centrifugation, filtration, ultrafiltration, ultracentrifugation, precipitation, adsorption chromatography as well as several polishing operations). Selective magnetic separation can be considered a standard tool in analytics due to its easy and efficient handling. An increasing number of commercially available isolation and purification kits enable for a wide range of applications, e.g. DNA separation and diagnostics. High levels of purification can be obtained from highly complex feed streams like human or animal blood in a one-step separation. However, the novel technology has not been transferred into industrial scale production of bioproducts yet.

Magnetically enhanced biotechnologies promise to improve the yield and reduce costs of bioprocessing. Research to explore the possibility of implementing magnetic separation for large-scale industrial bioseparation has been supported by the EU and a number of national funding agencies. Several magnetically assisted processes employing new techniques were developed and tested recently in laboratory scale. This includes, for example high-gradient magnetic fishing (HGMF) (Hubbuch and Thomas 2002), smart magnetic extraction phases (SMEPs) (Becker et al. 2009), magnetic field enhanced centrifugation (MEC) (Lindner et al. 2013) and magnetic field enhanced cake filtration (Eichholz et al. 2011). Further, the industrial feasibility of HGMF has also been demonstrated conclusively in a comparative study by the expanded bed adsorption chromatography (EBA) (Hubbuch et al. 2001). HGMF outperformed EBA by at least a factor of 4 based on an ECO-99 indicator regarding resources, ecosystem quality, and human health.

On the particle production side, synthesis methods have been established and optimised to deliver robust and reusable magnetic adsorbents (Franzreb et al. 2006) possessing targeted selectivity and high-target binding capacity. Furthermore, the use of magnetic adsorbents for in situ product recovery (Ottow et al. 2007), intensification of fermentative production and control of industrially relevant enzymatic modification reactions have been developed and large-scale magnetic particle production processes have been screened.

The low process yields and high costs, observed in the manufacture of many of today's approved biopharmaceuticals, are direct consequences of the conventional practice of using large numbers of discrete unit operations placed one after the other, with each performing just a single or limited number of function(s). Manufacturers of biotechnological products now face unprecedented pressure to reduce spending, make their manufacturing processes more cost effective, and bring new products to market more rapidly than ever before. Such pressures, therefore, encourage a departure from traditional thinking and separation methods, and have fuelled interest in the evaluation of newer 'multifunctional'

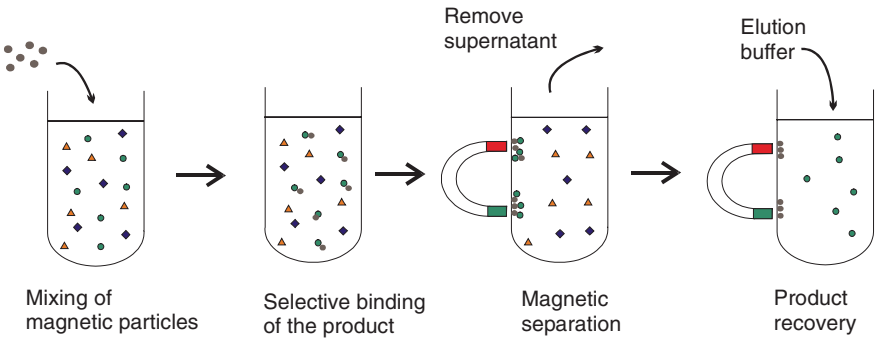

Fig. 1.1 General principle of magnetic separation in millilitre scale

technologies, which have hitherto been considered too avant-garde for adoption within the necessarily conservative biopharmaceutical sector. The implementation of such '*bioprocess intensification*' techniques signifies a reduction in the number of processing steps employed in manufacturing, and brings with it promises of improved yields and throughputs, reductions in plant size and waste generation, and lower manufacturing costs. In this context, the generation of robust adsorptive methods capable of *selectively 'fishing' soluble target molecules directly out of crude unclarifed bioprocess feedstocks*, i.e. those typically encountered during the early stages of a traditional downstream process scheme, has received considerable attention in recent years. Notable examples of such techniques include affinity aqueous two-phase extraction and expanded bed adsorption.

Commercial production of functionalized magnetic supports for use in biotech applications exist for use in batch binding mode with subsequent magnetic collection, typically achieved with simple permanent magnet racks. Useful magnetic support materials can be produced by: *encapsulation, infiltration* or *coating* of magnetic material into natural or synthetic polymers. A wide variety of magnetic particles are available for clinical and small-scale analytical applications. However, there has been no breakthrough to transform the production of the magnetic supports into large-scale with the goal to use them in downstream processing.

The basic principle of the millilitre-scale application of magnetic particle-based separations in biotechnology is illustrated in Fig. 1.1. A pure and concentrated product can be obtained at the end of the procedure involving an adsorption and desorption step. However, only microgram to milligram amounts of product is to be obtained by this technique.

This was an attempt to transfer the above-mentioned analytical technique into production technologies for high-value bioproducts (e.g. pharmaceutical proteins, DNA for gene therapy, etc.). Using a lab-scale 'High Gradient Magnetic Separator' (HGMS), it was demonstrated in the past the feasibility of the combination of

magnetic nanoparticle-based supports and magnet technology for the purification of a bioproduct (e.g. trypsin from a crude porcine pancreatin feedstock) is possible.

Regarding 'Magnetic Nanofluid Extraction' which is based on the principle of 'Magnetic aqueous two-phase separation', the state-of-the-art is defined by the work of two research groups located in Lund, Sweden and Nagoya, Japan. The group in Lund investigated the speed up of the phase separation in 'Aqueous Two-Phase Separation' (ATPS) when an inert magnetic fluid or magnetic particles were incorporated into one of the phases (Ottow et al. 2007). In these articles, the authors report of a **reduction of the separation time by a factor of 35–70** and sometimes in the case of high-viscosity phases by a factor of more than 100. The only article about the use of functionalised magnetic particles in combination with ATPS is by the group in Nagoya (Suzuki et al. 1995). Although the experiments were conducted only in small-scale batch mode, the achieved **improvement of the apparent separation factor was up to 35-fold**.

1.2 New Developments

In MagPro^{2}Life, the goal was to advance and scale-up novel particle and process technologies. A key objective was to support research and development on highly promising new magnetic nanoparticles composites that have unique physical and chemical properties while enabling scaling-up of the production of the highly promising new particles. The research and development projects allowed to produce innovative adsorbants with functional properties that will generate new modes of processing or overcome existing bottlenecks. The scientific and technical challenges of scaling-up particle production were estimated to be high—the price of magnetic particle adsorbents, when the project started in 2009, was a serious limitation in implementing magnetic enable bioprocess technologies in industry.

The implementation of this technology in industry with magnetically enabled bioprocesses has up to now not been established. MagPro^{2}Life established a set of advanced process technologies for magnetically enhanced bioprocessing through the production pilot plants. Feasibility studies were conducted on a set of model products that allow us to define the performance of these new technologies for specific markets. That is the production pilot lines demonstrate the industrial feasibility of the novel processing technology for fermentation and downstream processing. Through fermentation, intensification by in situ magnetic separation of target products or inhibiting products, production rates will be increased. In combination with smart magnetic enzyme catalysts and continuous selective magnetic separation, a production rate increase of 10–20 % was reached in lab-scale. In pilot-scale, downstream processing smart magnetic supports enabled efficient adsorption of target product from the crude fermentation broth. Following magnetic separation of the adsorbent particles recovered the target product and the magnetic bead for recycling after elution.

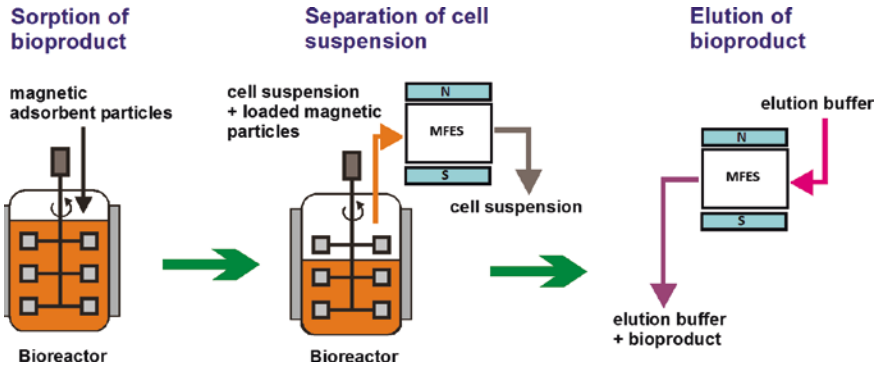

Fig. 1.2 Basic steps necessary to purify a bioproduct by magnetic separation directly from a crude fermentation broth

With the Magnetic Field Enhanced Centrifuge, separation efficiencies of more than 99 % have been reached for magnetic adsorbent particles in the size range of 1 μm and below. Theoretical analysis of the macroscopic and microscopic aspects of these processes using numerical tools made it possible to optimise and predict the performance of this process. MagPro^{2}Life introduced the possibility of having available several versatile separation and extraction techniques that require easily controllable external variables to change properties that are more ideal for selective separation.

One of the primary objectives of the project was to bring together lab-scale magnetic purification techniques already proven feasible in numerous analytical benchtop applications (protein analytics, etc.) and industrial magnetic separation technology being a state-of-the-art technology for some decades in mineral ore processing (High Gradient Magnetic Separation, etc.). This is an attempt to apply the above-mentioned analytical technique for the production of high-value bioproducts (e.g. pharmaceutical proteins, DNA for gene therapy, etc.). A possibility to transfer magnetic small-scale lab techniques into technologies for the industrial production of bioproducts is illustrated in Fig. 1.2. After the mixing of magnetic nanostructure-based adsorbent particles, the target product adsorbs selectively on the particle surface. The magnetic particles are selectively separated by a magnetic separation process and after elution the product is available in a pure and concentrated form. In theory, no prior clarification process is necessary like in conventional chromatographic techniques.

The objective of the project was to even transpose the above-mentioned cyclic process into a fully continuously operating process. Novel continuous magnetic separation and structuring processes were developed. The technologies developed relying on the utilisation of magnetic sub-micron sized particles that are themselves composed of magnetic nanoparticles. Moreover, the project was considered to have an enormous wide range of potential existing and new products as illustrated in Fig. 1.3. The surface of the magnetic particles can be functionalized with a broad range of ligands. Those ligands allow the separation of specific molecules out of a variety of bio, feed and food product sources.

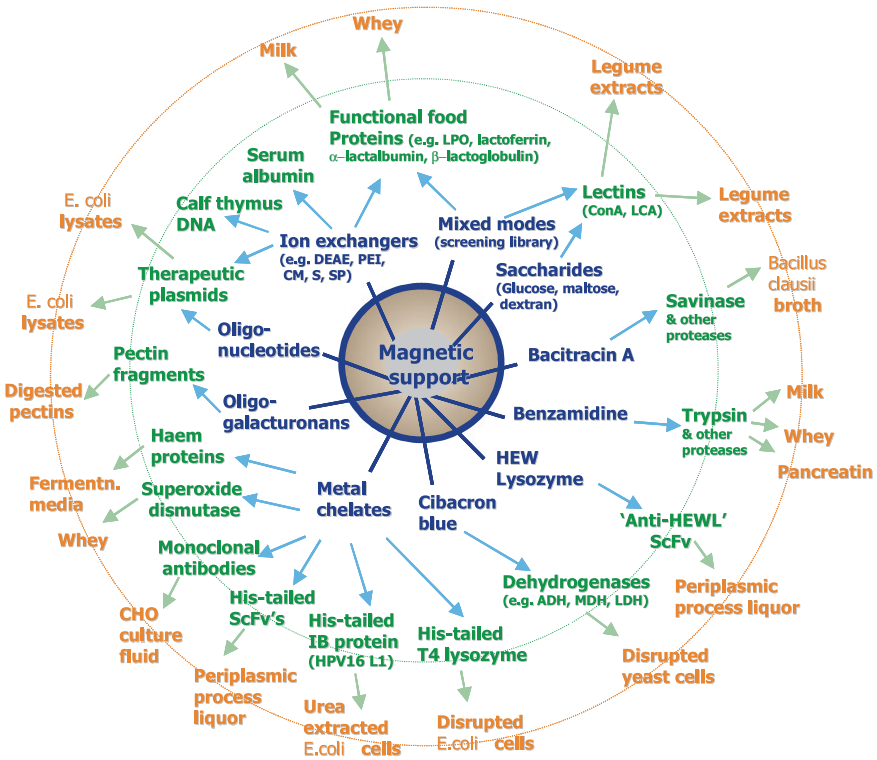

Fig. 1.3 Potential products and product sources for magnetic nanoparticle-based supports (Suzuki et al. 1995)

1.3 Overview

The link to market needs was represented by a preliminary product selection of natural soy-based nutraceuticals/pharmaceuticals such as Bowman-Birk Inhibitor (BBI), a protease inhibitor for MS treatment, and Lunasin which is reported to have anticarcinogenic properties as well as recombinant proteins and nucleic acids produced by microbial fermentation. The main thrust of the project was to develop: advanced and robust magnetic and structured or assembled nanoparticles and composites, industrial large-scale production and process technologies and then link them together to demonstrate safe industrial scale implementation.

The goals of the project were achieved through contributions from 16 partners. The following chart shows the Organisation (Fig. 1.4).

The main S&T objective was therefore to build on knowledge gained through preliminary work so as to produce constituent technologies for the large-scale production of functionalized magnetic particles and pilot-line-scale equipment for the novel processes. In broad terms, the project delivered complete and flexible

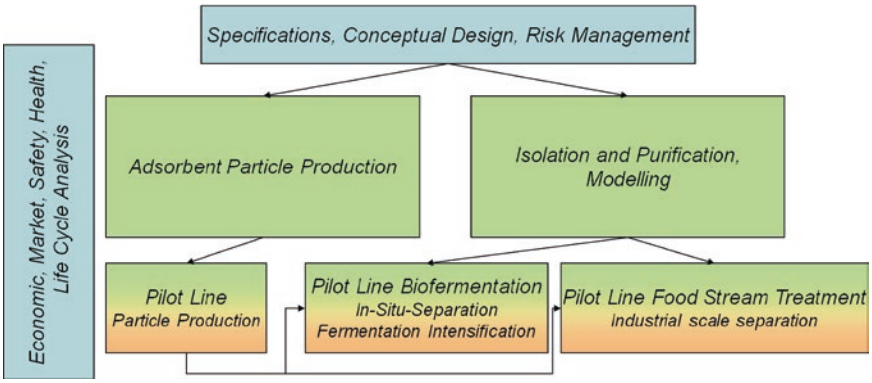

Fig. 1.4 Project organisation

modular manufacturing lines, which might be deployed to produce innovative target products, with applicability and performance sustainability. Both, major companies and European SMEs (in particular, suppliers of machinery, support materials and other consumables) were involved in pilot line demonstrations of the new magnetic processes.

By combining certain key advances in nanotechnology with others in biotechnology, magnetism and materials science, it was aimed to develop a robust and efficient set of smart (i.e. self-adapting) multifunctional and/or biospecific sorbents and macromolecular assembly processes. The planned research activities addressed: fabrication of bespoke magnetic nano- and microparticle assemblies; their functionalisation using advanced 'self-adapting' polymer materials combined with new highly specific biomolecular recognition systems and evaluation of produced adsorbents.

1.3.1 Particle Fabrication and Functionalisation

The consortia followed different approaches for carrier particle development to provide a maximum of flexibility in industrial take-up. The production also incorporates the equipping of the carriers with product-appropriate functionalisations and established Affinity Ligands. In general, two particle production pathways have been investigated. Depending on the target product value and amount to be purified a wet or dry processing can be used. Streamlined and economic manufacturing routes to magnetic nanocomposites based on magnetic nanofluids and synthetic monomers as starting materials have been developed. Commercially available intermediate products have been tested for their applicability in these processes to further reduce production costs. The following adsorbent particles have been produced in large-scale and used.

SolPro Solution Process for pilot-scale particle production is using sonochemical precipitation (magnetite), miniemulsion polymerisation (sorbent) and composite synthesis by spray drying (magnetic bead)

NanoMags Magnetic Nanoparticles are produced by Laser Pyrolysis and precipitation. A functional polymer coating is to provide binding sites

MagPrep Continuous synthesis of magnetic particles in suspension

MANACO Nanoparticle Membrane Pore Extrusion provides smart magnetic vesicles for extraction/separation and drug delivery. Rotating Membrane Extrusion (ROMER) upscales existing vesicle manufacturing equipment

Additionally to established ligands, new approaches for functionalising base support materials were followed after. Magnetic particles can in general be assembled with any ligands already known from chromatography (i.e. affinity, pseudo affinity, ion exchange, mixed mode, hydrophobic, etc.).

1.3.2 Isolation and Purification

The main goal was to design large-scale equipment to extract, classify and separate valuable products in innovative sorption processes based on smart, self-adapting micro-sorbents. To successfully compete with classical production processes, it is crucial to provide highly efficient process equipment especially regarding the recovery of the magnetic adsorbent particles. Ideally in case of a 100 % recovery, the actual costs generated by particle production might play a minor role in the total costs. MagPro^{2}Life therefore dedicated quite some resources into separation knowledge development and process equipment development:

CME Continuous Magnetic Extraction for the separation of target product out of crude bio-feedstocks.

MEC Magnetic Field Enhanced Centrifugation is a solid–liquid separation process using high-gradient magnetic fields to capture the particles on magnetic wires and discharge them continuously by centrifugal forces. Continuous discharge was realised by a decanter design.

1.3.3 Pilot Lines

All of the aforementioned sub-units demonstrate to be the tools of a product separation toolbox. Pilot lines have been realised by combination of the most appropriate tools from this toolbox. Depending on the target product in terms of tonnage, selling price, purity, etc. different carrier particles, different functionalisations and separations tools are needed. By combining afore introduced sub-units, the pilot lines are realised, wherein the sub-unit should be easily interchangeable to promote modular set up. The following pilot lines were set up:

1.3.3.1 Protein Production Stream

Several different types of consortia produced adsorbent particles are tested for their feasibility in industrial processing of soy feed streams. Products to be separated and purified are BBI and Lunasin. Different separation devices like MEC, Halbach magnet based HGMS and CME were tested. Model protein is the Bowman-Birk Inhibitor. It is a soybean-derived protease inhibitor that has anti-inflammatory and anticarcinogenic activities. In clinical studies, it has been shown that the ability to inhibit trypsin and chymotrypsin activities enable BBI as a treatment for multiple sclerosis (MS) and several forms of cancer. It might be a product as pharmaceutical or food additive.

1.3.3.2 Fermentation Intensification

Bioprocess intensification using magnetic particles is an approach developed in previous studies where inhibiting products are removed continuously during fermentation process to increase production rate. Magnetic separation using functionalised magnetic adsorbent particles during cultivation could be an alternative strategy to remove extracellular products in situ in an external loop. Removing, for example inhibiting components during the fermentation can increase yield and productivity of the biosystem. One part of the project has been the investigation of the interactions between the microorganism catalyst, the magnetic adsorbent particles and the separation unit. In addition to inhibiting species, unwanted by-products and/or valuable bioproduct can be magnetically separated and recovered. This pilot line combines E. coli fermentation with simultaneous affinity separation of inhibiting products. The adsorbent particles are produced by the consortia itself in pilot-scale production facilities. Magnetic separation of the adsorbent particles was performed by classic HGMS. As mentioned above, a portfolio of different demonstration products has been defined so far. Each of the products represents at least one of the market sections—food, feed and pharma—that are targeted on.

Model protein is phytase. This is an enzyme that can break down the undigestible phytic acid (phytate) part found in grains and oil seeds and thus release digestible phosphorus, calcium and other nutrients. Phytase is used as an animal feed supplement—often in poultry and swine—to enhance the nutritive value of plant material by liberation of inorganic phosphate from phytic acid (myo-inositol hexakisphosphate) and, thereby, to reduce environmental phosphorus pollution.

1.3.3.3 Economic, Market, Safety, Health and Life Cycle Analysis

In 2005, it has been estimated that the European Biotechnology Market could be worth over 100 billion EUR with a global market potential of above 2000 billion EUR in 2010 (EU 2004). Within the next decade, the market shares of relevant products are expected to more than double, thus the benefits of the proposed process

technology should be significantly higher. We conducted economic and market analyses for the pilot-line products as well as other promising candidates out of these market segments. For detailed economic studies, accurate documentation of energy consumption, possible safety and health precautions, etc. during the experimental studies would be crucial. A product map versus preferred production methods provides an excellent outcome for similar industrial applications and will show substitution potential of novel process to standard production. The study activities were completed by a Life Cycle Analysis according to ISO 14040ff. It allowed an efficient analysis and assessment of environmental impacts and resource intensity along the products, processes and services to judge the sustainability of the new technology.

Not only final economic studies were performed, but also tracked safety and health issues of the novel processes, including cGMP, and materials and compared these with established production methods. Food and FDA regulations were also sighted during the pilot-line development and necessary measures for future FDA approval were tracked.

REACH registration was considered for particle systems including intermediate products in case pilot line trials already result in competitive products.

The magnetic carriers for bioseparation applied in MagPro^{2}Life used mainly nano-magnetite to achieve their magnetic properties. Nano-magnetite is produced in different biological organisms. Thus it can be stated that nanoscale magnetite is a natural product.

In the MagPro^{2}Life products (magnetic carrier), it is necessary from the process technology point of view that the magnetite is encapsulated by a matrix material. It is one main quality feature that the magnetite does not interact with the surrounding. Thus, the final product is designed to for the full containment of the nanoparticles involved for safety reasons. Due to the elevated price, a 99.9 % recycling quota of the nanoparticle containing magnetic carriers was targeted in the project as well as in a future application.

From the synthesis of nano-magnetite to its encapsulation in the spray process, which leads to a nanocomposite material, where the nanoparticles are fixed in the polymeric matrix, the process is guided in a closed cycle. This production cycle as well as the life cycle of the product itself ensures the full containment of the magnetite nanoparticles, which are processed in closed process equipment and which are further embedded in a liquid or solid matrix. All process streams (aqueous liquid, drying gas) have been filtered and treated to maintain the full containment of the process.

1.4 Summary

MagPro^{2}Life pulled together advanced R&D efforts in Europe, integrating different blocks of research activities. MagPro^{2}Life shortened the distance between R&D and market deployment in established, emerging as well as in ‘niche’ market areas of bio, food and pharma.

References

Becker JS, Thomas ORT, Franzreb M (2009) Protein separation with magnetic adsorbents in micellar aqueous two-phase systems. Sep Purif Technol 65(1):46–53

Eichholz C et al (2011) Recovery of lysozyme from hen egg white by selective magnetic cake filtration. Eng Life Sci 11(1):75–83

EU (2004) Consequences, opportunities and challenges of modern biotechnology for Europe

Franzreb M et al (2006) Protein purification using magnetic adsorbent particles. Appl Microbiol Biotechnol 70(5):505–516

Hubbuch JJ, Thomas OR (2002) High-gradient magnetic affinity separation of trypsin from porcine pancreatin. Biotechnol Bioeng 79(3):301–313

Hubbuch JJ et al (2001) High gradient magnetic separation versus expanded bed adsorption: a first principle comparison. Bioseparation 10(1–3):99–112

Lindner J, Menzel K, Nirschl H (2013) Parameters influencing magnetically enhanced centrifugation for protein separation. Chem Eng Sci 97:385–393

Ottow K et al (2007) Avoiding proteolysis during fermentation by using high gradient magnetic fishing. J Biotechnol 131(2):S169

Suzuki M et al (1995) Affinity partitioning of protein a using a magnetic aqueous two-phase system. J Ferment Bioeng 80(1):78–84

Part I
Particle Synthesis and Functionalization

Chapter 2
New Advances in the Production of Iron-Based Nanostructures Manufactured by Laser Pyrolysis

Ion Morjan and Rodica Alexandrescu

Abstract Nanoparticles (NPs) are submicron moieties made of inorganic or organic materials, which have many novel properties compared with their bulk counterparts. The CO_2 laser pyrolysis of gas- and vapor-phase reactants offers an approach for the synthesis of uniform nanoparticles. The synthesis of iron oxide-based nanomaterials by laser pyrolysis has been achieved by a handling procedure, in which the oxidation process initiates and develops inside the laser-induced reaction zone. In a second step, a more complex experimental procedure is used, in which the iron precursor is allowed to dissociate alone in the flame with a surrounding oxidizing atmosphere. XRD and TEM analyses reveal a major content of maghemite/magnetite in samples SF. The power density and the nozzle diameter influence the particle size.

2.1 Introduction

Nanoparticles (NPs) are submicron moieties made of inorganic or organic materials, which have many novel properties compared with their bulk counterparts (Einar Kruis et al. 1998). Their diameters usually range from 1 to 100 nm, although there are examples of NPs several hundreds of nanometers in size. Magnetic NPs have many unique magnetic properties such as superparamagnetism, low Curie temperature, and high magnetic susceptibility. Magnetic NPs are of great interest for researchers from a broad range of disciplines, including magnetic fluids, data storage, catalysis, and bioapplications (Cristina Blanco-Andujar et al. 2010). Currently, magnetic NPs are used in important bioapplications, including magnetic bioseparation and detection of biological entities (cells, proteins, nucleic acids, enzymes, bacteria, viruses, etc.), clinic diagnosis and therapy (such as

I. Morjan (✉) · R. Alexandrescu
National Institute for Laser, Plasma & Radiation Physics, Atomistilot St. 409, Bucharest, Romania
e-mail: Ion.morjan@inflpr.ro

H. Nirschl and K. Keller (eds.), *Upscaling of Bio-Nano-Processes*,
Lecture Notes in Bioengineering, DOI 10.1007/978-3-662-43899-2_2

Magnetic Resonance Imaging) (Nydeia et al. 2013) and in order to reduce the toxicity associated with cytotoxic drugs (Baena and Marulanda 2011).

Iron-based nanomaterials (Abhilash et al. 2011) have found applications in many areas of science and technology due to their unique magnetic properties. A size reduction of these materials from bulk to the nanoscale allows them to display various size related properties. Among other changes, a significant decrease in size can alter reactivity, increase surface area and change the magnetic properties. The use of magnetic nanoparticles as molecular imaging probes enables noninvasive in vivo studies of antigen expression of diseases in various internal organs. Particularly, iron oxide nanoparticles (Shikwambana et al. 2011) with new subsequent functionalized procedures permit applications, such as conjugation of DNA, antibodies, proteins, etc. However, the synthesis of high-quality functionalized magnetic iron oxide NPs with tunable sizes and shapes in a controlled manner is still a challenge. The magnetic properties and function of naked or surface functionalized iron oxide NPs depend on their physical properties: their size, shape, microstructure, and the chemical phase in which they are present. A number of chemical methods are available and are extensively used for the synthesis of iron-based nanostructures, but these are often energy intensive and employ toxic chemicals. Despite the availability of chemical methods, the production of large amounts of pure, nonagglomerated NPs, with desired size and narrow size distribution, still proves to be an extremely difficult task.

The CO_2 laser pyrolysis of gas- and vapor-phase reactants offers an alternative approach for the synthesis of uniform nanoparticles (Cannon et al. 1982; Swihart 2003). This technique is mainly developed for its advantages of residing; (i) the well-defined interaction volume where no interaction with the reactor chamber walls and hence, no contamination occurs and (ii) the production of very fine particles (usually less than 50 nm). The laser pyrolysis belongs to the synthesis methods that function via a homogeneous nucleation in the gas phase (Srdic et al. 2000).

The current technology of laser pyrolysis is depicted below as is the preparation of iron-based nanostructures. In this paper, examples of laser pyrolysis processes of $Fe(CO)_5$-based gas mixtures will be presented. In parts these examples rely on our previous reported results. Therefore, the phenomenology of the process and the characterization of nanopowder structures is described. Some characteristics of the laser-sensitized pyrolysis for producing iron oxides in the gamma phase will be discussed. Using $Fe(CO)_5$ mixed with hydrocarbon precursors and a particular irradiation geometry, iron particles embedded in carbon sheets were obtained.

2.2 The Laser Pyrolysis

2.2.1 Process Description

Laser pyrolysis is based on the overlapping of the emission line of the laser with an absorption line of one or more precursors. The 10P(20) CO_2 laser line peaks at 10.591 μm and is the strongest emission line. An additional substance, the

so-called sensitizer is used in the case of nonabsorbing gas precursors. It absorbs the energy and transmits it to the precursors by collisions. As a final effect of a laser-absorbing system coupling, the laser acts as a heat source. When exposed to the laser and the prevalent gas pressure, the time between absorption of photons by the reactant gases is much greater than that necessary for distribution of the energy to nearby gas molecules through collisions. Thus, a thermal equilibrium is achieved. In this case, only one of the gas species needs to absorb the laser energy, since the others will be heated by collisions. The system is based on a cross-flow configuration. The reactant flow emerges in the reactor through a nozzle system where it is orthogonally intersected by the focused IR radiation beam. Pyrolysis in the gas phase occurs in the small volume defined by the crossing of the radiation gases, where usually a "flame" appears.

From the point of view of IR photochemistry, basic principles of the laser pyrolysis rely on (i) the resonant absorption of photons by IR-active vibrational modes of molecules in ground electronic state; (ii) collision-aided vibrational energy transfer towards the translational and rotational degrees of freedom and (iii) the heating of the reactant gases and dissociation, followed by nucleation and growth of aggregates.

Nanoparticle formation starts after reaching the degree of supersaturation of condensable products in the vapor phase. The condensable products result from the laser-induced chemical reactions that occur at the intersection point of the laser beam with the molecular flow of gas or vapor–phase precursors. Particle nucleation and growth are complex processes, which usually depend on reaction pathways given by the specific experimental conditions (particularly, the nature and number of reactants). Particles grow by collisions (the growth is proportional to the system pressure) and by coalescence. Nondispersible aggregates are formed. Once time intervals between collisions are too short to form dense spherical particles, agglomerates form. The confinement of the gas precursors and of the newly nucleated particles toward the flow axis is achieved by a coaxial argon flow. Nucleated particles are kept together by the gas stream and collected in a removable tank at the exit of the reaction cell. Alternatively, the particles may be deposited on a substrate positioned in the flow reactor. The main process parameters are: the nature of the gas (vapor) precursors, the gas flow rate, the pressure as well as the laser wavelength and power. For liquid precursors, the bubbled vapors are carried into the reaction zone by a carrier gas.

2.2.2 Advantages and Drawbacks

One clear advantage of laser pyrolysis over competing techniques is the high versatility that allows the production of a wide range of nanopowders iron and carbon-based, oxide semiconductors, metal-based, polymer nanocomposites, etc. Laser pyrolysis from the gas phase is a vapor-phase method of synthesis where the reactants are dilute and therefore yield a fine, loosely agglomerated powder,

narrow particle size distributions and controlled purity. Unlike furnace-heated, RF-heated and arc-plasma-heated processes, laser pyrolysis develops almost ideal thermal profiles and a reaction zone, which permits uniform nucleation and growth. As another advantage, this method generates ultrafine powders in a continuous way with narrow particle size distribution. The absence of potentially toxic surfactants makes the product ideal for the preparation of colloidal dispersions for use in biomedical applications (Bomatí-Miguel1 et al. 2010). It is of particular interest in the case of the iron nanoparticles due to their high magnetic response. The drawbacks of the laser pyrolysis technique are the constraints imposed on the reactants: the required elements must be present in a vapor phase and at least one reactant must contain an infrared absorption band for coupling the energy with the laser beam.

2.2.3 Characterization Techniques of the as-Synthesized Iron-Based Nanostructures

After synthesis, the morphology and composition of the iron oxide nanopowders were characterized by transmission electron microscopy (TEM), selected area electron diffraction (SAED), X-ray diffraction (XRD), energy dispersive X-ray analysis (EDX), and Mössbauer spectroscopy. The crystalline phases of the specimens (samples) were determined by XRD. The samples were scanned from $2\theta = 20$ to 85^{o} on a computer-controlled DRON DART UM2 diffractometer with a graphite monochromatized CuKα radiation in a step scan mode, with a step width of 0.050 and an acquisition time on each step of 5 s. For the phase identifications, the JCPDS file system was applied. The crystallite sizes were evaluated applying the Scherrer formula to the full width at half maximum (FWHM) of selected peaks. The instrumental errors are corrected beforehand. The FWHM values were extracted from the fitted profile spectra using Voigt functions. EDX was performed with an accuracy of 0.5 %, with a SiLi detector from EDAX Inc. inside a scanning electron microscope model Inspect S from FEI. The powdery deposits were imaged in a transmission electron microscope Philips CM120ST (Customized Microscope 120 Super Twin, 120 kV max. acceleration voltage, about 2 A resolution, Cs = ~1.2 mm). The samples were analyzed by the different electron microscopy techniques such as Bright Field TEM, SAED and HRTEM. The magnetization curves of nanopowders were determined using a vibrating sample magnetometer [VSM 880 ADE-DMS (USA)]. 57Fe Mössbauer spectroscopy was used for analyzing the samples at temperatures ranging from 80 to 280 K. Mössbauer spectra were collected in transmission geometry by inserting the sample in a liquid nitrogen bath cryostat. A Mössbauer drive system operating in constant acceleration mode combined with conventional electronics and a 57Co (Rh matrix) source of about 25 mCi activity, were used.

2.3 Nanostructured Iron Oxides

2.3.1 State of the Art

Very fine iron oxide nanoparticles have been the subject of numerous investigations and synthesis methods and drawn high interest with regards to the material science and their applications. Concerning the synthesis of ultrafine iron-oxide particles, several development routes have been followed so far. Methods such as conventional chemical processes, microwave plasma, pulsed laser ablation, pulsed laser-induced reaction, aerosol pyrolysis and continuous laser pyrolysis have been used.

In the following, the preparation and characterization of nano iron oxide-based materials obtained by three different handling procedures, is described: (a) The standard experimental procedure in which the oxidation process initiates and develops inside the laser-induced reaction zone by the simultaneous adduction of iron precursors and oxidizing agent (air); (b) A more complex experimental procedure in which the iron precursor is allowed to dissociate alone in the flame with a surrounding oxidizing atmosphere; (c) Core-shell iron–iron oxide nanoparticles using a variable nozzle geometry in which the established flows of precursor gases could maximize the desired particle morphology.

2.3.2 Iron Oxide Nanoparticles Obtained by Laser Pyrolysis Procedures

2.3.2.1 Iron Oxide Nanoparticles Obtained by Standard Laser Pyrolysis Procedure (SF–Type Samples)

In Fig. 2.1, a schematic general-purpose laser pyrolysis installation is depicted.

The flow reactor is the core of the laser pyrolysis technique, ensuring the practical application of the characteristic interplay between resonant and non-resonant processes. It was presented in details elsewhere (Majima et al. 1993). By using the same reactor set-up, the gas handling procedure of the active gas supply was varied, in order to modify the oxidation conditions. In a first set of experiments (labeled SF), a standard procedure was applied, in which the oxidation process initiates and develops inside the laser-induced reaction zone (the volume delimitated by the crossing of the radiation beam and the flow of reactive gases emerging through the nozzles where usually “a flame” appears). For producing iron oxide nanopowders in the standard procedure, the focused continuous wave CO_2 laser radiation (70 W maximum output power, $\lambda = 10.6\ \mu m$) orthogonally was made to cross the gas flows emerging through two concentric nozzles. The gas mixture which contained air and $Fe(CO)_5$ vapors (about 25 Torr vapor pressure at 20 °C) entrained by C_2H_4 was admitted through the central inner tube.

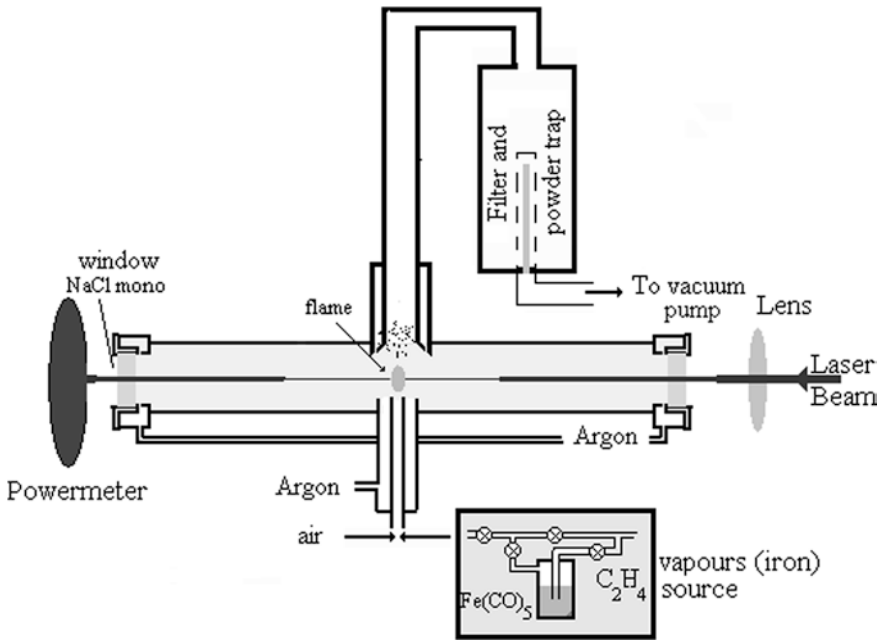

Fig. 2.1 Experimental set-up for obtaining nanometric iron oxides in a standard procedure

Table 2.1 Experimental parameters for the synthesis of iron oxides (SF- and F-type samples)

Sample	ϕ_{air} (sccm)	ϕ_{C2H4} (sccm)	P_L (W)	p kPa (mbar)
SF32	72	145	35	30 (300)
SF30	72	145	55	30 (300)
F5	100	300	25	30 (300)
F3	100	300	65	30 (300)

The confinement of gas precursors and of the freshly nucleated particles toward the flow axis is achieved by a coaxial argon flow. Iron oxide samples (SF32 and SF30) were obtained by varying the laser power between 35 and 55 W as presented in Table 2.1. The other experimental conditions, namely the reactor pressure, the relative flow of the oxidizing agent (air) and the flow of ethylene (as $Fe(CO)_5$ carrier), were maintained constant at 300 mbar, 70 and 145 sccm, respectively. In order to prevent the NaCl windows from being coated with powder they were continuously flushed with Argon.

2.3.2.2 Iron Oxide Nanoparticles Obtained by Laser Pyrolysis in a "Soft" Oxidation Procedure (F–Type Samples)

In a second set of experiments (labeled F), the vapors of $Fe(CO)_5$ (the iron precursor) entrained by ethylene emerge alone through the nozzle into the reaction chamber and are allowed to dissociate in the flame. At the same time, air (the

oxidizer agent) is introduced through the lateral outlets (100 sccm, located near the entrance windows), filling the entire reaction chamber, surrounding the flame and ensuring the oxidizing atmosphere for the freshly born iron fragments. A somehow similar procedure was applied by Veintemillas et al. (2001) and was termed "soft" oxidation. However, many experimental features (arrangement of gas flows and experimental parameters) in the actual procedure are different from (Kuncser et al. 2007). Thus, the iron fragments could suffer major oxidation after the laser focal point. The two representative F samples discussed here were obtained at different laser power densities (25 and 65 W). The pressure and carbonyl flow were kept constant. The experimental parameters needed for the preparation of both types of samples are presented in Table 2.1. Additional thermal treatment was applied to sample F5, by heating it in synthetic dry air. For this purpose, the temperature was increased at a rate of 20 °C/h, either to 120 °C or to 185 °C and maintained at these maximum temperatures for 2 h. The heated sample at 185 °C is hereafter labeled F5-185.

2.3.3 XRD Analysis of Nanoparticles

2.3.3.1 XRD Analysis of SF Nanoparticles

XRD analyses of SF nanoparticles are presented in Fig. 2.2. They exhibit rather broad peaks which could be assigned to the spinel-like iron (III) oxide, namely maghemite/magnetite iron phase. It is known that XRD alone is unable to differentiate between maghemite γ-Fe_2O_3 and magnetite Fe_3O_4 phases. The values of the

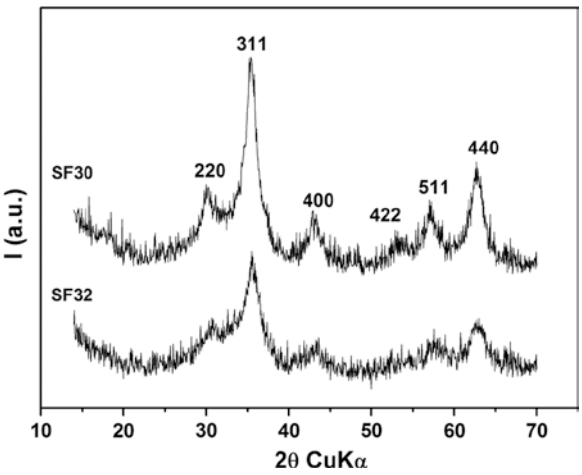

Fig. 2.2 Superposed X-ray diffractograms for SF iron oxide nanoparticles obtained at different laser powers (55 W-*upper curve* and 35 W-*lower curve*)

Table 2.2 Mean particle dimensions of the SF and F iron oxide nanoparticles, as estimated from XRD and TEM analysis

Sample	Scherrer crystallite dimensions D (nm) (from XRD analysis)			Mean particle diameter d_m (nm) (maxima of log normal distributions from TEM analysis)
	γ-Fe_2O_3/Fe_3O_4	α-Fe	Fe_3C	
SF32	3			4.5
SF30	4.2			5.9
F5	3.8	9.4	–	9.3
F3	4.4	14.4	13.0	10.6
F5 -185 °C	17.8	–	–	14.6

unit cell parameter **a,** as estimated from the (220) (311) (511) (440) reflections are $a = 0.836$ nm and $a = 0.837$ nm for samples SF30 and SF32, respectively.

The Scherrer crystallite dimensions for samples SF30 and SF32 are approximately 4.2 and 3 nm (Table 2.2).

The broadness of the diffraction lines may be associated with the formation of very small particles as well as with a high degree of structural/crystallographic disorder. The XRD analysis differentiates between the primary crystallites, which could further form agglomerates, but does not reveal extremely small particles, the so-called "amorphous" to XRD ones. For the samples prepared above the Scherrer crystallite dimensions measured via XRD are consistent with the mean particle dimensions measured via TEM analysis (Table 2.2), which suggests that the samples are formed mainly from primary particles.

2.3.3.2 XRD Analysis of F-Type Nanoparticle

XRD analysis of F-type nanoparticles is summarized in Fig. 2.3. The samples consist of a mixture of three iron-based phases: γ-Fe-$_2O_3$/Fe_3O_4 iron oxide, cementite Fe_3C and rather low-intensity, metallic Fe phase. The cementite Fe_3C phase is present in the sample as a mixture of both F_3C 34-0001 and F_3C 35-0772 (according to JCPDS file system). The corresponding peaks are marked in Fig. 2.3. The evaluation of the Scherrer mean crystallite size of sample F3 (Table 2.2) indicates values of about 4.4, 13 and 14.4 nm for the γ-Fe_2O_3/Fe_3O_4, Fe_3C, and α-Fe phases, respectively. An accurate differentiation between the various crystallographic phases is rendered difficult by the asymmetry of the line graph (mostly due to the overlapping peaks). The Fe peaks in particular, seem to be partially hidden by the dominant carbide phases. More information about the structural aspects of the chemical components of sample F3 can be derived from the Mössbauer analysis (see Fig. 2.3).

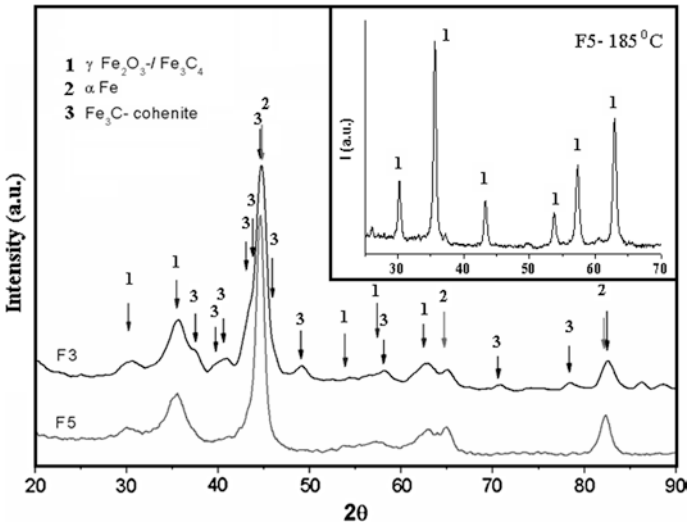

Fig. 2.3 XRD characterization of the as-synthesized samples F3 (*upper curve*) and F5 (*lower curve*). In the inset, the diffractogram of the heated F5 sample at 185 °C is presented

2.3.4 TEM Analysis

To obtain data on the particle composition, an EDX analysis was carried out for all SF and F samples (Table 2.3). A variety of scans over a wide sample area showed a rather constant concentration of Fe, O and C throughout the material. The Fe/O atomic ratio (last column in Table 2.3) for the samples SF32 and SF30 seems close to the value of bulk maghemite iron oxide of 0.67 atomic percent (at%). At the same time, the increased Fe/O ratio for samples F3 and F5 could account for the co-existence of the iron oxide with other Fe compounds (such as iron carbides and/or metallic iron). Most probably, the presence of carbon is mainly due to the synthesis method, in which unwanted decomposition of C_2H_4 could occur. This process increases significantly with increased reaction temperature (i.e., increased laser power). We may therefore observe that the carbon content increases from 9.8 to 13.8 at% for laser powers of 35 and 55 W (sample SF32 vs. SF30) and from 15.6 to 24.5 at% for laser powers of 25 and 65 W (sample F5 vs. F3).

The TEM analysis of samples SF32 and SF30 reveals an almost polycrystalline morphology (Fig. 2.4a, b). The nanoparticles show coalescent features. Cross-linked chains may sometimes be observed. The image of SF30 displays mostly faceted particles. Rather spherical nanoparticles (form factor $k = 0.86$) are revealed for sample SF32. The left insets in Fig. 2.4 present the histograms of particle size distributions. By a lognormal fitting, rather sharp particle diameter

Table 2.3 Comparative EDAX analysis of SF and F samples

	Fe_K (at%)	O_K (at%)	C_K (at%)	Fe/O
SF30	32.1	54.1	13.8	0.59
F3	47.2	28.3	24.5	1.67
SF32	35.1	55.1	9.8	0.64
F5	51.9	32.5	15.6	1.60

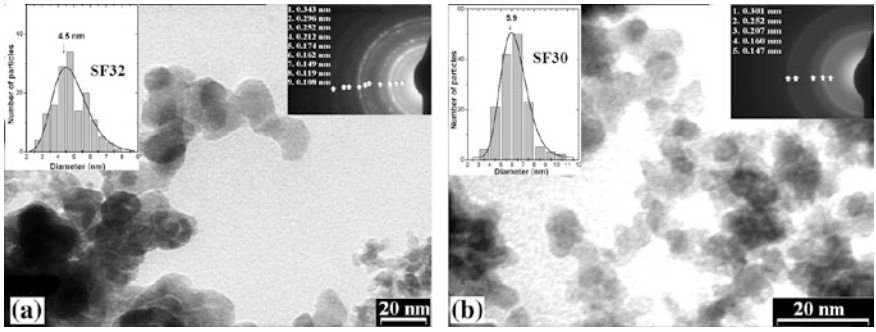

Fig. 2.4 TEM analysis of iron oxides obtained from: **a** sample SF32 and **b** sample SF30. The particle size distributions are presented inside the left insets. SAED patterns of samples SF32 and SF30, revealing main diffraction rings of maghemite/magnetite are presented inside the right insets

distributions are found, with maxima at $dm = 4.5$ and 5.9 nm, for SF32 and SF30. A tendency for increased mean particle diameter with increasing laser power may be observed.

An SAED analysis for both SF samples (presented inside the right insets in Fig. 2.4a, b) shows the cubic structure of the iron oxide, namely maghemite/magnetite. For both samples the strong diffraction rings at 0.25 and at 0.14 nm are noticed. As mentioned before, it is difficult to differentiate between these phases by using only diffraction techniques due to the closed values of their reflections. The electron diffraction pattern of sample SF32 (Fig. 2.4a) shows rather diffuse and blurred rings that possibly point to an incomplete crystallization and/or structural defects inside the nanograins. The nanomaterial obtained at higher laser power seems to be characterized by an increased crystallinity. This can be considered as a consequence of both the higher temperature gradients in the reaction zone and the fast quenching of the condensed nanoparticles in the condensation zone of the laser pyrolysis.

A TEM analysis of samples F3 and F5, obtained by the second oxidation procedure, are presented in Fig. 2.5a, b, respectively. Both samples reveal morphologies consisting of a majority of core-shell particles, with various thicknesses of the shells. The nanoparticles show coalescent features and cross-linked chains.

The right insets in Fig. 2.5 present the histograms of particle size distributions. In the case of the high power synthesis of samples F (Fig. 2.5a), a mean diameter

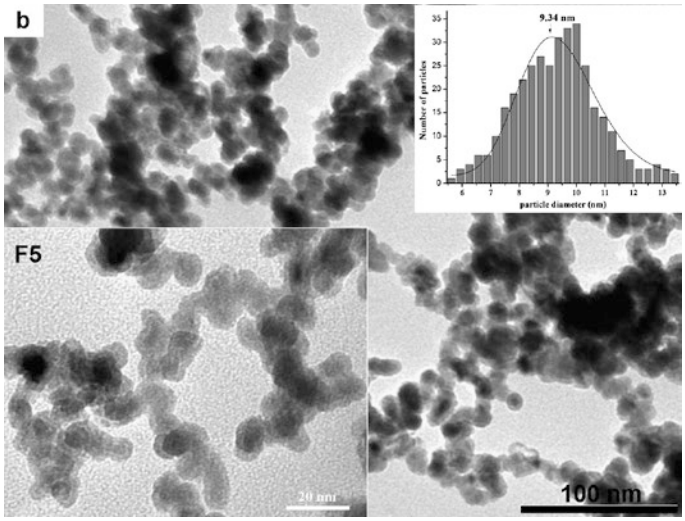

Fig. 2.5 TEM analysis of iron oxides obtained from: **a** sample F3 and **b** sample F5. The particle size distributions are presented inside the right insets

of about 10.6 nm is estimated. There is a decrease of the mean particle diameter with decreased laser power (not presented here). Broader particle distributions are found for samples F compared to those of samples SF (extending to about 10 nm).

2.3.5 Magnetic Properties of the Iron Nano-Oxide Particles Produced by Laser Pyrolysis

Magnetization curves obtained at 300 K for the representative samples of the SF and F series are displayed in Fig. 2.6 in the range from −800 to 800 kA/m. It shows the variation of magnetization *M* as a function of externally applied magnetic field *H* (measured *in* the SI units).

It is worth mentioning that none of the samples are saturated at the maximum available field of 800 kA/m. Excepting the ferrimagnetic type of coupling, this behavior can be considered at a certain extent also an evidence for a disordered spin configuration, connected with the defected structure inside nanoparticles and in agreement with the Mössbauer data (see Fig. 2.6). The magnetization at the maximum field has been denoted as M_S (specific magnetization). The specific magnetization of the SF30 sample, 46 emu/g, is much larger than for the other SF sample (16 emu/g for SF32). Two reasons might contribute to the rather different specific magnetization of the samples: either a different magnetic phase composition or a different "magnetic disorder" connected to a different structural disorder. More defects and lattice disorders in SF32 compared to SF30 seem likely when considering the XRD diffraction patterns as well as the lower average size of the particles in SF32.

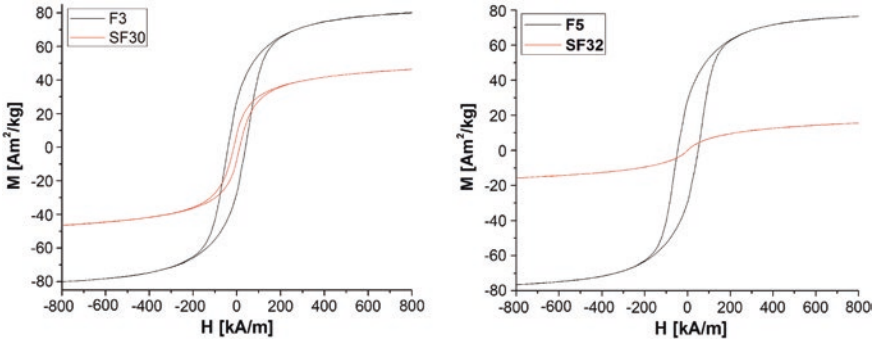

Fig. 2.6 Magnetization of the high-power laser samples SF30 and F3 (*upper curves*) compared to low-power laser samples SF32 and F5 (*lower curves*)

On the other hand, M_s has significantly higher values for F3 and F5 (80 and 78.5 emu/g, respectively) when compared to the SF samples. Here, the effect of the α-Fe phase, whose presence in the F samples was revealed by a XRD analysis, has to be considered (the room temperature magnetization for bulk Fe is about 220 Am^2/kg[23]). With regards to the coercivity, it is worth noting that the higher values obtained for F samples (40–48 kA/m) are in agreement with the agglomeration of the larger particles in those samples, giving rise to extended magnetic domains. On the other hand, the SF samples show either a superparamagnetic behavior of mono-domain nano-particles (H_c is about zero for sample SF32), or a mixture of superparamagnetic particles and agglomerated particles giving rise to less pinned magnetic domains ($H_c = 13$ kA/m for sample SF30).

For samples SF32 and SF30, the study of the Mössbauer spectra and of the derived blocking temperatures (of about 200 and 400 K, respectively) was performed [for more details see reference Teunissen et al. (2001)] Accordingly, average particle sizes of about 7 and 9 nm were estimated for samples SF32 and SF30 by considering noninteracting nanoparticles and average magnetic anisotropy constants of bulk magnetite and maghemite (Dumitrache et al. 2005). These average magnetic sizes are almost double compared to the above mentioned physical (TEM) and structural (XRD) ones.

2.4 Core-Shell Iron-Carbon Nanocomposites

2.4.1 State of the Art

In the following, we focus on magnetic iron-core carbon-shell nanoparticles. The major role of the nonmagnetic shell is to protect the functional core from damaging environments like oxygen, as well as to render the nanoscopic colloids water-soluble or even make them compatible with biological media (Hare et al. 1996). A better alternative to the polymer and silica coatings often employed in

literature is represented by coating with carbon-based materials. These coatings have the major advantage of a higher chemical and thermal stability and are in addition biocompatible. Well-developed graphitic carbon layers can be formed around metal nanoparticles by arc-discharge, laser ablation and electron irradiation, using a variety of organic molecules as the carbon source. These carbon layers provide effective barriers against oxidation and acidic corrosion. Moreover, they are easily formed around metal nanoparticles, which are usually more difficult to coat than corresponding oxides but have better magnetic properties. Unfortunately, carbon-coated nanoparticles are often not obtained as well-defined monodisperse cores but as agglomerated clusters since their formation mechanism and synthetic methods are not yet fully understood. Therefore, the preparation of dispersible well-defined carbon-coated core–shell nanoparticles still provides a major challenge in this field. Carbon nano-capsules, filled with metal nanoparticles, have been produced by arc-discharge, ion-beam sputtering methods, via solid-state reaction and chemical methods.

Recently, we have reported the successful fabrication of carbon-encapsulated iron nanoparticles by laser pyrolysis from gas phase precursors (Scheart 2010). The focused continuous wave CO_2 laser radiation (output power maximum 85 W, $k = 10.6$ lm) was orthogonally crossed with the reactant gas stream that was admitted to the center of the reaction cell through a triple nozzle system (Fig. 2.7).

The four representative Fe@C samples (labeled CF40–CF43) are presented in Table 2.4. They were obtained at different internal diameters of the central nozzle (varying from 0.55 to 1.5 mm). C_2H_4 was used as sensitizer. It absorbs the energy from the CO_2 laser radiation and transfers it by collision to the other reaction partners. The laser power, the pressure in the reaction cell, the flows of acetylene and ethylene were maintained at 85 W, 650 mbar, 100 and 30 sccm, respectively. The flame temperature was monitored with an optic pyrometer.

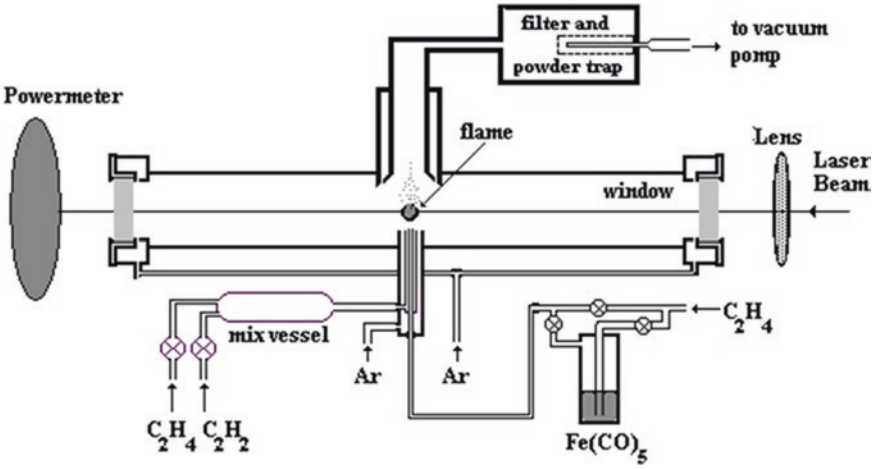

Fig. 2.7 Schematic of the laser pyrolysis installation for the synthesis of Fe@C nanocomposites

Table 2.4 Experimental parameters for the laser synthesized CF samples[a]. The element analysis (EDAX) and the mean crystallite sizes as evaluated from XRD analysis

Sample	C_2H_4 through $Fe(CO)_5$ sccm	C_2H_4 (middle) sccm	Internal nozzle diameter mm	τ Estimated residence time (10^{-3} s)	EDAX At%			XRD—Mean crystallite sizes (nm)	
					Ck	Ok	Fek	α-Fe	FexCy
CF40	50	30	0.55	0.22	76.80	13.30	9.9	10.5	1.4
CF41	50	30	0.9	0.59	81.36	8.77	9.73	10.0	1.5
`CF42	50	30	1.3	1.21	78.10	7.30	14.60	22.3	2.3
CF43	50	30	1.5	1.50	72.86	8.18	18.96	25.0	8.4 (Fe3C phase)

[a]The total pressure (650 mbar), the laser power (85 W), the acetylene flow (100 sccm) and the Argon flows (for confinement and windows clearing) were maintained constant (1,100 and 150 sccm, respectively)

The element compositions (Fe, C and O) were evaluated via X-ray energy dispersive analysis (EDAX) and are presented in Table 2.4. One may observe the large carbon quantity (around 70–80 at%) which probably enters in the carbon matrix surrounding iron-based nanoparticles (partly as iron carbides). In this respect, it is worth noting that the EDAX reveals the highest iron content in the sample with the larger nozzle (sample CF43).

In order to describe the growth of Fe@C nanoparticles in the laser pyrolysis, we refer to a model for the formation of SiC, proposed in 1994 by Lihrmann and Cauchetier which is based on the decomposition of the reactants in the laser pyrolysis flame, followed by growth from collisions and coalescence (Lihrmann and Cauchetier 1994). Thus we consider that intermediate species such as Fe and C are assumed to play a key role in the growth process. The size of the final nanoproducts is evaluated from the residence time within the flame. The residence time inside the flame is considered equivalent to the time of residence in the laser beam (t) and can be estimated from the total gas flow velocity (v), $t = d/v$, where d is the diameter of the laser beam (0.4 cm). The velocity v is considered proportional to the gas flow rate (in cm^3/min) and to the temperature T (K) and inverse proportional to the nozzle surface (cm^2) and to the working pressure P (mbar) (Dumitrache et al. 2003). Even if C_2H_4 plays the role of a sensitizer in the precursor mixer, its partial decomposition cannot be overruled and could contribute to the graphenic sheets of the particle coverage.

2.4.2 XRD Analysis

A comprehensive XRD analysis of the four generic Fe@C samples first analyzes the common features of samples CF40, CF41 and CF42. The diffractogram for sample CF40 is presented in Fig. 2.9 and reveals a large peak in the 2 θ 40–46 domain, in which the higher intensity peak of α-Fe (2 θ = 44.712) overlaps the characteristic region of iron carbide. The broad maximum characterizes a quasi-amorphous iron/iron carbide phase [FeC, Fe_2C, Fe_7C_3 or Fe_3C (with lower carbon content)], possibly indicating that transformation and constitution/crystallization processes occur in the region of the iron carbide maxima. Also visible are the other two peaks of α-Fe (at 2θ = 65.082 and 82.146). In Fig. 2.9, where the two XRD patterns of samples CF40 and CF43 are superposed, the large peak in the region of the iron carbide maxima phases (they are labeled Fe_xC_y in Table 2.4) is also presented. The diffraction pattern of sample CF43 exhibits a higher crystallinity than that of sample CF40 (Fig. 2.8).

The estimation of mean crystallite dimensions (the values are listed in Table 2.4) was performed using the Scherrer formula. The Voigt function was used for the approximation of the profile maximum at 2θ = 44.712. When looking at the estimated values of the Fe crystallite dimensions of sample CF43, one finds that they are higher than for sample CF40. Larger mean crystallite sizes are revealed, whose dimensions slightly increase with the increased nozzle diameter (from about 10 nm to about 25 nm, for sample CF40 to CF43). It is however

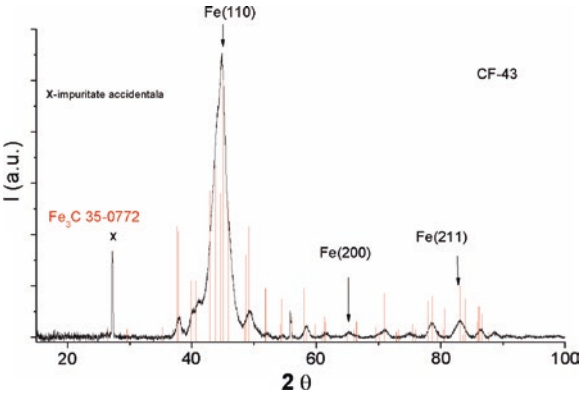

Fig. 2.8 The XRD analysis of sample CF43. Marked with red are the characteristic diffraction peaks of Fe_3C cementite

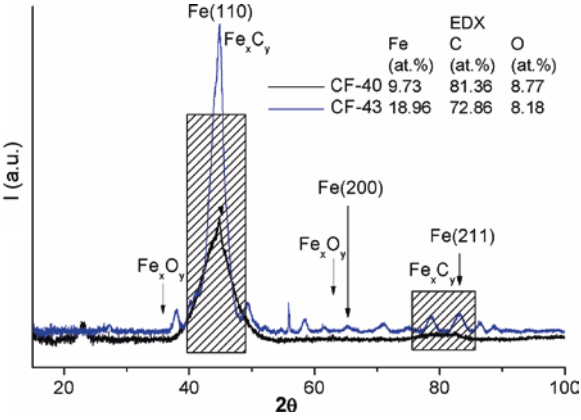

Fig. 2.9 Comparison between the diffraction patterns of samples CF40 and CF43. Dashed contours separate the characteristic diffraction regions of Fe_3C. The inset presents the elemental values given by EDX analysis for the two samples

possible that only a minor part of the Fe phase is represented by large Fe crystallites while a more amorphous Fe phase could be represented by much smaller crystallites, which are not detected by the XRD analysis. We could characterize the material as constituted by very low dimension crystalline domains, which do not extend enough to form a defined crystalline phase. In case of sample CF43, the carbide phase clearly indicates the formation of the crystalline Fe_3C-cementite phase, with higher Fe_3C mean crystallite dimensions (about 8.4 nm diameter).

2.4.3 TEM Analysis

TEM analysis of the nanocomposite morphology reveals mostly particles that seem encapsulated in an amorphous matrix. TEM images of samples CF40 and CF43 are presented in Fig. 2.10a, b, respectively.

The histograms (lognormal fit) of particle size distributions are presented in Fig. 2.11. Rather sharp particle diameter distributions are found, with maxima

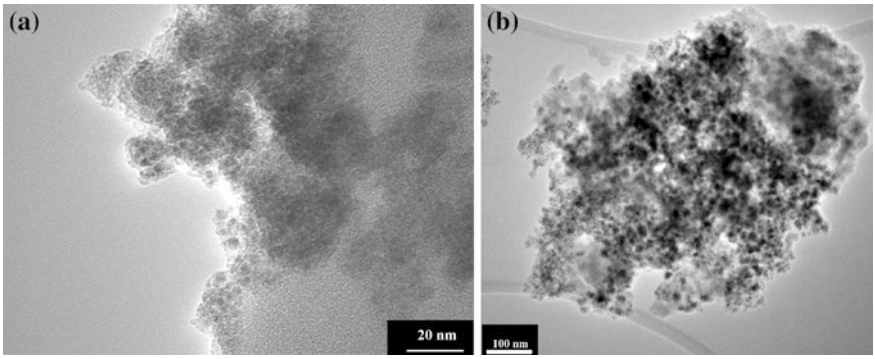

Fig. 2.10 TEM images of samples CF40 (**a**) and CF43 (**b**)

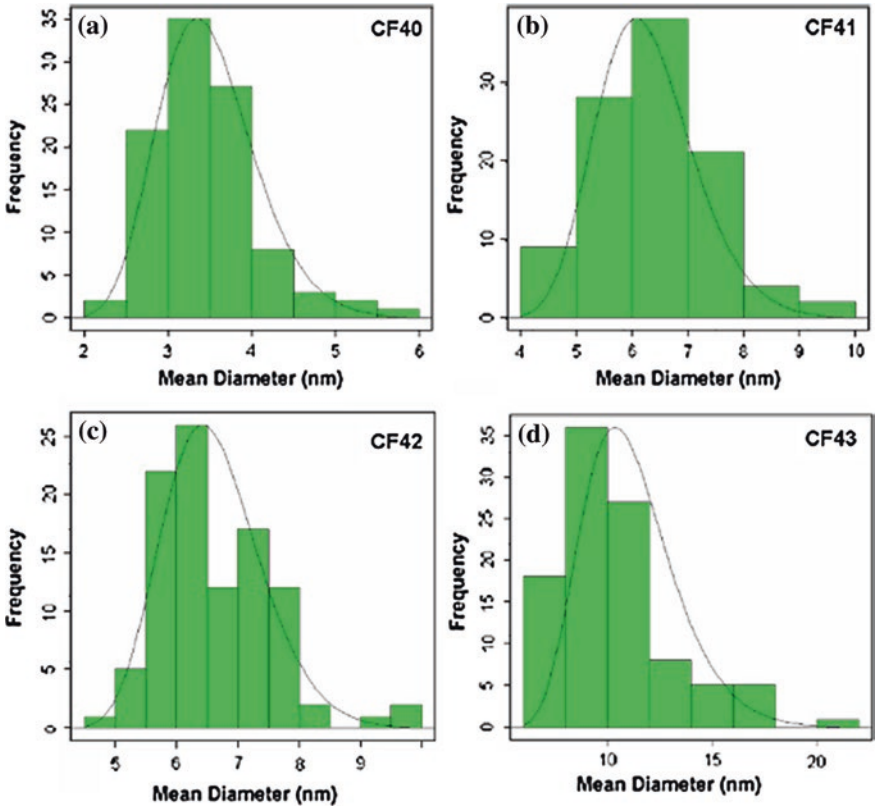

Fig. 2.11 **a, b, c** and **d**. Particle size distributions for the representative samples, evidencing increased mean particle diameter (from around 3.5 nm to around 10.5 nm) with increasing diameter of the inner nozzle

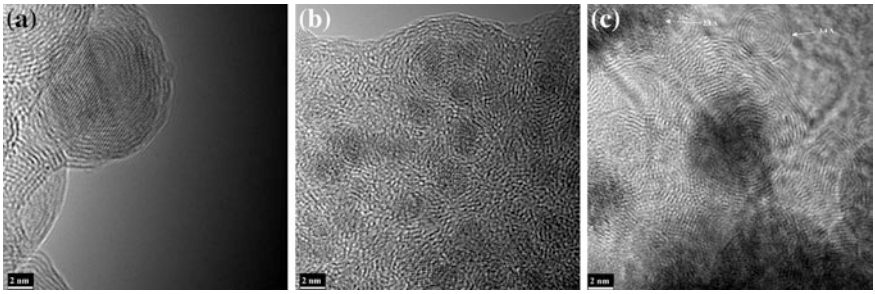

Fig. 2.12 HRTEM images of the sample CF43: well distinguishable round iron core of about 11 nm diameter (showing an identified interplanar distance of d = 2.1Å for Fe/Fe_3C) surrounded by graphene layers (a); agglomerated iron-based nanoparticles (dark contrasts) separated by a varying number of graphene sheets

at about d_m = 3.5, 5.7, 6.4 and 10.5 nm, for CF40, CF41, CF42 and CF43, respectively. An increasing mean particle diameter with increasing internal nozzle diameter may be noticed.

HRTEM images of the CF43 nanoparticles are presented in Fig. 2.12. The sample reveals a morphology consisting of a majority of core–shell particles, with various thicknesses of the shells. Agglomerated iron-based nanoparticles (dark contrast) separated by a varying number of graphene sheets and onion-like shape of the surrounding carbonaceous layers often appear. In Fig. 2.12a, the well distinguishable round iron core (of about 11 nm diameter) shows an identified interplanar distance of $d = 2.1$ Å (which belongs to Fe/Fe_3C cementite). This core is surrounded by about eight graphene layers with identified interplanar distance of $d = 3.5$ Å, which is close to that of the graphitic carbon.

2.4.4 Magnetic Analysis

The magnetization curves obtained at 300 K for the representative Fe@C samples are displayed in Fig. 2.13a in the range from −800 to +800 kA/m and in Fig. 2.13b in the range from −25 to +25 kA/m (detail around the origin). They show the variation of the magnetization M as a function of the external applied magnetic field H. One may observe that for the samples CF40 and CF41 the hysteresis loops are missing. The superparamagnetism of these samples is largely due to their mean particle dimensions (equal or much less than 10 nm, for the Fe and the iron carbide phases, respectively, as determined by XRD). The magnetization at the maximum field has been denoted as MS (saturation magnetization). The saturation magnetization of 65.9 emu/g of the sample CF43 is much greater than that for the other CF samples, particularly of sample CF40 (28.38 emu/g). More defects and lattice disorder in CF40 in comparison to CF43 can be assumed. It is worth mentioning that none of the samples are saturated at the maximum available field of 800 kA/m.

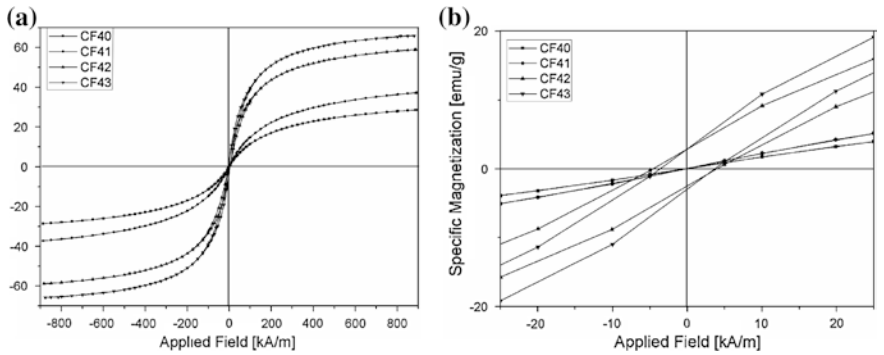

Fig. 2.13 Magnetization curves of the Fe@C samples obtained by laser pyrolysis with different diameters of the internal nozzle (**a**). Detail from Fig. 2.13 for the domain -25 kA/m $\leq$ H $\leq$ 25 kA/m (around origin) (**b**)

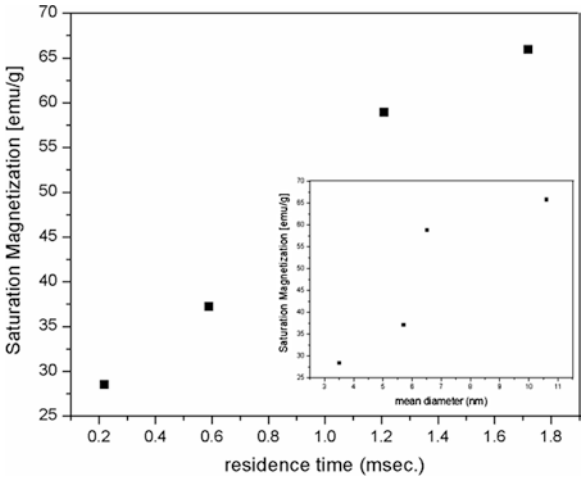

Fig. 2.14 The variation of the saturation magnetization (in A m^2/kg) of Fe@C nanoparticles with the residence time. The inset displays the increasing trend of the saturation magnetization with increasing Fe@C mean particle size

This behavior can be considered at a certain extent also an evidence for a disordered spin configuration. As to the magnetic disorder, more defects and lattice disorder in CF40 compared to CF43 are easily explained by the XRD diffraction patterns. One may observe a direct correlation between the residence time in the laser beam and the saturation magnetization (see Fig. 2.14). For all four representative samples discussed here, the magnetization M at the maximum H values increases as the residence time increases, i.e., the dominance of a mixture of crystalline cementite-iron carbide and of the α-Fe phase becomes apparent. Here we can refer to the literature (Madler et al. 2002) where a saturation magnetization value of 110 emu/g was found. On the other hand, the effect of the α-Fe phase (with a higher contribution in sample CF43, as revealed by XRD analysis) has to be considered (the room temperature magnetism).

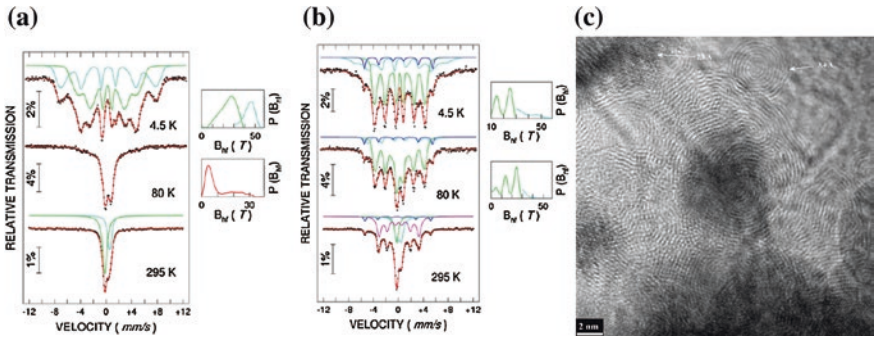

Fig. 2.15 Mössbauer spectra at different representative temperatures for sample CF40 (**a**); Mössbauer spectra at different representative temperatures for sample CF43 (**b**)

The Fe phase composition was studied by a temperature dependent ^{57}Fe Mössbauer spectroscopy. Figure 2.15a, b present the Mössbauer spectra for samples CF40 and CF43, respectively. The derived probability distributions of the hyperfine field are presented at the right side of the figures. By means of a Mössbauer spectroscopy one can perform a phase analysis of the magnetic component as well as an analysis of the magnetic relaxation. This is especially valid at low temperatures where spin dynamic effects may be eliminated. In case of nanoparticles with distributions of particle dimensions, it is possible to have different phase compositions for particles of different sizes. The phase information obtained at low temperatures should be correlated with the development of the magnetic relaxation.

Sample CF43 (Fig. 2.15b), obtained at the largest diameter of the inner nozzle, presents three distinct phases, i.e., the two phases mentioned before (for CF40) and another phase which is characterized in the Mössbauer spectrum by a sextet with a hyperfine field of 34 T, specific to the bcc iron. The 4.5 K spectrum evidences 27 % oxide phase, 6 % bcc iron and 67 % iron carbide. The probability distribution corresponding to the carbide phase presents two peaks (at 15 T and at 24 T), which suggest the superposition of two phases (a major cementite Fe_3C phase and another carbide phase Fe_5C_2). At room temperature, the oxide phase appears in a magnetically relaxed state. As to the carbide phase, only about 15 % is in a relaxed phase while 50 % of it, together with the 7 % iron phase, remains ferromagnetic. This behavior could indicate the presence of two particle types, namely oxide particles with a blocking temperature below 80 K and particles of carbides and carbides with metallic cores, with a blocking temperature above 100 K.

If we analyze the ratio of iron carbide to bcc iron at different temperatures we may deduce that the magnetic relaxation mainly affects the carbide phase while the iron-containing carbide phase relaxes at much higher temperature. Summarizing, at 295 K, the oxide particles, as well as a fraction of 15 % of the carbides, are superparamagnetic. The rest of the particles (6 % metallic Fe and 50 % iron carbide—most of them with core–shell structures) are ferromagnetic at room temperature.

2.5 Conclusion

Iron-based nanomaterials have found applications in many areas of science and technology due to their unique magnetic properties. A size reduction of these materials from bulk to the nanoscale allows them to display various size related properties. Among other changes, a significant decrease in size can alter reactivity, increase surface area and change the magnetic properties.

The synthesis of iron oxide-based nanomaterials by laser pyrolysis has been achieved by a handling procedure (standard), in which the oxidation process initiates and develops inside the laser-induced reaction zone (samples SF). In a second step, a more complex experimental procedure is used, in which the iron precursor is allowed to dissociate alone in the flame with a surrounding oxidizing atmosphere (samples F).

XRD and TEM analyses reveal a major content of maghemite/magnetite in samples SF. A mixture of three iron-based phases, namely γ-Fe-$_2O_3$/Fe_3O_4 iron oxide, cementite Fe_3C and metallic Fe phase is found in samples F. The relative proportion of these phases depends on the reaction temperature (laser power). Agglomerated core-shell structures are often observed. For both kinds of samples, the crystallinity (crystallographic order) is enhanced by increasing the laser power. As determined by TEM, mean particle sizes depend on the laser power density and vary between about 4 and 6 nm for samples SF and between about 9 and 11 nm for samples F. By controlled heating of samples F (maximum temperature 185 °C), a pure crystalline maghemite/magnetite oxide phase was found as well as an increase of mean particle diameters.

Looking at the hysteresis loops at room temperature, one finds that the saturation magnetization values of samples F are much higher (about 80 Am^2/kg) compared to the samples SF (between 16 and 46 Am^2/kg). Depending on the laser power, either superparamagnetic or a superposition of superparamagnetic and ferromagnetic behavior are exhibited by the samples SF at room temperature. Agglomerations of the larger particles give rise to a magnetic domain structure and to enhanced coercive forces in samples F.

The temperature dependent Mössbauer measurements confirm the formation of larger particles at higher laser power densities as well as the presence of interparticle magnetic interactions. For samples SF, more than 90 % of the particles are formed by defected maghemite/magnetite mixtures and only 5–10 % are of cementite. The much lower specific magnetization, as compared with the expected one from the Mössbauer phase composition, is due to a large quantity of defected structures of the nanoparticles.

Well crystallized Fe phases are observed in the F samples. Regarding the oxide phase in sample F5, the particles are either fully oxidized or they form a core (α-Fe)-shell (Fe oxide) structure. Relatively thicker oxide shells are found for higher laser power densities, when larger particles are formed. The rest of the particles (about 15 %) are made up by defected cementite. For sample F3 a more complex composition is deduced comprising of an α-Fe phase (17 %) surrounded

by Fe-oxide shells (10 %) fully oxidized superparamagnetic particles (30 %) and a well crystallized cementite phase (14 %) surrounded by defected cementite (30 %).

In a third step, we have demonstrated the synthesis of iron-core oxide-shell nanocomposite by a two-step method: the laser pyrolysis of an iron pentacarbonyl and ethylene mixture followed by a controlled step-by-step passivation process. Iron particles with 14 nm mean diameter and about 4 nm oxide shell thickness were produced. The morphology of the nanocomposite particles was determined. They are made up by an α-Fe core surrounded by an γ-Fe_2O_3/Fe_3O_4 shell.

Based on the versatility of the laser technique (exemplified here by different oxidizing processes based on gas-handling procedures) further variations of the experimental conditions are pursued in order to prepare optimized magnetic iron-based nanostructures.

Iron-based carbon core–shell Fe@C nanostructures were produced by the one-step laser pyrolysis technique. An acetylene/ethylene mixture was used as carbon precursor. The possibility to vary the chemical content and the nanoparticle dimensions by varying the nozzle diameter of the emergent reactive gas flow (from 0.55 to 1.5 mm diameter) is demonstrated. The XRD analysis shows that at increased nozzle diameter, an increased ordering of the crystallographic network is apparent, with dominant α-Fe and Fe3C iron carbide phases. EDAX reveals the highest Fe content for the sample produced with the larger nozzle diameter. TEM images of the Fe@C particles and the histograms of the particle size distributions suggest the increase of the particle diameter (from about 3.5 to 10.5 nm) with increasing nozzle diameter. Onion-like surrounding graphenic layers often cover the buried iron-based (Fe/Fe_3C) cores. The magnetic measurements of the composite nanoparticles indicate an almost direct correlation between the residence time in the laser beam and the saturation magnetization. Complementary details of the Fe phase composition and the superparamagnetic character of the samples are provided by the Mössbauer analysis. Experiments for obtaining stable water-based magnetic nanofluids from Fe@C nanoparticle precursors are under way.

References

Abhilash, K Revati, Pandey BD (2011) Microbial synthesis of iron-based nanomaterials for bimedical applications—review. Bull. Mater. Sci., 34(2):191–198 (J. Phys.: Conf. Ser. 332 012042)

Baena J, Marulanda JI (2011) Analysis of chemical processes for the synthesis of magnetite for biomedical applications. J Phys: Conf Ser 332:012042

Blanco-Andujar C, Tungc LD, Thanhab NTK (2010) Synthesis of nanoparticles for biomedical applications. Annu Rep Prog Chem, Sect A 106:553–568

Bolden NW, Rangari VK, Jeelani S, Boyoglu S, Singh SR (2013) Synthesis and evaluation of magnetic nanoparticles for biomedical applications. J Nanopart 2013, Article ID 370812 (9 pages)

Bomatí-Miguel O, Zhao XQ, Martelli S, Di Nunzio PE, Veintemillas-Verdaguer S (2010) Modeling of the laser pyrolysis process by means of the aerosol theory: case of iron nanoparticles. J Appl Phys 107:014906(7 pages)

Cannon WR, Danforth SC, Flint JH, Haggerty JS, Marra RA (1982) Sinterable ceramic powders from laser driven reactions, Part 1: Process description and m odeling. J Am Ceram Soc 65:324

Dumitrache F, Morjan I, Alexandrescu R, Ciupina V, Prodan G, Voicu I, Fleaca C, Albu L, Savoiu M, Sandu I, Popovici E, Soare I (2005) Iron-Iron oxide core –shell nanoparticles synthesized by laser pyrolysis followed by superficial oxidation. Appl Surf Sci 247:25–31

Dumitrache F, Morjan I, Alexandrescu R, Morjan RE, Voicu I, Sandu I, Soare I, Ploscaru M, Fleaca C, Ciupina V, Prodan G, Rand B, Brydson R, Woodword A (2003) Nearly monodispersed carbon coated iron nanoparticles for the catalytic growth of nanotubes/nanofibres. Diam Relat Mater 13(2):362–370

Einar Kruis F, Fissan Heinz, Peled Aaron (1998) Synthesis of nanoparticles in the gas phase for electronic, optical and magnetic applications—a review. J Aerosol Sci 29(5–6):511–535

Hare JP, Hsu WK, Kroto HW, Lapas A, Prassides K, Terrones M, Walton DRM (1996) Nanoscale encapsulation of molybdenum carbide in carbon clusters. Chem Matter Commun 8:6–8

Kuncser V, Schinteie G, Sahoo B, Keune W, Bica D, Vékás L, Filoti G (2007) J Phys: Condens Matter 19:016205

Lihrmann SJM, Cauchetier M (1994) A model for the formation of nanosized SiC powders by laser induced gas phase reaction. J Eur Ceram Soc 13:41. (Studies of Fe(CO)5

Madler L, Kammler HK, Mueller R, Pratsinis SE (2002) Controlled synthesis of nanostructured particles by flame spray pyrolysis. J Aerosol Sci 33(2):369–389(21)

Majima T, Matsumoto Y, Takami M (1993) On the SF6-sensitized IR photodecomposition of Fe(CO)5: 5 μm transient absorption measurements and absorption energy measurements. J Photochem Photobiol, A 71:213

Scheart Wolfgang (2010) Current directions in core–shell nanoparticle design. Nanoscale 2:829–843

Shikwambana L, Govender M, Mwakikunga B, Sideras-Haddad E, Forbes A (2011) A review of the laser pyrolysis technique used to synthesize vanadium and tungsten oxide thin films. Adv Mater Res 227:80–83

Srdic VV, Winterer M, Hahn H (2000) Sintering behavior of nanocrystalline zirconia prepared by chemical Vapor synthesis. J Am Ceramic Soc 83:729

Swihart MT (2003) Vapor-phase synthesis of nanoparticles. Curr Opin Colloid Interface Sci 8:127

Teunissen W, de Groot FMF, Geus J, Stephan O, Tence M, Colliex C (2001) The structure of carbon encapsulated NiFe nanoparticles. J Catal 204:169–174

Veintemillas-Verdaguer S, Morales MP, Serna CJ (2001) Appl Organomet Chem 15:365

Chapter 3
Hydrophobic and Hydrophilic Magnetite Nanoparticles: Synthesis by Chemical Coprecipitation and Physico-Chemical Characterization

Vlad-Mircea Socoliuc and Ladislau Vékás

Abstract The building blocks for the fabrication of biocompatible magnetoresponsive carriers are the subdomain magnetite nanoparticles surface coated by biocompatible molecular layers which ensure their stabilization and dispersion in an appropriate carrier liquid, in order to obtain stable magnetic nanofluids that are the primary materials for the envisaged magnetic nanocomposites. The synthesis by chemical coprecipitation is the most simple and cost effective route to obtain hydrophobic and hydrophilic magnetite nanoparticles at industrial scale. Manifold physico-chemical characterization of the magnetic nanofluids is employed in order to certify their requested composition and structure.

3.1 Introduction

Polymer-magnetic nanocomposite particles have received continuously increasing attention during the last years due to their widespread potential applications in biotechnology and biomedicine. High magnetic moment, nano- or micron-sized carriers with superparamagnetic behavior and various added functionalities provide advanced therapeutic, diagnostic or bioprocessing capabilities (Dave and Gao 2009; Reddy et al. 2012). The strongly magnetoresponsive character and appropriate design of surface properties are among the main requirements for nano- or micro-adsorbents to be used in magnetic bio-separation processes, such as protein purification (Müller et al. 2011) involving high gradient magnetic separation (HGMS) steps (Brown et al. 2013). The building blocks for the fabrication

V.-M. Socoliuc (✉) · L. Vékás
Romanian Academy-Timisoara Branch, Center for Fundamental and Advanced Technical Research, Mihai Viteazul Street 24, 300223 Timisoara, Romania
e-mail: vsocoliuc@gmail.com

H. Nirschl and K. Keller (eds.), *Upscaling of Bio-Nano-Processes*,
Lecture Notes in Bioengineering, DOI 10.1007/978-3-662-43899-2_3

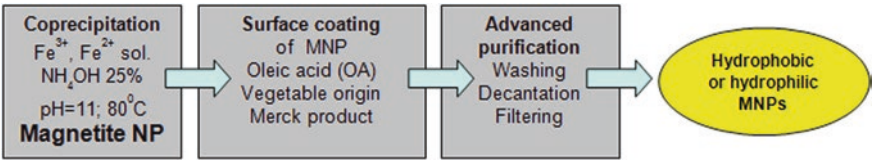

Fig. 3.1 Synthesis by chemical coprecipitation of oleic acid coated magnetite nanoparticles (main steps)

of magnetoresponsive microcarriers are the *subdomain magnetite nanoparticles surface coated by biocompatible molecular layers*, such as carboxylic (lauric, myristic, oleic) acids, which ensure their stabilization and dispersion in an appropriate carrier liquid, to obtain *stable magnetic nanofluids*—the primary materials for the envisaged magnetic nanocomposites. Controlled clusterization of magnetite nanoparticles from well stabilized magnetic nanofluids is a widely applied procedure to synthesize polymer-magnetic nanoparticles hybrid microspheres with sizes well above 50 nm displaying both high magnetic moment and superparamagnetic behavior (Banert and Peuker 2006; Darwish et al. 2011; Vékás et al. 2011). The above procedure ensures the transfer of superparamagnetic behavior specific to magnetic nanofluids to the micrometer-sized beads, which is an essential requirement for most of the applications, in particular for magnetic bio-separation.

The synthesis by chemical coprecipitation of hydrophobic and hydrophilic magnetite nanoparticles (Fig. 3.1) as stable dispersions in appropriate carriers, i.e., magnetic nanofluids, will be presented in this chapter, together with the results of manifold investigations of their structure and properties, relevant for the preparation of magnetoresponsive microspheres.

The surfactant coating on magnetic nanoparticles prevents, due to steric repulsion, the surface-to-surface contact and irreversible clustering of particles. The stabilization and dispersion of nanoparticles in organic liquids or water using various chain length organic surface-active molecules (e.g., fatty acids, polymers), i.e., steric stabilization, is dependent on the liquid carrier properties. During preparation, repulsive forces between magnetic cores are introduced by the coating to prevent irreversible aggregation of particles produced by attractive van der Waals and magnetic dipolar interactions. The colloidal stability of magnetic nanofluids obtained by dispersing magnetic nanoparticles in various carrier liquids is dependent on the interplay between isotropic van der Waals and anisotropic dipolar forces (Rosensweig 1985). The relative strengths and ranges of various interaction potentials can be controlled by the diameter of magnetic cores and the thickness and nature of the stabilizing layer, depending also on the nonpolar or polar character of the carrier. In order to keep the energy of attractive interactions less than the thermal energy, i.e., to ensure the colloidal stability of the nanofluid, the mean size of magnetite nanoparticles should be less than 10 nm. An important consequence of this size range is that the resulting magnetite nanoparticle systems (nanofluids, nanocomposites) will have *superparamagnetic* behavior (Rosensweig 1985).

The particle surface layers have to fulfill several requirements. Among these, biocompatibility, as well as efficient coating and functionalization capacities are the main requirements. Carboxylic acids are good candidates and are frequently used. The efficiency of hydrophobic coatings of magnetite nanoparticles with lauric (LA), myristic (MA), palmitic (PA), stearic (SA), or oleic (OA) acid monolayer for nonpolar organic magnetic nanofluids was thoroughly investigated by Small Angle Neutron Scattering (SANS) (Avdeev et al. 2007). Palmitic and stearic acids proved to be "bad" stabilizers in comparison with lauric, myristic, or oleic acid. Oleic acid showed the best efficiency in coating magnetite nanoparticles, both as a monolayer with hydrophobic and as bilayer with hydrophilic properties.

3.2 Magnetite Nanoparticles with Hydrophobic Surface Coating: Magnetic Nanofluids with Nonpolar Organic Carrier

According to (Khalafalla and Reimers 1973), subdomain magnetite nanoparticles can be prepared under oxygen-free (nitrogen) atmosphere from the coprecipitation of hydroxides from an aqueous solution of Fe^{3+} and Fe^{2+} in the molar ratio of 2:1 using ammonium hydroxide in excess. Under atmospheric conditions and at a temperature of 80 °C, oleic acid coated magnetite nanoparticles are obtained with a ratio of $Fe^{3+}/Fe^{2+} = 1.7$ (Bica 1995). An essential feature is to ensure the optimum temperature of 80–82 °C (Bica 1995; Moeser et al. 2002) for coprecipitation and stabilization with unsaturated (oleic) or saturated carboxylic (lauric or myristic) acid, in order to obtain only magnetite nanoparticles with an adequate chemisorbed stabilizing layer. The synthesis procedure for hydrophobic magnetite nanoparticles (Fe_3O_4.OA), described in detail in (Vékás et al. 2009), has the following steps: coprecipitation (at $t \approx 80$ °C) of magnetite from an aqueous solutions of Fe^{3+} and Fe^{2+} ions in the presence of concentrated NH_4OH solution (25 %) → subdomain magnetite particles → sterical stabilization (chemisorbtion of oleic acid; 80–82 °C) → phase separation → magnetic decantation and repeated washing → monolayer covered magnetite nanoparticles + free oleic acid → extraction of monolayer covered magnetite nanoparticles (acetone added; extraction) → *magnetite nanoparticles with hydrophobic (chemisorbed OA monolayer) coating*. To be used in preparation of functionalized magnetic nanocomposites (e.g., magnetic microgels, various magnetic nanocontainers), the hydrophobic magnetite NPs are dispersed in light hydrocarbon carriers, such as hexane, cyclohexane or toluene. Free oleic acid and some residual water are eliminated by repeated flocculation and re-dispersion of magnetic nanoparticles. High colloidal stability magnetic nanofluids are obtained having a well-defined magnetite NP volume fraction. For bio-applications, vegetable oleic acid (produced by Merck) was used to produce surface coated magnetite nanoparticles with hydrophobic properties. In spite of the significant content of different chain length saturated carboxylic acids in vegetable oleic acid, the optimized synthesis

procedure for magnetite nanoparticles with biocompatible hydrophobic coating is highly reproducible on a lab-scale and was recently extended to micro-pilot scale (http://roseal.topnet.ro/ang/index1.html).

3.3 Magnetite Nanoparticles with Hydrophilic Coating: Water-Based Magnetic Nanofluids

Magnetite nanoparticles with hydrophilic coating are of outstanding interest for biomedical applications, from bio-separation and MRI to drug targeting and hyperthermia of tumors (Dave and Gao 2009; Reddy et al. 2012; Müller et al. 2011). The nature, binding, and thickness of the hydrophilic coating of magnetite nanoparticles (such as citric acid (CA), gallic acid (GA), poly(acrylic acid) (PAA), poly(acrylic-co-maleic acid) (PAM), humic acid (HA), sodium oleate (NaOA) or oleic acid (OA) bilayer) determines their behavior in bio-relevant media and efficient use as magnetic carriers (Tombácz et al. 2013) or contrast agents (Jedlovszky-Hajdú et al. 2012a, b). Magnetite nanoparticles with biocompatible (lauric, myristic, and especially oleic acid) surface coating and water-based magnetic nanofluids were synthesized according to the basic procedures given in (Bica et al. 2007; Tombácz et al. 2008). The oleate coating on magnetite is favored because of the surface complex formation between the Fe-OH sites (Tombácz et al. 2004) and carboxylate groups.

The procedure applied for the synthesis of magnetite nanoparticles with a double layer oleic acid coating and of water-based magnetic nanofluids consists of the same basic steps as the preparation of hydrophobic magnetite NPs (Vékás et al. 2009; Bica et al. 2007) with some variations. The essential difference between this procedure and that for hydrophobic magnetite NP synthesis lies in tailoring the second, physically adsorbed oleic acid layer which ensures the hydrophilic character of particles. The consistency of this second layer is determined by a certain amount of excess oleic acid dissolved in the water carrier. The amount of excess surfactant was optimized in order to limit the formation of particle clusters and to keep the mean hydrodynamic diameter of particles/clusters below 50 nm.

3.4 Magnetic Properties

The need for the highest magnetic moment and superparamagnetic behavior, i.e., zero remanent magnetization imposed on nano and micro magnetic composites, sets certain requirements on the magnetic properties of the precursor magnetite particles, as is reviewed in (Krishnan 2010). Magnetite ($Fe^{2+}Fe_2^{3+}O_4$) belongs to the spinel group and it is a ferrimagnetic soft material. In its bulk state, magnetite has a multidomain magnetic structure. Magnetite nanoparticles with

diameters below 20 nm have a monodomain magnetic structure, which renders them superparamagnetic with a uniform magnetization oriented along the nanoparticle's easy axis of magnetization. Because magnetite is a soft magnetic material, i.e., its magnetocrystalline anisotropy is weak, the shape anisotropy prevails. Thus, the magnetic moment of magnetite monodomain nanoparticles is oriented along the shape anisotropy axis, provided that the later exists. The modulus of the nanoparticle magnetic moment is given by:

$$m = M_d \cdot v_m \tag{3.1}$$

where M_d is the saturation (domain) magnetization and v_m is the particle's magnetic volume which, as shown below, is smaller than the particle's physical volume. The saturation magnetization of bulk magnetite is $M_d = 480$ kA/m $= 92.8$ $Am^2/kg = 92.8$ emu/g (Kittel 1967) [$\rho_{magnetite} = 5175$ kg/m^3 (http://www.handbookofmineralogy.com/pdfs/magnetite.pdf)]. However, the saturation magnetization of magnetite nanoparticles rarely exceeds 70 emu/g (Fang et al. 2012). Due to the loss of magnetic exchange interaction symmetry between the spins at their surface ("spin canting"), the magnetite nanoparticles have an outer shell which does not contribute to the particle magnetic moment (Rosensweig 1985; http://www.handbookofmineralogy.com/pdfs/magnetite.pdf). The thickness of the nonmagnetic layer, albeit still a matter of debate in the literature, is roughly $\delta_{nm} = 0.85$ nm, which is the size of the magnetite unit cell (Rosensweig 1985). Therefore, the MNPs are characterized by their magnetic diameter (D_m) which is related to the physical diameter (D_p) by:

$$D_p = D_m + 2 \cdot \delta_{\mathrm{nm}} \tag{3.2}$$

The existence of the nonmagnetic layer at the surface of the (magnetite) magnetic nanoparticles is the main factor that limits the magnetic moment of the nano/micro composites. Neglecting the surfactant and other chemical compounds, the maximum saturation magnetization (M_{sMAX}) of the composites made of magnetite particles with D_m average magnetic diameter is:

$$M_{\mathrm{sMAX}} = M_{\mathrm{d}} \cdot \left(\frac{D_m}{D_m + 2 \cdot \delta_{\mathrm{nm}}} \right)^3 = M_d \cdot \left(\frac{D_p - 2 \cdot \delta_{\mathrm{nm}}}{D_p} \right) \tag{3.3}$$

Figure 3.2 shows the dependence of the maximum saturation magnetization of the composites on the average physical diameter of the magnetite nanoparticles. For particles with an average physical diameter below 8 nm and $\delta_{\mathrm{nm}} = 0.85$ nm, it appears that the maximum saturation magnetization of the composites is less than half of the magnetite saturation magnetization, but will increase with decreasing nonmagnetic layer thickness (Fig. 3.2). The maximum saturation magnetization of the composites may be even less, as the magnetite nanoparticles enter the structure of the composites together with a certain mass of surfactant and polymer. For example, the mass percentage of an oleic acid single surfactant layer, covering magnetite nanoparticles with 7 nm average physical diameter, is approximatively 22 %.

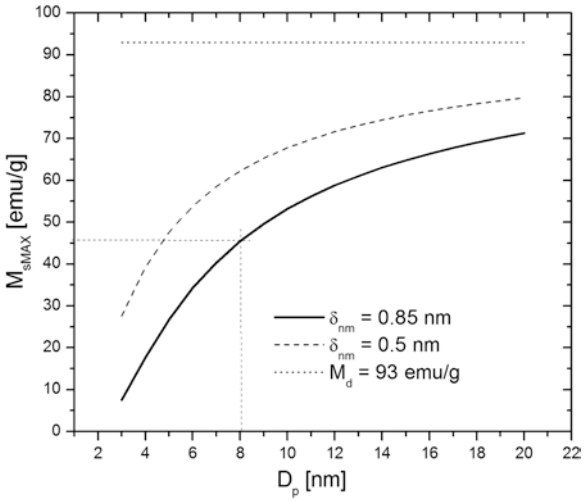

Fig. 3.2 Size dependence of saturation magnetization of magnetite nanoparticles

The superparamagnetism of the nano- and micromagnetic composites is not necessarily implied by the superparamagnetism of the precursor magnetic nanoparticles. When the magnetic nanoparticles are highly packed in the structure of the nano/micro magnetic composites, as in the case of most of the core-shell types, magnetic dipole-dipole interactions may lead to a resultant permanent magnetic moment. The average *per particle* magnetic dipole-dipole interaction parameter is given by:

$$\lambda^{\mathrm{def}} = \frac{1}{2} \cdot \frac{U_{m,\mathrm{d-d,Max}}}{k_B T} = \frac{\pi}{144} \cdot \frac{\mu_0 M_{\mathrm{d}}^2}{k_B T} \cdot \left(\frac{\bar{D}_m^2}{\bar{D}_m + 2\left(\delta_{\mathrm{nm}} + \bar{\delta}_s\right)} \right)^3, \qquad (3.4)$$

where k_B is Boltzmann's constant, μ_0 is the magnetic permeability of vacuum and $\delta_s \sim 1$ nm is the thickness of the surfactant layer. For $\lambda = 1$, Eq. (3.4) shows that highly packed magnetite nanoparticles with physical diameter larger than ~13 nm will lead to composites with permanent magnetization at room temperature. Following this line of reasoning, MNPs that show no remanent magnetization when measured in the dried state will have an average diameter small enough to lead to superparamagnetic nano/micro magnetic composites. In Fig. 3.3 the magnetization curve of a sample of dried surfacted magnetite nanoparticles is shown. The magnetization shows no hysteresis, indicating that, although the particles are closely packed, no significant magnetic dipole-dipole interactions occur.

The static magnetization of concentrated colloidal dispersions of magnetic nanoparticles is described by the *second-order modified mean-field model* developed by Ivanov and Kuznetzova (2001). The model is a generalization of the Langevin magnetization (M_L) formula (Rosensweig 1985) for polydisperse MNPs (Rasa 2000; Ivanov et al. 2007) for the case of moderately concentrated magnetic

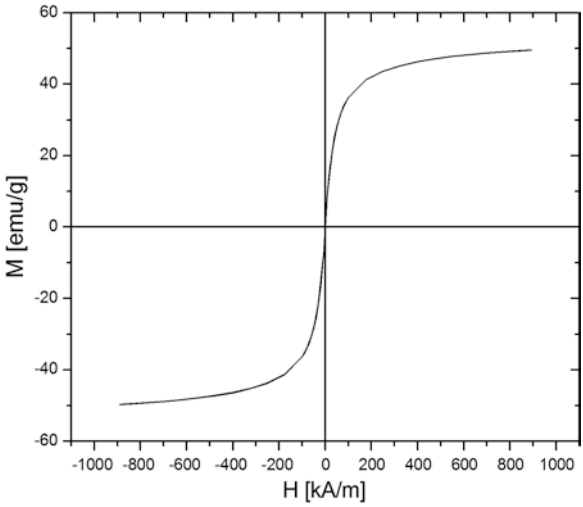

Fig. 3.3 The magnetization *curve* of dried surfacted magnetite nanoparticles

colloids, by including the influence of the magnetic dipole-dipole interactions on the magnetization through the modified effective-field H_e.

The expression of the magnetic field intensity (H) dependence of the magnetization $M(H)$ in S.I. units is (Ivanov et al. 2007):

$$M(H) = M_L(H_e(H)) = n_{\mathrm{MNP}} \int_{D_m=0}^{\infty} m(D_m) \cdot f(D_m) \cdot L\left(\frac{\mu_0 m(D_m) H_e(H)}{k_B T}\right) \cdot \mathrm{d}D_m$$

$$H_e(H) = H + \frac{M_L(H)}{3} \cdot \left(1 + \frac{1}{48} \cdot \frac{\mathrm{d}M_L(H)}{\mathrm{d}H}\right), \tag{3.5}$$

where D_m is the magnetic diameter of the MNP, n_{MNP} is the MNP concentration, $m(D_m) = M_{\mathrm{d}}\pi(D_m)^3/6$ is the magnetic moment of the particle, L is the Langevin function $\mathrm{L(x)} = \coth(\mathrm{x})\text{-}1/\mathrm{x}$ and $f(D_m)$ is the probability distribution function of the MNP's magnetic diameter. When the magnetic dipole-dipole interactions can be neglected, i.e., when either the nanoparticle concentration is low or their size is sufficiently small, the above equation reduces to the Langevin magnetization formula (Rasa 2000):

$$M(H) = M_L(H) = n_{\mathrm{MNP}} \cdot \int_{D_m=0}^{\infty} m(D_m) \cdot f(D_m) \cdot L\left(\frac{\mu_0 m(D_m) H}{k_B T}\right) \cdot \mathrm{d}D_m. \tag{3.6}$$

Equations (3.5) and (3.6) are the basis for magnetogranulometry, which is a technique that allows for the determination of the probability distribution function of the MNP's magnetic diameter, using the measured magnetization curve of the colloid. Details and examples of magnetogranulometry analysis are given in the next section.

The choice of the probability distribution function $f(D)$ of the MNP's diameter remains an open question until a sound physical model will ground it. For example, the log-normal distribution can be considered:

$$\mathrm{LogNorm}(D) = \frac{1}{\sqrt{2\pi} \cdot S \cdot D} \cdot \exp\left(-\frac{\left[\ln\left(D/D_0\right)\right]^2}{2S^2}\right), \tag{3.7}$$

where D_0 is the median diameter and S is the log-normal standard deviation. The mean and standard deviation of the log-normal distribution are:

$$\begin{aligned} \langle D \rangle &= D_0 \cdot e^{S^2} \\ \sigma &= D_0 \cdot e^{S^2/2} \cdot \sqrt{e^{S^2} - 1}. \end{aligned} \tag{3.8}$$

The gamma distribution may also be used (Ivanov et al. 2007).

3.5 Particle Size Distributions (Physical, Magnetic and Hydrodynamic Size)

Knowledge of the size, shape, and structure of the magnetic nanoparticles is a prerequisite for both the elaboration of the synthesis procedure and the characterization of the magnetic nano/micro composites.

The size and shape of magnetite nanoparticles synthesized by means of the chemical coprecipitation method are statistical in nature, therefore described by means of probability distribution functions. The size statistics of the magnetic nanoparticles can be determined by different means of investigation, among which the most widely used are TEM (Transmission Electron Microscopy), magnetogranulometry and DLS (Dynamic Light Scattering). The synthesis process of magnetic nano/microcomposites commonly use liquid dispersions of magnetic nanoparticles as precursors, being hydrophobic or hydrophilic as necessary. Therefore, the structure of the magnetic nanoparticles is described by three main size measures: (1) The physical size, (2) The magnetic size, and (3) The hydrodynamic size. The physical (or solid) size D_p measures the dimensions of the nanoparticle and is most easily obtained by means of TEM. When good quality TEM or HRTEM (High Resolution TEM) are available, nonspherical particles can be approximated by rotation ellipsoids and thus two size measures of the physical size can be obtained, namely the major and the minor axes. As explained in the previous section, the magnetic size is smaller than the physical size due to the nonmagnetic or spin-canted shell, and can be indirectly measured from the magnetization curve of the magnetic nanoparticle liquid dispersions. The hydrodynamic size of the nanoparticles most easily measured by means of DLS is larger than the physical size due to the surfactant layer. Usually, the magnetic and the hydrodynamic size of the magnetic nanoparticles are given in the spherical approximation, i.e., in terms of the magnetic (D_m) and hydrodynamic (D_h) diameter respectively.

Figure 3.4 shows an example of a TEM image of magnetite nanoparticles from a transformer oil based magnetic nanofluid (Susan-Resiga et al. 2012). A histogram of the effective physical diameter of 468 nanoparticles, carefully chosen to avoid sampling clusters or partially overlapped particles is shown in Fig. 3.4. The size of the particles was measured using the program *ImageJ* (http://rsbweb.nih.gov/ij/), using manual freehand selection and subsequent ellipse fitting of the selection. The procedure delivers estimates for the minor and the major axes of the particles approximated as rotation ellipsoids. For simplicity, an effective physical diameter can be calculated, with sphere diameter chosen to yield the same volume as the rotation ellipsoid. A measure of the particle deviation from spherical shape can also be calculated as the ratio of the major and minor axes, after correcting the projective distortion of the major axes of the particles (Susan-Resiga et al. 2012). For the sampled magnetite nanoparticles, the (effective) physical diameter, and deviation from spherical shape were found to be $D_p = 6.9 \pm 1.6$ nm and $e = 1.34 \pm 0.12$, respectively. The physical diameter histogram is very well approximated by a log-normal distribution (Eq. 3.6) with parameters $D_{0p} = 6.63$ nm and $S_p = 0.22$, and $\langle D_p \rangle = 6.8$ nm average diameter and $\sigma_p = 1.5$ nm standard deviation, with a fit goodness parameter R^2 of 0.9538. Other distributions for positive random numbers were tested, but no significant improvement of the fit R^2 was found: 0.9553 for beta distribution, 0.9545 for chi-square distribution, and 0.9545 for gamma distribution. Therefore, the choice for the log-normal distribution may at least be justified by its mathematical simplicity. In the following, the 6.8 nm average physical diameter $\langle Dp \rangle$ will be compared with the average magnetic diameter $\langle D_m \rangle$ obtained by means of magnetogranulometry.

The magnetization curves of 11 samples obtained by successive dilution from a highly concentrated magnetic nanofliud based on transformer oil carrier are presented in Fig. 3.5 (Susan-Resiga et al. 2012). The samples' magnetite volume fraction is in the range of 0.8–20.8 %. The TEM image from Fig. 3.4 was obtained for nanoparticles from this magnetic nanofliud. The magnetite nanoparticles were sterically stabilized with oleic acid. The magnetization curves were corrected for the demagnetizing field (Chen and Brug 1991) of the cylindrical sample holder

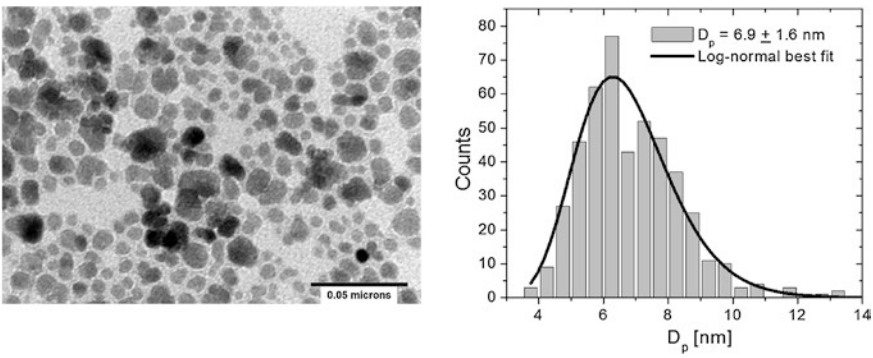

Fig. 3.4 TEM image of the magnetite nanoparticles (*left*) and the physical diameter distribution of the magnetic nanoparticles (*right*)

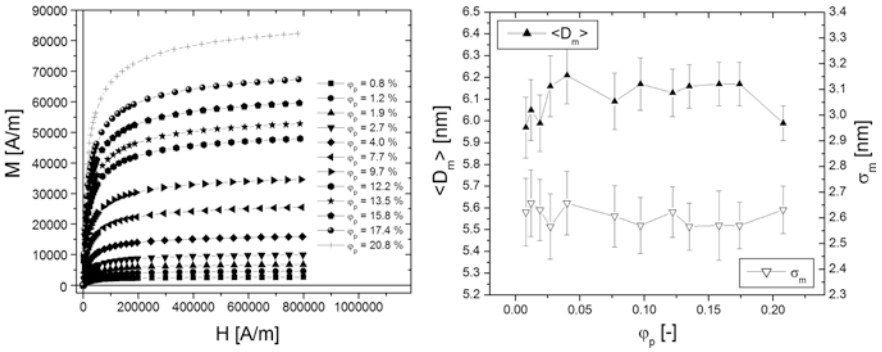

Fig. 3.5 Magnetization *curves* (*left*) and fit results (*right*) for the magnetic diameter distribution (the bars represent the fit errors)

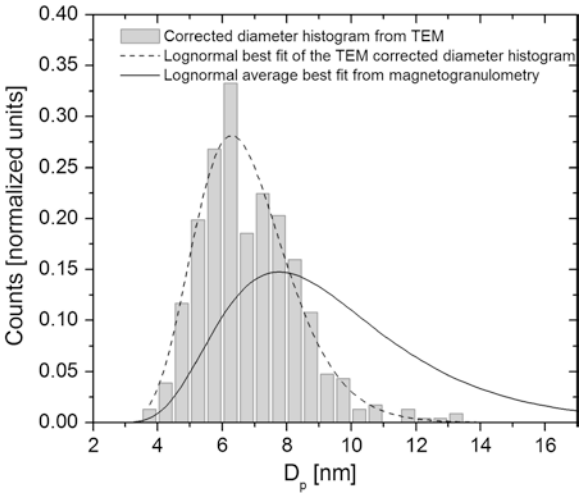

Fig. 3.6 Physical diameter distributions as obtained from TEM (*solid*) and magnetogranulometry (*dashed*)

with aspect ratio h/d = 0.5, radially mounted in our experimental setup. The corrected magnetization curves were fitted with the magnetization model of Ivanov and Kuznetsova (Eq. 3.5) for concentrated polydisperse magnetic nanoparticle ferrofluids. The fit parameters were the saturation magnetization of the sample and the parameters of the magnetic diameter log-normal distribution. The log-normal distribution was chosen in order to allow the comparison with the estimates from TEM granulometry. The fit parameters of the log-normal distribution were used to determine the magnetic diameter mean ($\langle D_m \rangle$) and standard deviation (σ_m), whose dependence on sample concentration is presented in Fig. 3.5. The fit R^2 for all samples was very high, in the range 0.9993–0.9997.

$\langle D_m \rangle$ is slightly smaller than the mean physical diameter $\langle D_p \rangle$ due to the nonmagnetic layer at the surface of the magnetite nanoparticles, but the difference $\langle D_p \rangle - \langle D_m \rangle \cong 0.8$ nm is much smaller than twice the nonmagnetic layer thickness $\delta_{nm} \cong 0.85$ nm. This, together with the fact that σ_m is almost twice σ_p, shows particle

Table 3.1 The mean hydrodynamic diameter obtained from DLS

No.	Sample physical volume fraction φ_p [%]	$<D_h>$ [nm]
1	0.8	18.3 ± 0.3
2	1.2	18.1 ± 0.3
3	1.9	18.9 ± 0.6
4	2.7	17.4 ± 0.7

clustering in the structure of the samples. Figure 3.6 shows both physical and magnetic diameter log-normal distributions obtained from TEM and magnetogranulometry respectively, as functions of the physical diameter D_p, in normalized units. The transformation of the magnetic diameter distribution to the physical diameter variable D_p was made with the variable change $D_m \rightarrow D_p$—$2\delta_{nm}$ and under the assumption that the existence of the nonmagnetic layer has no effect on the difference between the widths of the physical and magnetic diameter distributions. From the comparison of the two distributions, one can conclude that the particles spontaneously agglomerate in the investigated samples and that mostly two-particle clusters are formed, which, as shown below, is consistent with the DLS results.

DLS investigations were made on the four most diluted samples, with volume fractions up to 2.7 %, by means of backscattering, in the absence of external magnetic field, at 25 °C (Susan-Resiga et al. 2012). Each sample was measured six times. Table 3.1 summarizes the mean hydrodynamic diameter <> of the scatterers in the samples $<D_h>$ shows no significant dependence on sample concentration and is about 18 nm, larger than the mean hydrodynamic diameter of about 11 nm, due to the ~2 nm thick oleic acid surfactant shell on the surface of the 6.9 nm diameter particle observed using TEM. This observation indicates the existence of particle clusters in the samples, predominantly two-particle clusters, consistent with the conclusions of the magnetogranulometry analysis. This is explicable by the presence of a significant amount (over 10 %) of saturated acids, especially palmitic and stearic, in the vegetable oleic acid used for stabilization. These are poor stabilizers and favor incomplete covering and therefore clustering of magnetite nanoparticles due to van der Waals interactions. The magnetically induced clustering may be neglected since the MNPs are small enough such that the average *per particle* magnetic dipole-dipole interaction parameter is lower than one (see previous section).

The above three-fold characterization of the size of magnetic nanoparticles unveils the spontaneous clustering phenomena in magnetic colloids. This was found crucial to explain the dependence of the relative viscosity on the solid particle volume fraction (Susan-Resiga et al. 2012).

3.6 Single Particles Versus Clusters: Colloidal Stability

The application potential of the magnetic colloids depends on their colloidal stability under the influence of various factors such as temperature, external magnetic field, concentration and dispersion medium pH.

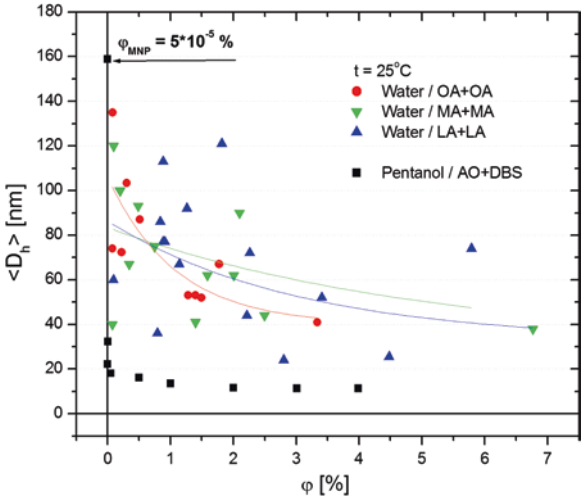

Fig. 3.7 Magnetic nanoparticle volume fraction dependence of the cluster hydrodynamic diameter for the three types of water-based magnetic nanofluids (the smooth lines are the exponential decay fits)

Figure 3.7 shows the dependence of the particle clusters' hydrodynamic diameter, on the magnetic nanoparticle concentration for three water-based MFs (with MNPs stabilized with a double-layer of oleic acid (OA), lauric acid (LA) and myristic acid (MA) respectively) and for a pentanol based MF for comparison (Socoliuc et al. 2010). Like water, pentanol is a polar solvent. All measurements were performed at 25 °C and in the absence of an external magnetic field. The difference between the measured mean hydrodynamic diameter and the magnetic nanoparticle mean diameter is due to the nanoparticle clustering in the first stage of the preparation process, the first stage of the elaboration procedure described in 2.1, where no surfactant is added to the coprecipitation reaction.

The cluster hydrodynamic diameter ranges from 20 to 140 nm and decreases with increasing MNP volume fraction for all three water MFs, most likely due to second surfactant layer desorption as a result of the dilution process. Water / (OA + OA) MF shows the steepest decay of clustering tendency with increasing concentration but the smallest dispersion, while the opposite holds true for Water / (LA + LA) MF (Water /(MA + MA) MF is intermediate).

The temperature dependence of the cluster hydrodynamic diameter is presented in Fig. 3.8 for samples with roughly the same magnetic nanoparticle volume fraction (~2 %) of each of the three types of water-based MFs.

All water-based MFs show a much higher clustering tendency and clustering dispersion for a given concentration than the pentanol based MF, which at high concentrations actually shows no clustering tendency. The samples were exposed to a continuous heat-up /cool-down cycle and were maintained for about 30 min at each temperature level. Water /(OA + OA) MF shows a monotonous decrease of clustering with increasing temperature, while the other two show a clustering peak in the 20–30 °C temperature range. The clustering in Water /(OA + OA) and Water /(MA + MA) MFs slightly diminishes after the heat-up process.

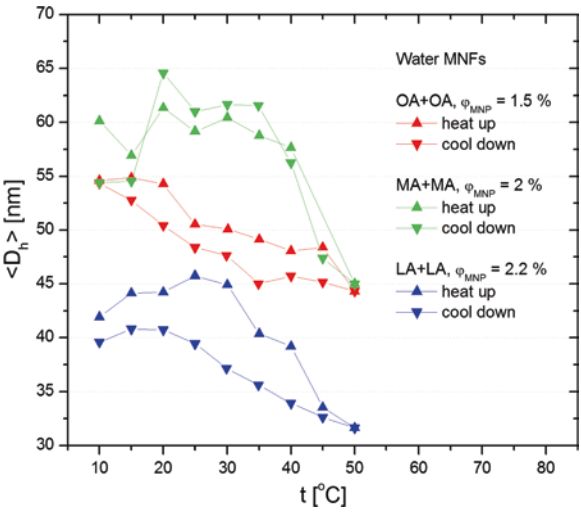

Fig. 3.8 Temperature dependence of the cluster hydrodynamic diameter for three types of water-based magnetic nanofluids during a heat-up /cool-down cycle

Due to their magnetic properties, the magnetic colloids are susceptible to magnetically induced aggregation, as a result of which nanoparticle clusters may form with sizes ranging from the micro to the macro scale. Among the magnetically induced structuring phenomena in magnetic colloids, the magnetically induced phase condensation (Bacri and Salin 1983; Cebers 1990; Buyevich and Ivanov 1992; Socoliuc and Bica 2002; Socoliuc et al. 2011) leads to the formation of oblong condensed phase drops (CPDs) of highly packed magnetic colloidal particles. The condensed phase is in equilibrium with the depleted aqueous dispersion of magnetic colloidal particles. The condensed phase drops are aligned parallel to the external magnetic field and may grow up to several microns thickness and tens or even hundreds of microns length (Bacri and Salin 1983; Socoliuc and Bica 2002). Thus, the magnetically induced phase condensation could be an advantage in magnetic separation applications, whereas in magnetic drug targeting applications it could lead to blood vessel clogging as well as to a significant decrease of the specific surface.

Due to their micron range size, the condensed phase drops can be investigated by means of optical microscopy. The magnetically induced phase condensation in an aqueous magnetic nanofliud was investigated by optical microscopy at room temperature (25 °C), in a 12 kA/m magnetic field oriented parallel to the plane of the optical cell. The thickness of the cell was 10 μm. A few seconds after the sudden onset of the magnetic field, small (~0.5 × 5 μm) but numerous needle-like drops of condensed phase become visible at the limit of the microscope resolution. These primary condensed phase drops (CPDs) are oriented in the field direction and move fast and chaotically in the cell. After a few more seconds, the density of the primary drops begins to decay, while larger ~1 × 50–100 μm, needle-like secondary condensed phase drops begin to emerge. For minutes after that, the slow moving secondary drops stick together, to form massive (~4 × 50–300 μm)

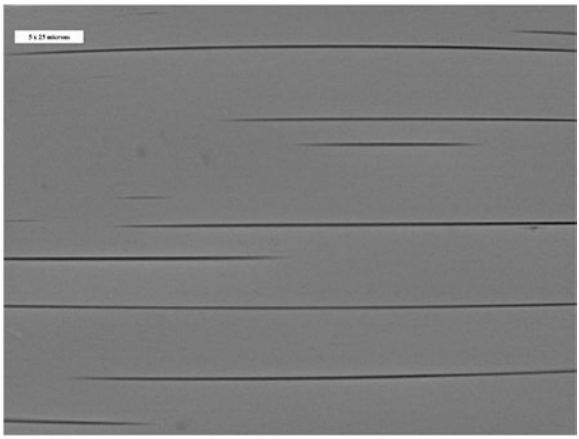

Fig. 3.9 Optical microscopy image of magnetically induced condensed phase drops 10 min after the sudden onset of the field (the scale bar is 5 × 25 μm)

and almost motionless spindle-like condensed phase drops (Fig. 3.9). After the magnetic field was turned off, the condensed phase drops dissolved almost instantaneously (Socoliuc et al. 2013).

The observed evolution of the condensation process fits well into the theoretical picture of the magnetically induced phase condensation kinetics developed by Ivanov and Zubarev (Zubarev and Ivanov 1997, 1998; Ivanov and Zubarev 1998a, b) for magnetic nanofluids. Due to the combined effect of dipole-field and dipole-dipole interactions, an external magnetic field may induce a thermodynamic instability, i.e., magnetic supersaturation or magnetic supercooling, thus leading the magnetic colloid to a metastable state. Three basic stages can be distinguished in the evolution of the colloid towards equilibrium: (1) the origination of initial critical nuclei, (2) the simultaneous origination of new initial critical nuclei and their growth into primary drops of the liquid-like condensed phase, and (3) the formation of much larger secondary drops by means of the Ostwald ripening of the primary drops. The evolution of the colloid through these three stages is increasingly tempered by the metastability reduction of the continuously depleted gas-like phase. The initial nuclei, the primary, and the secondary drops are highly elongated ellipsoids oriented parallel to the magnetic field direction. As described above, our observations indicate that a final fourth evolution stage takes place: the coalescence of the secondary drops into giant spindle-like condensed phase drops. From structural point of view, the phase condensation process leads to the gradually volume increase of a continuously smaller number of large liquid-like phase of CPDs, at the expense of the diminishing density of the free MNPs in the gas-like phase. Static Light Scattering (SLS) experiments allow for the macroscopic characterization of the magnetically induced phase condensation kinetics (Socoliuc et al. 2013). When illuminated at normal incidence by a laser beam, scatterers much larger than the wavelength, highly elongated, and oriented in the same direction, will scatter the light in the plane perpendicular to their anisotropy

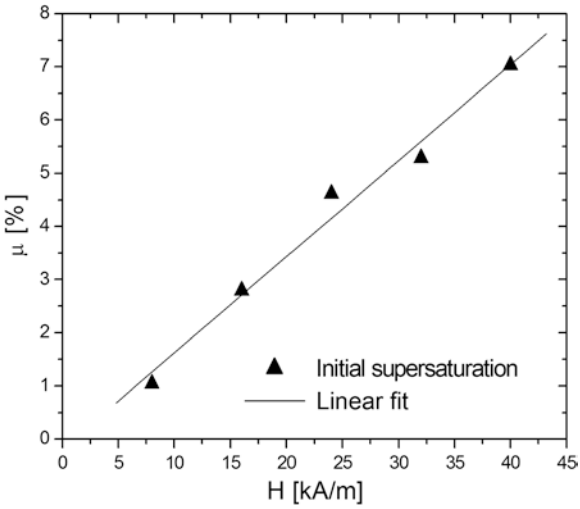

Fig. 3.10 Magnetic field intensity dependence of the initial supersaturation at 30 °C

axis. Consequently, the forward scattered light intensity diminishes with increasing condensed phase volume. Thus, one can estimate the sample initial magnetically induced supersaturation. Following (Zubarev and Ivanov 1998), the initial magnetically induced supersaturation is the difference between the MNP volume fractions of the sample and of the equilibrium gas-like phase, i.e., the MNP volume fraction that will eventually end in the condensed phase.

Figure 3.10 presents the magnetic field intensity dependence of the initial supersaturation (μ) of an aqueous magnetic nanogel dispersion (Socoliuc et al. 2013). The initial supersaturation, expressed as a percentage of the sample's magnetic nanogel volume fraction, shows a linear dependence on the magnetic field intensity within the measured range. At the maximum field intensity used in our experiments (40 kA/m), the initial supersaturation is approximatively 7 % from the magnetic nanogel content of the sample (Socoliuc et al. 2013).

3.7 Conclusions

Chemical coprecipitation proved to be a highly versatile procedure for the cost effective synthesis of magnetite nanoparticles in the 6–10 nm size range. Single- or double-layers of vegetable oleic acid were used for hydrophobic or hydrophilic surface coating, as well as for efficient screening of magnetic dipole-dipole interactions of particles. Clusters of surface coated magnetite nanoparticles have no remnant magnetization and show superparamagnetic behavior, as required for their further use as primary particles in manufacturing magnetoresponsive microspheres (e.g., microgels, nanocontainers) for magnetic separation applications.

References

Avdeev MV, Bica D, Vékás L, Marinică O, Bălăşoiu M, Aksenov VL, Rosta L, Garamus VM, Schreyer A (2007) On the possibility of using short chain length mono-carboxylic acids for stabilization of magnetic nanofliuds. J Magn Magn Mater 311(1):6–9

Bacri J-C, Salin D (1983) Bistability of ferrofluid magnetic drops under magnetic field. J Magn Magn Mater 39(1–2):48–50

Banert T, Peuker UA (2006) Preparation of highly filled super-paramagnetic PMMA-magnetite nano composites using the solution method. J Mater Sci 41(10):3051–3056. doi:10.1007/s10853-006-6976-y

Bica D (1995) Preparation of magnetic nanofliuds for various applications. Rom Rep Phys 47(3–5):265–272

Bica D, Vékás L, Avdeev MV, Marinica O, Socoliuc V, Balasoiu M, Garamus VM (2007) Sterically stabilized water based magnetic nanofliuds: synthesis, structure and properties. J Magn Magn Mater 311:17–21. doi:10.1016/j.jmmm.2006.11.158

Brown GN, Müller C, Theodosiou E, Franzreb M, Thomas ORT (2013) Multi-cycle recovery of lactoferrin and lactoperoxidase from crude whey using fimbriated high-capacity magnetic cation exchangers and a novel "rotor–stator" high-gradient magnetic separator. Biotechnol Bioeng 110(6):1714–1725. doi:10.1002/bit.24842

Buyevich YuA, Ivanov AO (1992) Equilibrium properties of ferrocolloids. Phys A 190(3–4):276–294

Cebers A (1990) Phase separation of magnetic colloids and concentration domain patterns. J Magn Magn Mater 85:20–26

Chen D-X, Brug JA (1991) Demagnetizing factors for cylinders. IEEE Trans Magn 27(4):3601–3619

Darwish MSA, Peuker U, Kunz U, Turek T (2011) Bi-layered polymer–magnetite core/shell particles: synthesis and characterization. J Mater Sci 46(7):2123–2134. doi:10.1007/s10853-010-5048-5

Dave SR, Gao X (2009) Monodisperse magnetic nanoparticles for biodetection, imaging, and drug delivery: a versatile and evolving technology. Wiley Interdiscip Rev Nanomed Nanobiotechnol 1(6):1583–1609. doi:10.1002/wnan.51

Fang M, Ström V, Olsson RT, Belova L, Rao KV (2012) Particle size and magnetic properties dependence on growth temperature for rapid mixed co-precipitated magnetite nanoparticles. Nanotechnology 23(14):145601. doi:10.1088/0957-4484/23/14/145601

http://roseal.topnet.ro/ang/index1.html

http://www.handbookofmineralogy.com/pdfs/magnetite.pdf

http://rsbweb.nih.gov/ij/

Ivanov AO, Kuznetsova OB (2001) Magnetic properties of dense ferrofluids: an influence of interparticle correlations. Phys Rev E 64:041405. doi:10.1103/PhysRevE.64.041405

Ivanov AO, Zubarev AYu (1998a) Ostwald ripening kinetics in a magnetic nanofliud made metastable by a strengthening of an external magnetic field. Phys Rev E 58:7517–7522. doi:10.1103/PhysRevE.58.7517

Ivanov AO, Zubarev AYu (1998b) Non-linear evolution of a system of elongated drop like aggregates in a metastable magnetic nanofliud. Phys A 251:348–367

Ivanov AO, Kantorovich SS, Reznikov EN, Holm C, Pshenichnikov AF, Lebedev AV, Chremos A, Camp PJ (2007) Magnetic properties of polydisperse ferrofluids: a critical comparison between experiment, theory, and computer simulation. Phys Rev E 75:061405. doi:10.1103/PhysRevE.75.061405

Jedlovszky-Hajdú A, Tombácz E, Bányai I, Babos M, Palko A (2012a) Carboxylated magnetic nanoparticles as MRI contrast agents: relaxation measurements at different field strengths. J Magn Magn Mater 324(19):3173–3180

Jedlovszky-Hajdú A, Baldelli Bombelli F, Monopoli MP, Tombácz E, Dawson KA (2012b) Surface coatings shape the protein corona of SPIONs with relevance to their application in vivo. Langmuir 28(42):14983–14991. doi:10.1021/la302446h

Khalafalla SE, Reimers GW (1973) Magnetofluids and their manufacture, US Patent 3764540

Kittel C (1967) Introduction to solid state physics. Wiley, New York

Krishnan KM (2010) Biomedical nanomagnetics: a spin through possibilities in imaging, diagnostics, and therapy. IEEE Trans Magn 46(7):2523–2558. doi:10.1109/TMAG.2010.2046907
Moeser GD, Roach KA, Green WH, Laibinis PE, Hatton TA (2002) Water-based magnetic nanofluids as extractants for synthetic organic compounds. Ind Eng Chem Res 41:4739–4749
Müller C, Wagner K, Frankenfeld K, Franzreb M (2011) Simplified purification of equine chorionic gonadotropin (eCG)—an example of the use of magnetic microsorbents for the isolation of glycoproteins from serum. Biotechnol Lett 33(5):929–936. doi:10.1007/s10529-010-0512-5
Rasa M (2000) Magnetic properties and magneto-birefringence of magnetic nanofliuds. Eur Phys J E 2:265–275
Reddy LH, Arias JL, Nicolas J, Couvreur P (2012) Magnetic nanoparticles: design and characterization, toxicity and biocompatibility. Pharm Biomed Appl Chem Rev 112(11):5818–5878. doi:10.1021/cr300068p
Rosensweig RE (1985) Ferrohydrodynamics, Cambridge University Press, Cambridge, p 344, Reprinted with slight corrections by Dover, Mineola, New York (1997)
Socoliuc V, Bica D (2002) Experimental investigation of magnetic induced phase-separation kinetics in aqueous ferrofluids. In: Dekany I (ed) Adsorption and nanostructures, Book series: progress in colloids and polymer science, vol. 117, pp 131–135. doi:10.1007/3-540-45405-5_25
Socoliuc V, Taculescu A, Podaru C, Dobra A, Daia C, Marinica O, Turcu R, Vékás L (2010) Clustering in water based magnetic nanofluids: investigations by light scattering methods. In: 8th international conference on the scientific and clinical applications of magnetic carriers (AIP conference proceedings), vol 1311. Rostock, pp 89–95, 25–29 May 2010
Socoliuc V, Bica D, Vékás L (2011) Magnetically induced phase condensation with asymptotic critical temperature in an aqueous magnetic colloid. Magnetohydrodynamics 47:201–206
Socoliuc V, Vékás L, Turcu R (2013) Magnetically induced phase condensation in an aqueous dispersion of magnetic nanogels. Soft Matter 9:3098–3105. doi:10.1039/C2SM27262H
Susan-Resiga D, Socoliuc V, Boros T, Borbáth T, Marinica O, Han A, Vékás L (2012) The influence of particle clustering on the rheological properties of highly concentrated magnetic nanofluids. J Coll Interface Sci 373:110–115
Tombácz E, Libor Z, Illés E, Majzik A, Klumpp E (2004) The role of reactive surface sites and complexation by humic acids in the interaction of clay mineral and iron oxide particles. Org Geochem 35(3):257–267
Tombácz E, Bica D, Hajdú A, Illés E, Majzik A, Vékás L (2008) Surfactant double layer stabilized magnetic nanofluids for biomedical application. J Phys: Condens Matter 20(20):204103. doi:10.1088/0953-8984/20/20/204103
Tombácz E, Tóth IY, Nesztor D, Illés E, Hajdú A, Szekeres M, Vékás L (2013) Adsorption of organic acids on magnetite nanoparticles, pH-dependent colloidal stability and salt tolerance. Colloids Surf A 435:91–96
Vékás L, Avdeev MV, Bica D (2009) Magnetic nanofluids: synthesis and structure Chapter 25. In: Donglu S (ed) NanoScience in biomedicine. Springer, Berlin (USA), pp 645–711
Vékás L, Tombácz E, Turcu R, I. Morjan, Avdeev MV, Krasia-Christoforou T, Socoliuc V (2011) Synthesis of magnetic nanoparticles and magnetic nanofliuds for biomedical applications. In: Alexiou C (ed) Nanomedicine-basic and clinical applications in diagnostics and therapy, vol 2. Karger Publication. Basel, Switzerland, pp 35–52
Zubarev AYu, Ivanov AO (1997) Kinetics of a magnetic nanofliud phase separation induced by an external magnetic field. Phys Rev E 55:7192–7202. doi:10.1103/PhysRevE.55.7192
Zubarev AYu, Ivanov AO (1998) Nucleation stage of ferrocolloid phase separation induced by an external magnetic field. Phys A 251:332–347

Chapter 4
Magnetic Microgels: Synthesis and Characterization

Rodica Turcu, Izabell Craciunescu and Alexandrina Nan

Abstract Magnetic microgels—obtained by encapsulation of magnetic nanoparticles into polymers acting as clustering agents—represent good candidates for biomedical applications and high gradient magnetic separation process because they fulfill important requirements, such as: superparamagnetic behavior, high saturation magnetization, and rich in surface functional groups. Biocompatible magnetic microgels were obtained using high colloidal stability magnetic nanofluids as primary materials in various synthesis procedures that allow encapsulation of clusters of magnetite nanoparticles into different polymers including polyacrylic acid, poly(*N*-isopropylacrylamide), poly(3-acrylamidopropyl trimethylammonium chloride). Our results show that polymer encapsulation of magnetite nanoparticles from magnetic nanofluid allows for the tailoring of the magnetic microgels' properties by controlling the synthesis parameters.

4.1 Introduction

Polymer-magnetic nanoparticle hybrid nanomaterials came into the focus of current research as they offer a wide range of applications in the fields of biotechnology and biomedicine, such as therapeutics, multimodal imaging, targeted drug delivery, hyperthermia, analyte monitoring as well as enzyme and protein separations (Oh and Park 2011; Zhou et al. 2011; Hwu et al. 2009; Liu et al. 2009). In a hybrid magnetic nanoparticle—polymer system, the specific composition of the polymeric material allows for the functionalization, morphology design and control of the magnetic nanoparticle volume distribution.

R. Turcu (✉) · I. Craciunescu · A. Nan
National Institute for Research and Development of Isotopic and Molecular Technologies,
65-103 Donath Str., 400293 Cluj-Napoca, Romania
e-mail: rodica.turcu@itim-cj.ro

H. Nirschl and K. Keller (eds.), *Upscaling of Bio-Nano-Processes*,
Lecture Notes in Bioengineering, DOI 10.1007/978-3-662-43899-2_4

For specific applications in the field of high gradient magnetic separation, magnetic nanoparticle clusters of controlled size and high magnetic moment in applied magnetic field are of particular interest (Oh and Park 2011; Zhou et al. 2011; Hwu et al. 2009; Liu et al. 2009; Zha et al. 2011; Karg and Hellweg 2009).

In this contribution, recent results concerning the synthesis and manifold characterization of magnetic microgels are summarized. In particular, these magnetic microgels display the required properties for magnetic separation: superparamagnetic behavior, controlled size, structures, high magnetization, chemical and mechanical stability, cation exchange (CEX) or anion exchange (AEX) functionalities, as well as good redispersability.

4.2 Preparation Methods of Magnetic Microgels

Magnetic nanoparticles can be entrapped in microgels using a variety of emulsion polymerization methods or in situ synthesis techniques (Landfester and Ramírez 2003; Murakami and Maeda 2005; Satarkar et al. 2010; Chen et al. 2011; Pich et al. 2004; Bhattacharya et al. 2007; Wong et al. 2008). These existing techniques present difficulties in ensuring the homogenous distribution of magnetic nanoparticles in the microgels. This is important as the content of magnetic nanoparticles within a microgel particle determines its magnetic field responsiveness.

Three main types of microgel structures are obtained depending on the preparation procedure used: (i) core-shell microgels in which the nanoparticle cores are coated with polymer shell, (ii) microgels covered with nanoparticles and (iii) microgel particles with embedded nanoparticles.

The encapsulation of magnetic nanoparticles from magnetic nanofluids into polymer gels is a promising strategy resulting in homogenous dispersion, high loading of magnetic nanoparticles and superparamagnetic properties of magnetic gels (Menager et al. 2004; Mak and Chen 2005). Magnetic nanofluids are ultrastable colloids of nano-sized subdomain magnetic dipolar particles in appropriate carrier liquids. The magnetic nanofluids (MF) with organic solvents or water carriers presented here were prepared at the Laboratory of Magnetic Fluids, CFATR Timisoara (Romania). They display the required physical and chemical properties for preparation of magnetic nanogels.

Preparation methods for magnetic microgels were developed using magnetite nanoparticles with hydrophilic or hydrophobic coating using the following approaches:

- Preparation of magnetic microgels using water-based magnetic nanofluid—hydrophilic magnetite nanoparticles
- Preparation of magnetic microgels by the mini-emulsion method using toluene-based magnetic nanofluids with hydrophobic magnetite nanoparticles

4.2.1 Preparation of Magnetic Microgels Using Hydrophilic Magnetite Nanoparticles

A simple method for the preparation of thermoresponsive magnetic microgels involves the encapsulation of magnetite nanoparticles coated with a double layer of oleic acid from water-based magnetic nanofluids into polymer poly(*N*-isopropylacrylamide) (Turcu et al. 2010; Socoliuc et al. 2013). Moreover, the copolymerisation of monomers *N*-isopropylacrylamide (NIPA) and acrylic acid (AAc) allows tuning the microgel's sensitivity to temperature and pH by adjusting the polymer content.

Poly(*N*-isopropylacrylamide), pNIPA was chosen due to its biocompatibility, thermoresponsive character, and the possibility of obtaining it as spheres with tunable size from the nanometer range up to several micrometer. The magnetic microgels consisting of poly(*N*-isopropylacrylamide) encapsulating magnetic nanoparticles can respond to external stimuli such as temperature and magnetic field by shape and volume changes. Polyacrylic acid (pAAc) was deposited on the surface of magnetic clusters either by copolymerization with *N*-isopropylacrylamide or by layer by layer (LbL) polymerization.

The water-based MF was prepared by chemical coprecipitation and subsequent electrosterical stabilization of the magnetite nanoparticles by a double-layer of lauric acid (LA + LA) or oleic acid (OA + OA) in the carrier liquid, applying an optimized version of the procedure described in (Bica et al. 2007).

The stabilization procedure of magnetite nanoparticles involves the existence of a quantity of free surfactant dissolved in the water carrier to ensure the equilibrium with the secondary surfactant layer, physically adsorbed on the first chemically adsorbed one. For the preparation of magnetic microgels using water-based magnetic fluids, a relatively high concentration of free surfactant can hinder the clusterization of magnetic nanoparticles during the polymerization process. Another important factor in the formation and encapsulation of clusters of magnetic nanoparticles into polymeric spheres is the efficient surfactant coating of individual nanoparticles to prevent agglomerate formation. The existence of an important fraction of large (over 80-100 nm) aggregates in the primary water-based magnetic fluid impedes the control of the size distribution of the resulting magnetic microgel particles. The successful preparation of magnetic microgels requires well-dispersed surfactant coated magnetic nanoparticles in a water carrier, narrow size distribution, and a moderate concentration of free surfactant.

4.2.1.1 Preparation of Magnetic Microgels by the Single-Step Copolymerization Method

The magnetic copolymeric gels of poly(*N*-isopropylacrylamide-acrylic acid), M-p(NIPA-AAc), were prepared by free radical polymerization. In a typical route, the water-based magnetic fluid containing magnetite nanoparticles

coated with a double-layer of oleic acid (Fe_3O_4/OA + OA), was mixed in an argon atmosphere with the proper amount of monomers (NIPA, AAc) and the cross-linker *N*,*N*-bisacrylamide (BIS). The mixture was heated to 70 °C in an oil bath and then the oxidant ammonium persulfate (APS) was added to initiate the polymerization. The magnetic microgel particles were separated from the synthesis solution by centrifugation at 10,000 rpm, then washed several times and redispersed in water.

4.2.1.2 Preparation of Magnetic Microgels by Two Steps, Layer by Layer Polymerization Method

The magnetic microgels were prepared by using the two-steps method for the encapsulation of magnetic nanoparticles into polymeric shells synthesized sequentially, layer by layer (LbL). In the first step, the magnetic nanoparticles are encapsulated into the polymer pNIPA by using the method described earlier. The synthesized pNIPA magnetic microgel particles were separated from the synthesis solution by centrifugation, then washed several times with distilled water, and redispersed in an aqueous medium. The polymerization of the second layer of pAAc coating the pNIPA magnetic microgel particles was performed in a solution containing these microgel particles, the AAc monomer, the BIS cross linker, and APS oxidant (1 wt%). The solution was heated to 70 °C in an oil bath in an argon atmosphere. In order to adjust the thickness and the network structure of the pAAc coating layer, the following parameters were varied: (i) the polymerization time in the range 5 min–2 h and (ii) the AAc/BIS molar ratio in the range 5–15. The magnetic microgel particles of poly(*N*-isopropylacrylamide)-polyacrylic acid, M-pNIPA-pAAc obtained by LbL polymerization were separated from the synthesis solution by centrifugation at 10,000 rpm, then washed several times and redispersed in water.

4.2.2 Preparation of Magnetic Microgels Using Hydrophobic Magnetite Nanoparticles

The preparation of magnetic microgels based on hydrophobic nanoparticles was performed using the miniemulsion method, a promising strategy to obtain reproducible, size-controlled magnetic nanoparticle clusters encapsulated into polymers (Qiu et al. 2010; Paquet et al. 2011; McGorty et al. 2010; Shang et al. 2006; Landfester 2006; Turcu et al. 2014).

The miniemulsion method describes the process whereby fine droplets with high stability in a continuous phase are created using high shear, forming a colloidal system. In order to obtain stable droplets, it is necessary to add an agent which dissolves in the dispersed phase, but is insoluble in the continuous phase.

Depending on the nature of the dispersed phase, the miniemulsions are classified as:

- Oil-in-water emulsions (O/W): oil is present as the dispersed phase and water as the dispersion medium (continuous phase).
- Water-in-oil emulsion (W/O): water forms the dispersed phase and the oil act as the dispersion medium.

We applied the oil-in-water miniemulsion method for the preparation of CEX and AEX magnetic microgels, using toluene-based magnetic nanofluid as the dispersed phase. The preparation of magnetic microgels consists of the following main steps:

(i) the preparation of magnetic nanoparticles clusters (NPCs) by emulsification of toluene-based magnetic nanofluid in water;
(ii) the encapsulation of NPCs into polymers such as: polyacrylic acid, poly(*N*-isopropylacrylamide, and poly(3-acrylamidopropyl trimethylammonium chloride).

4.2.2.1 Preparation of Clusters of Magnetic Nanoparticles by the Miniemulsion Method

The basic procedure for the preparation of magnetic nanoparticle clusters (NPCs) stabilized with sodium dodecyl sulfate (SDS) using the miniemulsion method is represented schematically in Fig. 4.1.

Toluene-based MF with Fe_3O_4 nanoparticles, stabilized with a hydrophobic layer of oleic acid, was used as the dispersed component in water. The magnetic nanofluid was added to the aqueous solution containing sodium dodecyl sulfate as surfactant and treated ultrasonically to obtain small stable droplets of magnetic

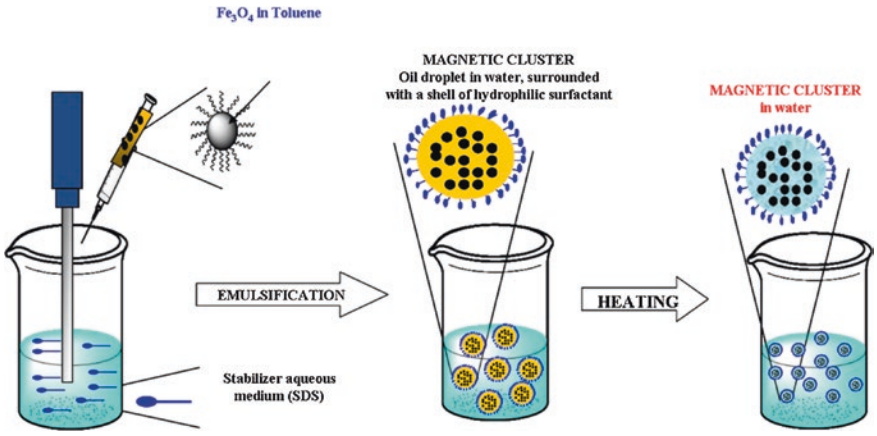

Fig. 4.1 The main steps of the preparation procedure of magnetic microgels using oil in water miniemulsion method

nanofluid. An UP400S Compact Ultrasonic processor (100 W, 24 kHz) with PC control, with a titanium sonotrode of 7 mm diameter and approx. 80 mm length was used to obtain the magnetic miniemulsion. The prepared magnetic miniemulsion was heated to remove the toluene and then carefully washed several times with a methanol-water mixture, magnetically separated and redispersed in water. Stable aqueous dispersions of magnetic nanoparticle clusters coated with the surfactant SDS were obtained and used for encapsulation into polymers.

4.2.2.2 Encapsulating the Nanoparticle Clusters into Polymers with Cation Exchange or Anion Exchange Functionality

The magnetic nanoparticle clusters (NPCs) coated with SDS obtained by miniemulsion method were coated either with one or two polymer shells using layer by layer (LbL) free radical polymerization (Turcu et al. 2014).

CEX magnetic microgels were obtained with the following polymer coating shells of NPCs core:

Polymerization of Acrylic Acid on the Surface of NPCs Coated with SDS

The solution containing the NPCs, the monomer AAc and the crosslinker BIS was stirred for 10 min, after that the oxidant APS was added to start the polymerization. The reaction mixture was kept under argon atmosphere at temperature 70 °C and vigorous stirring. The prepared CEX microgel was precipitated using excess of acetone, washing several times to remove the unreacted products, and redispersed in water.

Layer by Layer Polymerization of NIPA and AAc

The NPCs were coated with a first shell of poly(*N*-isopropyl acrylamide) by free radical polymerization of NIPA in the presence of BIS and APS. The prepared microgel was precipitated using excess of acetone, washing several times to remove the unreacted products and redispersed in water. The synthesis of the second layer, the polyacrylic acid, was performed by free radical polymerization of AAc in aqueous solution containing the NPCs coated with pNIPA, the crosslinker BIS, and the oxidant APS.

In the case of AEX microgels, the layer by layer polymerization procedure was used to encapsulate the NPCs coated with SDS. Therefore, the NPCs were coated first with a layer of poly(*N*-isopropylacrylamide) or poly(3-acrylamidopropyl trimethylammonium chloride) and then with the second layer of poly(3-acrylamido-propyl trimethylammonium chloride). The polymerization of monomers for the first shell takes place in water by free radical polymerization, as previously described. The as-prepared microgel was precipitated using excess of acetone,

washing several times to remove the unreacted products and redispersed in water. The second layer of poly(3-acrylamidopropyl trimethylammonium chloride) was obtained by free radical polymerization. The aqueous solution containing the NPCs coated with a polymer shell, the monomer (3-acrylamidopropyl)trimethyla mmonium chloride (APTAC), the crosslinker BIS and an accelerator (*N*,*N*,*N'*,*N'*-tetramethylethylenediamine) was stirred for 10 min, after that the oxidant APS was added to start the polymerization and the reaction mixture was kept under argon, vigorous stirring at temperature 70 °C, 20 min. The prepared AEX microgel was precipitated using excess of acetone, washing several times, and redispersed in water.

4.3 Physical-Chemical Characterization of Magnetic Microgels

The physical properties of the magnetic microgels combine the nature of polymer, solvent, and magnetic nanoparticles. The correlation between the synthesis parameters and the physical properties of the magnetic microgels was investigated using different techniques: transmission electron microscopy (TEM, HRTEM), dynamic light scattering (DLS), Zeta potential, X-ray Photoelectron Spectroscopy (XPS), and vibrating sample magnetometer (VSM). Our main goal was to control the microgel particles' size distribution and the dispersion properties in order to increase the mass magnetization of particles and the concentration of carboxylic or ammonium groups on the surface.

4.3.1 Morphological Characterization by Transmission Electron Microscopy

The morphology of magnetic microgels and of the magnetic nanofluids used as primary material was investigated by transmission electron microscopy (TEM, HRTEM).

The mean physical size of magnetite nanoparticles from magnetic nanofluids determined from TEM images (Fig. 4.2) is in the range 7–11 nm (Socoliuc et al. 2013; Turcu et al. 2014).

The TEM, HRTEM images of the magnetic microgels prepared using hydrophilic nanoparticles from water-based magnetic nanofluid (Fe_3O_4/OA + OA) show that clusters of magnetite nanoparticles from the water-based magnetic nanofluid were successfully encapsulated into microgels either by copolymerization of p(NIPA-AAc), Fig. 4.3a and b, or by LbL polymerization of pNIPA and pAAc, Fig. 4.3c. The cluster's size is in the range of 50–150 nm. The polymer shells encapsulating the clusters can be better observed in the Fig. 4.3c for the microgels obtained by LbL polymerization.

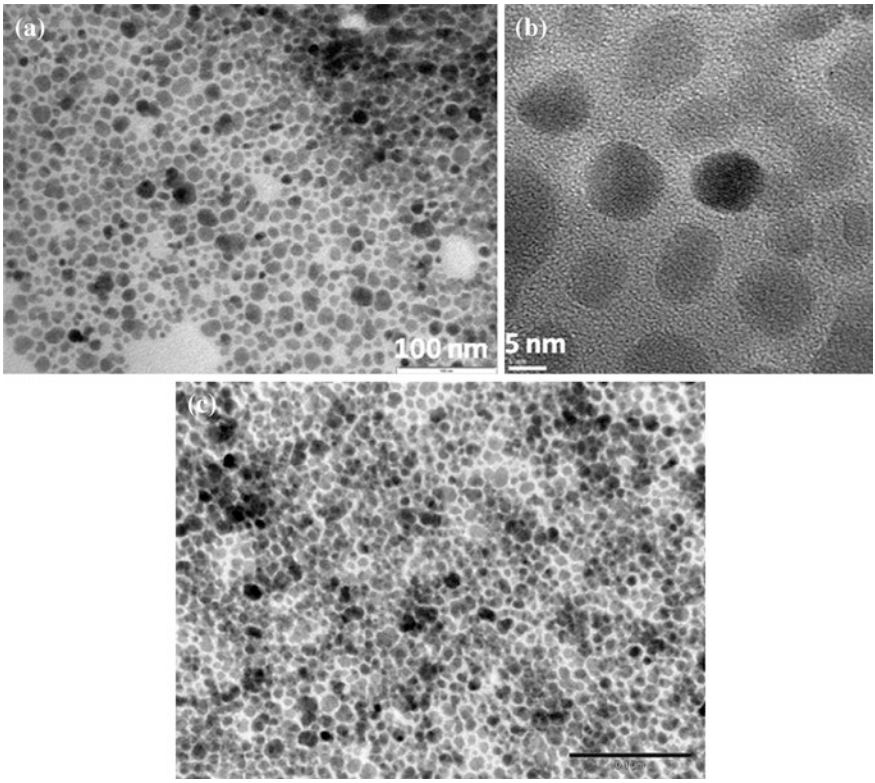

Fig. 4.2 TEM (**a**), HRTEM (**b**) images of a typical water-based magnetic nanofluid sample of oleic acid double layer-coated magnetite nanoparticles (Fe_3O_4/OA + OA) and of toluene based magnetic nanofluid (**c**) containing monolayer oleic acid coated magnetite (Fe_3O_4/OA), respectively

The application of miniemulsion method results in well-defined spherical clusters of magnetic nanoparticles by emulsification of toluene-based magnetic nanofluid in water (Fe_3O_4/OA) (Turcu et al. 2014). Figure 4.4A shows the TEM image of magnetic nanoparticles clusters stabilized with SDS. Hydrophobic nanoparticles Fe_3O_4/OA are densely packed into spherical clusters coated with SDS with sizes in the range of 100–500 nm. Representative TEM images of CEX and AEX magnetic microgels, samples M-pNIPA-pAAc 1E and M-pAPTAC-pAPTAC 2E, obtained by coating the NPCs with double layer of polymers are shown in Fig. 4.4B and C, respectively.

Similar morphology of magnetic nanoparticle clusters prepared in different conditions has been reported in the literature (Qiu et al. 2010; Paquet et al. 2011; Shang et al. 2006; Luo et al. 2010; Yu et al. 2010; Jia et al. 2012; Leal et al. 2012). The solvothermal method was successfully applied for the preparation of well-defined magnetic nanoparticle clusters. Magnetic microspheres of silica-coated magnetite nanoparticle clusters with a mean diameter of about 206 nm have been obtained by Luo et al. (2010). Yu et al. report the preparation of monodispersed hydrophobic magnetite microspheres via a high-temperature hydrolysis reaction

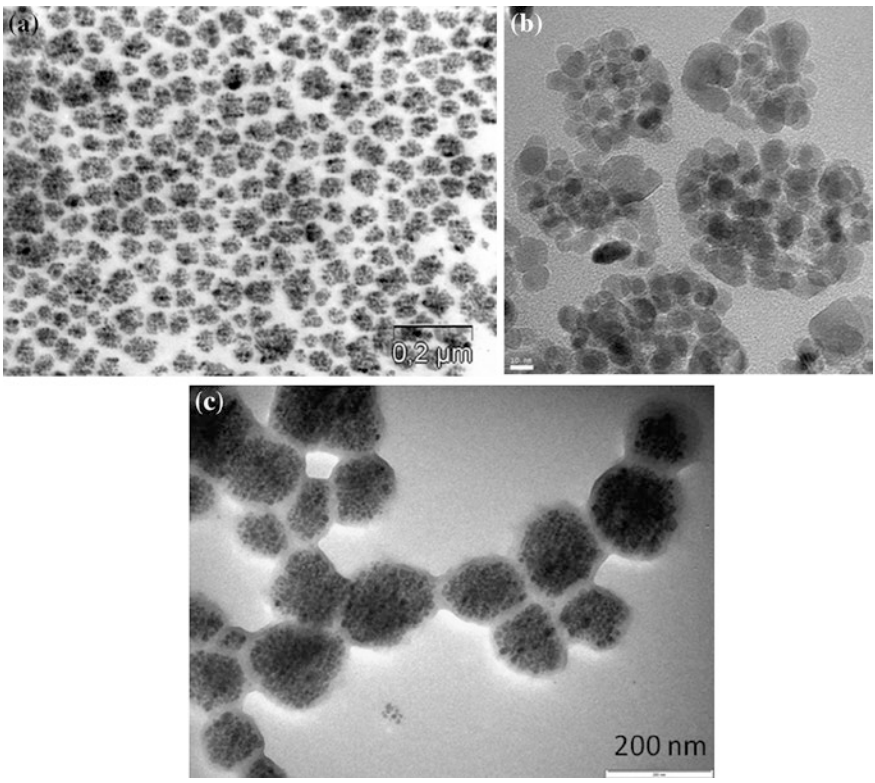

Fig. 4.3 **a** TEM image of the CEX magnetic microgel M-p(NIPA-AAc)1 prepared using hydrophilic magnetite nanoparticles from water based magnetic nanofluid and copolymerization method; **b** HRTEM image of the magnetic microgel M-p(NIPA-AAc)1 from figure (**a**); **c** TEM image of the CEX magnetic microgel M-pNIPA-pAAc 2 prepared using hydrophilic magnetite nanoparticles from water based magnetic nanofluid and layer by layer polymerization

of iron–oleate complex in diphenyl ether in the presence of oleic acid using the solvothermal method (2010). Recently, an ultra-fast method for the preparation of magnetite nanoclusters under microwave-irradiation has been reported by Jia et al. (2012). Magnetic nanoparticle clusters with controlled sizes larger than 50 nm have been reported using polymers or block copolymers as both stabilizer and clustering agent (Jia et al. 2012; Leal et al. 2012; Sondjaja et al. 2009).

4.3.2 Characterization by Dynamic Light Scattering and Zeta Potential Measurements

The hydrodynamic diameter, D_h of the microgel particles was determined by dynamic light scattering (DLS) measurements using a Malvern Zetasizer Nano ZS instrument.

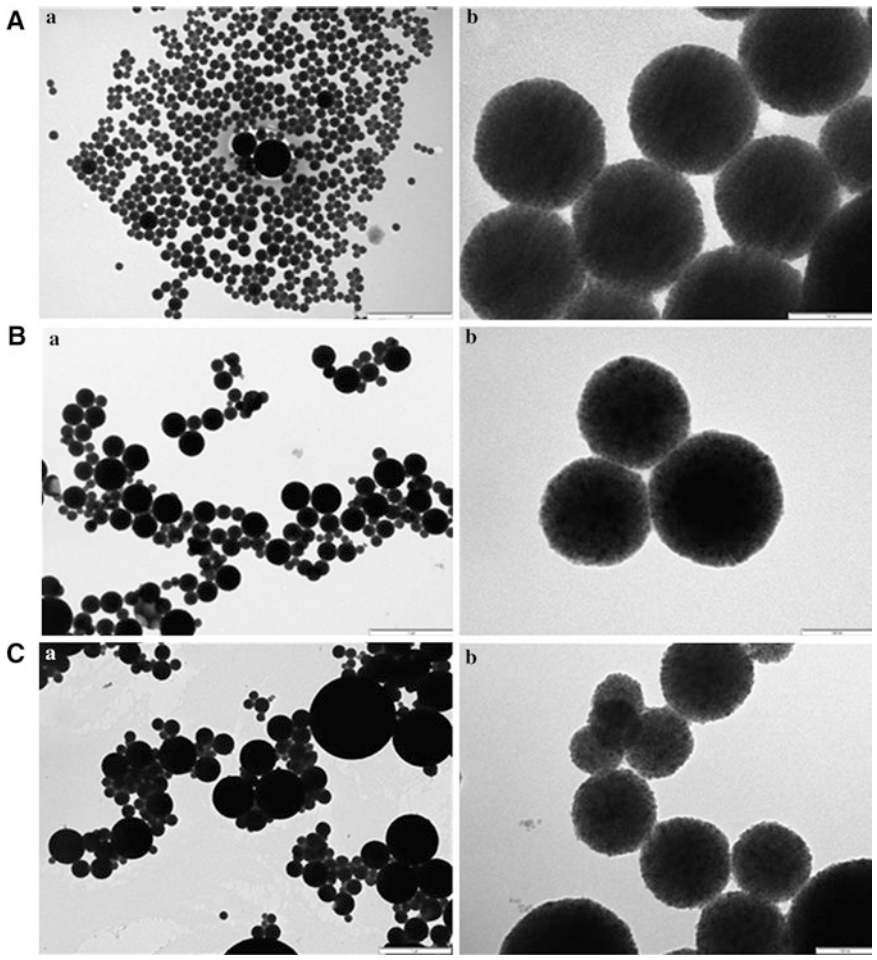

Fig. 4.4 **A** TEM image of NPCs stabilized with SDS prepared by oil in water miniemulsion method; **B** TEM image of the CEX magnetic microgel M-pNIPA-pAAc 1E obtained by coating the NPCs with double layer of polymers poly(*N*-isopropyl acrylamide) and polyacrylic acid; **C** TEM image of the AEX magnetic microgel M-pAPTAC-pAPTAC 2E obtained by coating the NPCs with double layer poly(3-acrylamidopropyl trimethylammonium chloride). *a* the bar is 1 μm; *b* the bar is 100 nm

DLS investigations of magnetic microgels prepared using hydrophilic nanoparticles Fe_3O_4/OA + OA from water-based nanofluid show that the mean hydrodynamic diameter of microgels is in the range of 100–500 nm, depending on the polymerization conditions and the hydrodynamic size distribution of magnetite nanoparticles from the magnetic fluid. The Zeta potential measurements show negative values for CEX microgels between −33 and −36 mV at pH = 4.7 and positive values for AEX microgels between 44 and 54 mV.

The values of the hydrodynamic diameter of magnetic microgels prepared using hydrophobic nanoparticles from toluene-based magnetic nanofluid are in the range 500–920 nm, these values being higher than that obtained for the microgels prepared with hydrophilic nanoparticles. Values of the zeta potential between −23 and −37 mV for CEX microgels and between +35 and +39 mV for AEX microgels have been obtained.

The magnetic microgels based on pNIPA and pAAc are sensitive to temperature and pH changes. The polymer pNIPA is a thermo-sensitive material undergoing volume change at a lower critical solution temperature (LCST) in water, at around 32–35° C (Hoare and Pelton 2004; Oh et al. 2008; Regmi et al. 2010). The change in the hydration state, which causes the volume change transition, reflects competing hydrogen bonding properties, where intra and intermolecular hydrogen bonding of the polymer molecules are favored in comparison with water solubilisation effects. The pH sensitivity of the polymer pAAc due to a deprotonation with increasing pH, results in a transition of the microgel from collapsed state (at low pH values) to swollen state (at high pH values).

The transition of CEX microgel between swollen and collapsed states, induced by temperature and pH, respectively, was evidenced by DLS measurements, Fig. 4.5a,b. DLS measurements at different temperatures from 20 to 40 °C and reverse (Fig. 4.5a), show a reversible decrease of 24 % of D_h of the microgel particles with increasing temperature. One should note that the swelling ratio $(D_{h\ 20\ °C}/D_{h\ 40\ °C})^3 = 2.3$ is lower for the magnetic microgel prepared by LbL polymerization of pNIPA and pAAC as compared to the case of magnetic microgel prepared only with pNIPA (Turcu et al. 2010; Regmi et al. 2010). The thermoresponse of pNIPA microgels is influenced by the cross-linking density (Luo et al. 2010) and by the presence of pAAc (Karg and Hellweg 2009). The swelling ratio of pNIPA microgel decreases with increased cross-linking density. The copolymerizations of pNIPA with polymers such as pAAc, polymethacrylic acid, and polymaleic acid hinder the microgel swelling (Karg and Hellweg 2009).

4.3.3 X-Ray Photoelectron Spectroscopy

X-ray Photoelectron Spectroscopy (XPS) is a surface analysis method that provides the element composition (atomic concentration) of the surface as well as the chemical state of the atoms (valence states, oxidation degree, etc.). The former information is inferred from the areas delimited by the photoelectron peaks, and the latter relates to the chemical shifts of the peaks with respect to the elemental state. Chemical shift information is a very powerful tool for functional group, chemical environment, and oxidation state.

The chemical surface analysis of magnetic microgels was performed by XPS using an UHV XPS spectrometer SPECS equipped with a dual-anode X-ray source Al/Mg, a PHOIBOS 150 2D CCD hemispherical energy analyzer. The $Al_{K\alpha}$ X-ray source (1486.6 eV) operated at 200 W was used for XPS

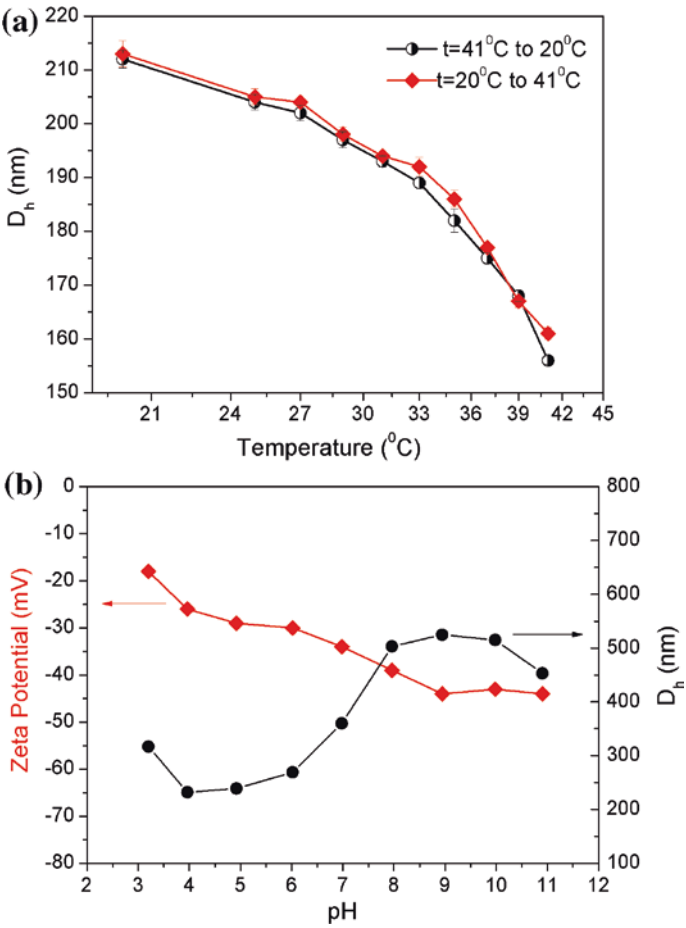

Fig. 4.5 **a** Temperature dependence of hydrodynamic diameter of magnetic microgel M-pNIPA-pAAc 2 prepared using hydrophilic magnetite nanoparticles; **b** The pH dependence of hydrodynamic diameter and zeta potential for magnetic microgels M-pNIPA-pAAc 2 prepared using hydrophilic magnetite nanoparticles

investigations. The XPS survey spectra were recorded at 30 eV pass energy, 0.4 eV/step. The high resolution spectra for individual elements were recorded by accumulating 10 scans at 30 eV pass energy and 0.1 eV/step. The microgel water suspension was dried on an indium foil to allow XPS measurements. A cleaning of the samples surface was performed by argon ion bombardment (500 V) and the spectra were recorded before and after cleaning.

Data analysis and curve fitting was performed using CasaXPS software with a Gaussian-Lorentzian product function and a nonlinear Shirley background subtraction.

The high-resolution XPS core-level spectra of C1s, O1s, N1s, Fe2p from the magnetic microgel M-(pNIPA-pAAc) 2 prepared using hydrophilic magnetite

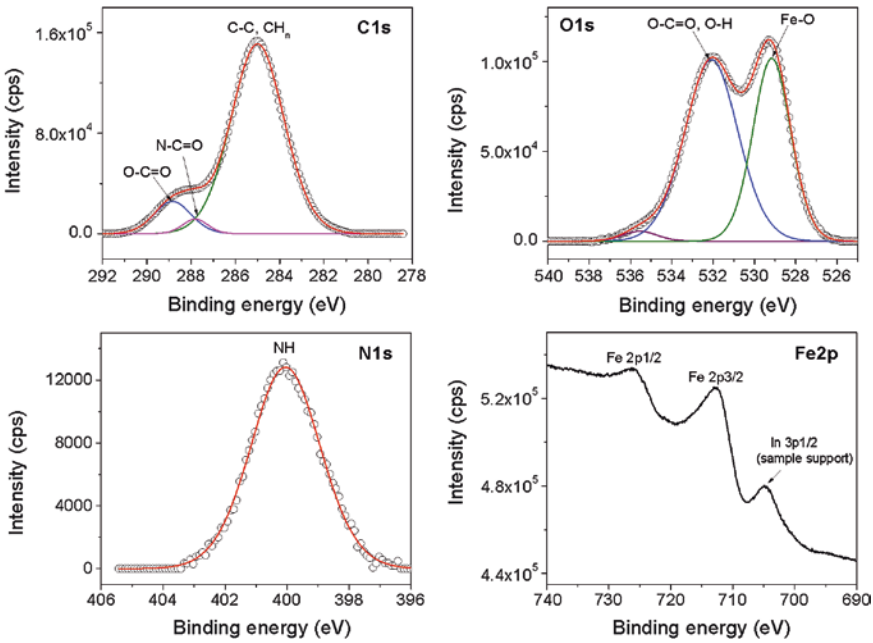

Fig. 4.6 High resolution XPS core-level spectra of C1s, O1s, N1s, Fe2p from the magnetic microgel M-(pNIPA-pAAc) 2 prepared using hydrophilic magnetite nanoparticles

nanoparticles by LbL polymerization are shown in Fig. 4.6. The spectrum of C1s can be deconvoluted into three peaks corresponding to carbon atoms from different groups. The higher binding energy components at 288.2 and 289 eV correspond to carbon atoms in the amide group N–C=O from p-NIPA and to the O–C=O group from pAAc. The most intense and broad component at 285 eV corresponds to C–C/CH$_n$. The oxygen spectrum in the Fig. 4.6 exhibit two components assigned to the oxygen atoms from carboxyl group –O–C=O of p-AAc (532.2 eV) and from Fe–O (529.2 eV), respectively. The N1s core-level spectrum shows one peak ascribed to amine group –NH– from pNIPA. The Fe2p core-level spectrum contains the doublet Fe 2p3/2 and Fe 2p1/2, but the low intensity of these peaks makes their deconvolution difficult.

The high resolution XPS spectra of C1s, O1s, N1s, S2p, and Fe2p core levels from CEX microgel sample M-pNIPA-pAAc 1E prepared by coating the NPCs of hydrophobic nanoparticles with a double layer of polymers poly(*N*-isopropylacrylamide) and polyacrylic acid, are given in Fig. 4.7. The intense band located at 530 eV is evidence of the SDS coating of NPCs, ascribed to OSO_3 group in the O1 s spectrum (Fig. 4.7) and also by the S2p spectrum containing the doublet S2p3/2 and S2p1/2 at binding energies 168.8 and 169.8 eV, respectively, which correspond to sulfur atoms from sulfate (Lindberg et al. 1970). The coating of NPCs with double layer of polymers poly(*N*-isopropylacrylamide) and polyacrylic acid is evidenced by the characteristic peaks in XPS spectra from Fig. 4.7: (i)

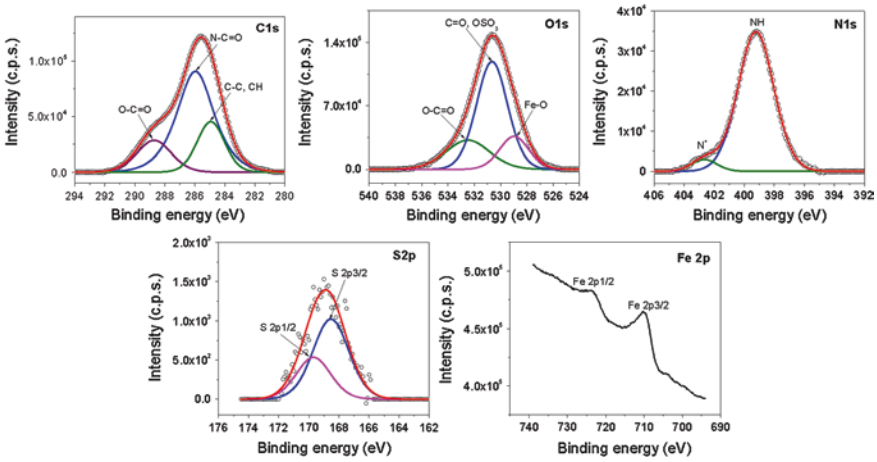

Fig. 4.7 High resolution XPS spectra of C1s, O1s, N1s, S2p, Fe2p core levels from CEX microgel sample *M*-pNIPA–pAAc 1E obtained by coating the NPCs with double layer of polymers poly(*N*-isopropylacrylamide) and polyacrylic acid

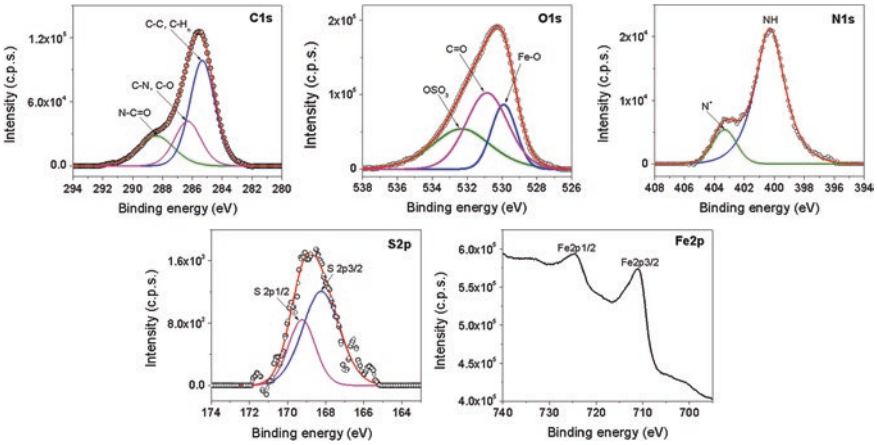

Fig. 4.8 High resolution XPS spectra for C1s, O1s, N1s, S2p, core levels from AEX microgel sample M-pNIPA-pAPTAC 3E obtained by coating the NPCs with double layer of polymers poly(*N*-isopropylacrylamide) and poly(3-acrylamidopropyl trimethylammonium chloride)

amide group N–C=O (286 eV) in C1s spectrum, NH (399 eV) in N1 s spectrum, C=O (532.5 eV) in O1s spectrum, which are specific for pNIPA; (ii) -carboxyl group O–C=O in C1s and O1s spectrum, specific for pAAc. In the spectrum N1 s from Fig. 4.7, one can see a low intensity peak located at 402.6 eV ascribed to positively charged nitrogen which could be from the oxidant APS.

XPS spectra of AEX magnetic microgel, sample M-pNIPA-pAPTAC 3E, from the Fig. 4.8 confirm the double layer polymer coating of SDS stabilized NPCs with

poly(*N*-isopropylacrylamide) and poly(3-acrylamidopropyl trimethylammonium chloride). The N1 s spectrum from the Fig. 4.8 exhibits two components assigned to the nitrogen from amine group –NH– and to positively charged nitrogen.

4.3.4 Magnetic Properties

The magnetization curves of magnetic microgel samples prepared using hydrophilic magnetite nanoparticles from water-based magnetic nanofluid and dried at room temperature (Fig. 4.9a) show superparamagnetic behavior, as is expected for magnetite nanoparticles of small sizes (less than 10 nm), which are stabilized by a double layer of surfactant. Moreover, this fact indicates that the magnetite nanoparticles

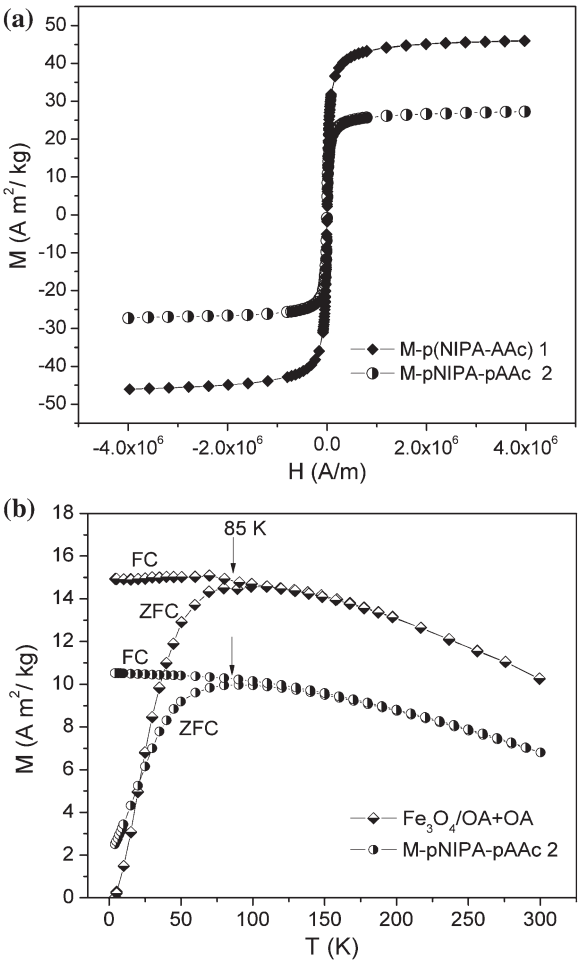

Fig. 4.9 **a** Magnetization curves of magnetic microgels prepared using hydrophilic magnetite nanoparticles at room temperature (dried samples); **b** Temperature dependence of the magnetization at low field (0.1 T) under zero-field cooling (ZFC) and field cooling (FC) of magnetic microgel (sample *M*-pNIPA-pAAc 2) and of water based magnetic nanofluid (Fe_3O_4/OA + OA) used for microgel preparation

are still well separated in the polymer matrix. The values of the saturation magnetization, M_S, for the magnetic microgels prepared with hydrophilic nanoparticles are in the range 27–47 Am^2/kg. Relatively high magnetization values mean that our synthesis procedure favors close packing of magnetite nanoparticles and allows for the encapsulation of a relatively high fraction of magnetite nanoparticles either into the copolymer p(NIPA-AAc) or into the LbL polymers pNIPA-pAAc.

The temperature dependences of the magnetization for the magnetic microgel, sample M-pNIPA-pAAc 2 and for the water-based magnetic nanofluid (Fe_3O_4/OA + OA) used for the microgel preparation, in zero-field cooling (ZFC) and field cooling (FC) regimes are presented in the Fig. 4.9b. They show a typical superparamagnetic behavior for an assembly of nanoparticles whose moments block progressively with decreasing temperature according to the distribution of their blocking temperatures. The ZFC magnetization curves exhibit a maximum at average blocking temperature $\langle T_B \rangle$ related to an average volume of the magnetic nanoparticles. The FC and ZFC curves split below a temperature termed the irreversibility temperature, T_{ir} associated with the blocking of the biggest nanoparticles. The difference between $\langle T_B \rangle$ and T_{ir} is determined by the width of magnetic particles' size distribution, assuming the same anisotropy constant and the absence of interparticle interactions. The values of both temperatures, $\langle T_B \rangle$ and T_{ir} increase with interparticle interactions. A comparison between the blocking temperatures from ZFC magnetization curves for the magnetic nanofluid and magnetic microgel sample shows the same values (Fig. 4.9b). This indicates that the polymer encapsulation of stabilized magnetite nanoparticles from the magnetic nanofluid does not significantly change the interparticle interactions.

In the case of magnetic microgels prepared using hydrophobic nanoparticles from toluene-based magnetic nanofluid, the magnetic measurements were performed on dried samples of NPCs stabilized with SDS and on the microgels obtained by polymer coating of NPCs. The magnetization versus applied magnetic field at room temperature for NPCs stabilized with SDS (Fig. 4.10)

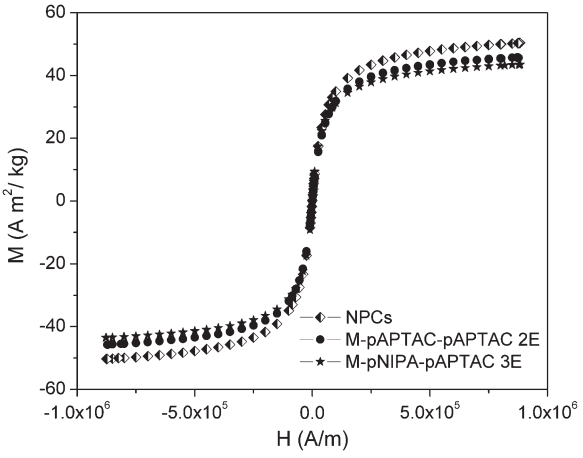

Fig. 4.10 Magnetization curves at room temperature of NPCs stabilized with SDS obtained by miniemulsion method and of magnetic microgels obtained by coating the NPCs with double layer of polymers

has superparamagnetic behavior, as expected for oleic acid-coated magnetite nanoparticles with a mean size of 6–8 nm from the magnetic nanofluid used as primary material. The saturation magnetization for NPCs has relatively high values in the range of 54–56 Am^2/kg. After polymer coating of NPCs, the magnetization of the CEX and AEX microgels has superparamagnetic behavior and the saturation magnetization values are in the range 46–49 Am^2/kg. These values for saturation magnetization are higher than those reported in the literature for magnetic nanoparticles encapsulated into polymers (Paquet et al. 2011; Shang et al. 2006; Luo et al. 2010; Jia et al. 2012; Lindberg et al. 1970).

4.4 Conclusions

Magnetic microgels represent a special category of hybrid materials of increasing interest due to their unique combination of magnetism, gel properties, and colloidal stability.

The successful applications of these materials depend on the development of synthesis methods, allowing a precise design of magnetic microgels with controlled size, structure, surface functionality, superparamagnetic behavior, high magnetization, and chemical and mechanical stability. High saturation magnetizations require dense packing of magnetic nanoparticles, whereas keeping the superparamagnetic behavior requires having magnetite nanoparticles of less than 15 nm solid size that are well separated by the adsorbed organic stabilizing layer. Consequently, the controlled clustering process of surface-coated magnetic nanoparticles and their entrapping into the polymer matrix are highly relevant for the successful preparation of magnetic microgels.

Design of biocompatible CEX and AEX magnetic microgels was achieved by using high colloidal stability magnetic nanofluids as primary materials in various synthesis procedures that allow encapsulation of clusters of magnetite nanoparticles into different polymers: polyacrylic acid, poly(*N*-isopropylacrylamide), poly(3-acrylamidopropyl trimethylammonium chloride).

Stable suspensions of functionalized magnetic microgels in water have been obtained using magnetite nanoparticles with hydrophilic or with hydrophobic coating from water- or organic solvent-based magnetic nanofluids.

High magnetization (up to $Ms = 47$ Am^2/kg) magnetic microgels were obtained by a simple procedure that allows the encapsulation of hydrophilic magnetite nanoparticles stabilized with a carboxylic acid double layer from water-based magnetic nanofluid into almost spherical polymeric structures poly(*N*-isopropylacrylamide)-polyacrylic acid. The morphology of magnetic microgels depends strongly on the characteristics of the primary water-based magnetic nanofluid (pH, excess of surfactant). The poor reproducibility of magnetic microgels prepared using water-based magnetic nanofluids makes scaling up the production of magnetic microgels with the required properties for magnetic separation difficult.

Clusters of hydrophobic magnetite nanoparticles from toluene-based nanofluid were prepared in a reproducible fashion using the miniemulsion method. The coating of the clusters of magnetite nanoparticles with a double layer of polymers results in magnetic microgels with a core-shell structure, high magnetization ($Ms = 46–49$ Am^2/kg), and good stability as water-based suspensions. The magnetization curves of the dried samples of magnetic microgels showed no measurable hysteresis or coercivity, consistent with the superparamagnetic behavior of these composite particles.

The magnetic properties, chemical stability, and biocompatibility of the CEX and AEX magnetic microgels prepared by the miniemulsion method using hydrophobic magnetite nanoparticles make these materials suitable for applications in magnetic bioseparation and nanomedicine.

References

Bhattacharya S, Eckert F, Boyko V, Pich A (2007) Temperature-, pH-, and magnetic-field-sensitive hybrid microgels. Small 3:650–657. doi:10.1002/smll.200600590

Bica D, Vékás L, Avdeev MV, Marinica O, Socoliuc V, Balasoiu M, Garamus VM (2007) Sterically stabilized water based magnetic fluids: synthesis, structure and properties. J Mag Mag Mat 311:17–21. doi:10.1016/j.jmmm.2006.11.158

Chen T, Cao Z, Guo X, Nie J, Xu J, Fan Z, Du B (2011) Preparation and characterization of thermosensitive organic–inorganic hybrid microgels with functional Fe_3O_4 nanoparticles as crosslinker. Polym Lond 52:172–179. doi:10.1016/j.polymer.2010.11.014

Ditsch A, Laibinis PE, Wang DIC, Hatton TA (2005) Controlled clustering and enhanced stability of polymer-coated magnetic nanoparticles. Langmuir 21:6006–6018. doi:10.1021/la047057

Hoare T, Pelton R (2004) Functional group distributions in carboxylic acid containing poly(*n*-isopropylacrylamide) microgels. Langmuir 20:2123–2133. doi:10.1021/la0351562

Hwu JR, Lin YS, Josephrajan T, Hsu MH, Cheng FY, Yeh CS, Su WC, Shieh DB (2009) Targeted paclitaxel by conjugation to iron oxide and gold nanoparticles. J Am Chem Soc 131:66–68. doi:10.1021/ja804947u

Jia J, Yu JC, Zhu XM, Chan KM, Wang YXJ (2012) Ultra-fast method to synthesize mesoporous magnetite nanoclusters as highly sensitive magnetic resonance probe. J Colloid Interface Sci 379:1–7. doi:10.1016/j.jcis.2012.04.035

Karg M, Hellweg T (2009a) Smart inorganic/organic hybrid microgels: synthesis and characterization. J Mater Chem 19:8714–8727. doi:10.1039/B820292N

Karg M, Hellweg T (2009b) New "smart" poly(NIPAM) microgels and nanoparticle microgel hybrids: properties and advances in characterization. Curr Opin Colloid Interface Sci 14:438–450. doi:10.1016/j.cocis.2009.08.002

Landfester K (2006) Synthesis of colloidal particles in miniemulsions. Annu Rev Mater Res 36:231–279. doi:10.1146/annurev.matsci.36.032905.091025

Landfester K, Ramírez LP (2003) Encapsulated magnetite particles for biomedical application. J Phys Condens Matter 15:S1345–S1361. doi:10.1088/0953-8984/15/15/304

Leal MP, Torti A, Riedinger A, La Fleur R, Petti D, Bertacco RCR, Pellegrino T (2012) Controlled release of doxorubicin loaded within magnetic thermo-responsive nanocarriers under magnetic and thermal actuation in a microfluidic channel. ACS Nano 6:10535–10545. doi:10.1021/nn3028425

Lindberg BJ, Hamrin K, Johansson G, Gelius U, Fahlman A, Nordling C, Siegbahn K (1970) Molecular spectroscopy by means of ESCA II. Sulfur compounds. Correlation of electron binding energy with structure. Phys Scr 1:286–298. doi:10.1088/0031-8949/1/5-6/020

Liu TY, Hu SH, Liu DM, Chen SY, Chen IW (2009) Biomedical nanoparticle carriers with combined thermal and magnetic responses. Nano Today 4:52–65. doi:10.1016/j.nantod.2008.10.011

Luo B, Song XJ, Zhang F, Xia A, Yang WL, Hu JH, Wang CC (2010) Multi-functional thermosensitive composite microspheres with high magnetic susceptibility based on magnetite colloidal nanoparticle clusters. Langmuir 26:1674–1679. doi:10.1021/la902635k

Mak SY, Chen DH (2005) Binding and sulfonation of poly(acrylic acid) on iron oxide nanoparticles: a novel, magnetic, strong acid cation nano-adsorbent. Macromol Rapid Commun 26:1567–1571. doi:10.1002/marc.200500397

McGorty R, Fung J, Kaz D, Manoharan VN (2010) Colloidal self-assembly at an interface. Mat Today 13:34–42. doi:10.1016/S1369-7021(10)70107-3

Menager C, Mangili J, Sandre O, Cabuil V (2004) Preparation and swelling of hydrophilic magnetic microgels. Polymer 45:2475–2481. doi:10.1016/j.polymer.02.018

Murakami Y, Maeda M (2005) DNA-responsive hydrogels that can shrink or swell. Biomacromolecules 6:2927–2929. doi:10.1021/bm0504330

Oh JK, Park JM (2011) Iron oxide-based superparamagnetic polymeric nanomaterials: design, preparation, and biomedical application. Prog Polym Sci 36:168–189. doi:10.1016/j.progpolymsci.2010.08.005

Oh KJ, Drumright R, Siegwart DJ, Matyjaszewski K (2008) The development of microgels/nanogels for drug delivery applications. Prog Polym Sci 33:448–477. doi:10.1016/j.progpolymsci.2008.01.002

Paquet C, de Haan HW, Leek DM, Lin HY, Xiang B, Tian G, Kell A, Simard B (2011) Clusters of superparamagnetic iron oxide nanoparticles encapsulated in a hydrogel: a particle architecture generating a synergistic enhancement of the T2 relaxation. ACS Nano 5:3104–3112. doi:10.1021/nn2002272

Pich A, Bhattacharya S, Lu Y, Boyko V, Adler HJP (2004) Temperature-sensitive hybrid microgels with magnetic properties. Langmuir 20:10706–10711. doi:10.1021/la040084f

Qiu P, Jensen C, Charity N, Towner R, Mao C (2010) Oil phase evaporation-induced self-assembly of hydrophobic nanoparticles into spherical clusters with controlled surface chemistry in an oil-in-water dispersion and comparison of behaviors of individual and clustered iron oxide nanoparticles. J Am Chem Soc 132:17724–17732. doi:10.1021/ja102138a

Regmi R, Bhattarai SR, Sudakar C, Wani AS, Cunningham R, Vaishnava PP, Naik R, Oupicky D, Lawes G (2010) Hyperthermia controlled rapid drug release from thermosensitive magnetic microgels. J Mat Chem 20:6158–6163. doi:10.1039/C0JM00844C

Satarkar NS, Biswal D, Hilt JZ (2010) Hydrogel nanocomposites: a review of applications as remote controlled biomaterials. Soft Matter 6:2364–2371. doi:10.1039/B925218P

Shang H, Chang WS, Kan S, Majetich SA, Lee GU (2006) Synthesis and characterization of paramagnetic microparticles through emulsion-templated free radical polymerization. Langmuir 22:2516–2522. doi:10.1021/la052636f

Socoliuc V, Vékás L, Turcu R (2013) Magnetically induced phase condensation in an aqueous dispersion of magnetic nanogels. Soft Matter 9:3098–3105. doi:10.1039/C2SM27262H

Sondjaja R, Hatton AT, Tam MKC (2009) Clustering of magnetic nanoparticles using a double hydrophilic block copolymer, poly (ethylene oxide)-b-poly (acrylic acid). J Mag Mag Mat 321:2393–2397. doi:10.1016/j.jmmm.2009.02.136

Turcu R, Socoliuc V, Craciunescu I, Petran A, Marinica O, Daia C, Paulus A, Franzreb M, Vékás L (2014) Magnetic microgels, a promising candidate for enhanced magnetic adsorbent particles in bioseparation: synthesis, physico-chemical characterization and separation performance (in preparation)

Turcu R, Nan A, Craciunescu I, Leostean C, Macavei S, Taculescu A, Marinica O, Daia C, Vékás L (2010) Synthesis and characterization of magnetically controllable nanostructures using different polymers. AIP Conf Proc 1311:20–27. doi:http://dx.doi.org/10.1063/1.3530014

Wong JE, Gaharwar AK, Muller-Schulte D, Bahadur D, Richtering W (2008) Dual-stimuli responsive PNiPAM microgel achieved via layer-by-layer assembly: Magnetic and thermoresponsive. J Colloid Interface Sci 324:47–54. doi:10.1016/j.jcis.2008.05.024

Yu S, Wan J, Yu X, Chen K (2010) Preparation and characterization of hydrophobic magnetite microspheres by a simple solvothermal method. J Phys Chem Sol 71:412–415. doi:10.1016/j.jpcs.2009.11.011

Zha L, Banik B, Alexis F (2011) Stimulus responsive nanogels for drug delivery. Soft Matter 7:5908–5916. doi:10.1039/C0SM01307B

Zhou L, Zhinan C, Jinying Y, Kang Y, Yuan W, Shen D (2011) Multifunctional hybrid magnetite nanoparticles with pH-responsivity, superparamagnetism and fluorescence. Polym Int 60:1303–1308. doi:10.1002/pi.3081

Chapter 5
Vesicles and Composite Particles by Rotating Membrane Pore Extrusion

Elisabeth Rondeau, Sebastian Holzapfel, Helen Engel and Erich J. Windhab

Abstract We present an innovative processing route based on dynamic membrane pore extrusion and multiphase flow, which allows for the controlled production of particle and core-shell microstructures with tailored techno-functional properties. In the context of MagPro^{2}Life, two scalable continuous processes based on this technology were specifically designed and implemented for the preparation of (i) surface functionalized magnetic composite particles and (ii) functional vesicles, using two respective devices: (i) a novel ROtating MEmbrane Reactor (ROMER) device and (ii) a NAno Membrane Pore EXtruder (NAMPEX) device. Extrusion and detachment of liquid drops and vesicles from pores in a surrounding immiscible continuous fluid phase under various flow conditions like co-flow, flow focusing and cross flow have been studied intensively at our Laboratory of Food process Engineering for a variety of different rheological and interfacial material characteristics within the past decade. Drop- and capsule deformation and breakup were studied in mechanistic detail utilizing in particular microfluidics technology. The coupling of drop/capsule formation with functionalization steps by either entrapment/encapsulation of components for controlled release or surface/interface modification for adjusted and more or less specific adsorption characteristics have been addressed with respect to the overarching goal of the project being the separation of specific protein fractions from soy whey streams.

5.1 Introduction

In the context of MagPro^{2}Life, the utilization of dynamic membrane pore extrusion technology for the large-scale production of functional particles and vesicles was investigated. A new scalable process allowing for the preparation of magneto-responsive

E. Rondeau (✉) · S. Holzapfel · H. Engel · E.J. Windhab
LinkedIn Corporation, Mountain View, CA, USA
e-mail: Elisabeth.rondeau.pro@gmail.com

H. Nirschl and K. Keller (eds.), *Upscaling of Bio-Nano-Processes*,
Lecture Notes in Bioengineering, DOI 10.1007/978-3-662-43899-2_5

adsorbent particles with specific surface binding properties was developed based on the controlled generation of micro droplets with a tunable composition and a well-defined simple or multiple emulsion-based microstructure using membrane emulsification in a novel ROtating MEmbrane Reactor (ROMER) device. In parallel, a continuous and scalable process was developed for the controlled production of defined vesicle morphologies using a NAno Membrane Pore EXtruder (NAMPEX) device.

In mechanistic detail pore extrusion and detachment of liquid drops from pores in a surrounding immiscible continuous fluid phase under various flow conditions like co-flow, flow focusing and cross flow has been studied intensively at our Laboratory of Food process Engineering for a variety of different rheological and interfacial material characteristics within the past decade. The favorite experimental toolbox used was "Microfluidics" enabling us to generate a multitude of different drop and capsule multiphase morphologies and narrow to mono-disperse size distributions. Such microfluidics approaches are however not suitable for up-scaling in order to approach a robust process for industrial applications. Our scalable process solution derived is "Dynamic Controlled Pore Distance Membrane Emulsification" (DCPDME). If the pore distance is appropriately adjusted, there is minimal to negligible influence of the drop extrusion and detachment at one membrane pore on the similar process at the neighboring pores. This is however limited by critical values of (i) the volume flow rate ratio of the disperse to continuous fluid phase, (ii) the wetting characteristics of the membrane surface by the two fluid phases and (iii) the pore diameter to pore distance ratio.

5.2 Dynamic Membrane Emulsification

Over the past 10 years, successive dynamic-enhanced membrane processes were developed and implemented in our group for the formation of emulsion and foam-based systems of varying complexity. These processes have consistently shown improved performance compared to conventional processes, in terms of product quality and productivity. On the basis of this expertise, we developed a process, in which complex wax-in-water emulsions are generated at relatively high processing temperatures. The structure-tailored droplets thus produced are solidified into functional particles. The device and the related process were developed with a strong focus set on demonstrating the process-structure relationships. The performance of the new device was investigated using a model system and within a parameter field relevant to the processing conditions for particle production.

5.2.1 Membrane Emulsification Technology

Conventional emulsification processes such as rotor/stator systems or high-pressure homogenizers allow for the production of small droplets of a disperse phase in an immiscible continuous phase, mostly under turbulent flow conditions. High stresses

are applied to deform and disrupt the droplets, ultimately leading to a reduction in their size, but at the cost of high-energy inputs and degradation of shear-sensitive components. Cross flow membrane emulsification on the other hand allows for the generation of well-defined droplets with low energy input resulting in a gentle treatment of the components (Charcosset et al. 2004; Joscelyne 2000). The process was originally introduced by Nakashima (Nakashima et al. 2000), in which a disperse liquid phase is pushed through the pores of a membrane into the continuous liquid phase, the two liquids being at least partially immiscible. Drops form at the membrane pores and are detached by the continuous liquid cross flow. In membrane emulsification, conventionally, the membrane remains static. A pressure driven flow of the continuous phase is directed along the membrane surface and its mean velocity directly correlates to the size of the resulting drops. The production of smaller drops requires higher continuous phase throughputs, resulting in a lower disperse phase volume fraction, which can restrict from using such conventional membrane emulsification for large-scale production. To overcome this, our group developed a process based on dynamically enhanced membrane emulsification where a well-defined homogeneous shear field is induced above the membrane surface, which can be implemented using two different configurations: (1) a setup with a cylindrical membrane rotating within an outer static cylinder (Schadler and Windhab 2006; Windhab et al. 2006; Eisner 2007; Mueller-Fischer et al. 2007; Graber 2010) and (2) a cylindrical rotor within a cylindrical static membrane (Eisner 2007; Mueller-Fischer et al. 2007). In both cases a narrow annular gap between the rotating and the fixed cylinder ensures the approximately constant shear rate and related shear stress conditions. Within these setups, control over the median drop size is achieved by adjusting the speed of the rotor, independently of the continuous liquid throughput. At low Taylor numbers, corresponding to a laminar Couette flow within the shear gap, emulsions with a relatively narrow width of the drop size distribution were obtained, but within a reduced range of droplet sizes. In the Taylor vortex regime, drops with a median size smaller than the pore diameter were produced. However, the size distribution width of the resulting emulsions was generally broad. Additionally to these limitations, adequate membranes with well-defined pores size and distance between pores were available only with restricted porosity and pressure resistance.

Within MagPro^{2}Life, we developed an improved ROME process allowing for better control of the flow conditions across the membrane. The design and fabrication of membranes with adequate properties were both essential to implementing this process and optimize it.

5.2.2 MagPro^{2}Life ROMER Setups

Two setups based on two distinct rotating membrane devices, ROMER I and II respectively, were successively implemented and optimized for the production of surface-functionalized magnetic composite micro-particles for application in the MagPro^{2}Life pilot lines. These are presented in Fig. 5.1.

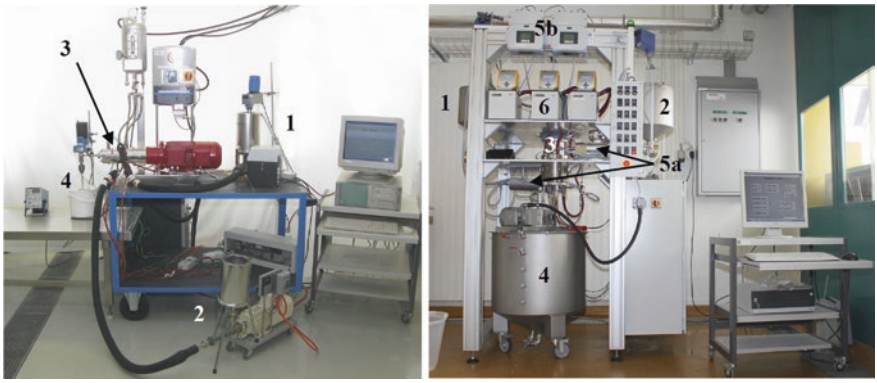

Fig. 5.1 Pictures showing the two experimental setups for the ROMER I (*left*) and for the ROMER II (*right*), as implemented in our pilot plant, and presenting some process key features: liquid phase containers with stirrers for the disperse phase (*1*) and the continuous phase (*2*), emulsification chamber with pressure and temperature sensors (*3*), product collection vessel with stirrer (*4*) and for the ROMER II device only: two flow rate sensors (*5a*) and two associated display screens (*5b*), three thermostat controllers for the heating containers and for the emulsification chamber (*6*)

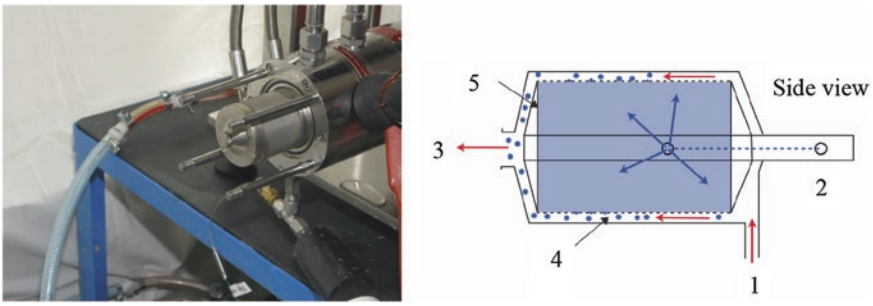

Fig. 5.2 Cylindrical inner membrane module of the ROMER I (*left*), and schematic reresentation of the ROMER I and the main functional parts of the device: continuous phase inlet (*1*), disperse phase inlet (*2*), emulsion outlet (*3*), shear gap between inner and outer cylinder (*4*), inner rotating cylinder with membrane mounted (*5*)

A pre-version of the ROMER I device (FM 1-56 SO, Kinematica AG, Switzerland) was implemented in 2004 in our laboratory. It consists of an emulsification head and a motor. As shown in Fig. 5.2, the emulsification head is composed of a cylindrical membrane module, mounted concentrically on a hollow shaft, and an outer cylinder, which was also mounted concentrically. To form an emulsion, the disperse phase liquid is pushed through the hollow shaft into the membrane cylinder and then through the pores of the membrane. The continuous fluid phase is pumped through the shear gap through a radial inlet. The shear field is induced in the shear gap between the inner and outer cylinder by the rotation of the inner

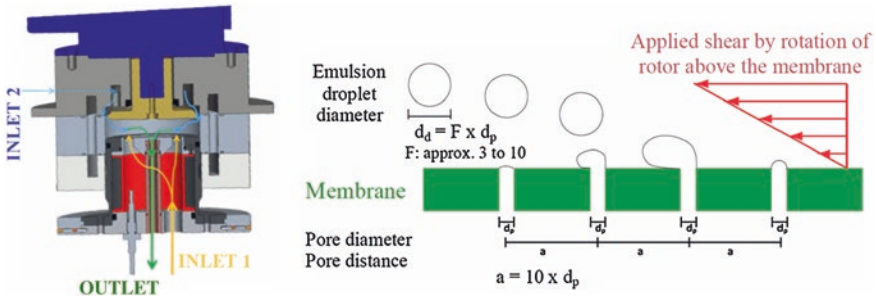

Fig. 5.3 Transverse section of ROMER II emulsification chamber drawn without membrane (*left*) and illustration of membrane design and resulting droplet size in ROMER II device (*right*)

membrane cylinder. The shear rate is adjusted by controlling the rotational speed of the membrane up to 8,000 rpm. In addition, two stator housings with different inner diameters allowed for selecting the shear gap size (0.5, 1 or 2.0 mm).

The ROMER II device was designed and built in collaboration with Bühler AG (Utzwil, Switzerland) and was implemented during the MagPro^{2}Life project in our laboratory. The emulsification chamber of this apparatus was constructed using a cone-plate geometry (cone: rotor, plate: static membrane), in order to allow for the use of flat micro-engineered membranes. To form an emulsion, the disperse phase is pushed through the circular flat membrane. The continuous phase is introduced above the rotor and is forced to enter the gap between the rotor and the membrane. This is illustrated by the scheme in Fig. 5.3, which also shows how drops form and grow at the membrane pores and eventually detach, under the shear flow induced by the rotation of the rotor. The emulsion exits the apparatus through a hole in the center of the membrane plate and a connected hollow shaft.

The cylinder-in-cylinder design of the ROMER I corresponds to a constant gap along the rotor length. The ROMER II has a cone-shaped rotor, which is positioned as such, that the "virtual" tip of the rotor touches the membrane surface. The ratio of the velocity of the rotor at a local radius r, and the local distance, d, to the stator is constant over the rotor radius, which results in a constant shear rate over the whole membrane area. A laminar Couette flow, without secondary flows, is obtained, in the configuration of a cylinder-in-cylinder geometry, under conditions corresponding to low Taylor numbers ($Ta < 41$) (Breitschuh 1998), and in the case of cone-plate setup, under conditions corresponding to low gap Reynolds numbers. Ellenberger and Fortuin (1985) defined a Reynolds criterion to maintain purely laminar flow in a cone-plate rheometer design. The Taylor numbers and the Reynold numbers, as expressed in these two works, are defined in Eqs. (5.1) and (5.2) respectively.

$$Ta = \frac{D_i \mathrm{ns}\rho}{\eta}\sqrt{\frac{2s}{R_0 + R_i}}, \tag{5.1}$$

where D_i is the diameter of the inner rotating cylinder, n is the rotor speed, s is the gap between inner and outer cylinder ($= R_0 - R_i$), ρ is the density, η is the viscosity, and R_0 and R_i the radii of outer and inner cylinder, respectively.

$$\mathrm{Re}^* = \frac{\omega_0 \rho R \theta}{\eta}, \tag{5.2}$$

where ω_0 is the angular velocity of the rotor, ϱ is the density of the fluid in the gap, θ is the cone angle, R is the radius of the wetted part of the plate and η is the dynamic viscosity of the continuous phase.

According to the definition of both these dimensionless parameters (*Ta* and *Re**), laminar flow conditions can be best maintained through a wide range of shear rates when the gap size (s) or the cone angle (θ) is small. Accordingly, the ROMER II was built with a small cone angle (0.13°).

5.2.3 Droplet Formation and Detachment

Key to the size and size distribution of emulsions produced with dynamically enhanced membrane emulsification is the individual formation and detachment of drops at the membrane pores. There are two distinct droplet formation mechanisms which are commonly reported, and which exist in both cross-flow and co-flow conditions: dripping and jetting. Depending on the forces acting on a growing droplet attached at a pore rim, the development of the drop morphology during detachment corresponds to one or the other of these two regimes. The mechanisms of droplet expansion and detachment in cross-flow conditions are well described in the literature, based on studies conducted using model configurations such as capillaries of microfluidic channels with a T-shape junction (der Graaf et al. 2005; Xu et al. 2006; Peng and Williams 1998; Schröder et al. 1998). In addition, related studies using computational fluid dynamics (CFD) simulations and more especially the combination of these with experimental works, gave further insight into droplet formation mechanisms (Abrahamse et al. 2001; Timgren et al. 2009; Feigl et al. 2010). Diverse flow cells were developed as model lab-scale configurations to investigate specifically, based on visualization studies, the influence of fluid properties, flow processing parameters and membrane characteristics on the emulsion properties (Abrahamse et al. 2002; Kobayashi et al. 2002; Geerken et al. 2007; Holzapfel et al. 2014). The quality of an emulsion produced in a rotating membrane extrusion device is resulting form the combination of diverse factors, including the processing parameters defining the flow conditions (e.g. disperse and continuous flow rates, rotating speed), the properties of the material system (e.g. viscosity, interfacial tension, chemical properties), and the membrane properties. Membrane parameters such as surface wettability, pore size and size distribution, pore distance, and pore geometry, as well as pore arrangement, were shown to influence significantly the properties of the produced emulsion (der Graaf et al. 2005; Peng and Williams 1998; Schröder et al. 1998;

Vladisavljević a et al. 2004). The selection of an adequate membrane is key to process efficiency and product quality.

Holzapfel et al. investigated drop formation and detachment in a specifically designed flow cell, where a laminar Poiseuille flow across a membrane sample can be induced by adjusting the cross flow velocity (Holzapfel et al. 2014). Drop detachment was visualized using high-speed imaging, under flow conditions corresponding to the operation of the larger scale rotating membrane device, and for different types of membranes. The ROMER process was developed based on criteria derived from the results obtained using the flow cell, considering a calculated wall shear stress to relate flow conditions at the different setup scales.

5.2.4 Micro-Engineered Membranes

The material and the design of the membrane are both integral to the development of any process based on membrane emulsification. The selection of its shape and dimensions, and of all membrane pore characteristics (size, arrangement, etc.) depend not only on the apparatus configuration but also on the emulsion material characteristics, as well as on the product target properties. In addition, parameters related to processing conditions, such as high flux and high trans-membrane pressures, high mechanical resistance, resistance against chemicals and high temperatures (especially relevant for cleaning procedure) are to be considered, especially for the choice of membrane material and membrane fixation.

Various commercial membranes and at a later stage, micro engineered membranes were successively utilized in the ROMER I and in ROMER II. Two types of cylindrical membranes were utilized in the ROMER I: commercial sintered mesh membranes (Absolta, Bopp AG, Zurich, Switzerland) and micro engineered Controlled Pore Distance Nano Membranes (CPDN). The sintered mesh membranes consist of five layers of woven stainless steel threads, with different shapes and patterns corresponding to different mesh sizes. The finest mesh consists of slit shaped pores between the threads, which are about 2 μm in width. The inter pore distance is defined by the size of the thread between the pores and was about 22 μm (10× pore width). These membranes were found to be robust: they resisted trans membrane pressures up to 10 bars. CPDN-membranes are nickel membranes (Stork Veco B. V., Eerbeek, Netherlands). They are coated with a layer of diamond like carbon by chemical vapor deposition in order to shrink the pore diameter to 1.5 μm diameter. CPDN membranes have uniform pore size, with an inter pore distance of 67 μm (45× pore diameter). CPDN-membranes were found to resist trans-membrane pressures up to 2 bars, which limited their use for the production of emulsions with reduced drop size using the ROMER I.

The design and fabrication of specific membranes with the most adequate surface properties and with adjusted pore size and pore distance are certainly essential to develop further processes based on ROMER devices, and which are meant to allow for the production of emulsions with well-defined target properties. Two

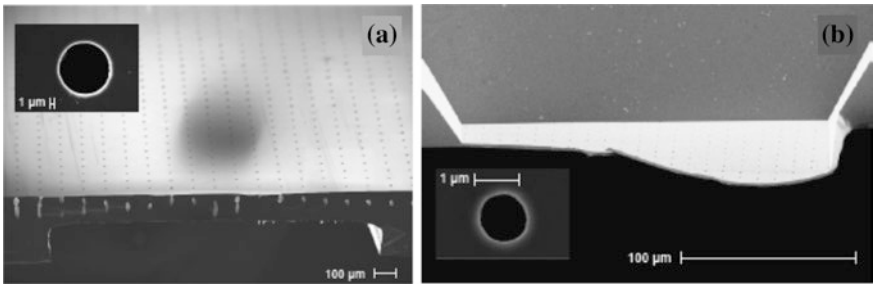

Fig. 5.4 SEM micrographs showing the pore size and pore distribution -with regular inter-pore distance- on a silicon membrane (**a**) and on a silicon nitride membrane (**b**)

protocols for the fabrication of flat micro engineered membranes were developed for applications in the scope of MagPro^{2}Life. Figure 5.4 shows SEM micrographs of two membranes produced in-house, using these procedures.

According to the first protocol, membranes with circular pores of 12 µm diameter are produced from a 300 µm thick silicon wafers. Both sides of the wafer are patterned with photolithography and by Plasma Enhanced Reactive Ion etching (PE-RIE) using the BOSCH process. This process allows for etching structures into silicon with a high aspect ratio (height/width up to >20) with steep sidewalls. Part of the silicon from the backside is etched to create membranes areas, framed by a thicker silicon support. Membrane sections have an area of about 1.5 mm^2 and a thickness of 100 µm. After the support structure is created, pores are etched into the membranes from the front side of the sample. In the same step the membrane macroscopic shape is cut out from the wafer sample.

According to the second protocol, membranes with circular pores of 0.4–5 µm are produced from wafers coated with 1 µm of silicon nitride from Low Pressure Chemical Vapor Deposition (LPCVD). Electron beam lithography was used as a patterning method, because patterning pores below 0.5 µm in size with optical lithography is not applicable. Briefly, the support structure is patterned at the backside of the substrate by performing optical lithography and reactive ion etching to etch out square shaped parts of the silicon nitride. This is followed by selective wet etching of silicon in KOH. Freestanding, square shaped membrane areas of 250 µm width, supported by the silicon substrate at the sides can thereby be produced. In the following step, pores are etched into these membrane areas. Therefore a hard mask of titanium has to be deposited onto the membrane surface and spin-coated with the electron beam resist. The resist is patterned with electron beam lithography. The pore pattern is then transferred into the titanium layer by reactive ion etching in a SF6 plasma. Pores are then etched into the silicon nitride membrane layer in a CHF_3 plasma which was alternated with an O2 plasma to achieve steep side walls [see (Kaspar 2012) for further information on the etching process]. Finally the residual titanium hard mask is removed by wet etching in a mixture of HF, water and H_2O_2.

Both types of micro-engineered membrane were utilized in the flow cell, as well as in the ROMER II device for the lab-scale and pilot-scale production of oil-in-water (O/W) emulsions.

5.3 Production of Emulsion-Based Functional Particles Using the ROMER II Device

Within the scope of MagPro^{2}Life, the process based on the ROMER II, as it is described in the previous section, was applied to the production of functional particles. A model O/W emulsion system was used to test and optimize all device functions. Adding complexity to the formulation, the process was further adapted for the large-scale production of magnetic composite particles and surface-functionalized composite particles.

5.3.1 Production of Model W/O Emulsions

For the preparation of oil-in-water (O/W) emulsions, filtrated Hydrioil SOD.24 (Hydrior AG, Switzerland), which is composed of hydrated alcylesters of oleic acid, was used as the disperse phase. The continuous phase consisted of a mixture of water, polyethylene glycol (Polyglykol 35,000 S, Clariant, Germany) and Polysorbate 20 (Sigma Aldrich, Germany). Polyethylene glycol was used to adjust the viscosity of the continuous phase within a range from 1 to 22 mPa s (at T = 20 °C) by varying concentration from 0 to 9%. Polysorbate 20 was used as an emulsifier to guarantee a fast stabilization of drops after detachment from membrane pores. Emulsions were prepared using the ROMER II by pumping the disperse phase (Hydrioil) through the membrane into the aqueous continuous liquid phase, which was pumped through the shear gap. Emulsion samples were systematically analyzed off-line by laser diffraction (LS13 320, Beckman Coulter, CA, USA) to measure their size and size distribution.

In general, the results from experiments conducted in the ROMER II device were in good agreement with ones performed in the lab-scale flow cell. The visualization of drop detachment in the cell showed that drops only form when using plasma oxidized membranes, whereas the disperse oil phase systematically wets the surface of untreated membranes, which prevents from the formation of drops in the dripping mode.

The evolution of the size and size distribution of emulsions produced in the ROMER II, using treated silicon membranes as a function of the applied wall shear stress was investigated by varying two main processing parameters: the rotational speed and the viscosity of the continuous liquid phase. Figure 5.5 shows the variation of the median drop size and the corresponding span as a function of the wall shear stress, in the case of O/W emulsions produced using a plasma

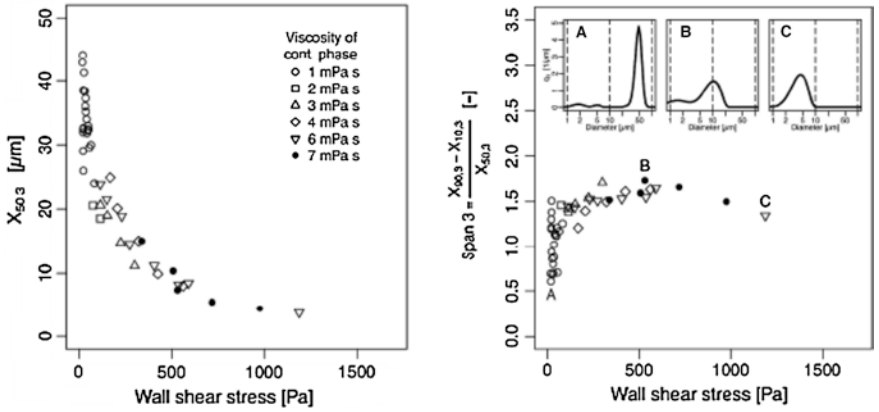

Fig. 5.5 Droplet median diameter (*left*) and span (*right*) versus wall shear stress in pilot scale apparatus. Droplet size distributions are shown for three particular points (*A*, *B*, *C*)

oxidized silicon membrane with a pore diameter of 12 µm. The different curves, which correspond to different continuous phase viscosities, fall onto one master curve. The median size decreases exponentially with the wall shear stress, while the width of the distribution increases strongly, up to a wall shear stress of about 50 Pa. For wall shear stress within a range of 50–600 Pa, the span is close to constant. At higher wall shear stresses, the span decreases again. The spans are overall relatively low ($\leq$1.7) for all samples measured.

In the flow cell, with treated silicone membranes, drops were observed to form in a dripping regime at low wall shear stresses. For high wall shear stresses (about 100–500) jetting started, and drops detached further downstream from the pore. At a wall shear stress of about 490, drops with a size equal or smaller than the pore diameter were seen to detach from the tip of the jets. The variation of the span when increasing wall shear stress, se observed for experiments in the ROMER II, correlates well to the transition from dripping to jetting observed during the visualization experiment in the cell. Indeed, drop breakup in the jetting mode leads typically to less controlled drop detachment (Rayleigh breakup) and thereby to drop sizes that are less uniform, compared to the case of drop breakup in the dripping mode. At wall shear stresses higher than 600 Pa the span of the resulting size distribution decreased. It was possible to achieve high values for the wall shear stress only by increasing the viscosity of the continuous liquid phase. Under laminar flow conditions, increasing the viscosity of the continuous phase leads to damping the filament surface waves (Rayleigh instabilities), which are responsible for the breakup of the jet. Thus, the jets were more stable and their ends broke up in a more ordered manner. A similar behavior was already observed under co-flow conditions, during experiments conducted and described within our group (Cramer et al. 2002).

The influence of the pore diameter on the drop size was also examined in the visualization flow cell. The relationship between pore diameter and drop diameter at a given wall shear stress was found to be almost linear, in the case of

silicone membranes with circular pores with a mean diameter of 12, 10 and 5 μm respectively. Additionally, emulsification experiments were conducted using silicone nitride membranes with 1 μm pores. While well-defined emulsions could be produced, these membranes showed a significantly reduced longevity within the ROMER II device. In the flow cell, the same membranes were found to resist high cross flow velocities, corresponding to similar pressure conditions as the ones used in the large scale device. This indicates that some additional compatibility factors, more than the fragility of the membrane, are limiting the lifetime of silicone membranes in the ROMER II device.

The production of model O/W emulsions in the ROMER II and the related study conducted in a separate flow cell showed that the main parameters influencing the median drop size and the width of the drop size distribution are the wetting of the membrane surface by the disperse phase, the amplitude of the applied wall shear stress and the membrane pore size. To achieve a narrow drop size distribution, emulsification should be produced using membranes with adequate surface properties, at wall shear stresses between 20 and 60 Pa.

5.3.2 Magnetic Composite Particles

Emulsion-based composite particles (Fig. 5.6), consisting of a beeswax matrix embedding fatty acid-coated magnetite nanoparticles (MNPs), were produced by generating an O/W type emulsion in the ROMER II, using a process directly adapted from the one used for the O/W model emulsions and presented in the paragraph above. Magnetic nanoparticles (MNPs) are pre-suspended in the disperse phase in the liquid form in order to produce composite micro-droplets in the ROMER II at sufficiently high temperature, which are thereafter quenched using ice water and thereby solidified into composite magnetic beads. The magnetophoretic mobility of the beads can be adjusted by varying the MNPs concentration in the disperse phase before forming the emulsion.

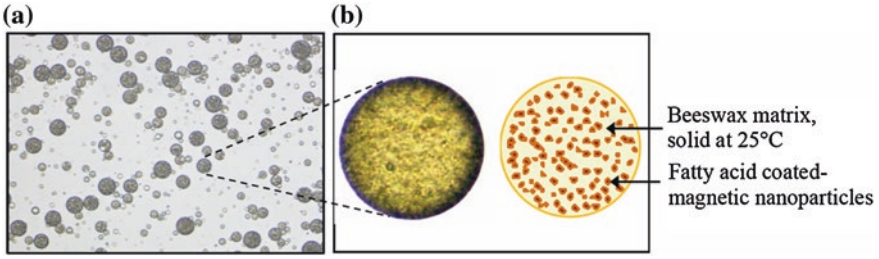

Fig. 5.6 **a** Light microscopy image showing a typical oil-in-water type emulsion, formed using a mixture of hot liquid PKS containing MNPs as the disperse phase and water with a thickening agent and surfactants as the continuous phase; **b** Picture of a solidifying composite droplet (*left*) and scheme showing the typical composite structure of MANACOs (*right*)

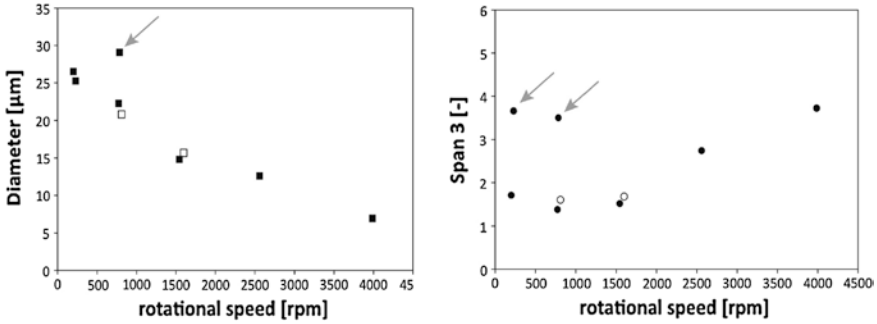

Fig. 5.7 Index values for the q3 distribution versus rotational speed during emulsification. The *arrow symbols* mark results corresponding to samples containing large agglomerates. *Open symbols* Hydrioil emulsion, *closed symbols* Bees wax suspension. *Left* Median diameter (D50;3) versus rotational speed, *right* Distribution width (Span of q3 distribution) versus rotational speed

In preliminary experiments, beeswax particles containing no MNPs were produced for comparison with model O/W emulsions prepared under similar processing conditions in the ROMER II. Pure beeswax was dispersed into a solution consisting of PEG and Polysorbate 20 in water, at 80 °C. After it is produced, the emulsion is instantaneously chilled down to 10 °C (3 °C/s) under gentle agitation in a vessel.

In Figure 5.7, the variation of the droplet/particle median size (X50;3) and of the span of the volume based distribution (q3) with the rotational speed is presented for Hydrioil droplets and for beeswax particles. Results for both products follow the same trend: for higher rotational speed the particle diameter decreases and the distribution width (Span 3 value) increases. Emulsification at higher temperature leads to increased coalescence and agglomeration of the product during cool down, which is reflected by the high median values for some measurements, for which agglomerates were present in the emulsion sample analysed. In general, the primary droplet size is relevant for evaluation the emulsification process and big agglomerates should be excluded. They can be easily isolated from the product using classification, after cooling down the wax-based emulsions.

The dispersion of the magnetic nanoparticles in the beeswax prior to emulsification is key to produce monodisperse emulsions resulting in particles with homogeneous properties. During the project, OA-coated magnetic nanoparticles were regularly provided by RATB at various stage of their development, in the form of a solid compound containing more or less water depending on the particle batch. Even in small quantity, the presence of water irremediably prevents from generating a homogenous dispersion of OA-coated MNPs in beeswax. The agglomerates formed by the nanoparticles were found to block and damage membranes of the rotating membrane device during the preparation of the wax-in-water emulsion, affecting the disperse phase volume throughput and the size dispersity of the resulting emulsions, which is illustrated in Fig. 5.8.

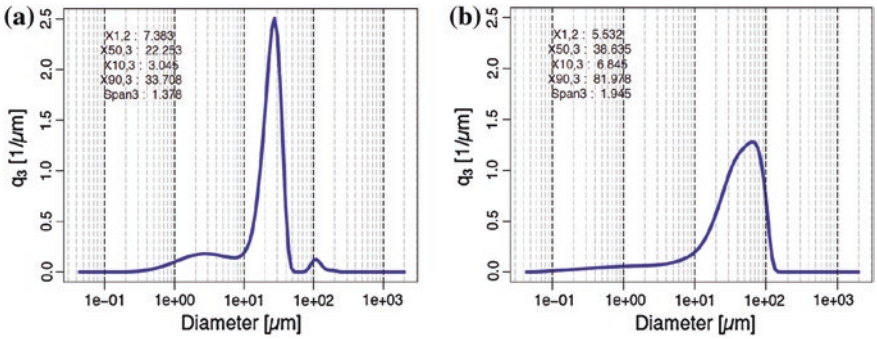

Fig. 5.8 Size distribution of emulsions consisting of **a** Beeswax in a 2 % Polysorbate solution (with no further classification), **b** Beeswax + MNPs mixture in a 2% solution of pre-synthesized AEX surface-active polymers (after sieving)

We have addressed this by developing a method based on azeotropic distillation using toluene, which allows to isolate most of the water contained in the RATB MNPs compound, and ultimately to prepare homogeneous wax-based mixtures with high MNPs concentrations, in sufficiently large quantities. This in turn allowed us to validate the utilization of the ROMER II process for the large-scale production of composite particles.

The mechanical resistance of the membrane and of its fixation is critical to product quality. In addition, as the cost of the emulsification process step depends directly on the fabrication cost of the membranes, but also on its lifetime, robustness is also key to process viability. Experience on ROME emulsion in our group has shown that technical solutions are very often specific to the material processed and to the processing conditions.

5.3.3 Surface-Functionalized Particles

AEX and CEX surface functionalized MANACOs were produced following a same two-step approach based on the ROMER II process developed for the production of naked composite particles. Briefly, a functional polymeric material is pre-synthesized (1) and subsequently used as a surface-active ingredient for the preparation of coated magnetic composite particles via emulsification in the ROMER II device (2). Step (2) is presented in the paragraph above, while step (1) is described in this section.

Functional block copolymers were specifically designed with a molecular structure such that they coat the wax droplets during emulsification and form, after drop solidification, an external functional layer, which is subsequently chemically bound onto the matrix of the resulting MANACOs via in situ radical polymerization. A scalable procedure allowing for the chemical synthesis of both cationic and anionic block copolymers with varying molecular composition and structure was developed, based

Table 5.1 Zeta potential values measured for particles produced using the ROMER II device, with different formulations

Emulsion formulation (surfactant)	ZP values measured in phosphate buffer (pH = 7) mV
1. AEX	+33.4 mV ± 3
2. AEX + Tween	+10.4 mV ± 0.8
3. Tween	−11.3 mV ± 1.7
4. CEX + Tween	−12.8 mV ± 0.3
5. CEX	−51.0 mV ± 1

Tween only, mixtures of Tween + AEX/CEX polymers, or AEX/CEX polymers only were used as surfactants

on Atom Transfer Radical Polymerization (ATRP). For AEX functional polymers, the synthesis route included the pre-synthesis of the ATRP initiator (reactive Ester) and a subsequent two-step reaction in the ATRP condition. The first polymerization reaction, conducted under absolutely water-free conditions, is to form a lipophilic block attached to the anchoring group (Ester). It is followed by the polymerization of the anion exchanger (AEX) monomer unit to form a second block, which is hydrophilic. CEX functional polymers were synthesized utilizing the same procedure than for the AEX functional polymers: their chemical synthesis is based on the ATRP process, using a CEX monomer for the last reaction step. All AEX and CEX functional block copolymers had the same generic architecture based on three key structural features: an anchoring group, a lipophilic spacer and a functional hydrophilic block.

Table 5.1 presents the zeta potential values measured for MANACOs produced in the ROMER II device, using different formulations: with and without AEX/CEX functional polymers.

This comparison of the surface properties shows that our processing strategy allows for the preparation of MANACOs with a functional surface layer. However, as indicated by the loss of AEX/CEX functionality after particle rinsing (not shown), the immobilization of the coating polymers onto the MANACOs is not robust enough. The polymer chains forming the functional layers on the particle surface have to be strongly, chemically anchored onto the particle matrix. If alternative functional polymers, allowing for a robust surface anchoring, can be synthesized in sufficiently large quantities, it is only a matter of adapting the formulation and the processing conditions, to produce functionalized particles with resistant properties, using the ROMER II device.

5.4 Shear-Enhanced Pore Extrusion of Vesicles in the NAMPEX Device

5.4.1 Functional Vesicles

Vesicles are nanometer- to micrometer-sized spherical compartment structures consisting of an aqueous core and one or several self-closed bilayer membranes of amphiphiles, typically phospholipids, which are the main components of biological

membranes (Walde 2004). Due to their adjustability in composition, size, charge, and surface properties and to their ability of encapsulating both hydrophilic and hydrophobic cargo, lipid vesicles have been recognized as versatile carrier systems allowing to design multifunctional and application-tailored vehicles (Sawant and Torchilin 2010; Bally et al. 2010; Kim et al. 2010; Chang and Yeh 2012).

For application within the scope of the MagPro^{2}Life project, vesicles entrapping magnetic nanoparticles were considered for the magnetic separation of high value pharmaceutical products based on affinity adsorption onto the magnetic vesicles. Surface functionalization for specific target molecules can readily be introduced by incorporating positively charged (AEX), negatively charged (CEX) or specifically functionalized (e.g. biotinylated, antibody-coupled) amphiphiles into the vesicle membrane without affecting vesicle integrity (Torchilin 2005). The passive encapsulation of a suspension of well-stabilized hydrophilic magnetic nanoparticles into the aqueous core and interlamellar space of uni- and oligolamellar vesicles during their synthesis imparts magnetophoretic mobility to the vesicular absorbent (Nappini et al. 2011; Garnier et al. 2012). Both the extent of magnetic loading and the density of surface functionalization are greatly influenced by the size and lamellarity of the vesicle carrier. The development of the NAMPEX process aimed at controlling these parameters by adjusting the shear flow field at the outlet of a nanopore membrane.

5.4.2 MagPro^{2}Life NAMPEX Setup

The NAMPEX device was constructed in collaboration with Bühler AG (Uzwil, Switzerland) and built at the Laboratory of Food Process Engineering at ETH Zurich. It is a lab-scale prototype device that combines the static extrusion process, which is conventionally used in a recirculation mode for vesicle homogenization, with a strong shear field at the membrane outlet. Figures 5.9 and 5.10 show schematic representations of the NAMPEX device and its principle, as well as the experimental setup as implement-ted in our laboratory.

The shear-enhanced extrusion chamber was constructed in a plate-plate conformation to allow for a flexible use and mounting of different types of flat membranes with well-defined nanopore channels.

The circular flat membrane is glued onto the static membrane holder (Fig. 5.10b) and the shear field is induced by the action of the rotor situated above the membrane. The shear rate at the membrane outlet is adjusted by controlling the rotor speed (up to 12,000 rpm) and the shear gap height via a µm-screw (up to 1 mm). The multilamellar vesicle (MLV) pre-suspension is spontaneously formed in excess water and forced through the nanopore membrane. As the deformed vesicles exit the pores, the flow stresses are expected to shear off the leading endcaps of extruded vesicles, which immediately self-close to form unilamellar to n-multilamellar vesicles after a single extrusion cycle, depending on the applied shear rate.

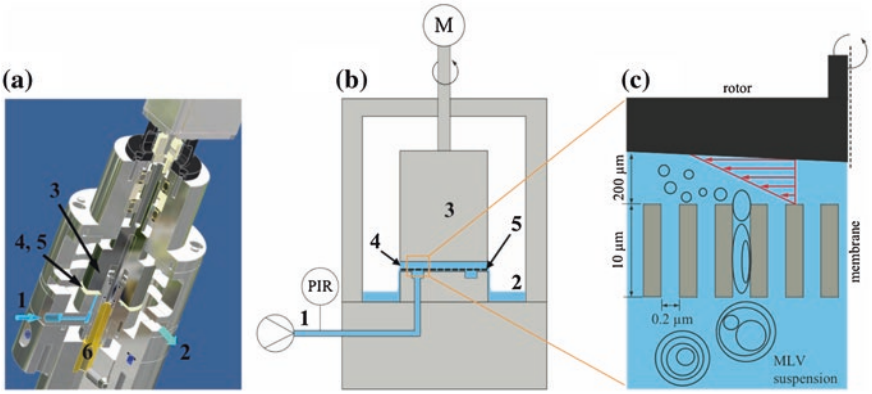

Fig. 5.9 Technical drawing (**a**) and schematic representation (**b**) of the NAMPEX device with the main functional components of the apparatus: MLV suspension inlet (*1*), collection of dynamically extruded vesicle suspension (*2*), rotor (*3*), shear gap between rotor and static membrane glued onto the membrane holder (*4*), flat nanopore membrane (*5*), µm-screw for shear height adjustment (*6*). Close-up of the shear-enhanced pore extrusion chamber illustrating the principle of the NAMPEX device (**c**)

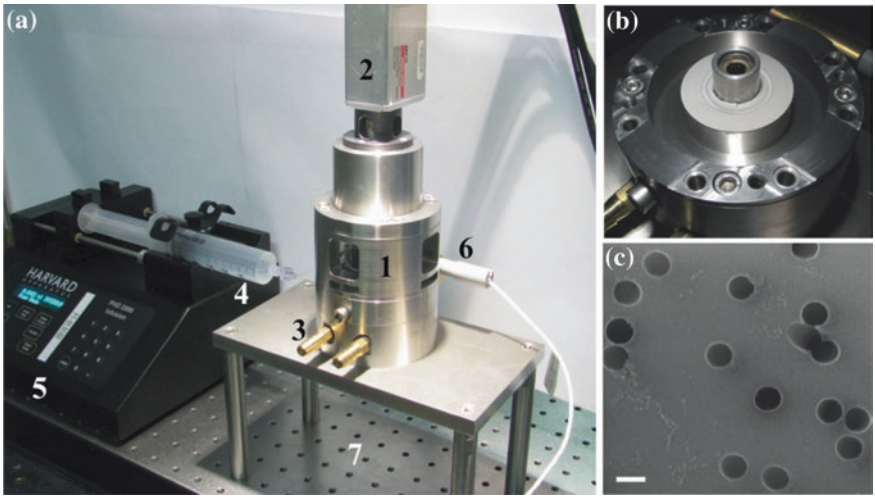

Fig. 5.10 Experimental setup showing the key components of the NAMPEX process (**a**) NAMPEX apparatus and housing (*1*), motor (*2*), connectors to optional thermostat controller for the NAMPEX housing (*3*), syringe containing the initial MLV suspension (*4*), flow rate-controlled syringe pump (*5*), pressure sensor at membrane inlet (*6*). Static membrane holder with flat membrane disc mounted (**b**). SEM micrograph of track-etched polycarbonate membrane with statistically distributed pores and a nominal mean pore diameter of 200 nm (scale bar: 200 nm) (**c**)

5.4.3 Vesicle Extrusion

The NAMPEX device allowed, for the first time, to investigate the effectivity of a shear field at the membrane outlet on the homogenization of multilamellar vesicles in dynamic membrane extrusion as developed in the frame of the MagPro^{2}Life project. In analogy to the process development for the controlled production of emulsion-based composite particles, optimum material and process parameters of the NAMPEX device were evaluated using a plane MLV suspension in ultrapure water. MLVs were prepared by the thin film hydration method (Walde 2004) using pharmaceutical grade phosphatidylcholine purified from soybean (soyPC; LIPOID S100, Lipoid AG, Switzerland). Prior to NAMPEX experiments, the MLV suspension was cleaned and regularized by pre-extruding it three times through a 800 nm-pore polycarbonate membrane using the conventional (static) LIPEX extruder (Northern Lipids, BC, Canada). The resulting MLV pre-suspension was taken through the NAMPEX process by pumping it through a 200 nm-pore membrane into the shear gap at varying rotor speeds (0, 1,000, 5,000, 10,000 rpm). Different vesicle membrane elasticities and different nanopore membrane types with respect to membrane material and pore shape were examined. The morphology of dynamically extruded vesicles was analyzed by dynamic light scattering (BI-200SM, Brookhaven Instruments, NY, USA) and by a colorimetric assay using 2,4,6-trinitrobenzene sulfonate (TNBS) to measure their hydrodynamic diameter D_h and polydispersity index *PDI*, as well as the relative external surface area E representing the degree of lamellarity (Engel 2013).

Figure 5.11 shows the evolution of vesicle size (Dh), polydispersity (PDI) and lamellarity (E) as a function of shear rate in the case of a soyPC MLV pre-suspension passed through a track-etched polycarbonate membrane with well-defined cylindrical

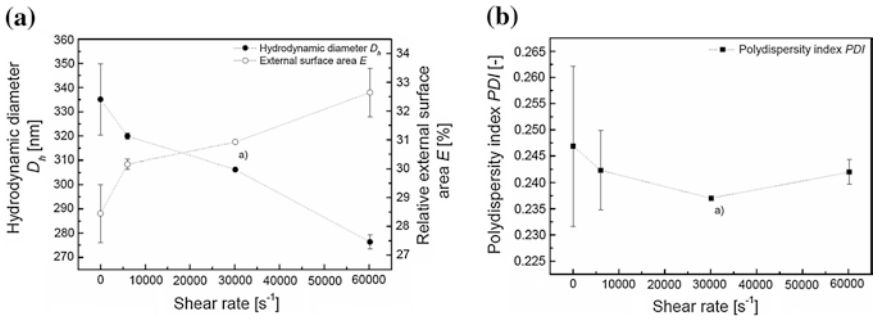

Fig. 5.11 Mean hydrodynamic diameter D_h (*closed circles*), relative external surface area E (*open circles*) (*left*) and polydispersity index *PDI* (*closed squares*) (*right*) of a 0.5 mg/ml soyPC vesicle suspension after three static pre-extrusion cycles through a 800 nm-pore PC membrane (index values of the initial MLV pre-suspension: $D_{h,i} = 969$ nm; $E_i = 16.3$ %; $PDI_i = 0.236$) followed by one extrusion pass through the ROMER device at increasing shear rates (0–60214 s^{-1}) using a 200 nm-pore PC membrane. Shear gap height: 0.2 mm; flow rate: 1 ml/min. Mean values and standard deviations were calculated from three independent NAMPEX experiments (*a*) one measurement point only

pore channels and a nominal mean pore diameter of 200 nm. The decrease in vesicle diameter with increasing shear rate nicely correlated with the reduction in vesicle lamellarity as reflected by the increasing relative external surface area.

It has to be noted, however, that the overall reductions in vesicle size and lamellarity observed over the entire shear rate range (D_h: 335 nm $\rightarrow$ 276 nm; E: 28 $\rightarrow$ 33 %) were small compared to the respective reductions achieved by the simple extrusion step in the absence of a shear field (D_h: 969 nm $\rightarrow$ 335 nm; E: 16 $\rightarrow$ 28 %). The values obtained after one shear-enhanced extrusion cycle at the maximum representative shear rate of 60,200 s^{-1} ($D_h = 276$ nm; $E = 33$ %) were still largely deviating from the values expected for unilamellarity ($D_h \approx 100$–140 nm; $E \approx 40$–50 %) (Mayer et al. 1986; Gruber and Schindler 1994; Fröhlich et al. 2001). The polydispersity index of dynamically extruded vesicles was not influenced by increasing shear forces in the evaluated shear rate range. In summary, the reduction in vesicle size and lamellarity by the extrusion technique was shown to be a pressure driven process primarily taking place at the pore inlet as previously suggested by Frisken et al. (2000). The shear field at the pore outlet had a minor effect on further size and lamellarity reduction.

5.5 Conclusion

Dynamic membrane pore extrusion has proved to be a flexible tool for tailoring drop or capsule microstructure of multiphase liquid systems and their techno-functional properties. Related structure engineering concepts were successfully worked out for (i) surface functionalized magnetic composite particles and (ii) functional vesicles within the MagPro^{2}Life Project. The coupling of drop/capsule formation with functionalization steps by either entrapment/encapsulation of components for controlled release or surface/interface modification for adjusted and more or less specific adsorption characteristics have been addressed with respect to the overarching goal of the project being the separation of specific protein fractions from soy whey streams.

Even though the functionalization steps applied need further refinement for improving the specific protein adsorption capabilities, it has become obvious that there is a huge potential for functionalized disperse particle or droplet structures generated by dynamic membrane pore extrusion far beyond the frame of this MagPro^{2}Life project approach.

References

Abrahamse A, van der Padt A, Boom R, de Heij W (2001) Process fundamentals of membrane emulsification: simulation with CFD. AIChE J 47:1285–1291

Abrahamse AJ, van Lierop R, van der Sman RGM, van der Padt A, Boom RM (2002) Analysis of droplet formation and interactions during cross-flow membrane emulsification. J Membr Sci 204:125–137

Bally M, Bailey K, Sugihara K, Grieshaber D, Voros J, Stadler B (2010) Liposome and lipid bilayer arrays towards biosensing applications. Small 6:2481–2497

Breitschuh B (1998) Continuous dry fractionation of milk-fat. Laboratory of food process engineering. PhD thesis, ETH Zürich, Zürich

Chang HI, Yeh MK (2012) Clinical development of liposome-based drugs: formulation, characterization, and therapeutic efficacy. Int J Nanomed 7:49–60

Charcosset C, Limayem I, Fessi H (2004) The membrane emulsification process—a review. J Chem Technol Biotechnol 79:209–218

Cramer C, Beruter B, Fischer P, Windhab E (2002) Liquid Jet stability in a laminar flow field. Chem Eng Technol 25:499–506

der Graaf S Van, Steegmans MLJ, van der Sman RGM, Schröen CGPH, Boom RM (2005) Droplet formation in a T-shaped microchannel junction: a model system for membrane emulsification. Colloids Surf A: Phys-Chem Eng 266:106–116

Eisner V (2007) Emulsion processing with a rotating membrane (ROME). Laboratory of Food Process Engineering. PhD thesis, ETH Zürich, Zürich. ISBN 3-905609-32-0

Ellenberger J, Fortuin J (1985) A criterion for purely tangential laminar flow in the cone-and-plate rheometer and the parallel-plate rheometer. Chem Eng Sci 40:111–116

Engel H, Rondeau E, Windhab E, Walde E (2013) External surface area determination of lipid vesicles using trinitrobenzene sulfonate (TNBS) and UV/Vis spectrophotometry. Anal Biochem 442:262–271

Feigl K, Tanner FX, Windhab EJ, Simos TE, Psihoyios G, Tsitouras C (2010) Numerical investigation of the formation and detachment of droplets from pores in a shear flow field. AIP Conf Proc 1281:1684–1687

Frisken BJ, Asman C, Patty PJ (2000) Studies of vesicle extrusion. Langmuir 16:928–933

Fröhlich M, Brecht V, Peschka-Süss R (2001) Parameters influencing the determination of liposome lamellarity by P-31-NMR. Chem Phys Lipids 109:103–112

Garnier B, Tan S, Miraux S, Bled E, Brisson AR (2012) Optimized synthesis of 100 nm diameter magnetoliposomes with hight content of maghemite particles and high MRI effect. Contrast Media Mol Imaging 7:231–239

Geerken MJ, Lammertink RGH, Wessling M (2007) Tailoring surface properties for controlling droplet formation at microsieve membranes. Colloid Surf A 292:224–235

Graber M (2010) Transport phenomena in rotating membrane processed W/O/W emulsions. Laboratory of food process engineering. PhD thesis, ETH Zürich, Zürich. ISBN 978-3-905609-46-2

Gruber HJ, Schindler H (1994) External surface and lamellarity of lipid vesicles—a practice-oriented set of assay methods. Biochim Biophys Acta-Biomembr 1189:212–224

Holzapfel S, Mühlich P, Rondeau E, Windhab EJ (2014) Drop detachment from micro engineered membrane surface in a dynamic membrane emulsification process

Joscelyne G SM (2000) Tragardh Membrane emulsification—a literature review. J Membr Sci 169:107–117

Kaspar P (2012) Active photonic crystal devices based on InP/InGaAsP/InP Slab waveguides. PhD thesis, ETH Zürich, Zürich

Kim KT, Meeuwissen SA, Nolte RJM, van Hest JCM (2010) Smart nanocontainers and nanoreactors. Nanoscale 2:844–858

Kobayashi I, Yasuno M, Iwamoto S, Shono A, Satoh K, Nakajima M (2002) Microscopic observation of emulsion droplet formation from a polycarbonate membrane. Colloid Surf A 207:185–196

Mayer LD, Hope MJ, Cullis PR (1986) Vesicles of variable sizes produced by a rapid extrusion procedure. Biochim Biophys Acta 858:161–168

Mueller-Fischer N, Bleuler H, Windhab EJ (2007) Dynamically enhanced membrane foaming. Chem Eng Sci 62:4409–4419

Nakashima T, Shimizu M, Kukizaki M (2000) Particle control of emulsion by membrane emulsification and its applications. Adv Drug Deliv Rev 45:47–56

Nappini S, Bonini M, Bombelli FB, Pineider F, Songregorio C, Baglioni P, Nordèn B (2011) Controlled drug release under a low frequency magnetic field: effect of the citrate coating on megnetoliposomes stability. Soft Matter 7:1025–1037

Peng SJ, Williams RA (1998) Controlled production of emulsions using a crossflow membrane, Part I: droplet formation from a single pore. Trans Inst Chem Eng 76:894–901

Sawant RR, Torchilin VP (2010) Liposomes as 'smart' pharmaceutical nanocarriers. Soft Matter 6:4026–4044

Schadler V, Windhab E (2006) Continuous membrane emulsification by using a membrane system with controlled pore distance. Desalination 189:130–135

Schröder V, Behrend O, Schubert H (1998) Effect of dynamic interfacial tension on the emulsification process using microporous ceramic membranes. J Coll Interf Sci 202:334–340

Timgren A, Tragardh G, Tragardh C (2009) Effects of pore spacing on drop size during crossflow membrane emulsification—a numerical study. Chem Eng Sci 64:1111–1118

Torchilin VP (2005) Recent advances with liposomes as pharmaceutical carriers. Nat Rev Drug Discov 4:145–160

Vladisavljevića G, Lambrichb U, Nakajimac M, Schubertb H (2004) Production of O/W emulsions using SPG membranes, ceramic α-aluminium oxide membranes, microfluidizer and a silicon microchannel plate—a comparative study. Colloids Surf A 232:199–207

Walde P (2004) Preparation of Vesicles (Liposomes). In: Nalwa HS (ed) Encyclopedia of nanoscience and nanotechnology, vol 9. American Scientific Publishers, California, pp 43–79

Windhab E, Schadler V, Troxler B, Duerig AK, Grohmann F, Duerig A, Eisner V, Grohmann FR (2006) Production of finely dispersed micro or nano emulsions with narrow drop size distribution comprises pressing fluid phase through e.g. filter cloth cylinder, from which drops are stripped by its motion and pass into non-miscible fluid. Patent Number(s): WO2006021375-A1; DE102004040735-A1; DE102004040735-B4; EP1781402-A1; EP1781402-B1; DE502005003021-G; JP2008510607-W; US2011038901-A1; JP4852042-B2; US8267572-B2

Xu JH, Li SW, Tan J, Wang YJ, Luo GS (2006) Preparation of highly monodisperse droplets in a t-junction microfluidic device. AIChE J 52:3005–3010

Chapter 6
Synthesis of Functionalized Magnetic Beads Using Spray Drying

Valéry Tchanque Kemtchou, Maria Schäfer and Urs Alexander Peuker

Abstract The goal of Technische Universität Bergakademie Freiberg (TUBAF) in MagPro^{2}Life was to develop, based on Solution Process (SolPro), a low-cost scalable synthesis process as well as to optimize the efficiency of particle production regarding safety and ecological aspects. Depending on target protein charges in the extraction pH range, magnetic beads with cationic and anionic functionalities (CEX– and AEX–SolPro beads) were successfully synthesized and characterized. Both types of beads were equipped with the appropriate functionalities allowing their application in bioseparation (superparamagnetic, ion exchange properties). Characterization analyzes of the SolPro beads (CEX und AEX) showed the high potential of the developed processes. CEX–SolPro particles possess a lysozyme extraction capacity of approximately 280 mg/g, which is about three times higher than similar CEX-SolPro beads (same composition) produced by Hickstein and Peuker (2009) (77.6 mg/g). The newly designed and produced AEX–SolPro beads using poly(allyl)amine (PAAm) as anion exchanger exhibit extraction capacities of 85 mg/g for BSA as well as 145 mg/g for BBI. Several investigations proved that a quaternization of amino groups of poly(allyl)amine anchored on the beads surface increase their extraction capacity by a factor of 3. One kilogram of produced PAAm–SolPro was successfully tested by Solae Denmark in a pilot food line application.

6.1 Introduction

Solution Process (SolPro) has been developed in previous works done by Hickstein and Peuker (2009). This process allows using the spray drying technology for the synthesis of magnetic beads with suitable properties for their application in

V.T. Kemtchou (✉) · M. Schäfer · U.A. Peuker
Bergakademie Freiberg, Institut für Mechanische Verfahrenstechnik und Aufbereitungstechnik, Agricolastr. 1, Freiberg, Germany
e-mail: Valery.tchanque-kemtcou@mvtat.tu-freiberg.de

H. Nirschl and K. Keller (eds.), *Upscaling of Bio-Nano-Processes*,
Lecture Notes in Bioengineering, DOI 10.1007/978-3-662-43899-2_6

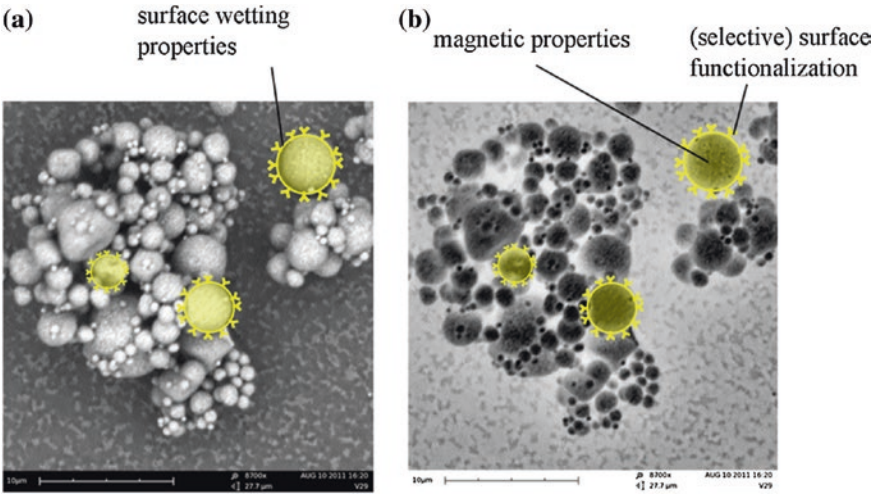

Fig. 6.1 **a** SEM magnetic beads with specifications; **b** inverted micrograph

bioseparation. Magnetic beads are composite particles provided with magnetic and protein extractive properties. In comparison to common protein extraction methods, like downstream processes, the use of magnetic beads in combination with High Gradient Magnetic Fishing (HGMF) technologies offers the integration of several unit operations in one single process step in bioseparation. Hence, the final number of process steps decreases and thus product losses too (Hickstein 2009).

To design such functional composite particles, Hickstein et al. have developed a modular process incorporating the synthesis of different types of components:

- *Superparamagnetic iron oxide nanoparticles* as core material, allowing for a magnetic separation of the beads,
- *Ion exchange resin* essential for protein extraction.

After their synthesis, these components are integrated into magnetic beads via spray drying. Figure 6.1 shows SEM-micrographs of spray dried magnetic beads.

Spray drying is a well-established method for particle design in many technological fields like pharmaceutical, cosmetic, food or chemical industry (Masters 1979; Sano 1992; Giunchedi and Conte 1995; Maa et al. 1998; Re 2006; Banert 2008). The main bead components chosen by Hickstein are summarized in Table 6.1.

The spray drying process was run using dichloromethane as organic solvent. The magnetic beads produced in the lab scale show relatively high protein binding capacities by extracting lysozym and β-galactosidase. This good protein extraction behavior proved the high potential of the Solution Process product in bioseparation. However, a scalability of this technique is essential for industrial applications. In addition, the use of dichloromethane as solvent in the whole process is in ecological point of view, according to EU-instructions (EU-Comission 2009), a big issue to overcome. Therefore, the challenge for TUBAF in this project was to develop,

Table 6.1 Main components used by Hickstein in SolPro

Functionality	Component	Synthesis
Superparamagnetic separation	Magnetite iron oxide nanoparticles	Co-precipitation
Protein binding at pH < pl	Sulfonated copolymer polystyrene-divinylbenzene (cation exchanger)	Miniemulsion polymerization, aminination resp. sulfonation
Protein binding at pH > pl	Aminated copolymer vinylbenzyl-chloride-divinylbenzene (anion exchanger)	
Mechanical stability and wetting	Copolymer polyvinylbutyral (matrix polymer)	(supplied)

based on SolPro, a low-cost scalable synthesis process, as well as to optimize the efficiency of particle production regarding safety and ecological EU-instructions (EU-Comission 2009). Such a new technology producing low-cost adsorbents fitted with high protein binding capacity would offer a wide range of applications ranging from bioseparation and water conditioning up to rare earth element processing.

6.2 Synthesis of Components

As described above, magnetic beads from SolPro were synthesized using spray drying technology. For their application in bioseparation, SolPro particles should provide different features. The particles should show appropriate functionality for protein adsorption as well as superparamagnetic properties for a magnetic separation of the particles. Furthermore, the synthesis process should have a high scale-up potential allowing a prospective industrial production. Based on previous works (Hickstein 2009), the following main components, developing or providing the required bead properties, have been chosen to be processed to magnetic beads by SolPro:

- *Magnetite* core material allowing the use of magnetic separation technologies
- *Ion exchange resin* essential for extracting the target protein
- *Organic solvent* which allows a homogenous mixture of the solid components
- *Matrix polymer* crucial to keep together the first two components. Its chemical structure has a strong influence on the wetting properties of the beads.

6.2.1 Nanoscaled Superparamagnetic Iron Oxide Particles

To fit the SolPro particles with superparamagnetic properties allowing the use of magnetic fishing technologies during their processing, iron oxide magnetite Fe_3O_4 was synthesized both in batch process as well as in pilot scale process.

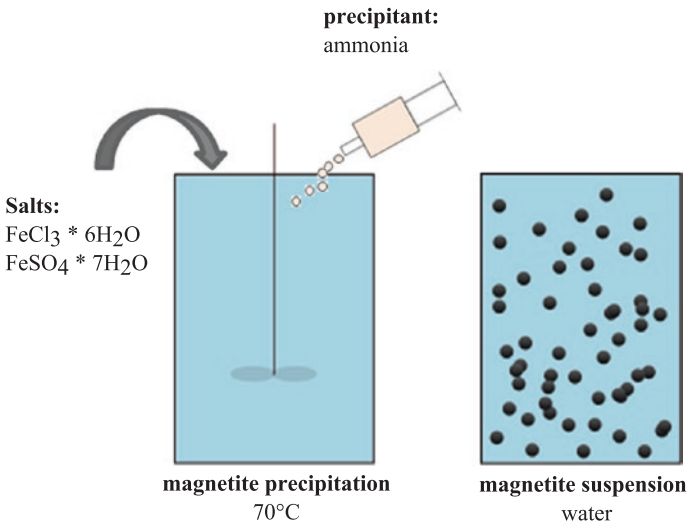

Fig. 6.2 Water-based magnetite nanoparticles synthesis in batch process

6.2.1.1 Synthesis in Batch Process

Using the batch process (Fig. 6.2), 1,000 ml/h (20 g solids) magnetic nanofluid has been produced on a lab scale. Iron oxide nanoparticles were co-precipitated using the following procedure:

- 47.03 g $FeCl_3$ 6f H_2O (0.174 mol) and 24.19 g $FeSO_4$ H_2O (0.087 mol) are dissolved in 1 L deionized water using a 1 L round bottom flask.
- The solution is stirred at 4000 min^{-1} for 10 min.
- During stirring, the solution is heated to 70 °C and maintained at this temperature.
- The stirring speed is raised to 9,000 min^{-1} and 60 ml of a 26 % NH_4OH solution are quickly added at the tip of the bottom flask using a syringe.
- After that, the stirrer is reduced to 4,000 min^{-1} again; the dispersion is stirred for another 20 min.
- At the end of the process step, the dispersion is cooled down to room temperature.

6.2.1.2 Pilot Scale Synthesis

The goal here was to prove the feasibility of a continuously operating process to produce water-based magnetic fluid using sono-precipitation. Pohl et al. have done some interesting works on the continuous synthesis of barium sulfate nanoparticles in ultrasound reactors (Pohl et al. 2012a, b). The synthesis technique used by Pohl et al. was chosen and adapted to targeted iron oxide particles. For this issue, the co-precipitation of magnetic nanoparticles was carried out following almost the same procedure as in the batch process; only the precipitant ammonia was substituted by potassium hydroxide. The sonochemical reactions were operated in two types of reactors: a conical reactor as well as a cavitational reactor (see Fig. 6.3).

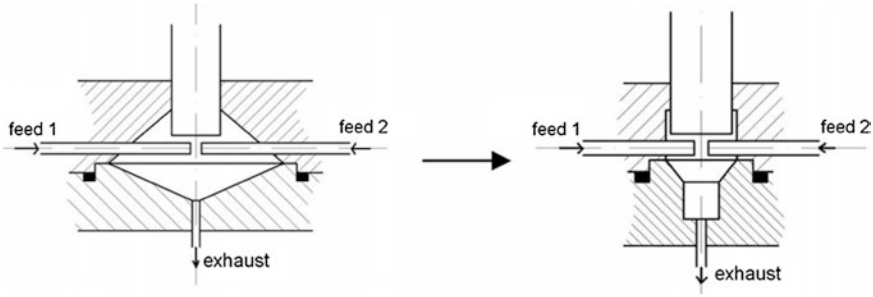

Fig. 6.3 *left* conical reactor, *right* cavitational reactor

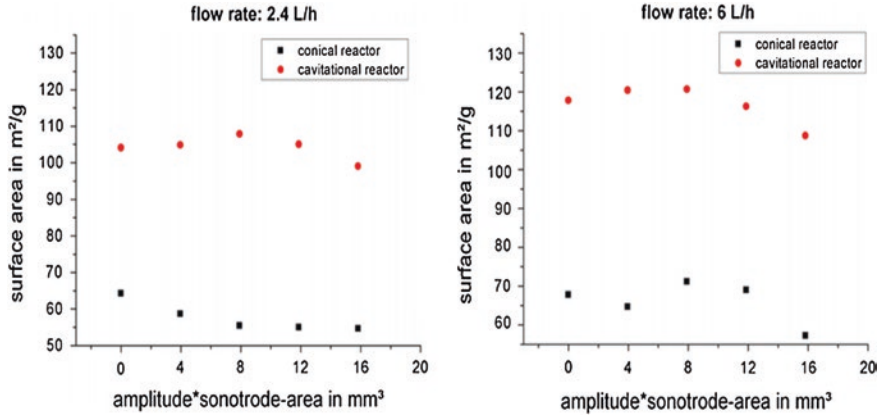

Fig. 6.4 The influence of ultrasonic energy input (amplitude * sonotrode area) on the specific surface area of the particles synthesized at different throughputs using both types of reactors

The reactors feature two different reaction chamber geometries. They are equipped each with a 20 kHz sonotrode getting a power of 200 W and possessing a diameter of 13 mm, which extends into the reaction chamber. In the conical reactor chamber, the injection pipes are located opposite to each other. The two injected feed streams are supposed to come into contact in the cavitation zone, which is located directly underneath the sonotrode. Experimental and numerical results show secondary effects like remixing in the conical reactor chamber.

Therefore, in order to reduce secondary flows and to optimize the power input of the ultrasonic field, the cavitional reactor has been chosen. Its geometry is based on the shape of the cavitation field, and the reaction chamber is smaller compared to the conical reaction chamber.

i. Comparison of the reactors by surface area measurements (BET)

In Fig. 6.4, the influence of ultrasonic energy input (amplitude * sonotrode area) on the specific surface area of the particles synthesized at different throughputs using both types of reactors is shown. Higher particle surfaces can be reached using the cavitational reactor. On the one hand, the reaction chamber is smaller

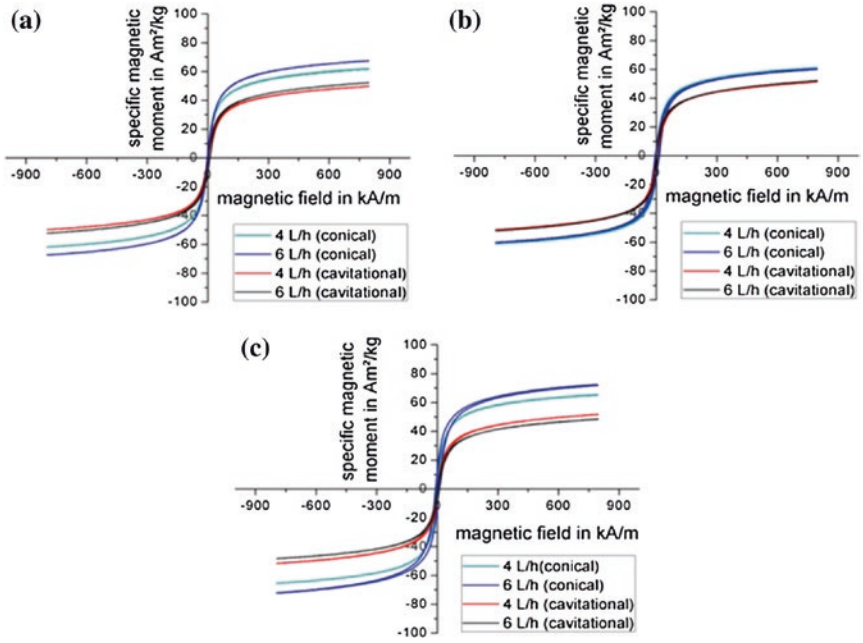

Fig. 6.5 Comparison of magnetic properties at different energy input: amplitude * sonotrode area takes values of 0 (**a**), 7.91 (**b**) and 11.86 mm^3 (**c**)

and so the retention time is shorter in this reactor. On the other hand, the effect of the cavitation intensity can be observed. The intensity is higher for the modified reactor chamber. Both factors cause a higher particle surface and therefore smaller particles. The flow rate correlates with the particle size produced in both reactors.

ii. Comparison of the reactors by magnetic properties of the particles

In Fig. 6.5, the comparison of the two reactor types is shown. In all cases, magnetite with superparamagnetic properties can be produced.

At the saturation magnetization, the energy input by ultrasound has no significant influence. The saturation magnetization of the magnetite produced in the conical reactor chamber is always higher than in the modified reactor chamber. The high local energy input (see also the high cavitation intensity and therefore the increased reactivity of the system) leads to smaller particles with lower saturation magnetization and lower quality. Thus, there is a damaging effect on the material quality in the reactor with cavitational geometry (c).

Using both types of reactor chambers, 120 g of superparamagnetic iron oxide nanoparticles were produced continuously as water dispersion (2 % solid mass fraction) with high flow rates up to 6000 ml/h.

In detail, it was concluded that the energy input by ultrasound has no significant positive influence on the particle size of precipitated magnetite. On the

Table 6.2 Comparison between magnetite produced in batch and in continuous process

	Throughput (g/h)	Specific magnetic moment (Am^2/kg)	BET (m^2/g)
Batch process	20	60	70
Continuous process using conical reactor	120	67	67

contrary, it leads to a decrease in the particle quality concerning the magnetic properties. Therefore, the use of a T-mixer as in the batch process would be sufficient to achieve the desired output.

Looking at the values of the specific magnetic moment and surface in Table 6.2, there are only marginal differences in the product quality from both kinds of production lines.

6.2.1.3 Nanoparticles Stabilization: Phase Transfer

After their synthesis, the nanoparticles should be stabilized for further processing. This is achieved through phase transfer from water solution to organic solvent. The nanoparticles are sterically stabilized due to adsorption of ricinoleic acid dissolved in the organic solvent (Rudolph 2012). According to Machunsky and Peuker (2007), Machunsky et al. (2009) a surfactant mass fraction in the solvent of 2 % and a ratio of 0.2 g surfactant per g iron oxide nanoparticles will guarantee the complete transfer of the particles and a minimum amount of fatty acid. Dichloromethane was used as solvent in this step. Erler et al. (2013) has investigated the influence of ammonia concentration on magnetite yield, pH and zeta potential during the phase transfer. Their results are shown in the Fig. 6.6.

According to Fig. 6.6, by choosing an ammonia mass concentration of 0.02 %, all magnetite particles (100 %) were transferred into organic phase. Furthermore, the zeta potential and pH value of the aqueous phase were −18 mV and 8.5, respectively. These parameters do not account for secondary effects like water entrapment, emulsion and ricinoleate formation.

Particle size distribution analysis of the suspension prior to as well as after the phase transfer was done using the dynamic light scattering (DLS) method. In Fig. 6.7, the effect of the phase transfer on the desagglomeration of the nanoparticles can be seen.

After precipitation, the nanoparticles are suspended in water as agglomerates with median size of approx. 3.95 μm (measured using laser diffraction). Due to their transfer to the organic phase by adsorption of ricimoleic acid on the surface, the primary particles are sterically stabilized (Rudolph 2012). So their median size in dichloromethane is approx. 20 nm (DLS measurement). This complies with literature values of superparamagnetic iron oxide nanoparticles, which where measured using transmission electron microscopy (TEM) or X-ray diffraction (XRD) analysis methods (Rudolph 2012).

To reduce the amount of dichloromethane used in the whole SolPro, dichloromethane was replaced with isopropanol, a more ecological organic solvent (Fig. 6.8).

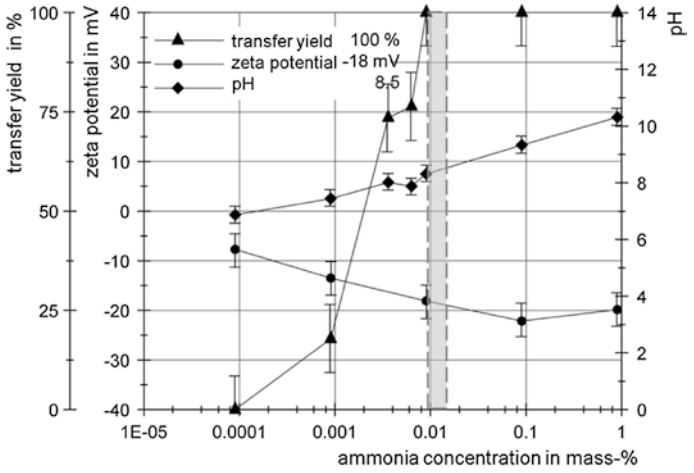

Fig. 6.6 The influence of ammonia concentration on magnetite yield, pH and zeta potential during magnetite transfer in dichloromethane

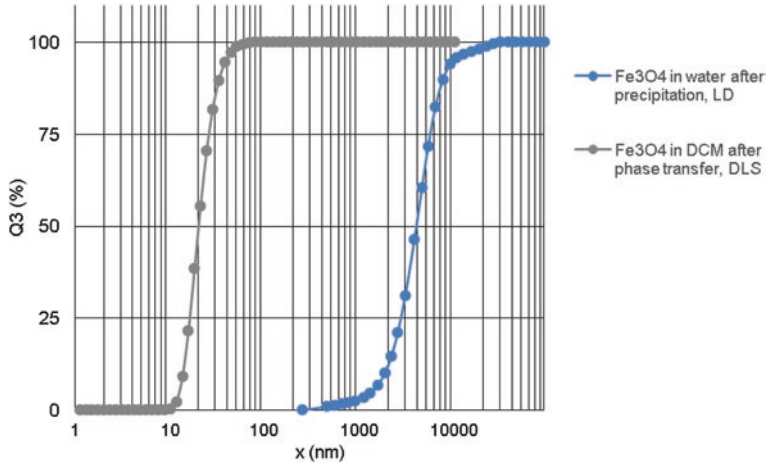

Fig. 6.7 PSD measurements of magnetite nanoparticles prior to as well as after phase transfer (logarithmic illustration)

6.2.2 Ion Exchanger

6.2.2.1 Cation Exchange Resin

Target proteins with positive charges at pH range of extraction were generally removed by a negatively charged cation exchanger. In case of SolPro, submicron sulfonated copolymer polystyrene-divinylbenzene (PS-DVB) resin was

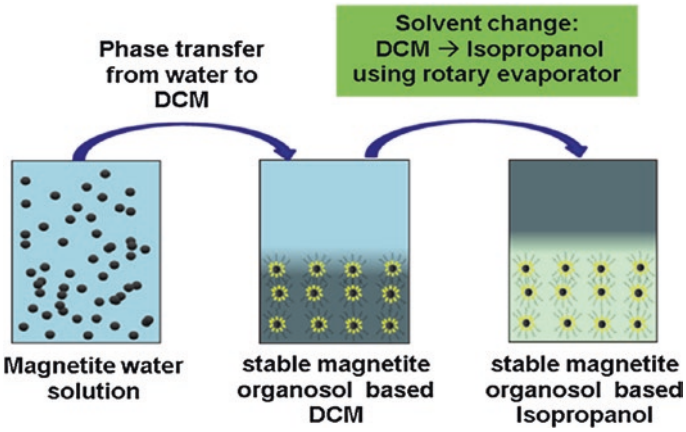

Fig. 6.8 Phase transfer and stabilization of magnetite nanoparticles in batch process

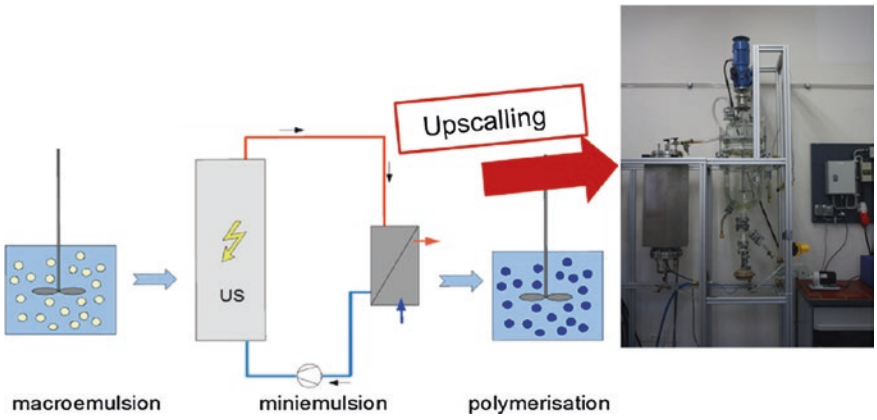

Fig. 6.9 Synthesis of sub micron scaled polystyrene-divinylbenzene particles

synthesized. The submicron scale of the Cation Exchange Resin (CEX) conveys their encapsulation during the spray drying process. The synthesis of CEX is illustrated in Figs. 6.9 and 6.10.

First, submicron polystyrene-divinylbenzene particles were produced using miniemulsion polymerization. After their synthesis, the cross-linked particles were sulfonated by adding sulfone groups on the resin through a chemical reaction in chlorosulfonic acid.

The CEX production process described above is time-consuming and costly. Therefore, an alternative process for the CEX production has been developed. The combination of ball and agitated ball milling allows the milling of commercial low-cost cation exchange resins from the micron scale down to submicron scale.

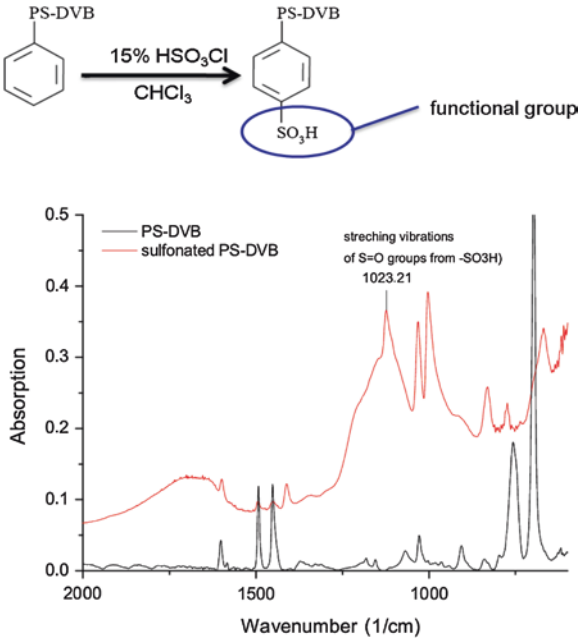

Fig. 6.10 Sulfonation reaction of polystyrene-divinylbenzene and sulfone groups characterized using FTIR-spectroscopy

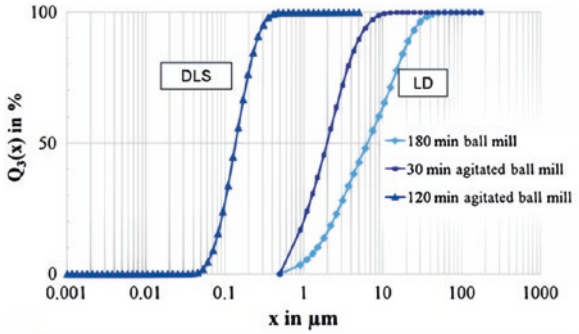

Grinding time	180 min ball mill	30 min agitated ball mill	120 min agitated ball mill
$X_{50,3}$	6.45 µm	2.0 µm	180 nm
capacity	2.96 eq/l	3.11 eq/l	3.04 eq/l

Fig. 6.11 Particle size distribution of commercially available cation exchange resins as well as capacity measured using acid/base titration

Figure 6.11 presents the influence of milling time and milling devices on the particle size distribution of the CEX resins. The capacity of the resins is also mentioned. With regard to particle size obtained over the different periods of time, laser diffraction (LD) or dynamic light scattering (DLS) measurements were carried out.

This new production process of submicron cation exchange particles offers a high potential with respect to production costs and complexity for application in bioseparation as well as in water conditioning.

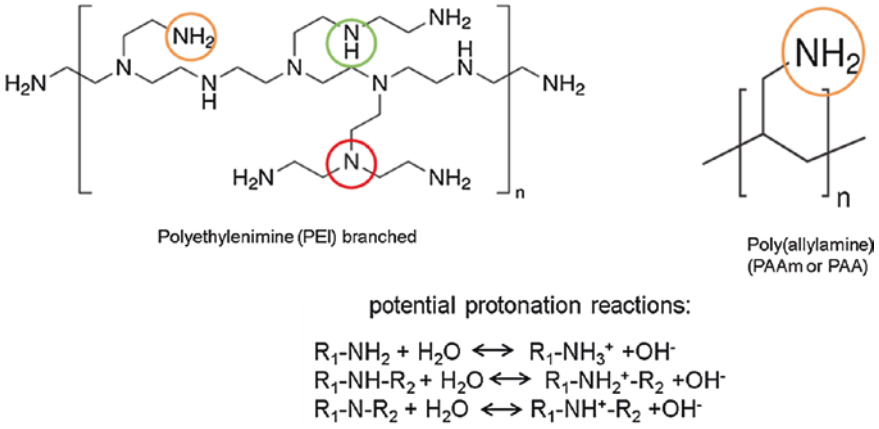

Fig. 6.12 Polyethylenimine and polyallylamine used as anion exchanger

6.2.2.2 Anion Exchange Resins

To extract negatively charged target proteins, the synthesis of aminated vinylbenzyl-divinylbenzene copolymer Anion Exchange Resins (AEX) was planned. However, the chemistry behind this synthesis is more sophisticated than the CEX chemistry (Hickstein 2009). For this reason, a new strategy to produce positively functionalized magnetic beads has been developed. Weak polyelectrolytes (PE) like polyethylenimine (PEI) and polyallylamine (PAA or PAAm) were chosen as positively charged functional polymer. Both polymers possess amino groups, which can be protonated in water or at low pH level. In this way, they exhibit the positive charges necessary for binding target proteins (Fig. 6.12).

6.2.2.3 Matrix Polymer

To promote the adsorption of target proteins, magnetic beads should provide good wetting properties in the bio-solution. Therefore, the matrix polymer should show light amphiphilic behavior. It should be sufficiently hydrophilic for wetting while at the same time it is hydrophobic to avoid loosening of the particles in aqueous solution. Moreover, the matrix polymer should be soluble in the solvent chosen for the spray drying process. Among the polymers we studied, Mowital B 30T copolymer (polyvinyl butyral) from Kuraray Europe GmbH showed the most suitable properties for this application. The chemical composition of polyvinyl butyral copolymer is shown in Fig. 6.13. While the alcohol part is responsible for the wetting feature, the butyral part makes the copolymer insoluble in water. Rudolph et al. have also found that polyvinyl butyral enhances the stability of iron oxide nanoparticles coated with ricinoleic acid in dichloromethane (Rudolph 2011, 2012).

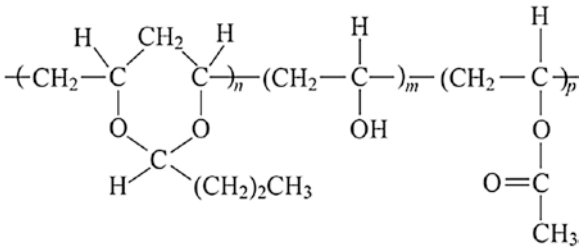

Fig. 6.13 Chemical structure of polyvinyl butyral with n butyral, m alcohol and p acetate subunits (Rudolph 2012)

6.3 Spray Drying of SolPro Particles

After production and purchasing of the basic components mentioned above, SolPro particles were synthesized using spray drying process. The cost factor is one of the major advantages between SolPro and other magnetic bead synthesis processes like polymerization techniques (ATRP, CFRP, etc.). After their synthesis, the magnetic bead components are simply mixed and subsequently spray-dried to result in functional particles. In continuous operation mode, this process can be run fully automatic with high throughputs. This makes the spray drying process one of the commonly applied technical processes to produce dry powder (particles) from suspension in many industrial fields (Hickstein 2009). The suspension is atomized to a controlled droplet size using a spray nozzle and an atomizing gas. The droplets are quickly dried by a hot gas at a temperature above the boiling point of the solvent used.

The lab scale production of SolPro particles was achieved via a commercial lab scale co-current spray dryer Büchi B-290 with an inert nitrogen atmosphere equipped with an external mixing two-fluids nozzle. A condenser Büchi B-295 allows closed cycle operation with solvent recovery. Figure 6.14 shows the principle scheme of the spray drying process:

6.3.1 CEX-SolPro Beads

SolPro particles with anionic functionality containing the following components were synthesized: magnetite coated with ricinoleic acid, sulfonated PS-DVB, PVB and isopropanol. After varying parameters such as the component's mass fractions in the feed and the type of CEX (produced through sulfonation and through the newly developed method), the results contained in Table 6.3 have been collected:

After the synthesis, the CEX-SolPro beads were characterized. The results of both the particle size distribution and the BET–analysis are presented in Table 6.4. The particle size distribution was measured using laser diffraction (HELOS from Sympatec) while the BET-analysis was performed using Flow Sorb from Micromeritics.

Binding capacity analyses of CEX-SolPro beads were carried out with lysozyme from chicken egg white (from Sigma Aldrich) as model protein. The BCA-Assay

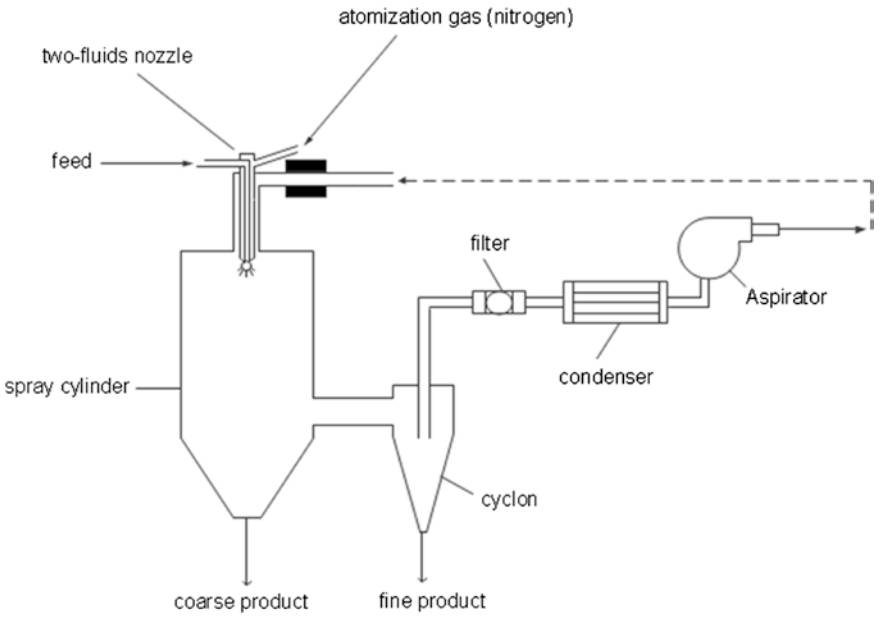

Fig. 6.14 Schematic spray drying process in closed cycle

Table 6.3 CEX-SolPro beads V38 (CEX containing milled cation exchanger)

Material	Mass fraction (%)
Magnetite	33.3[1]
Ricinoleic acid	6.7[1]
CEX (milled)	20[1]
Polyvinyl butyral	40[1]
Isopropanol	95[2]

Table 6.4 Particle size distribution using laser diffraction (HELOS from Sympatec), BET-analysis using flow sorb from micromeritics

Particle size distribution	X_{10} (3) (μm)	X_{50} (3) (μm)	X_{90} (3) (μm)
	0.85	2.60	6.94
Specific surface		S_m (m^2/g)	
		2.19	

was chosen as analysis method. The isoelectric point of lysozyme is 11.35 (Aldrich). Phosphate buffer at pH 8 and at pH 7 and an additional 1 M NaCl were used as binding and elution buffer, respectively. The results provided by Merck KGaA are displayed in Fig. 6.15.

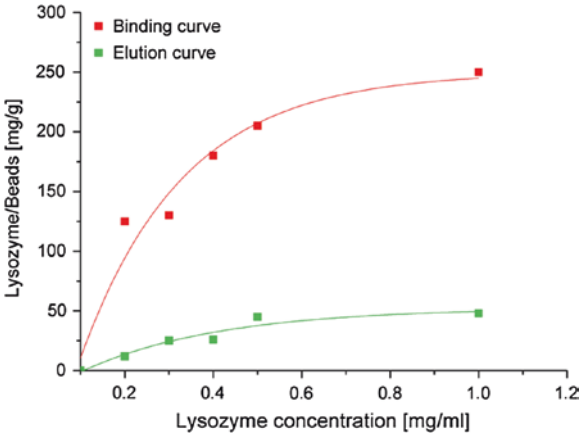

Fig. 6.15 Lysozyme binding capacity results of CEX-SolPro beads V38 measured by Merk KGaA using BCA-Assay

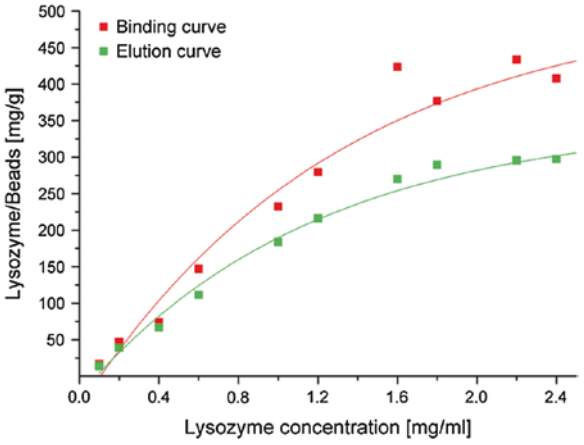

Fig. 6.16 Resulting lysozyme binding capacity of V51. Achieved by combination of pH-shift and salt elution step. Results gained using BCA-Assay

CEX-SolPro beads V38 show a lysozyme extraction capacity (binding and subsequent elution) of approx. 50 mg/g. The elution efficiency, which amounts to about 20 %, is relatively low. An explanation could probably lie in the strong binding properties of CEX particles (Hickstein 2009).

The beads also showed poor water wettability. To manage these problems, two modifications were made:

1. Increasing of CEX mass fraction in the beads from 20 to 40 %. Thereby, decrease of the mass fractions of PVB and magnetite with ricinoleic acid coating from 40 to 30 %.
2. Addition of sodium hydroxide in elution buffer to increase the pH to 9

More hydrophilic cation exchanger should improve the capacity as well as the wettability of the beads. At the same time, the combination of salt elution and pH-shift should enhance the elution efficiency (Hickstein 2009). Figure 6.16 shows the resulting binding capacity after the modifications presented above were made:

As expected, the modified CEX-SolPro beads (V51) possess a higher overall lysozyme extraction capacity. An increase about a factor of 6 can be observed. This derives from a doubled protein load and significantly increased elution efficiency. In addition to the salt elution, the pH-shift has increased the elution efficiency to 75 %. Furthermore, the dispersibility of the beads in aqueous milieu was improved.

6.3.2 AEX-SolPro Beads

The synthesis of magnetic beads with cationic functionalities was performed using the following components: magnetite coated with ricinoleic acid, polyelectrolytes (PEI and PAA or PAAm), activated PVB and dichloromethane. To avoid leaching of the PEs from the beads in aqueous solution, the polycations need to be cross-linked with the matrix polymer. After the activation step (Fig. 6.17), reactive particles were spray-dried in a closed cycle. Afterwards, the reactive particles were dispersed 72 h in a PE solution for cross-linking. These steps are illustrated in Figs. 6.18 and 6.19.

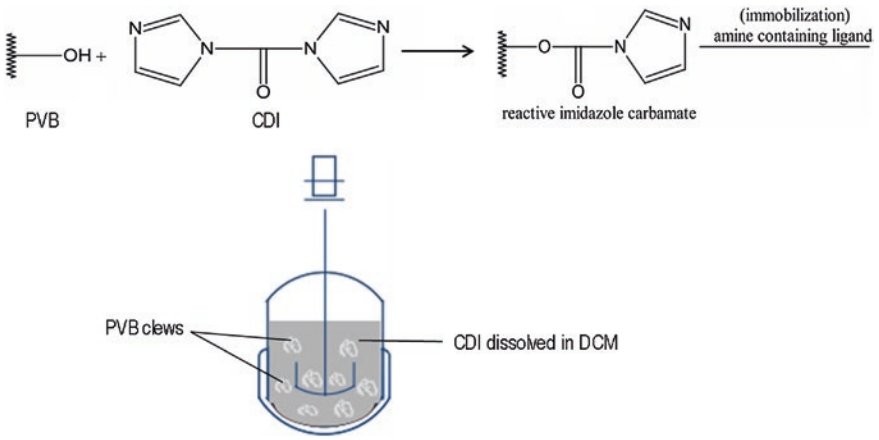

Fig. 6.17 Activation of PVB

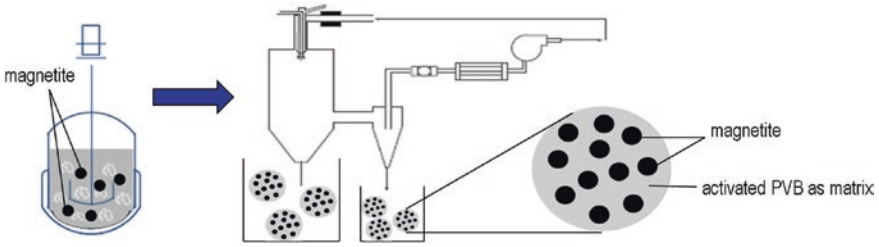

Fig. 6.18 Spray drying of reactive particles after PVB activation

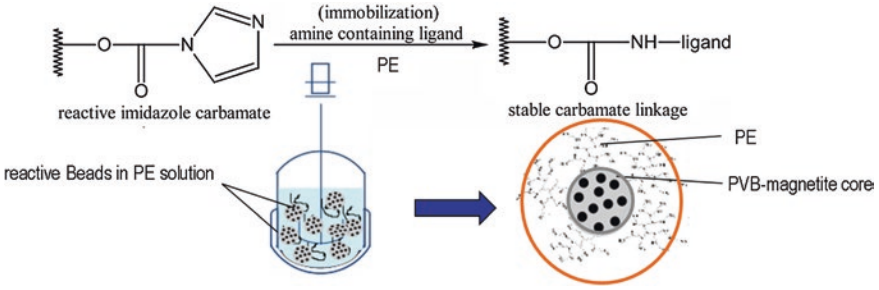

Fig. 6.19 Cross-linking of reactive beads with PE in water solution

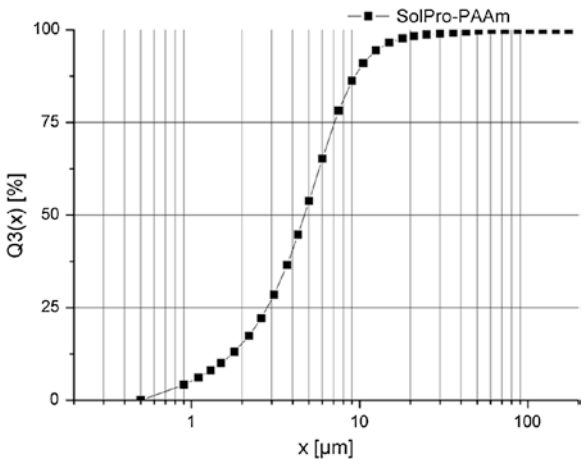

Fig. 6.20 Volume particle size distribution of SolPro-PAAm measured using laser diffraction

After the cross-linking step, unreacted carbamate groups were deactivated using 1 M ethanolamine solution.

PE beads were produced with the following composition (mass fraction):

25 % magnetite coated with 5 % ricinoleic acid; 7 % CDI; 63 % activated PVB. The PVB mass fraction during the activation was 3 %. The PE concentration in water was 0.4 g/l and the mass ratio of PE to reactive particles during the cross-linking was 0.4.

Subsequent to the synthesis process, AEX-SolPro beads were characterized.

The particle size distribution diagram in Fig. 6.20 shows a relatively broad distribution. All particles are smaller than 25 micron; the median size is approx. 5 µm. This size range allows good separation efficiency of the particles in a centrifugal field.

The protein extraction capacity was analyzed using two target proteins; Bowman-Birk inhibitor (BBI) and Bovine Serum Albumin (BSA). The BCA-Assay was used in this case too. BBI from two different sources was used: BBI from Sigma Aldrich and BBI from pretreated soy whey produced by Solae Denmark. The isoelectric points of BSA and BBI are at pH 4.0 and pH 4.7,

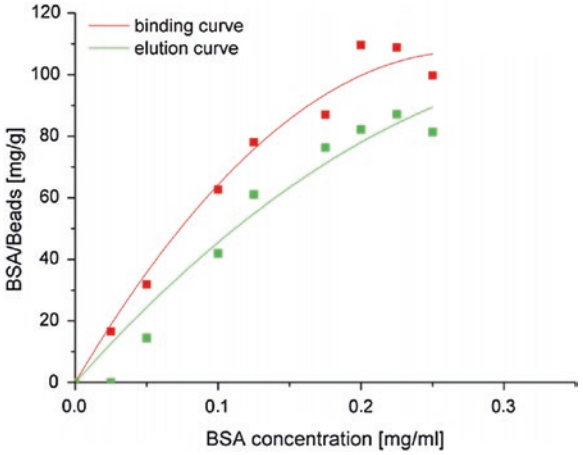

Fig. 6.21 Resulting BSA binding capacities of SolPro-PAAm beads. Results gained using BCA-Assay

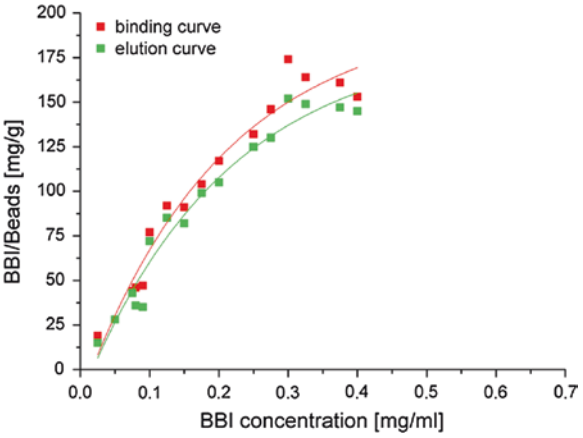

Fig. 6.22 Resulting BBI (from Sigma) binding capacities of SolPro-PAAm beads. Results gained using BCA-Assay

respectively (Aldrich; Aldrich). (Aldrich) Sodium acetate buffer (pH 6) was used as buffer solution during the adsorption analyses. The elution was carried out with 3 M NaCl in acetate buffer. Figures 6.21 and 6.22 show the adsorption isotherms of both proteins onto SolPro-PAAm. Using 1 g of the anionic beads, approx. 85 mg BSA and 145 mg BBI (from Sigma) were extracted. The elution efficiency was more than 77 %. These results show that more BBI molecules were extracted than BSA molecules. An explanation for this could lie in the molecular sizes of both proteins. The molecular weight of BBI is 66 kDa and thus almost eight times larger than that of BBI molecules (7.9 kDa).

The extraction of BBI from pretreated soy whey using SolPro-PAAm beads was investigated by Merck KGaA using SDS-PAGE (Fig. 6.23). The binding capacity was found to be very low (approx. 10 mg/g). This could be explained by the small specific surface area of the beads (bead sizes in micron scale) as well as

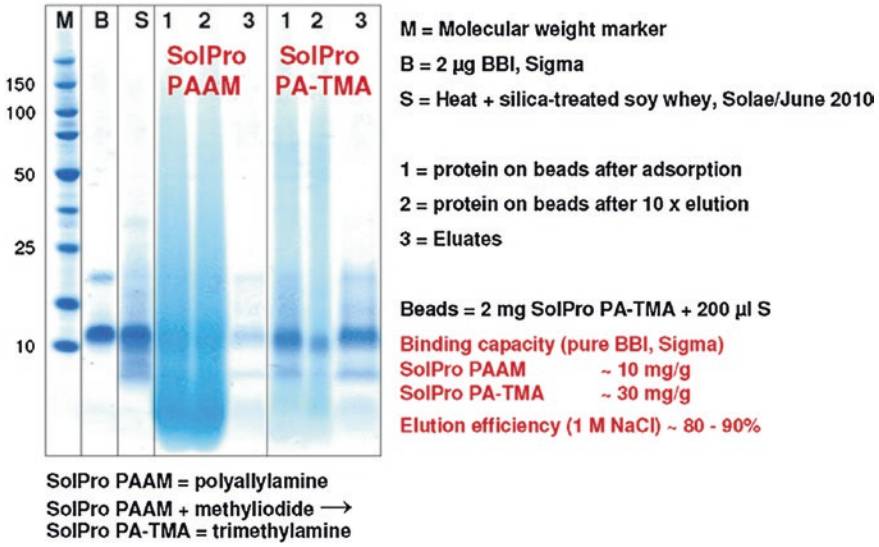

Fig. 6.23 Binding capacity of BBI from pretreated soy whey measured by Merck KGaA

by the presence of nonpermanent charges on the beads. To overcome this, constant positive charges were created on the particles using a methylation reaction. Through the methylation, amino groups are methylated and receive constant positive charges. Due to their competence as a chemical company, Merck KGaA carried out the quaternization. After this modification, the binding capacity increased by a factor of 3 (Fig. 6.23).

The extraction of BBI from pretreated soy whey was 15 times smaller than the BBI from Sigma. This discrepancy is probably due to different degrees of purity (see bands B and S in Fig. 6.23) as well as to the application of different buffering systems and analytical methods.

6.4 Summary

The goal of TUBAF in MagPro^{2}Life was to develop—based on SolPro—a low-cost scalable synthesis process and to optimize the efficiency of particle production regarding safety and ecological aspects. Depending on target protein charges in the extraction pH range, CEX-and AEX-SolPro beads were successfully synthesized and characterized. Both types of beads were provided with the appropriate functionalities allowing their application in bioseparation (superparamagnetic, ion exchange properties). The synthesis processes used for the beads and their components in the lab scale can also be scaled up. The protein binding capacities

of both bead systems have also confirmed their suitability for bioseparation applications. CEX-SolPro particles possess a lysozyme extraction capacity of approx. 280 mg/g, which is about three times higher than similar CEX-SolPro beads (with same composition) produced by Hickstein (77.6 mg/g) (Hickstein 2009). The newly designed and produced PAAm-SolPro beads exhibit extraction capacities of 85 mg/g as well as 145 mg/g for BSA and BBI, respectively. The extraction capacity for BBI decreases extremely in pretreated soy whey. However, a quaternization of poly(allyl)amine (PAAm) fixed on the beads' surface has improved that value by a factor of 3.

In future works, the basic chemistry used for the synthesis and modification (quaternization) of PAAm-SolPro beads could be improved to considerably increase their BBI extraction capacity in a real extraction milieu (nontreated or pretreated soy whey). The suitability of such adsorbents for water conditioning and rare earth element processing can also be investigated.

References

Aldrich S, Product information Trypsin chymotrypsin inhibitor. http://www.sigmaaldrich.com/etc/medialib/docs/Sigma/Product_Information_Sheet/1/t9777pis.Par.0001.File.tmp/t9777pis.pdf

Aldrich S, Product information: Albumin from bovine serum

Aldrich S, Product Information: Lysozyme from chicken egg white. http://www.sigmaaldrich.com/etc/medialib/docs/Sigma/Datasheet/7/l6876dat.Par.0001.File.tmp/l6876dat.pdf

Banert T (2008) Synthese Funktionaler Nanokomposit-Partikeln Für Die Bioseparation Durch Sprühtrocknung—Auswahl Und Eignung Von Stoffsystemen. Technische Universität Clausthal, Clausthal-Zellerfeld

Erler J et al. (2013) Liquid–liquid phase transfer of magnetite nanoparticles—evaluation of surfactants. Powder Technol 247:265–269

EU-Comission (2009) Amending Regulation (EC) No 1907/2006 of the European Parliament and of the Council on the Registration, Evaluation, Authorisation and Restriction of Chemicals (REACH) as regards Annex XVII (dichloromethane, lamp oils and grill lighter fluids and organostannic compounds). http://eur-lex.europa.eu/LexUriServ/LexUriServ.do?uri=OJ:L:2010:086:0007:0012:en:PDF

Giunchedi P, Conte U (1995) Spray-drying as a preparation method of microparticulate drug-delivery systems—an overview. Stp Pharma Sci 5(4):276–290

Hickstein B (2009) Magnetic beads for the bioseparation processes, Synthesis and application properties. Doctoral Doctoral TU-Clausthal

Hickstein B, Peuker UA (2009) Modular process for the flexible synthesis of magnetic beads-process and product validation. J Appl Polym Sci 112(4):2366–2373

Maa YF, Nguyen PA, Sit K, Hsu CC (1998) Spray-drying performance of a bench-top spray dryer for protein aerosol powder preparation. Biotechnol Bioeng 60(3):301–309

Machunsky S, Grimm P, Schmid H-J, Peuker UA (2009) Liquid-liquid phase transfer of magnetite nanoparticles. Colloids Surf A Physicochem Eng Aspects 348:186–190

Machunsky S, Peuker UA (2007) Liquid-liquid interfacial transport of nanoparticles. Phys Sep Sci Eng 2007:7

Masters K (1979) Spray drying handbook. Wiley, New York

Pohl B, Jamshidi R, Brenner G, Peuker UA (2012a) Charakterisierung der Mischung und Fällung bei sonochemischen Reaktoren unter besonderer Berücksichtigung der Reaktorform. Chem Ing Tech 84(1–2):70–80

Pohl B, Jamshidi R, Brenner G, Peuker UA (2012b) Experimental study of continuous ultrasonic reactors for mixing and precipitation of nanoparticles. Chem Eng Sci 69(1):365–372

Re MI (2006) Formulating drug delivery systems by spray drying. Drying Technol 24(4):433–446

Rudolph M (2012) Nanoparticle-polymer-composites the solution and spray drying process with an emphasis on colloidal interactions. Technische Universität Bergakademie Freiberg, Freiberg

Rudolph M, Peuker UA (2011) Coagulation and stabilization of sterically functionalized magnetite nanoparticles in an organic solvent with different technical polymers. J Colloid Interface Sci 357(2):292–299

Sano Y (1992) Drying of polymer-solution. Drying Technol 10(3):591–622

Chapter 7
Industrial Production, Surface Modification, and Application of Magnetic Particles

Karl Holschuh and Johann Bauer

Abstract Magnetite nanoparticles are produced in a continuous synthesis that allows the potentially unlimited production for large-scale applications. With the better control over the reaction parameters, the reproducibility is significantly improved. The particle size is tunable in a range of about 10–100 nm, and the distribution is significantly smaller than for those produced batch wise. The subsequent continuous surface modification of the pristine magnetite particles is difficult to date, especially if more than one chemical reaction is necessary. A batch preparation of kilogram of surface-modified ion-exchange magnetic particles for laboratory scale and pilot line purification experiments were realized. These ion-exchange particles could be recycled 50 times on an analytical scale without loss of efficiency. Several hundred grams of beads could be recovered 10 times with a stepwise efficiency of 99.9 %. A number of one-step protocols could be developed for the enrichment and purification of target proteins from different raw materials up to pilot-scale.

7.1 Introduction

Surface-modified magnetic particles have been used for many years in the Life Science area, especially in diagnostics for the isolation and purification of proteins and nucleic acids on an analytical scale. In manual or automated high-throughput applications, milligram or even sub-milligram quantities of beads are consumed in at most one cycle of binding, washing, and elution.

The idea of using magnetic particles in downstream processing of proteins or other target molecules has existed for many years. The needs to combine different technologies and the associated high costs for large-scale equipment, materials,

K. Holschuh · J. Bauer (✉)
Merck KGaA, Frankfurter Str. 250, 64293 Darmstadt, Germany
e-mail: johann.bauer@merckgroup.com

H. Nirschl and K. Keller (eds.), *Upscaling of Bio-Nano-Processes*,
Lecture Notes in Bioengineering, DOI 10.1007/978-3-662-43899-2_7

and samples have so far prevented appropriate marketable technologies. In addition, surface-modified magnetic particles have to compete against established conventional chromatography resins with respect to performance, price, and established purification procedures.

The obvious advantages of magnetic bead technology at least on an analytical or semi-preparative scale are the almost immediate binding and elution kinetics of target molecules, the possible use in unclarified raw materials and the fast separation of the particles in a magnetic field. This suggests applications in an early phase of downstream processes to capture and purify target molecules from untreated cell lysates, cell culture, supernatants, etc.

Compared to analytical one-time applications, the requirements for magnetic beads and the associated separation equipment for large-scale processing are significantly more challenging. Ideally, the synthesis of surface-modified magnetic particles is a continuous process with the least possible production steps and potentially unlimited quantities.

To be competitive with conventional chromatography resins, the particles need to have a high binding capacity in combination with sufficient chemical and mechanical stability to withstand manifold recycling. The specific surface area of nonporous resins is limited by the particle size itself, however, restrictions concerning harmful effects of nanomaterials require a particle size above 100 nm. For general purpose capturing of target molecules from large volumes, strong anion and cation exchange functionalities like those of trimethyl-ammonium and sulfonate are preferred. In addition, high surface charge with associated increased binding capacity can be achieved by tentacle-like structures. However, the polymer length is limited by the cumulative repulsive forces, which prevent an effective magnetic separation. The ideal method for fast protein purification is certainly affinity capture with specific antibodies, peptides, or other alternative binders. However, compared to chemical surface modifications these ligands are still rather expensive. Therefore, significant savings in time and equipment have to be weighed up against the costs of the separation medium, and the potential market value of the purified target molecule must also be considered. Depending on the application field in animal feed, food or pharma, the requirements on the quality of materials, equipment, procedures, and documentation must also to be accounted for.

7.2 Batch Synthesis of Magnetite

The classical synthesis of magnetite is typically carried out in batches by mixing aqueous solutions of iron salts under alkaline conditions as described (Massart 1981; Sugimoto and Matijewic 1980). Depending on the reaction conditions, this leads to a broad particle size distribution in the range of 10–150 nm (Fig. 7.1).

To protect the beads against oxidation and prepare them for further subsequent chemical modifications, they are usually coated with silica, silanes, organic acids, etc. (Schüth at al. 2007). For many analytical applications like manual and

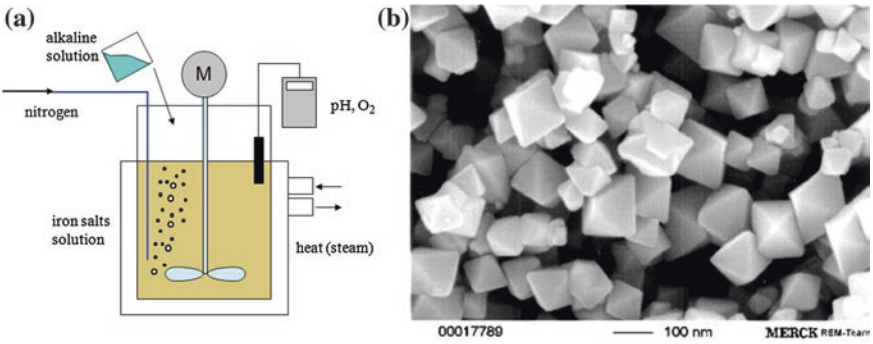

Fig. 7.1 Scheme of batch precipitation synthesis of magnetite (**a**) and resulting SEM image (**b**)

automated isolation and purification of nucleic acids, these kinds of particles fulfill most or even all requirements. More sophisticated procedures (e.g., lateral flow devices, biochips, therapeutic, or security applications) require preferably monodisperse particles with homogeneous magnetic and surface characteristics to ensure identical behavior for binding and elution of target molecules and during magnetic separation (van Amerongen et.al. 2009).

7.3 Continuous Production of Magnetite

The continuous precipitation method (Patent 2008) is based on the same principle as the above-mentioned batch production and has a number of significant advantages. It is a combination of the Messart precipitation and an oxidation method according to the ideas of Sugimoto and Matijewic. Two solutions are prepared in separate vessels and pumped through a mixing device. The precipitation takes place immediately in a volume of a few microliters at constant temperature, pH, and in absence of dissolved oxygen (Fig. 7.2).

Due to the controlled reaction conditions, the resulting crystals show a much narrower size distribution compared to the batch coprecipitation. The primary particles, an iron(oxo)hydroxide of mixed oxidation states also described as "green rust" (Bruun Hansen et al. 1994), is further dehydroxylated in a tempered loop to form pure magnetite. The mean particle size correlates with the composition of the educt solutions, especially the ratio of the oxidation states of iron. This is assumed to the speed of nucleation in dependency of the concentration of iron 2^+ or 3^+ species. As a result, the particle size can be fine-tuned between about 10 and 100 nm corresponding to a specific surface area of 200–20 m^2/g (Fig. 7.3). Depending on the application needs, it must be taken into account that beads below about 20 nm are superparamagnetic and thus can no longer be efficiently handled in a magnetic field. They are usually embedded in larger polymer matrices to enable magnetic separation.

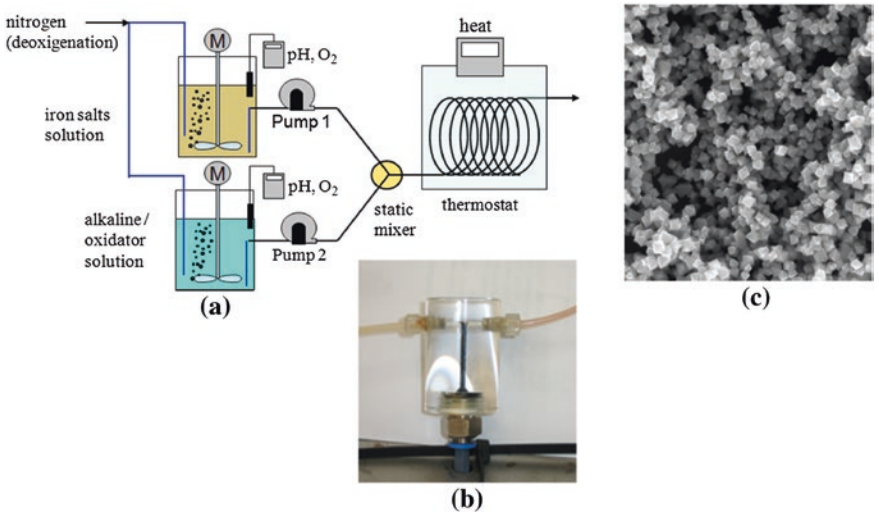

Fig. 7.2 Scheme of the continuous magnetite production setup (**a**) with a transparent mixing device to show the dark product to be formed from two translucent solutions (**b**) and SEM image of the resulting magnetite crystals (**c**)

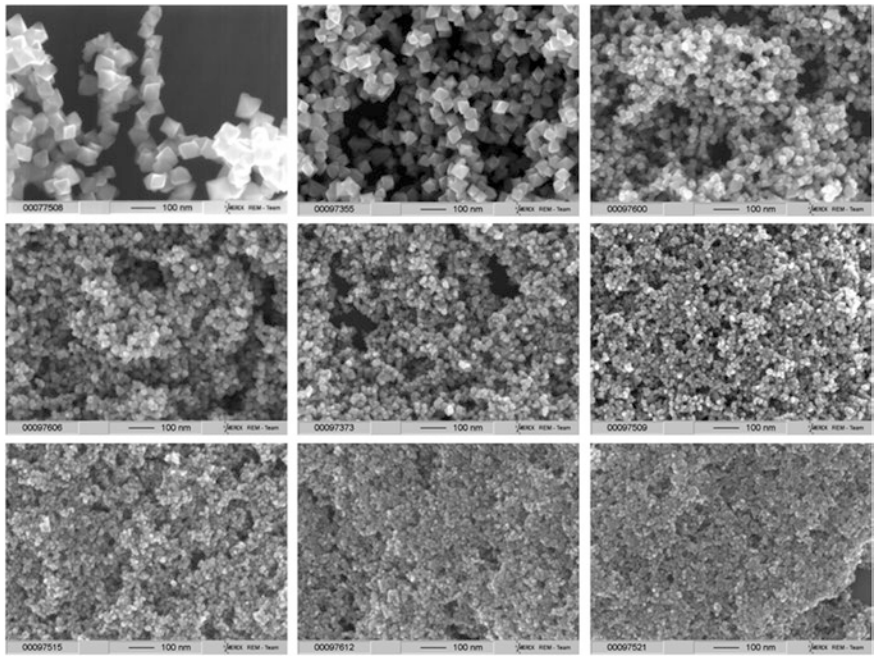

Fig. 7.3 Effect of educt composition, especially the concentration of iron 2^+ or 3^+ species on particle size and distribution. The particle size decreases with an increasing ratio of iron 3^+ to iron 2^+

7.4 Surface Functionalization

The basic particles need to be surface-modified with ion exchange and affinity functionalities to be able to capture the various target molecules. Anion and cation exchange resins usually only allow an unspecific adsorption of proteins from large volumes followed by high salt or stepwise elution. Such materials are normally used for capturing and concentrating target molecules in an early phase of downstream processing. However, as demonstrated in some applications within the project, the beads might even allow an almost affinity-like purification (e.g., monoclonal antibodies from cell culture supernatant, Fab fragments from bacterial cell lysate). The ultimate downstream processing is based on affinity particles using specific antibodies, peptides, or other ligands. These materials can be applied in a first step, e.g., for the capture of monoclonal antibodies from cell culture supernatant with protein A resins or as a final polishing procedure. Within MagPro^{2}Life the use of antibody-based anti-BBI magnetic particles allowed a one-step purification of BBI directly from untreated soy whey with unsurpassed purity and high specific activity.

The surface modification with anion exchange functionalities is a multistep process based on the grafting from ATRP (Atom Transfer Radical Polymerization) technology. The continuously produced basic 100 nm magnetite crystals are first coated with TEOS (tetraethoxy-silane) to obtain a protective and reactive silica layer. Subsequently the ATRP initiator is covalently immobilized, followed by the polymerization with functionalized monomers. In addition to or instead of this, affinity ligands, especially antibodies, may be linked to the particle surface (Fig. 7.4).

7.4.1 Surface Modification by Atom Transfer Radical Polymerization

The strategy to produce nonporous, nano-sized anion and cation exchange magnetic particles is the generation of functional polymeric tentacles on the surface. This is possible in a “grafting from” or a “grafting to” approach (Rühe 2004). For the “grafting to” strategy, a ready-made functional polymer is linked with a reactive anchor group for immobilization on the particle surface. Due to the collapsed (mushroom-like) structure of most polymers, the grafting density is rather low and possible interactions of target molecules with the underlying accessible surface lead to unspecific binding. For the “grafting from” route, a high density of small molecules is anchored on the particle surface which acts as a polymerization initiator. Starting from those groups, the functional polymer chains are grown to a brush-like structure shielding the resins from unspecific binding (Fig. 7.5).

In a first step, the magnetite crystals are coated with silica (Brinker and Scherer 1990). The deposition of a thin layer of pure silica is achieved by hydrolysis of

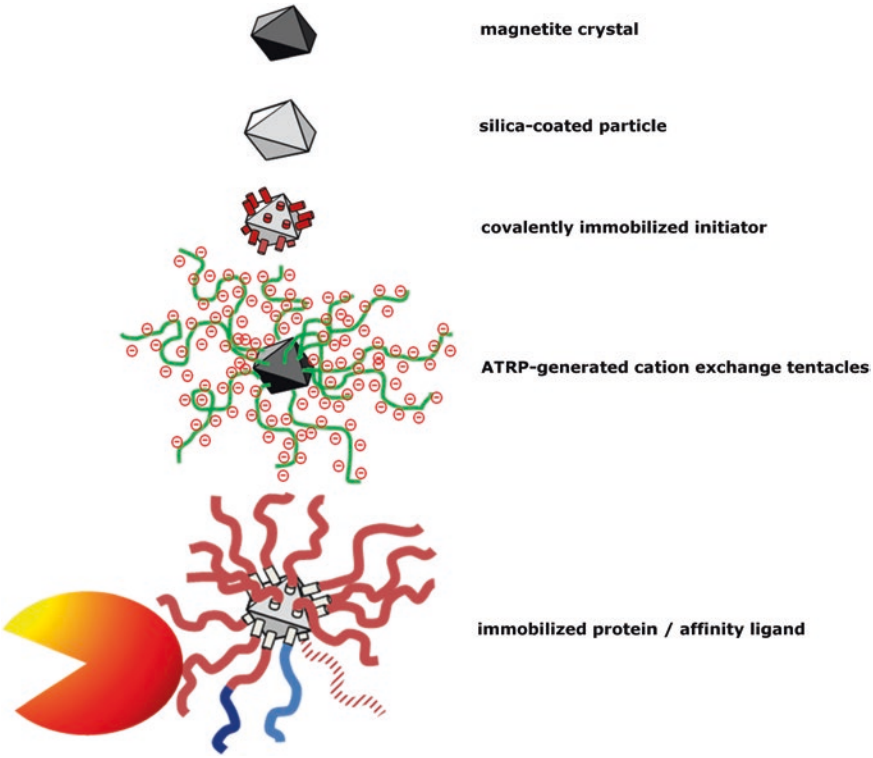

Fig. 7.4 Scheme for the stepwise surface modification of magnetite particles

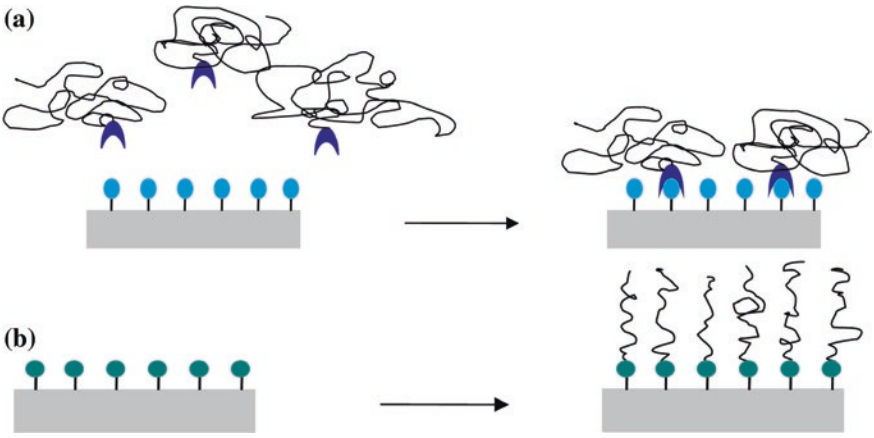

Fig. 7.5 Surface modification by grafting to (**a**) and grafting from (**b**)

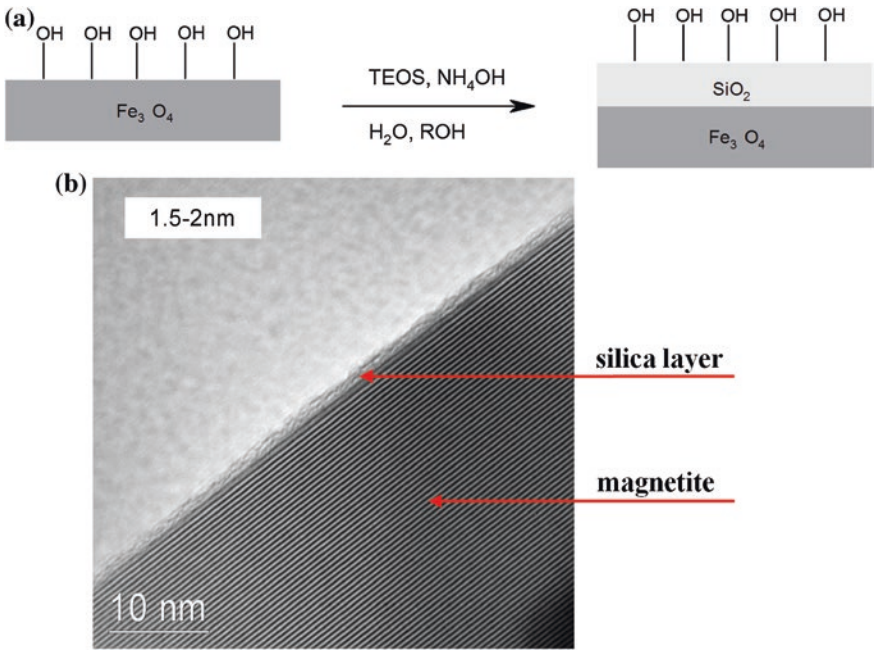

Fig. 7.6 Surface modification with TEOS (**a**) and analysis of the resulting particles by transmission electron microscopy (**b**)

tetraethoxy-silane (TEOS) in a diluted, alkaline suspension of magnetite particles. The primary material formed by a sol-gel reaction deposits on the surface resulting in an amorphous silica coating (Fig. 7.6).

Further reactions of the nonbridged Si-OH groups with, e.g., (organo)-functionalized (mono- to tri)-alkoxysilanes are possible to create specific surface modifications. The silanization of silica surfaces with functional alkoxy-/chloro-silanes R_nSiX_{4-n} (X = Cl, OR') offers an excellent method to covalently link new functionalities to the surface. The reaction proceeds along hydrolysis and condensation of these organosilanes, in the case of tri-reactive-silanes, creating a highly branched network.

The capacity of accessible functionalities on magnetic particles is broadly enlarged by the "grafting from" polymerization. The first step of this strategy is the immobilization of an ATRP initiator to the silica surface (Huang and Wirth 1997). This is generated directly with, e.g., ((chloromethyl)-phenylethyl)-trimethoxy-silane in THF at elevated temperature (Fig. 7.7). The grafting density is varied by mixing the initiator siloxane precursors with n-propyl-trimethoxy-silane.

The subsequent atom transfer radical polymerization (ATRP) is a "living" (controlled) radical polymerization technique (Matyjaszewski 1999; Matyjaszewski and Xia 2001). During the reaction, the molecular weight of the resulting polymer

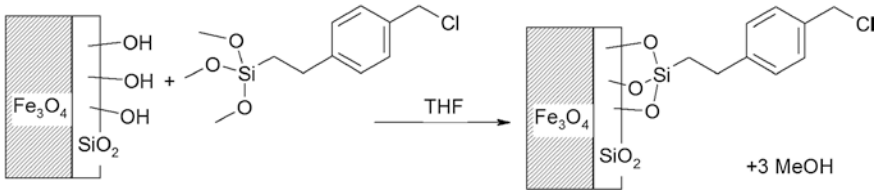

Fig. 7.7 Schematic initiator modification with ((chloromethyl)-phenylethyl)-trimethoxy-silane

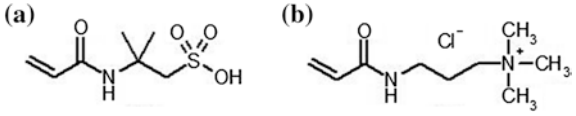

Fig. 7.8 Chemical structures of acrylamido-2-methylpropanesulfonic acid (**a**) and trimethylammoniumpropyl-acrylamide chloride (**b**) used as monomers for the generation of cation- and anion exchange tentacles by ATRP

grows linearly with the conversion. The "living" character arises in part from the ability to reinitiate a second polymerisation reaction (also with another monomer) after the isolation of the first product, without additional initiator modification. Unlike conventional radical polymerisation, the concentration of free radicals within the reaction medium is so low that termination reactions (radical combination or disproportionation) rarely occur. Thereby, control over length is improved and the polydispersity of the polymer reduced.

For the generation of a strong cation exchange surface, the sodium salt of acrylamido-2-methylpropanesulfonic acid (AMPS) as a monomer can be used. The modification of magnetic particles with a strong anionic exchanger may, for example, be achieved with the monomer trimethylammoniumpropyl-acrylamide chloride (TMAPAA) (Fig. 7.8).

The resulting tentacle length has to be well controlled. Short tentacles have a low capacity and eventually allow an unspecific adsorption of proteins (or other target molecules) to the underlying, still accessible silica surface. Very long tentacles exhibit a high binding capacity, but the extreme negative surface charge strongly prevents an effective magnetic separation. An empirical length optimum for both polymers is about 30–50 monomer units (Fig. 7.9).

7.4.2 Immobilization of Antibodies

A monoclonal anti-BBI antibody provided by the project partner fzmb has been covalently immobilized on carboxylated magnetic particles via standard aqueous carbodiimide-chemistry. The beads enabled a highly specific adsorption of BBI without any detectable background (Fig. 7.10b).

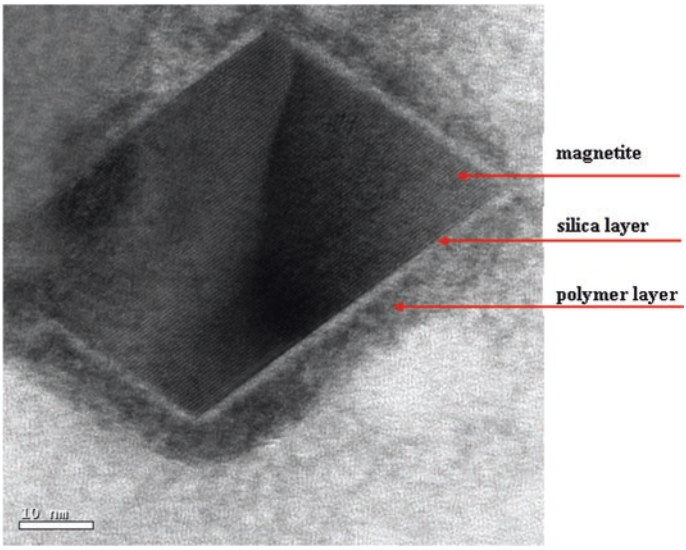

Fig. 7.9 TEM-image of TMAP-modified magnetic particles (The outer, polymeric layer is stained with WO3, the intermediate silica is layer is not stained because of its higher density and the core consists of magnetite)

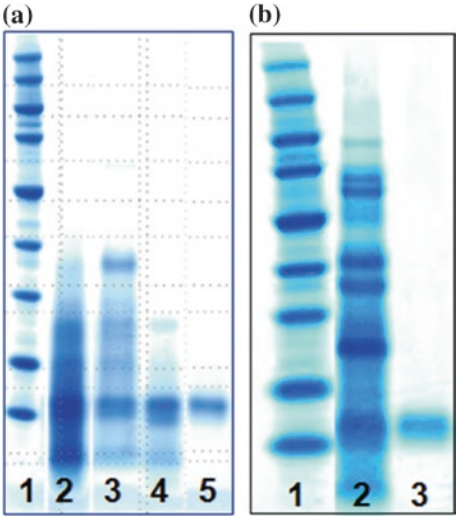

Fig. 7.10 **a** Lab-scale purification of BBI from untreated soy whey. *1* molecular weight marker; *2* untreated soy whey; *3* heat-treated soy whey; *4* heat + silica treated soy whey; *5* BBI purified with TMAP-modified magnetic particles. **b** Purification of BBI from untreated soy whey with anti-BBI immobilized on MagPrep beads. *1* molecular weight marker; *2* untreated soy whey; *3* eluted purified BBI

7.5 Applications

A number of applications have been developed with magnetic particles with TMAP, sulphonate, and anti-BBI modification for the capture and purification of proteins from different raw materials on a laboratory scale. The major target within MagPro^{2}Life was BBI from untreated soy whey. The purification strategy involved an initial heating step at 70–80 °C (at which BBI is unaffected) to remove unwanted heat-sensitive components. Subsequently, a silica-treatment eliminates most remaining proteins, leaving BBI in the supernatant. Finally, BBI is captured with TMAP-modified anion exchange magnetic particles and eluted with 1 M sodium chloride (Fig. 7.10a). Alternatively, BBI can be purified in one step using anti-BBI affinity particles. Here, the target molecule is captured directly from untreated soy whey with an immobilized monoclonal antibody against BBI and eluted at pH 3 in a small volume (Fig. 7.10b). This results in a 20-fold purification with a specific activity of 1,500–2,000 CI units/g, which is well above the projected target level of 1,000. The maximum theoretical purity is 3,194 CI units/g.

TMAP-grafted magnetic particles have also been successfully used to purify monoclonal antibodies from cell culture supernatant (Fig. 7.11a) and IgG from human plasma (Fig. 7.11b) in one step by removing unwanted proteins. The

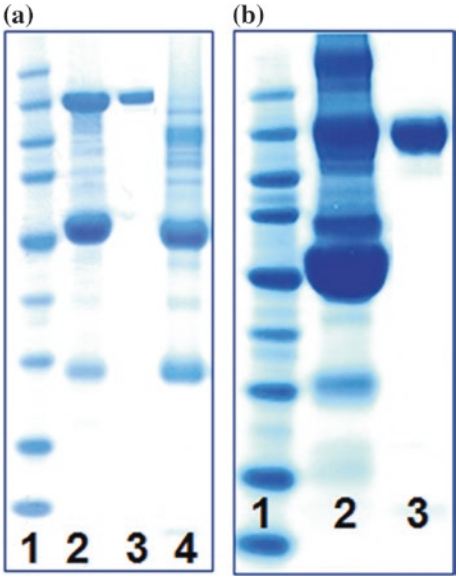

Fig. 7.11 **a** Lab-scale purification of monoclonal antibodies from cell culture supernatant. *1* molecular weight marker; *2* cell culture supernatant 1:3 diluted with water; *3* remaining antibodies in the supernatant; *4* proteins adsorbed to TMAP-modified magnetic beads; **b** Purification of IgG from human plasma. *1* molecular weight marker; *2* human plasma proteins; *3* remaining IgG in the supernatant

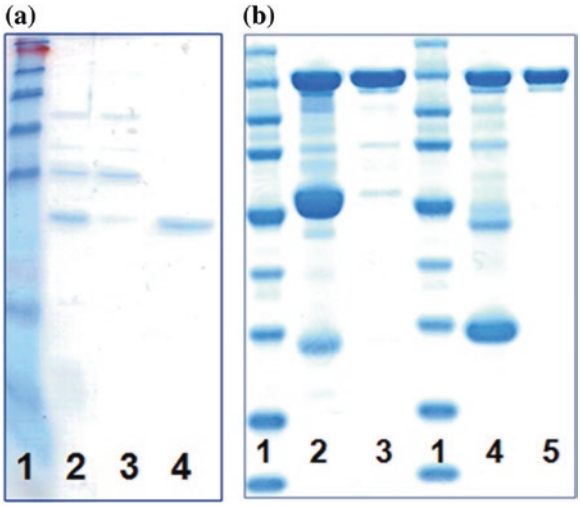

Fig. 7.12 **a** Lab-scale purification of Fab fragments from *E. coli* cell lysate. *1* molecular weight marker; *2* cell lysate; *3* remaining proteins in supernatant; *4* Fab eluate. **b** Purification of monoclonal antibodies from cell culture supernatant. *1* molecular weight marker; *2* + *4* different cell culture supernatants; *3* + *5* monoclonal antibody eluates

remaining antibodies can subsequently be concentrated and desalted by cross-flow filtration or directly used for downstream applications.

The main application of sulphonated magnetic particles within MagPro^{2}Life is the purification of Fab fragments from *Escherichia. coli* cell lysate (Fig. 7.12a). Fab is enriched in the periplasma during fermentation and released by destruction of the outer cell membrane. Sulphonated magnetic beads allow the selective capture and release of the target protein with high purity on a laboratory scale. Similar to TMAP-modified magnetic particles, the cation exchange beads can be used for the enrichment and purification of monoclonal antibodies from cell culture supernatant by adsorption at pH 5.8, leaving unwanted protein components in the supernatant and release of the target IgG at 0.5 M sodium chloride (Fig. 7.12b).

7.6 Summary

Magnetic particles could be an established alternative to conventional chromatography resins in automated, high-throughput protocols replacing centrifugation and filtration by simple magnetic separation steps. The basic magnetite crystals are typically synthesized in batches in limited amounts by aqueous coprecipitation. In contrast, continuous synthesis allows the potentially unlimited production of particles for large-scale applications. Moreover, the reliability and reproducibility is significantly improved as the reaction parameters can be controlled much

more. In addition, the particle size and distribution is tunable in a range of about 10–100 nm. The subsequent desirable continuous surface modification of the basic magnetite crystals is difficult to date, especially if more than one chemical reaction is necessary. We succeeded in a batch preparation of kilogram of surface-modified ion-exchange magnetic particles for laboratory scale and pilot line purification experiments. The resins could be recycled 50 times on an analytical scale without loss of efficiency. Several hundred grams of beads could be recovered 10 times with a stepwise efficiency of 99.9 %.

A number of one-step protocols could be developed for the enrichment and purification of target proteins from different raw materials up to pilot-scale, the most effective being the capture and elution of BBI with anti-BBI coated MagPrep beads directly from untreated soy whey. Overall, the project has demonstrated the feasibility of pilot-scale downstream processing with magnetic particles as a potential alternative or complement to conventional chromatography.

References

Brinker CJ, Scherer GW (1990) Sol-gel science: the physics and chemistry of sol-gel processing. Academic Press, Chapter 3

Bruun Hansen H Ch et al (1994) Evaluation of the free energy of formation of Fe(II)–Fe(III) hydroxide-sulphate (green rust) and its reduction of nitrite. Geochimica et cosmochimica Acta 58:2599

Huang XY, Wirth MJ (1997) Surface-initiated radical polymerization on porous silica. Anal Chem 69:4577

Massart R (1981) Preparation of aqueous magnetic liquids in alkaline and acidic media. IEEE Trans Magn 17:1247

Matyjaszewski K (1999) Polymers at interfaces: using atom transfer radical polymerization in the controlled growth of homopolymers and block copolymers from silicon surfaces in the absence of untethered sacrificial initiator. Macromolecules 32:8716

Matyjaszewski K, Xia J (2001) Atom transfer radical polymerization. Chem Rev 101:2921

Patent DE (2008) 102008015365

Rühe J (2004) Polymer brushes: on the way to tailor-made surfaces. In: Advincula RC (ed) Polymer brushes, Wiley-VCH, Weinheim, pp 1. doi:10.1002/3527603824.ch0

Schüth F et al (2007) Angew Chem 119:1242. doi:10.1002/ange.200602866

Sugimoto T, Matijewic K (1980) Formation of uniform spherical magnetite particles by crystallization from ferrous hydroxide gels. J Colloid Interf Sci 74:227

van Amerongen A et al (2009) Anal Bioanal Chem 393:569. doi:10.1007/s00216-008-2287-2

Part II
Magnetic Separation Devices

Chapter 8
Magnetically Enhanced Centrifugation for Industrial Use

Johannes Lindner, Karsten Keller, Gunnar Grim, Johannes Feller, Christian Fiil Nielsen, Niels Dalgaard, Katharina Menzel and Hermann Nirschl

Abstract Magnetically enhanced centrifugation is a new approach in high-gradient magnetic separation possible in continuous mode, which promises a large potential for industrial use. Magnetic particles are separated to a wire filter, from which they are cleaned by centrifugal forces to the chamber wall. The simulation of magnetic particles collected by a wire were possible by the discrete element method. The simulation shows the detachment of particles from the wires by the centrifugal force. Two prototype machines were set up to investigate the process. The discharge of particles from the wire filter depends on the magnetic field strength and the centrifugal velocity. It was possible to set up a machine reaching a separation efficiency of 99 % at a volume flow of 1 m^3/h (excluding dead times) in a batch-wise mode. A second machine built as magnetically enhanced decanter separates particles and transports them out of the bowl by a screw conveyor in a completely continuous mode. Instead of the common electromagnets a permanent magnet assembly can be combined with a magnetically enhanced centrifuge to save costs.

J. Lindner (✉) · G. Grim · J. Feller · C.F. Nielsen · N. Dalgaard · K. Menzel
Mechanical Process Engineering and Mechanics, Karlsruhe Institute of Technology, Karlsruhe, Germany
e-mail: Johannes.lindner@kit.edu

K. Keller
DuPont, Wilmington, DE 19980, USA
e-mail: Karsten.Keller@dupont.com

H. Nirschl
Institute of Mechanical Process Engineering and Mechanics, Karlsruhe Institute of Technology, 76131 Karlsruhe, Germany
e-mail: hermann.nirschl@kit.edu

H. Nirschl and K. Keller (eds.), *Upscaling of Bio-Nano-Processes*,
Lecture Notes in Bioengineering, DOI 10.1007/978-3-662-43899-2_8

8.1 Introduction

High-gradient magnetic separation (HGMS) is a method for the separation of magnetic matter from liquid. It is based on a magnetic wire filter inserted in a chamber. The wires are magnetized by an external magnet (Svoboda 2004). A suspension passes through the chamber and the particles deposit on the wires by magnetic forces. The discharge is enabled by removing the magnet to release the particles from the wires. Then the chamber is flushed back to discharge the magnetic particles. Calculations for the filter capacity of a primitive cell are shown in (Ebner et al. 2007). A quasi-continuous HGMS variant is a carousel which enables a quick swapping of chambers for quasi-continuous use (Franzreb 2001). A different approach for magnetic separation is magnetic cake filtration (Eichholz et al. 2011; Eichholz et al. 2008).

A process based on magnetic functionalized particles would be an interesting alternative to adsorption chromatography or expanded bed adsorption. The kinetics of adsorption and elution are in this case fast, while the fluid flow in a batch-wise process is the limiting factor for the kinetics in the process. A particle-based process might allow lower cycle times and a continuous process, resulting in a more efficient use of the expensive functionalization. A Magnetically enhanced centrifuge (MEC) separates magnetic particles continuously. A star-shaped magnetic wire filter is integrated in the centrifuge. It is placed inside a magnet, which magnetizes the wire filter. Particles are separated to the wire filter and are discharged continuously to the wall in large agglomerates by centrifugal forces. The parameters that influence the MEC process are already published (Lindner et al. 2010; Lindner et al. 2013a). A continuous discharge of the particles from the decanter wall is possible, one possibility is by a decanter screw (Lindner and Nirschl 2014). This is necessary in order to take advantage of the low-adsorption cycle times of micron-scaled particles. Different approaches for the simulation of magnetic separation have already been executed (Hournkumnuard and Chantrapornchai 2011; Gerber and Birss 1983). The simulation is important for the optimization of separation. Additionally, influences such as magnetically induced agglomeration have an important influence on separation (Lindner et al. 2013b).

This chapter deals with the possibilities of MEC for industrial use. A simulation is shown combining finite element modeling (FEM) of the magnetic field around a wire with a discrete element model for magnetic particles. The core of the chapter is a batch-wise industry centrifuge set up by Andritz KMPT. It handles volume flow of up to 1 m^3/h at high separation efficiency. A longitudinal permanent magnet arrangement is introduced, which was optimized for and tested with MEC. A test on a decanter centrifuge is shown to demonstrate its capabilities as a continuous device.

8.2 Theory

The equations shown below were used to simulate a particle collection on a wire. The force on a magnetic particle depends on the field gradient. Distortion of an external field allows high gradients. The magnetic force of the gradient of a field

H on a particle of magnetization M_P and volume V_P is, with the magnetic permeability μ_0 (Svoboda 2004):

$$\partial F_m = \mu_0 M_P \nabla H \partial V_P \tag{8.1}$$

Satoh used the magnetic dipole force for the simulation of magnetic particles (Satoh et al. 1998). The dipole–dipole force between two particles can be simplified for particles aligned in the direction of a homogenous magnetic field. A discussion on assumptions made in this approach can be found in (Lindner et al. 2013b). The following equation was used in a discrete element model simulation:

$$F_{m,ij} = -\frac{3\mu_0 m_{Pi} m_{Pj}}{4\pi} \frac{1}{r_{ij}^4} \begin{pmatrix} \left(5 * t_x^2 - 3\right) t_x \\ \left(5 * t_x^2 - 1\right) t_y \\ \left(5 * t_x^2 - 1\right) t_z \end{pmatrix} \tag{8.2}$$

The centrifugal force F_Z on a particle is given by the particle mass m, the rotational speed ω, and the radius r.

$$F_Z = -m * \omega \times (\omega \times r) \tag{8.3}$$

The mechanic force $F_{n,ij}$ used in the simulation was implemented based on a spring-damper model with the coefficients k_n and $\eta_{n,ij}$, the normal overlap δ in normal direction n_{ij} in the spring part, and the relative normal velocity $v_{rel,n,ij}$ in the damper model (Lindner et al. 2013b; Deen et al. 2007; Langston et al. 1995).

$$F_{n,ij} = k_n \delta^{3/2} n_{ij} - \eta_{n,ij} * v_{rel,n,ij} \tag{8.4}$$

$\boldsymbol{F}_{t,ij}$ is the tangential frictional force proportional to the tangential sliding velocity $\boldsymbol{v}_{rel,t,ij}$. It is necessary to reduce the sliding of particles since without this force, a particle tends to oscillate around the dipole end of another particle.

$$F_{t,ij} = -\eta_{t,ij} * v_{rel,n,ij} \tag{8.5}$$

The parameters are summarized in Table 8.1.

8.2.1 Considerations for Scaling

Separation efficiency of one wire for a certain volume flow of HGMS scales with fluid velocity $v_0^{-1/3}$ as long as $v_m / v_0 \gg 1$. The velocity of a particle in proximity to a

Table 8.1 Overview over simulation parameters

Parameter	Equation	Parameter	Equation
Normal stiffness	$k_{n,ij} = \frac{4}{3}\sqrt{r_{eq}} E_{eq}$	Normal damping	$\eta_{n,ij} = 0.3 * \sqrt{\frac{9}{2} m_{eq} \sqrt{\delta} k_{n,ij}}$
Tangential stiffness	$k_{t,ij} = \frac{2\sqrt{2R_{eq}} G_{eq}}{2-\upsilon} \sqrt{\delta}$	Tangential damping	$\eta_{t,ij} = 2\sqrt{\frac{2}{7} m_{eq} k_{t,ij}}$
Equalized mass	$m_{eq}^{-1} = m_i^{-1} + m_j^{-1}$	Equalized radius	$r_{eq}^{-1} = r_i^{-1} + r_j^{-1}$
Equalized rigidity modulus	$G_{eq}^{-1} = \frac{1-\upsilon_i^2}{G_i} + \frac{1-\upsilon_j^2}{G_j}$	Equalized elasticity modulus	$E_{eq}^{-1} = \frac{1-\upsilon_i^2}{E_i} + \frac{1-\upsilon_j^2}{E_j}$

wire v_m is deduced from the resistance force of fluid and the magnetic force (Watson 1973). Parameters are the particle diameter b, the wire diameter a, the fluid viscosity η, the wire magnetization M_D, and $\Delta\kappa$, the volume susceptibility difference between the fluid and the particle (Svoboda 2004; Gerber and Birss 1983).

$$v_m = \frac{2}{9}\mu_0 \Delta\kappa M_D H_0 \frac{b^2}{a\eta} \tag{8.6}$$

It is hence possible to scale the volume flow linear with the volume of the filter cell and magnet, enabling the setup of larger centrifuges than those presented in this work.

8.3 Simulation of Magnetically Enhanced Centrifugation

The discrete element method allows the simulation of particle deposition by calculating forces between particles. In case of HGMS, it is necessary to implement as well the magnetic forces between particles, which are essentially dipole forces.

8.3.1 Simulation Results

The commercial program EDEM 2.3 from DEM Solutions was used as software platform with a custom contact model implemented for the simulation of particle deposition in HGMS and MEC. Equation (8.2) was implemented as a custom contact force for magnetic interparticular forces. Equations (8.3) and (8.4) were implemented as mechanical models. To simulate the force resulting from the magnetic wire, a finite element simulation was done with the software Comsol 3.4. The field gradient around a cylinder was calculated and read in EDEM. Equation (8.1) was implemented to calculate the force of the wire on particles.

The magnetic field around a dipole is enhanced on two opposite sides parallel to the field direction. Perpendicular to the field direction, the background field is weakened. As magnetic matter is attracted by strong field regions and repulsed by weak regions, particles agglomerate in needle shape. An important assumption is that the mutual influence of each particle's magnetization may be neglected if both particles are in saturation magnetization. Distant magnetic forces were cut off after a specific distance to stabilize the simulation and to reduce computational effort. A time step of 10^{-5} s was applied in the simulation (Table 8.2).

The simulation was performed in order to better understand the behavior of particles in the magnetic field. A simulation was done with the magnetic field of a round wire read in the DEM model. For a certain time, particles collected on top of the wire. Figure 8.1 left shows the deposit of magnetic particles on a wire without centrifugal force. The centrifugal force was added as constant acceleration in Fig. 8.1 right. The particles leave the wire, with some notable deposits left at the end of the wire. A high gradient at the wire end showed to retain particles. The simulation showed needle-shaped agglomeration before the particles settle on the wire and after detaching.

Table 8.2 Parameters in the simulation

Symbol	Value	Unit	Denotation
M_P	480 000	[A/m]	Particle magnetization (except given otherwise)
ν	0.3	[-]	Poisson ratio
E	$2*10^5$	[Pa]	Elasticity modulus
ρ_P	2 000	[kg/m^3]	Density Particle
R	$0.5*10^{-6}$	[m]	Physical particle radius (mechanic force)
r_c	$4*10^{-6}$	[m]	Contact radius (magnetic force)
v	0.001	[m/s]	Initial velocity
a	$5*10^{-4}$	[m]	Wire radius
b	$1*10^{-5}$	[m]	Particle radius (except given otherwise)
M_W	$1.6*10^6$	[A/m]	Wire magnetization

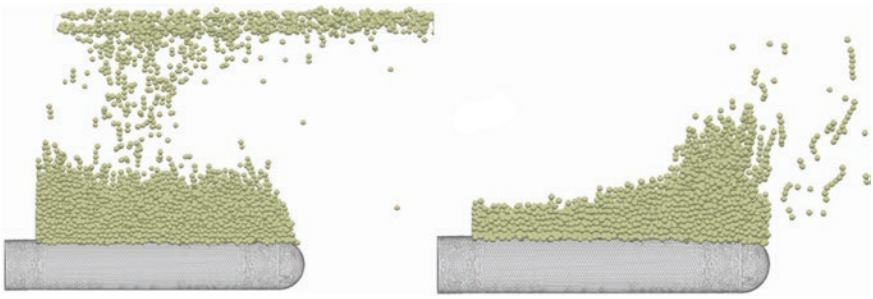

Fig. 8.1 Deposit of magnetic particles on a wire in a HGMS process without centrifugal force (*left*) and with centrifugal force (*right*)

8.3.2 Validation

Figure 8.2 shows a comparison of particle deposits seen in the HGMS experiment and particle deposition calculated in the simulation. In the validation experiment, footage of the particle deposit on a wire is shown. It was produced by inserting an endoscope into a HGMS cell. A cut wire was introduced within the cell to be able to observe particle separation from the side of the wire. Bayferrox magnetite was used as magnetic matter. An electromagnet was installed outside of the cell, with the magnetic field pointing in the same direction as the fluid flows. The deposit of particles on the wire points in the direction of the inlet, with few particles attaching to the side opposite of the inlet. Repulsive zones on the sides of the wire show no collection of particles. A film was produced during separation, from which the picture in Fig. 8.2 (left) was taken. It showed a defined particle deposit shape, which is characteristic for HGMS. The experiment showed the attachment of particles to the wire upstream of the flow. The deposit still increased past what is shown in Fig. 8.2 (left) and is barely limited.

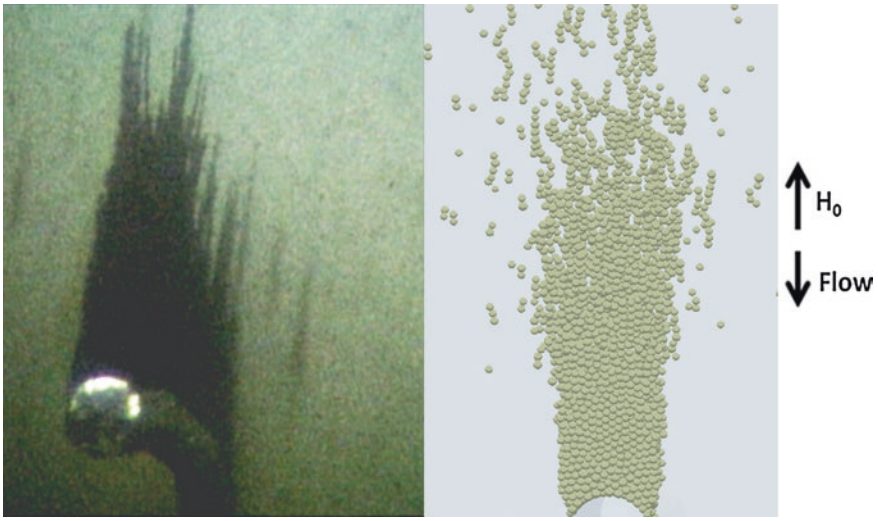

Fig. 8.2 Comparison of magnetic deposit in an HGMS process (*left*) with simulated deposit (*right*)

Figure 8.2 (right) shows a simulation of 100 µm particles collected on a 1 mm wire. The deposit shows a dense structure close to the wire which gets porous at a distance from the wire. The simulation fits the experiment well, despite the difference in particle size. Needle-shaped agglomeration is observable in the fluid. The same shape is visible as well in the simulation.

In summary, simulation and experiment agree well. The discrete element method delivers good results for the comparison of the simulation of magnetic suspensions.

8.4 Batch-Wise Magnetically Enhanced Centrifugation in Industrial Scale

For the investigation of magnetic separation, an industrial-scale machine was set up. It is batch-wise to limit the amount of particles and fluid, but shows separation comparable to the continuous version shown in Sect. 8.5.

8.4.1 Setup

The industrial-scale machine, shown in Fig. 8.3, was set up to show that the volume flow in the range of 1 m^3/h is realistic. It was manufactured by Andritz KMPT.

Fig. 8.3 The industrial-scale MEC (*left*) with the blue electromagnet installed around the machine; the machine is fed from the bottom and discharges at the top; a window is installed in the top to allow study of particle deposits; the wire matrix after cleaning (*right*)

The centrifuge is sealed, and a Plexiglas cover allows the fluid outlet to be viewed to supervise cleanliness and wire coverage. Tests were performed in a pilot line set up at a Solae plant in Aarhus, Denmark. The centrifuge chamber in the magnet has a volume of 6 l. The MEC was fed out of a container by a piston pump, which delivered up to 1 m^3/h. The diameter is 250 mm and the maximum rotational velocity is 4 000 rpm. Blades for preacceleration at the inlet and to avoid swirling at the outlet were implemented. The magnet installed around the machine delivers a flux density of up to 0.4 T at the center of the device. The matrix installed turns at a differential velocity of 120 rpm to disperse the particles. The concentration was measured gravimetrically by weighing the container, the suspension, and the particle mass after drying. Samples were washed to eliminate contamination. Merck MagPrep Silica particles, which are commercially available, were used for the separation tests. The density is 3.25 g/cm^3 and the saturation magnetization is 67 Am^2/kg.

8.4.2 Wire Cleaning by Centrifugal Forces

Figure 8.4 left shows wires covered with magnetic particles after stopping the centrifuge from 2 250 rpm at a flux density of 240 mT. Centrifugation allows the particle deposit to be cleaned from the wires to the wall. A sufficiently high rotational speed allowed the wires to be completely cleaned. Figure 8.4 right shows a photograph taken after centrifuging at 240 mT and 3 000 rpm. A clear line in the center of the wire is visible.

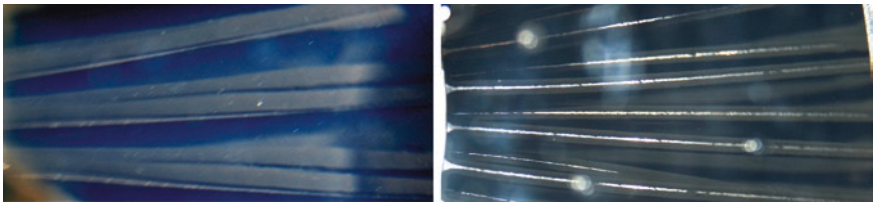

Fig. 8.4 Wires were covered with magnetic particles by magnetism, then the centrifugal force was increased to discrete velocities to test wire discharge; at 240 mT and centrifugation at 2 250 rpm wires are still completely covered (*top*); at 240 mT and 3 000 rpm a *center line* is clean while particles are still attached to wire edges (*bottom*)

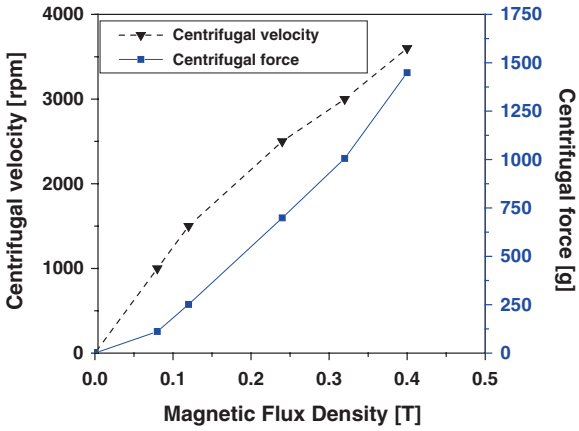

Fig. 8.5 Cleaning of filter wires by centrifugal forces depends on the magnetic field; the relation seems to be quadratic

The cleaning of the wire in Fig. 8.4 was used as a criterion to determine the correlation for the wire cleaning between the centrifugal velocity and the magnetic field. The rotational speed necessary was determined at different magnetic field strengths to discharge particles from the center line. The results are shown in Fig. 8.5. The relation seems to be linear for centrifugal velocity, and calculated to be quadratic for centrifugal force. Saturation magnetization of particles and wires did not show to reduce the necessary centrifugal force. A consequence is the necessity of increasing the centrifugal velocity if the magnetic flux density is increased.

8.4.3 Performance

The industrial-scale centrifuge was set up to demonstrate the potential of the process for handling large particle amounts. The separation efficiency was determined by the concentration of feed and effluent.

$$\eta = 1 - \frac{c_{Feed}}{c_{Effluent}} \tag{8.7}$$

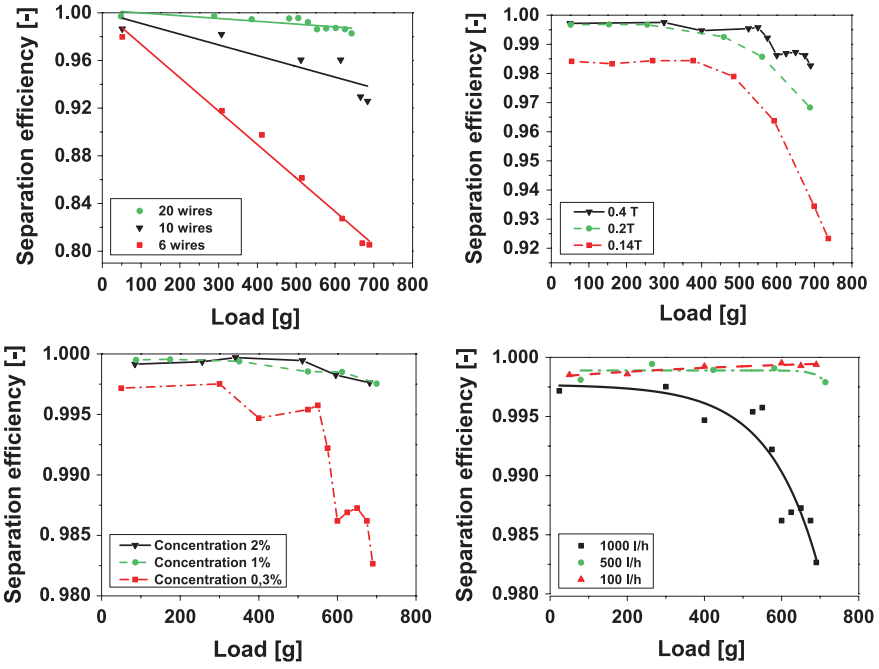

Fig. 8.6 Load over time depends on the number of wire stages implemented in the device (*top left*, 500 l/h; 1 000 rpm; 0.3 wt%; 0.4 T), on the flux density (*top right*, 1 000 l/h; 1 000 rpm; 0.3 wt%; 20 wire stages in matrix) and on the particle concentration (*bottom left*, 1 000 l/h; 1 000 rpm; 0.4 T; 20 wire stages); a completely filled device with 20 matrix wire stages allows high particle load, while separation is slightly reduced at 10 wires and heavily reduced at 6 wire stages; Separation over load at different volume flow (*bottom right*, 1 000 rpm; 0.4 T; 0.3 wt%; 20 wire stages): high volume flow reduces the amount of separated particles, especially at high loads

The centrifuge stored more than 600 g of particles and handled volume flows of up to 1 000 l/h (excluding dead times for the discharge). Figure 8.6 shows the influence of different parameters on the separation during the filling of the centrifuge. Figure 8.6 top left documents the behavior of particle deposits in the machine over time for a different number of wire stages. With 20 wire stages built into the machine, the separation was more than 99.7 % and close to the analytic measuring limit. At high load, the efficiency dropped after loading 500 g of particles. Introducing lower wire numbers led to a slightly lower separation value of 98.7 % at 10 wires at low load. Taking into account that the measurement was taken at a volume flow of 1 000 l/h, the separation was still at a high level. With 6 wire stages in the machine and a filling of more than 600 g, separation dropped significantly to 81 %.

Figure 8.6 top right shows the influence of the flux density over varying particle loads. There was no significant difference in the experiment between 0.4 and 0.2 T up to the limit of the device capacity. A drop of the flux density to 0.14 T

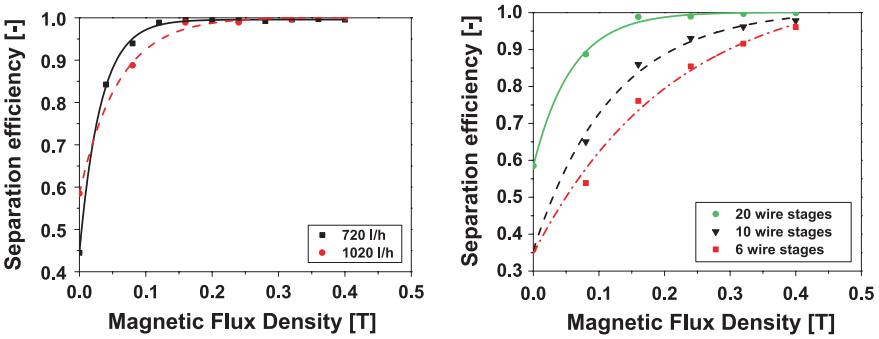

Fig. 8.7 The separation over the magnetic field for a different number of wire stages (*left*, 1 000 rpm; 0.3 w%; 20 wire stages) and for different volume flow (*right*, 1 000 l/h; 1 000 rpm; 0.3 w%) shows a significant influence; a volume flow of 1 m^3/h allows high separation efficiency; at low magnetic field strengths, low volume flow increases separation efficiency

reduces separation from 99.7 to 98.4 %. The reason for this is the saturation of the magnetization of the wires and particles at about 0.2 T. Figure 8.6 bottom left shows the influence of the concentration at different loads. A logarithmic influence was documented in Lindner et al. (2013a). In this experiment with particle load, no significant drop was noticed from 2 to 1 %, but a slight drop when the concentration was reduced to 0.3 % magnetic matter. The concentration influences the separation because of its effect on the agglomeration of particles. In Fig. 8.6 bottom right, the influence of different volume flows for different loads is shown. At 1 000 l/h, separation drops below 99 % at 600 g load. At a lower volume flow of 500 or 100 l/h, separation is almost unchanged when the centrifuge is filled with up to 700 g. The magnetic flux density is the most important influence for separation.

The influence of the flux density at varying volume flow and wire stages was investigated as well. Figure 8.7 left shows the separation behavior at high volume flow for different magnetic field strengths. Separation was good at 99 % from 0.2 T on, even for 1 m^3/h. At low magnetic flux density, a volume flow of 720 l/h proved to reduce separation to a lesser extent. Without a magnetic field applied, the separation showed unsteady results around 50 % separation which are caused by turbulence introduced at the inlet of the centrifuge. A different number of wire stages in Fig. 8.7 right showed a much higher influence at 1 000 l/h than in the previous experiment at 500 l/h in Fig. 8.6 top left.

8.4.4 Discharge in a Batch-Wise Magnetically Enhanced Centrifuge

Redispersion of the batch-wise machine was done by flushing 10 l of liquid in a cycle for 5 min while stirring the matrix at 120 rpm, and for another 5 min without

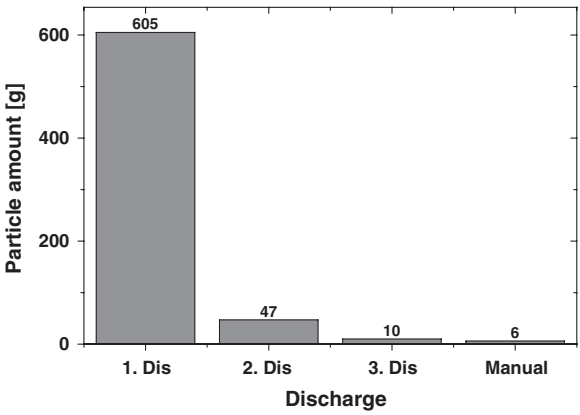

Fig. 8.8 Discharge characteristics: particle amounts discharged by redispersing in three batches in 10 l liquid each; redispersing was done by pumping in a cycle during 5 and 5 min matrix stirring; manual discharge by removing filter matrix and flushing manually 1.5 Continuous Magnetically Enhanced Centrifugation

stirring. Then the machine was drained and the suspension collected. The machine was filled again with washing water. The redispersion method was repeated before displacing the washing water and repeating the discharge a third time. The concentration and volume were measured each time. Then the matrix was unloaded, chamber and matrix were flushed manually, and the particle amount was again determined. Figure 8.8 shows the result of the discharge experiment. While a batch-wise centrifuge did not take advantage of the potential of the process in continuous mode, it is possible to use this device in a batch-wise automatic process.

8.5 Continuous Magnetically Enhanced Centrifugation

Besides the batch-wise magnetically enhanced centrifuge, a continuous centrifuge design was set up and tested. It performed similar to the batch-wise centrifuges in terms of separation, but it is used continuously.

8.5.1 Setup

Figure 8.9 left shows a decanter screw with a wire matrix implemented in the cylindrical part (Lindner and Nirschl 2014). Figure 8.9 right shows the complete decanter centrifuge set up at the Karlsruhe Institute of Technology. The screw is integrated into the centrifuge. Within the decanter screw, a magnetizable wire filter is installed in the cylindrical inner part. An electromagnet is installed around the centrifuge. The centrifuge is sealed to control the pressure. This is necessary in order to achieve different fill levels, like in a siphon, in the cylindrical part and conic part of the centrifuge. The cylindrical part is filled with liquid, covering the wire filter completely. The conic part is filled with particles at a lower fill level. Particles flow through a tube in the screw and are fed in between the cylindrical and conic parts. In the cylindrical part, particles are collected on

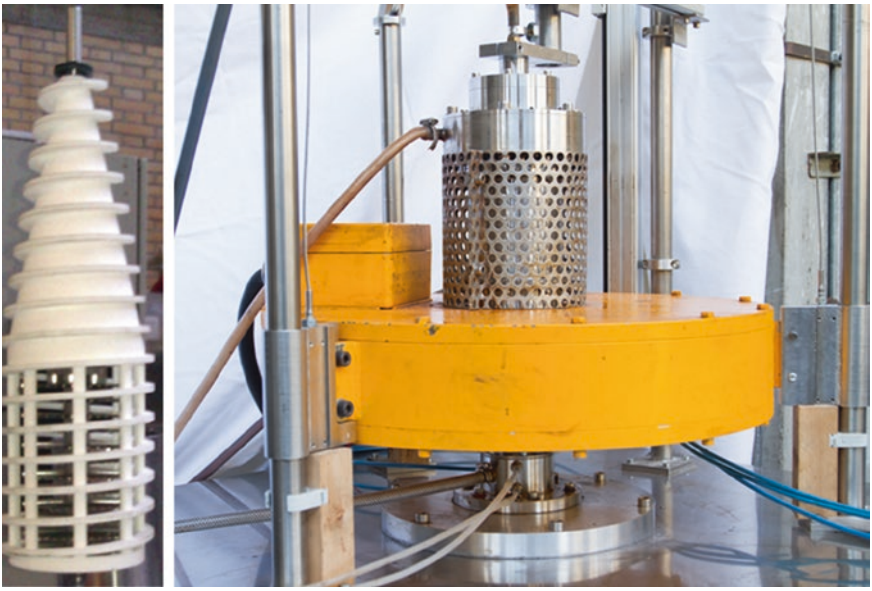

Fig. 8.9 The decanter screw is mounted on the shaft (*left*) with the bowl next to it, inside of the screw a wire filter is implemented; Magnetic decanter assembled with yellow magnet (*right*), feed inlet on top; the particle discharge is next to it linked with a hose for the flushing of particles; the particle discharge is at the bottom. Additionally, hoses are connected to cool the seals

the wall and separated from the liquid by the screw, which transports them over the cone and out of the liquid. They are collected in a round container on top of the device. Clean water flushes particles out, flowing from a tangential inlet, swirling through the container, and is discharged tangentially through a second hose. The particles, having dried and shed the original liquid in the decanter cone, are now in clean liquid. In our tests the cleaned particle-free effluent was used to flush the particles from the container back into the stirred feed tank to realize a continuous process at steady state in a cycle. The electromagnet created a flux density of 0.2 T. A volume flow of 50 l/h was used. In the system, 200 g of particles in 8 l of demineralized water circulated in the cycle. The decanter did not transport particle amounts below 100 g. The particles used in this test are still in development and are less efficient in separation compared to the Merck MagPrep Silica used in the Andritz KMPT centrifuge. The particle kind used is research-grade and has a saturation magnetization of 47 Am^2/kg and a remanence of 11 Am^2/kg.

8.5.2 Continuous Separation

The separation showed to be mainly dependent on the magnetic field, while the centrifugal force was necessary to convey particles out of the machine. Figure 8.10 shows the concentration of fluid discharge and particle discharge. The separation

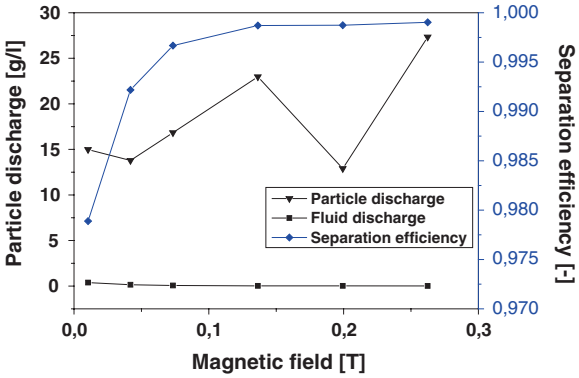

Fig. 8.10 Influence of magnetic field strength in a magnetically enhanced decanter (1 650 rpm; 54 l/h; 2 wt%; 11 wire stages)

efficiency is shown as second axis, rising from 62 % without magnetic flux to 99 % at 0.33 T. The whole separation process was tested successfully at steady state for several hours at a volume flow of 50 l/h.

The continuous magnetically enhanced centrifuge proves to be capable of continuously separating magnetic particles at high volume flow. Two requirements for the use in a continuous pilot line for protein separation are:

- a centrifuge for each process step is required in a continuous process, resulting in at least two for separation after adsorption and elution;
- the high cleaning effort and particle loss when stopping the machine, together with the high minimum fluid and particle amount (200 g) make the machine inappropriate for tests of low volume.

It is an interesting option for industrial production at large scale though, while batch-wise HGMS devices are more interesting for the processing of low particle amounts.

8.6 Permanent Magnet Arrangement for Magnetically Enhanced Centrifugation

HGMS bases either on conventional permanent magnets or on electromagnets. While conventional permanent magnets do not create a field in a longitudinal direction necessary for MEC, electromagnets are expensive in investment and operation. An alternative is the use of a permanent magnet arrangement creating a field in axial direction.

8.6.1 Setup

The design was deduced from the work of Hugon (Hugon et al. 2010a, b) on a patent of Aubert. Hugon investigated an arrangement, which allowed the generation

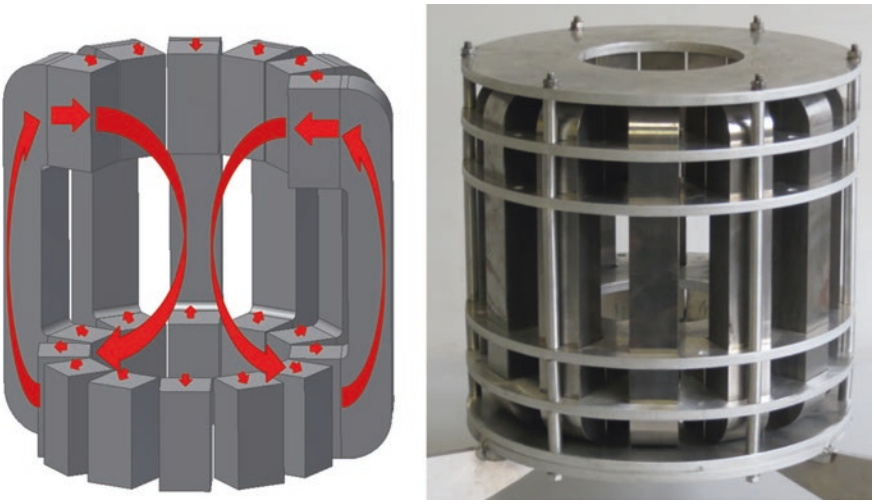

Fig. 8.11 Principle and setup magnet of the longitudinal magnet arrangement

of a field rotationally symmetric to an axis and longitudinal in axis direction. Magnets are arranged in two circles. In the top magnet circle, the magnet north pole points inwards, whereas in the bottom magnet circle north pole points outwards. The arrangement is large compared to the original magnet set up by Hugon at an inner magnet diameter of 125 and 120 mm of spacing between the top and bottom circles. The magnet was improved by finite element modeling set up at the Karlsruhe Institute of Technology. An improvement resulting from FEM was the implementation of pole yokes to close the field lines on the outside and enhance the field in the center. Additionally, the magnet was enhanced by implementing magnets which are longish ($35 \times 35 \times 70$ mm^3). The magnetic flux density was hence increased to 230 mT, but has a significant gradient at the magnet surface. The principle is shown in Fig. 8.11 left and the magnet in Fig. 8.11 right.

8.6.2 Performance of the Permanent Magnet Arrangement Compared to an Electromagnet

The longitudinal permanent magnet arrangement was tested on a batch-wise pilot MEC. The centrifuge was already presented with an electromagnet in (Lindner et al. 2013). While the flux density is weaker than that of a classic permanent magnet of comparable size of 0.4 T and a Halbach magnet of 0.32 T, those magnets' fields cannot be aligned with the centrifuge axis. An electromagnet has a less homogeneous field but can be more easily controlled by adjusting the current. In industrial machines, the use of electromagnets is limited by their high electricity consumption and the fact that they are prone to overheating.

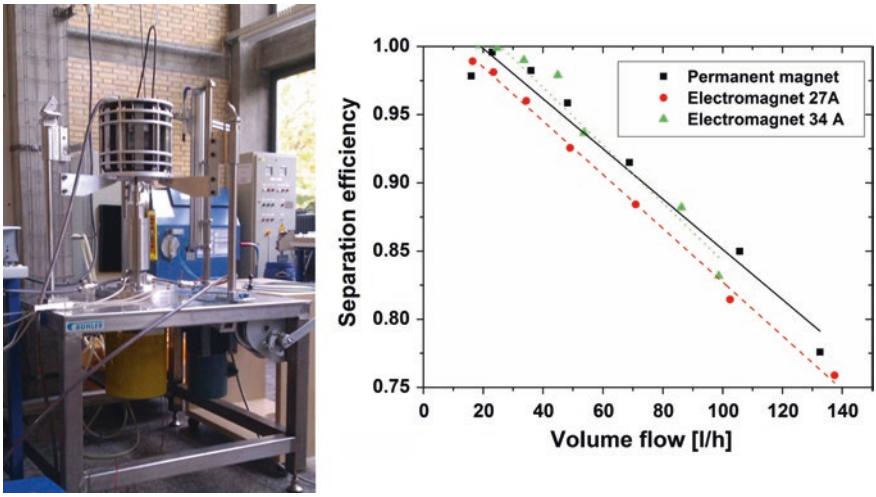

Fig. 8.12 The permanent magnet mounted on the batch-wise centrifuge; Influence of the volume flow on separation with electromagnet at 0.23 T in the center (*34 A*) and at the wall (*27 A*): permanent magnet separation is in between the two values

In the tests, a rotational velocity of 1 500 rpm was used, corresponding to 63 times the acceleration of the earth's gravity. Figure 8.12 left shows the magnet mounted on top of the centrifuge. It was installed with a cable pull, to allow it to be removed upwards from the MEC. This removes the magnetic field, which is necessary for the discharge of the device. During the separation test, it was placed around the centrifuge center. The separation of the magnet was tested at different volume flows in Fig. 8.12 right. A comparison with an electromagnet at the same magnetic flux density of 0.23 T in the center (34 A) and at the wall (27 A) was done. The separation efficiency was shown to be at a level similar to the comparison experiment.

8.7 Conclusion

A simulation of one MEC wire was performed, revealing agglomeration before separation and long particle chains when particles detach from the wire. The validation of the simulation was possible. MEC is a promising technology for the separation of magnetic particles. The amount of particle deposit on a wire is a function of the centrifugal velocity and the magnetic field. Separation of up to 1 m^3/h in a pilot machine was possible. A continuous process proved to be possible using a decanter approach. This is an interesting option for the processing of large volumes in pilot lines. A permanent magnet was developed which showed similar separation compared to an electromagnet. It reduces investment cost, machine weight, and energy cost drastically.

References

Deen NG et al (2007) Review of discrete particle modeling of fluidized beds. Chem Eng Sci 62(1–2):28–44

Ebner NA et al (2007) Filter capacity predictions for the capture of magnetic Microparticles by high-gradient magnetic separation. IEEE Trans Magn 43(5):1941–1949

Eichholz C et al (2011) Recovery of lysozyme from hen egg white by selective magnetic cake filtration. Eng Life Sci 11(1):75–83

Eichholz C et al (2008) Magnetic field enhanced cake filtration of superparamagnetic PVAc-particles. Chem Eng Sci 63(12):3193–3200

Franzreb M (2001) New design of high-gradient magnetic separators using permanent magnets. In: Proceedings of 6th world congress of chemical engineering, Melbourne, Australia, 23–27 Sept 2001

Gerber R, Birss RR (1983) High gradient magnetic separation. Research Studies Press, New York

Hournkumnuard K, Chantrapornchai C (2011) Parallel simulation of concentration dynamics of nano-particles in high gradient magnetic separation. Simul Model Pract Theory 19(2):847–871

Hugon C et al (2010a) Design, fabrication and evaluation of a low-cost homogeneous portable permanent magnet for NMR and MRI. Comptes Rendus Chimie 13(4):388–393

Hugon C et al (2010b) Design of arbitrarily homogeneous permanent magnet systems for NMR and MRI: theory and experimental developments of a simple portable magnet. J Magn Reson 205(1):75–85

Lindner J et al (2010) Efficiency optimization and prediction in high-gradient magnetic centrifugation. Chem Eng Technol 33(8):1315–1320

Lindner J, Menzel K,Nirschl H (2013a) Parameters influencing magnetically enhanced centrifugation for protein separation. Chem Eng Sci 97:385–393. doi:10.1016/j.ces.2013.04.044

Lindner J, Menzel K, Nirschl H (2013b) Simulation of magnetic suspensions for HGMS using CFD, FEM and DEM modeling. Comput Chem Eng 54:111–121. doi:10.1016/j.compchemeng.2013.03.012

Lindner J, Nirschl H (2014) A hybrid method for combining high-gradient magnetic separation and centrifugation for a continuous process. Sep Purif Technol 131:27–34

Langston PA, Tüzün U, Heyes DM (1995) Discrete element simulation of granular flow in 2D and 3D hoppers: dependence of discharge rate and wall stress on particle interactions. Chem Eng Sci 50(6):967–987

Svoboda J (2004) Magnetic techniques for the treatment of materials. Kluwer Academic Publishers, Dordrecht

Satoh A et al (1998) Stokesian dynamics simulations of ferromagnetic colloidal dispersions in a simple shear flow. J Colloid Interface Sci 203(2):233–248

Watson JHP (1973) Magnetic filtration. J Appl Phys 44(9):4209

Chapter 9
Design and Performance of a Pilot Scale High-Gradient Magnetic Filter Using a Mandhala Magnet and Its Application for Soy–Whey Protein Purification

Katharina Menzel, Victor Alvan Amasifuen and Hermann Nirschl

Abstract The scalability of economic high-gradient magnetic separation (HGMS) technology is essential in order to demonstrate the feasibility of the concept. One of the means is the application of a permanent magnet with a hollow cylindrical volume made from identical magnetic blocks (e.g., Mandhala), another is the development of a High-Gradient Magnetic Filter (HGMF) with a new backwashing concept. The Mandhala (*M*agnetic *A*rrangement for *N*ovel *D*iscrete *H*albach *L*ayout) magnet produces a dipolar transversal magnetic field in the center of the bore and its usable volume is easily adaptable to the separation device's extensions. The chapter presents the pilot scale design of the Mandhala magnet and the HGMF as well as experimental performance tests using a water—magnetic beads model system. Subsequently, experiments using soy–whey as a real feedstock demonstrate the purification of the protein Bowman-Birk inhibitor (BBI), an agent against cancer and multiples sclerosis.

9.1 Introduction

Conventional High-Gradient Magnetic Separation (HGMS) is a batchwise process with alternate magnetic particle separation and backwashing: Smart magnetic supports with selective functionalization enable an efficient adsorption of target products from the crude stock. Followed by magnetic separation and washing, the product is isolated by elution, then the beads are recyclable.

K. Menzel (✉) · V. Alvan Amasifuen
Karlsruhe Institute of Technology, Institute of Mechanical Process Engineering and Mechanics, Karlsruhe, Germany
e-mail: katharina.menzel@kit.edu

H. Nirschl
Institute of Mechanical Process Engineering and Mechanics, Karlsruhe Institute of Technology, 76131 Karlsruhe, Germany
e-mail: hermann.nirschl@kit.edu

H. Nirschl and K. Keller (eds.), *Upscaling of Bio-Nano-Processes*,
Lecture Notes in Bioengineering, DOI 10.1007/978-3-662-43899-2_9

Recently, several new magnetically separation devices have been developed and tested at lab scale, e.g., (Becker et al. 2009; Kaeppler et al. 2009; Lindner et al. 2010). To demonstrate the feasibility of the concept for industrial applications, it is essential to develop large-scale HGMS apparatuses. Two major obstacles so far were the lack of an up-scalable and economic magnetic field generating device as well as a separation cell optimized regarding efficient particle detachment from the separation matrix. The application of cylindrical permanent magnets made from identical magnet blocks (Menzel et al. 2013, 2014) and the new concept of High-Gradient Magnetic Filter (HGMF) design help to overcome these barriers.

This chapter demonstrates the application of a Mandhala magnet (*M*agnetic *A*rrangement for *N*ovel *D*iscrete *Ha*lbach *La*yout) (Raich and Blümler 2004) for HGMS. The magnet generates a dipolar transversal field, which implies an axial and/or transversal wire to field to flow configuration (Gerber and Birss 1983). The openable hinged concept adapted from Windt et al. (2011) is convenient for easy placement and accessibility of the separation device. The arrangement is compact, light, and therefore easy transportable in contrast to an electromagnets or a c-shaped magnet. The present work adjusts the magnetic flux density calculation concept by Menzel et al. (2013) based on the dipole approach by Soltner and Blümler (2010). The comparison between the adapted analytic approach and field measurement proves if the modifications remedy the gap between them, which was present in (Menzel et al. 2013).

The filter cell is equipped with rotatable wire matrices, intermediate pitched blade impellers and a spraying nozzle array below the top of the filter cell. The work presents performance tests of the pilot scale separation apparatus carried out with a water-magnetic beads model system. The first criteria is the separation efficiency, the second is the backwashing behavior. Subsequently, a real feedstock is used to demonstrate the separation of Bowman-Birk inhibitor (BBI) from soy–whey using magnetic ion-exchange particles. The process is assessed regarding protein content, sucrose content, purity and purification factor as well as target protein concentration factor.

9.2 Design of the Mandhala Magnet

The work on the Mandhala magnet for NMR (nuclear magnetic resonance) applications by Raich and Blümler (2004), Soltner and Blümler (2010) and Windt et al. (2011) gave the major inspiration for its application as a magnetic field generating device in HGMS. The transversal dipolar Mandhala magnet, shown in Fig. 9.1a, consists of n magnets,[1] whose magnetization direction differs by $720°/n$ between neighboring magnets. The field in the center of such a Mandhala ring is directed in z-direction (transversal), perpendicular to the fluid flow direction along the x-axis. Figure 9.1b shows schematically the magnetic flux density distribution, simulated using the finite element method (FEM) (www.comsol.com), generated by a Mandhala magnet.

[1] Where n is the number of identical permanent magnet blocks within one Mandhala ring and $n = 8 + k \cdot 4$ $\left(k \in \mathbb{N}^0\right)$, zero is included: $\mathbb{N}^0 = 0, 1, 2, \ldots$

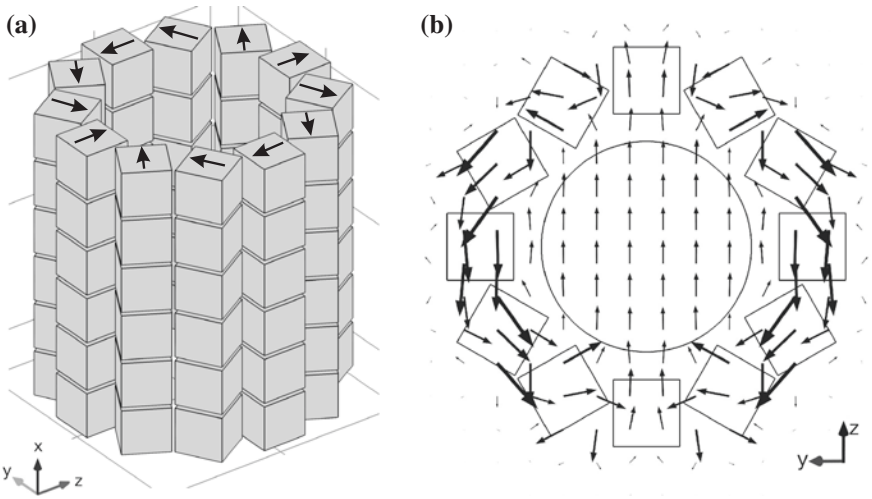

Fig. 9.1 Mandhala magnet design and magnetic field with definition of the coordinate system, whose origin is located in the *center* of the hollow inner volume. **a** Mandhala magnet with equidistant stacking of *six rings* consisting of twelve magnets each. **b** FEM vector field of the magnetic flux density in and around the Mandhala magnet (www.comsol.com) (*top view* y-z plane). *Arrow* size is proportional to the magnetic flux density B

Menzel et al. (2013) presented an analytic concept that allows to calculate the magnetic flux density in the center of the hollow inner volume of a Mandhala magnet. Nevertheless, the comparison between measurement and analytic field calculation emerged an offset. There are two reasons for the difference. First is that Raich and Blümler (2004) investigated Mandhalas with $n = 8 + k \cdot 8$ magnets per ring and calculated the auxiliary function $\Xi(n)$. The function describes the ratio a/r between the side length of the magnet a and magnet's center radius r as $a/r = 2 \cdot \Xi(n)$. Later Soltner and Blümler (2010) found that the restriction to $n = 8 + k \cdot 8$ is not necessary and it is sufficient to define $n = 8 + k \cdot 4$. They showed how to stack multiple Mandhala rings, but did not redefine the auxiliary function $\Xi(n)$. For $n = 12 + k \cdot 8$ the original auxiliary function $\Xi(n)$ causes an overlapping of magnets and is therefore not applicable in this case. Second is that former works did not consider that neighboring cubes in real arrangements must not touch each other due to space requirements of the structural material. The use of a reduced side length corrects this disagreement. The next subsections present a summary of the calculation concept and introduce the two adjustments, which close the gap between measurement and analytic solution.

9.2.1 Dipole Approximation for a Mandhala Magnet

The dipole approximation is based on the replacement of cube magnets by point source dipoles of the same magnetic moment, which are located in the center of the substituted geometry. It is valid if the distance between the magnet surface and

the observation point z in relation to the magnet side length a is sufficiently large ($z/a > 1$). The concept permits to develop a formula for the magnetic flux density along the bore axis x for a series of stacked rings (Menzel et al. 2013). It is

$$B_{z,m}(x) = 3/\pi \cdot n \cdot B_r \cdot \Xi(n)^3 \cdot f(x), \tag{9.1}$$

with the number of magnets within the ring $n = 8 + k \cdot 4$, the remanence of the magnet B_r and the auxiliary function $\Xi(n)$ defined through $a = 2r \cdot \Xi(n)$. The dimensionless superposition function f includes the contribution of an even number of multiple rings m to the total magnetic flux density:

$$f(x) = \sum_{i=1}^{m/2} \left\{ [1 + ((x - s_i)/r)^2]^{-5/2} + [1 + ((x + s_i)/r)^2]^{-5/2} \right\}. \tag{9.2}$$

The choice of the normalized x-coordinates of the dipole rings, s_i/r, strongly influences the magnetic flux density, its distribution, and therefore its homogeneity. The use of an equidistant stacked rings ensures a high magnet packing density and easy construction. The normalized displacement in x-direction, s_i/r, for an equidistant array is deduced from geometry. It is

$$s_i/r = 0.5\gamma + \Xi + (i - 1)(\gamma + 2\Xi) \tag{9.3}$$

for $i = 1, 2, 3, \ldots, m/2$ with relative distance $\gamma = b/r$ and the absolute distance b between the Mandhala rings. Each magnet ring generates a magnetic flux density along the center axis x, which describes a Voigt peak function (similar to a Gauss function). The stacking of the rings corresponds to the superposition of the curves. To ensure curve continuity, γ has to be chosen in the range of $0 \leq \gamma \leq 0.1$.

In real arrangements, structural material is necessary to fit the magnets into their positions. Hence, the neighboring magnets edges might not touch each other, which was an assumption in former works. Therefore, a reduced magnet's side length

$$a^* = \nu a \tag{9.4}$$

with the reduction ratio ν corrects this disagreement.

As stated before the auxiliary function Ξ for $n = 8 + k \cdot 8$ magnets per ring was developed by Raich and Blümler (2004). To extent the scope to $n = 8 + k \cdot 4$, the geometric layout of Mandhala rings with $n = 12 + k \cdot 8$ have to be regarded. Figure 9.2a depicts the schematic representation of the magnet coordinates for this case. The angle between two magnet centers α is $\frac{2\pi}{n}$. The two magnets which surround the angles $45° + l \cdot 90°$ ($l = 0, 1, 2, 3$), respectively, have maximum extension along the circumference of the circle with radius r. Their edge distance is shortest for a^* or even vanishes if the maximum side length a is considered.

Figure 9.2b depicts the two adhering magnets in more detail. The side length a, the reduced side length a^* and subsequently the auxiliary function Ξ are retrievable with the following geometric correlations: First, the length $\overline{\mathrm{AB}}$ within the triangle ΔOriginAB results in

$$\overline{\mathrm{AB}} = r \sin \alpha/2. \tag{9.5}$$

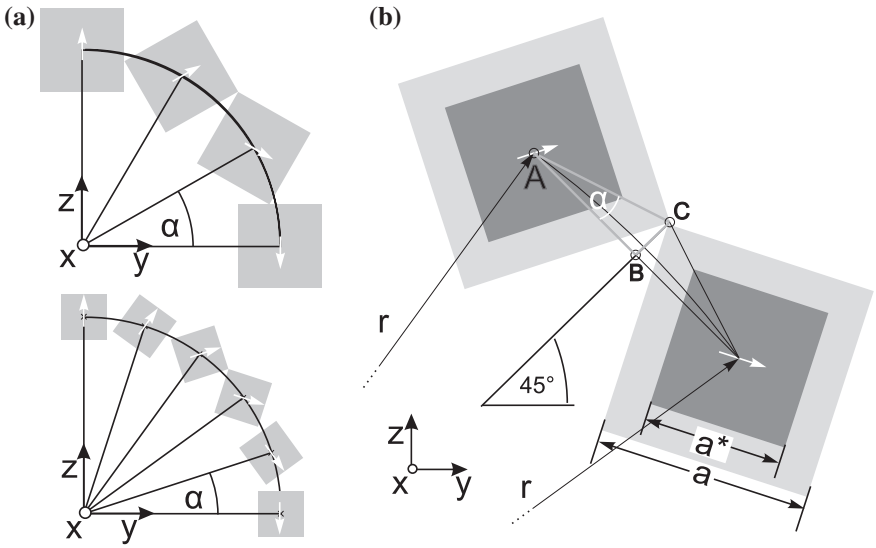

Fig. 9.2 Schematic representation of the magnet coordinates in Mandhala rings with $n = 12 + k \cdot 8$ magnets per ring. *Arrows* indicate the magnetization direction. Definition of the coordinate system and the symbols used. **a** Quarter of Mandhala rings Quarter of Mandhala rings with $n = 12$ and 20 magnets. **b** Detail cross-section

Second, the distance between point A and B within the connection ΔABC equals

$$\overline{\mathrm{AB}} = \overline{\mathrm{AC}} \cos \alpha. \tag{9.6}$$

Third, it applies that

$$\overline{\mathrm{AC}} = \frac{a}{\sqrt{2}} = \frac{a^*}{\nu \cdot \sqrt{2}}. \tag{9.7}$$

The insertion of Eqs. 9.5 and 9.7 into Eq. 9.6 and resolving for a^* gives

$$a^* = 2r \cdot \frac{\nu\sqrt{2}\sin(\pi/n)}{2 - 4\sin^2(\pi/n)}. \tag{9.8}$$

Finally, the auxiliary function is

$$\Xi(n, \nu) = \begin{cases} \frac{\nu \cdot \{\cos(\frac{2\pi}{n}) - \sin(\frac{2\pi}{n}) - \sqrt{2}\sin(\frac{\pi}{4} - \frac{4\pi}{n})\}}{2\cos(\frac{\pi}{4} - \frac{4\pi}{n}) + \sqrt{2}}, \\ \text{if } n = 8 + k \cdot 8 \text{ for } k \in \mathbb{N}^0 or \\ \frac{\nu\sqrt{2}\sin(\pi/n)}{2 - 4\sin^2(\pi/n)}, \\ \text{if } n = 12 + k \cdot 8 \text{ for } k \in \mathbb{N}^0. \end{cases} \tag{9.9}$$

9.2.2 Comparison of Dipole Model Results and Measurement

The built hinged Mandhala magnet (see Fig. 9.4a) can be opened easily. It consists of $n = 12$ magnets/ring with side length $a^* = 35$ mm and $m = 6$ magnet rings.

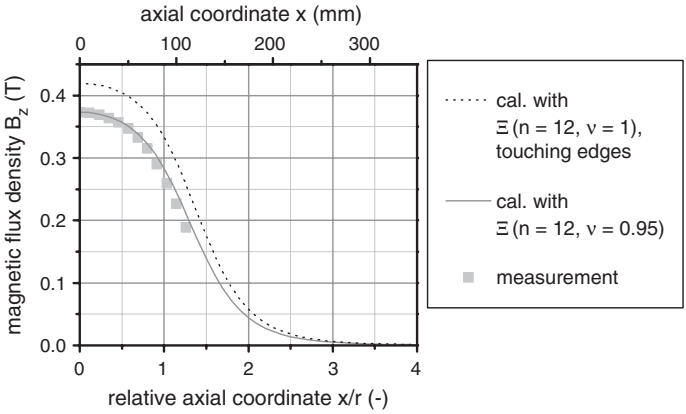

Fig. 9.3 Magnetic flux density B_z as a function of the relative axial coordinate x/r or axial coordinate x of a Mandhala magnet with $n = 12$ magnets/ring and $m = 6$ magnet rings that are equidistantly stacked with $\gamma = 0.034$. Comparison between measurement and the calculation using $\Xi(n, \nu)$ of Eq. 9.9

The design and construction is reported in more detail by Menzel et al. (2013). The structural material has 2.08 mm minimum wall thickness and the magnet's center radius r is 87.208 mm, which gives a maximum magnet's side length $a = 2r \cdot \Xi(n = 12, \nu = 1)$ of 36.89 mm. Therefore, the reduction factor $\nu = a^*/a$ is 0.95.

It is possible to calculate the magnetic flux density B_z along the bore axis x using Eqs. 9.1, 9.2, 9.3 and 9.9 and compare it with flux density measurement. The magnetic field is scanned with a Hall-sensor, type FH 51 of Magnet-Physik Dr. Steingroever GmbH. Figure 9.3 depicts the measurement and the calculation of B_z using $\nu = 1$ and $\nu = 0.95$ as a function of the (relative) axial coordinate x or x/r. The measured magnetic flux density is 0.37 T in the center and does not decrease below 0.27 T within the filter length of 160 mm. The calculation using $\nu = 0.95$ shows good agreement with the measurement. The effect of the reduced side length $a^* = \nu a$ and the new auxiliary function Ξ is to lower the magnetic flux density by 17.6 % in the center of the magnet. With these two modifications, the gap between measurement data and the calculation, which was present in (Menzel et al. 2013), reconciles.

9.3 Design of the Filter Cell and Its Operation

The filter cell, shown in Fig. 9.4, is placed inside the hollow volume of the dipolar Mandhala magnet. The filter cell's inner diameter is 100 mm and its height is 160 mm. It is made of glass to enable the observation of the backwashing process. A capillary (Fig. 9.4b, 2) equipped with three flat jet inserts is installed at the top of

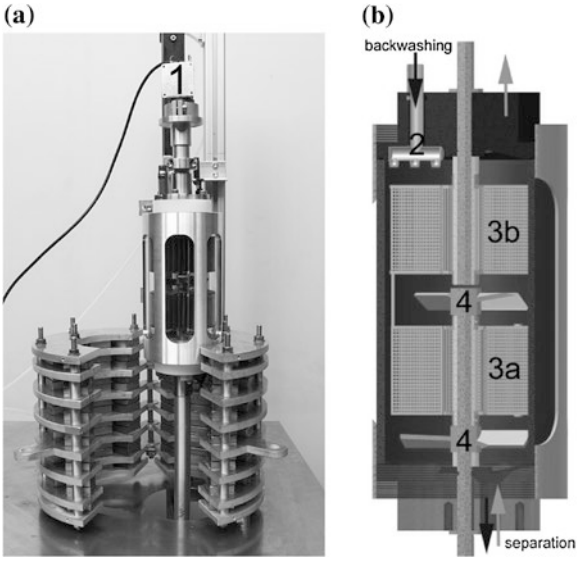

Fig. 9.4 Dipolar transversal Mandhala magnet and separation cell equipped with stirrer motors (*1*) at the *top* and *bottom*. The motors rotate the two *star*-shaped matrix elements (*3a*, *3b*) and two impeller elements (*4*) with four inclined blades independently from each other. The wash liquid is introduced pulsewise by a capillary equipped with three flat jet inserts (*2*). **a** Opened Mandhala magnet and elevated filter cell. **b** Interior view of the filter cell

the filter cell in order to inject the backwashing liquid. The two lateral nozzles possess a spraying angle of 30° with a volume flow of 1 l/min at 2 bar liquid pressure (flat jet insert from Lechler GmbH AV 634.40217). The center nozzle has a spraying angle of 120° and a volume flow of 0.63 l/min at 2 bar liquid pressure (flat jet insert AV 634.367 17). The matrices (Fig. 9.4b, 3a, 3b) have a height of 50 mm and are rotatable by a motor (Fig. 9.4a, 1). They are made of magnetizable stainless steel (X6 Cr 17 (1.4016), AISI 430) wire meshes that are starlike arranged. The coarse matrix mesh (Fig. 9.4b, 3a) has a wire diameter of 0.4 mm and a mesh width of 1 mm. The fine matrix (Fig. 9.4b, 3b) is made of wire mesh with a wire diameter of 0.25 mm and a mesh width of 0.375 mm. The detachment of the particles is assisted by two impeller elements (Fig. 9.4b, 4) with four inclined blades, which are revolving independently from the matrices. They are angled by 45° to the left (regarding to the impeller axis) and are considered as mixed-flow turbines because they exhibit velocity components in both axial and radial direction (Paul 2004).

A pneumatic lifting device vertically moves the filter cell into and out off the magnetic field. Naturally, during filtration the cell is placed inside the hollow volume of the Mandhala magnet. For backwashing, it is removed from the magnetic field. Although the forces are small enough to manually split, open, and close the magnet a convenient pneumatic piston, which controls the separation of the two halves, is installed.

The pilot setup, shown in Fig. 9.5, consists of a stirred feed vessel (Fig. 9.5, 1), a peristaltic pump (Fig. 9.5, 2), the developed HGMS apparatus (Fig. 9.5, 3) and a collecting vessel for the filtrate (Fig. 9.5, 4). The stirred feed suspension is fed into the separation cell at the bottom and leaves it as filtrate at the top. The filter cell collects particles until the matrix is saturated. After the separation process, the filter cell is removed from the magnet and regenerated by backwashing. A pressurized

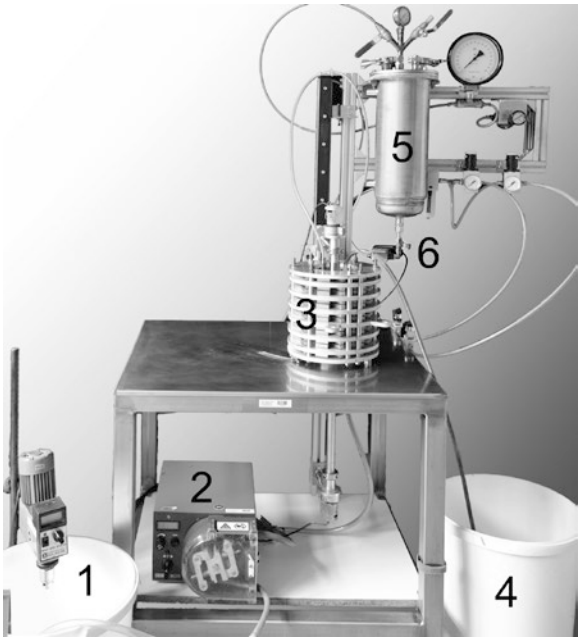

Fig. 9.5 Pilot setup with stirred feed vessel (*1*), a peristaltic pump (*2*), the developed HGMS apparatus (*3*) and a collecting vessel for the filtrate (*4*). Backwashing is performed pulse by pulse with a pressurized tank (*5*) and a programmable 2/2 way valve (*6*)

tank (Fig. 9.5, 5) contains the washing liquid. A 2/2-way solenoid valve (Bürkert GmbH, Type 0330 with timer unit 1078) pulses the flow with an adjustable repetition frequency (*PRF*) and time t_s. The repetition frequency is the reciprocal of the time between the pulses *T*.

9.4 System Performance

The soy–whey protein purification involves magnetic separation and resuspension of the magnetic particles. Therefore, it is important to characterize the system's performance by looking at both unit operations. Lab scale experiments showed that the BBI-antibody functionalized MagPrep beads are best suited to purify BBI, but their utilization is too expensive. Hence, the application of magnetic anion exchange carriers MagPrep® TMAP (Trimethylammoniumpropyl-functionalized magnetic silica particles) and Orica Watercare MIEX® DOC resin ('Magnetic Ion EXchange' with anion exchange group that binds 'Dissolved Organic Carbon') are substitute particles that performed well enough to justify further experiments at larger scale. However, only Orica particles were available in sufficient quantity for pilot experiments on BBI purification. As the Orica particles are large and easily separable, the separation of smaller plain MagPrep® Silica beads (courtesy of Merck Millipore KGaA, Darmstadt) is more challenging. Therefore, the plain MagPrep® Silica beads are suitable to accomplish the system performance tests.

The next two sections present the evaluation of particle loss as a function of the inflow velocity and the backwashing behavior of the developed HGMS cell with the Mandhala magnet.

9.4.1 Particle Loss

A low particle loss, which translates to a high separation efficiency of magnetic beads, is important in order to reduce costs for subsequent particle addition and to increases productivity. Therefore, it is essential to determine the maximum inflow velocity with economically justifiable particle loss.

9.4.1.1 Method

The experiments are realized at volume flows of 20, 50, 70, 100, 150, and 200 l/h, which is equivalent to inflow velocities between 0.71 and 7.07 mm/s. The MagPrep® Silica beads are suspended in deionized water, which exhibits pH 7.0 adjusted with 0.05 M Na_2HPO_4 and 0.05 M NaH_2PO_4. Before it is adjusted to the final concentration, a rotor–stator disperser T 25 Ultra-Turrax® disagglomerates the particles within the suspension for 15 min at 8,000 rpm. The final feed suspension (10 l total volume) exhibits a concentration of 18 g/l and is poured into a stirred feed vessel (Fig. 9.5, 1).

The analysis of feed and filtrate takes place at equidistant time intervals. The relative particle loss c_f/c_0 relates the mass concentration of the filtrate c_f to the concentration of the feed c_0. High concentrated feed and filtrate suspensions were measured gravimetrically using weighed empty glasses for sampling. The mass concentration

$$c = \frac{m_p}{m_{\text{susp}}} \tag{9.10}$$

is given by dividing the solid mass m_p by the total suspension mass m_{susp}. The two masses are both determined by weighing the glass after and before separating and evaporating the liquid.

The concentration of dilute filtrate samples is determinable offline by a 90° scattering light absorption turbidimeter (Hach 2100P). It measures between 0 and 800 nephelometric turbidity unit (NTU). In this range, the scattering intensity is straight proportional to the concentration. However, the slope of the linear correlation is a function of the size and absorption properties of the particles. Therefore, a calibration of turbidity as a function of the suspension concentration is necessary (not shown). Foster et al. (1992), Lewis (1996) showed that the calibration slope of smaller particles is steeper than that of larger particles. It is a matter of fact that bigger particles are separated more easily than smaller ones. Hence, assuming that the particle size distribution does not change within the magnetic separation process, which corresponds to a constant grade efficiency, overestimates the particle loss.

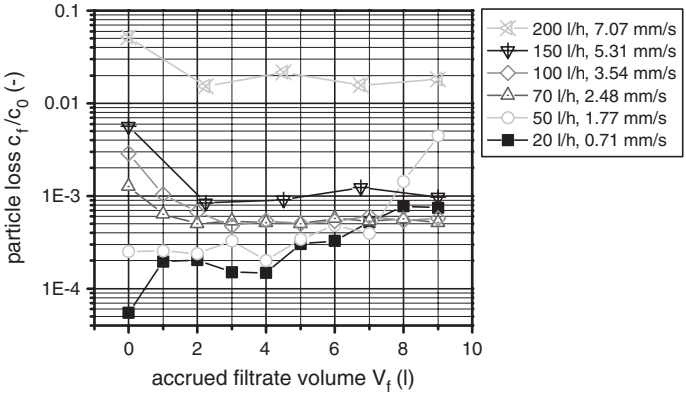

Fig. 9.6 Particle loss of MagPrep® Silica increases with growing volume flow or flow velocity, respectively. The feed concentration is approximately 18 g/l

9.4.1.2 Results

In Fig. 9.6 the relative particle loss c_f/c_0 is shown as a function of the accrued filtrate volume V_f at six different volume flows or flow velocities. As expected, the curves shift to higher product loss with growing volume flow. Between 20 l/h and 100 l/h the particle loss averages to below 0.001, which is equivalent to a separation efficiency above 99.9 %. At 200 l/h the particle loss ascends to 0.02 and the separation decreases to 98 %. The graph depicts that no drastic particle loss increase (break-through) took place. The filter capacity amounts therefore to at least 160 g MagPrep® Silica. If the apparatus is applied in production process, an online monitoring system, e.g., turbidity measurement, at the exit of the filter chamber is advisable to prevent particle loss and to determine when backwashing has to be initiated.

9.4.2 Backwashing Behavior

The backwashing behavior of the developed HGMS cell with Mandhala magnet is the second criterion for performance evaluation. To save process time and costs, the required cleanliness of the separation cell is reached with as little washing liquid as possible. The experiments investigate the influence of rotational speed and the sense of rotation of the wire matrices and impellers. The residue of particles in the separation chamber is examined as a function of the necessary volume of wash liquid.

The observation of the flow pattern inside the filter chamber aims to ascertain how the different parameters influence the backwashing results and to identify those for optimized performance. The analysis reveals the effects of the rotational direction of impellers and matrices. They can either rotate separately or simultaneously and in clockwise or counter clockwise direction.

9.4.2.1 Theory

The characterization of the backwashing process follows a concept adapted from the scientific work on filter cake washing by Ruslim et al. (2009). The wash diagram displays the relative residue r^* of magnetic particles in the HGMS cell as a function of the wash ratio W. It enables the dimensionless characterization of the backwashing and therefore the prediction of a large-scale process.

The wash ratio is

$$W = \sum_{i=1}^{j} \frac{V_{\mathrm{ws},i}}{V_{\mathrm{cell}}} \tag{9.11}$$

with the volume of liquid that leaves the cell in each washing step i

$$V_{\mathrm{ws},i} = \frac{m_{\mathrm{susp,ws},i}}{\rho_{\mathrm{wl}}} \cdot (1 - c_{\mathrm{ws},i}) \tag{9.12}$$

and the cell volume $V_{\mathrm{cell}} = 1.261$. The density of the clean wash liquid ρ_{wl} is assumed to be 1 g/cm^3. The mass of the flushed suspension $m_{\mathrm{susp,ws},i}$ and its mass concentration $c_{\mathrm{ws},i}$ were determined for every washing step $i = 1, 2,\ldots j$ by gravimetric analysis, described in Sect. 9.4.1.1.

Furthermore, the relative residue r^* is

$$r^* = 1 - \frac{\sum_{i=1}^{j} m_{\mathrm{ws},i}}{m_{\mathrm{sep}}}. \tag{9.13}$$

The particle mass $m_{\mathrm{ws},i}$, which is flushed out of the cell, isrepetition frequency

$$m_{\mathrm{ws},i} = c_{\mathrm{ws},i} \cdot m_{\mathrm{susp,ws},i} \tag{9.14}$$

with particle mass concentration $c_{\mathrm{ws},i}$ and the suspension mass $m_{\mathrm{susp,ws},i}$. The particle mass m_{sep}, which was incorporated inside the cell before washing, cannot be detected directly. It therefore has to be calculated with data retrieved during the separation process according to

$$m_{\mathrm{sep}} = c_0 \cdot m_0 - c_f \cdot m_f - c_d \cdot m_d. \tag{9.15}$$

It includes the feed mass concentration c_0, the feed suspension mass m_0, the filtrate mass concentration c_f, the filtrate suspension mass m_f, the drain mass concentration c_d, and drain suspension mass m_d. The drain suspension is the residual liquid that remains inside the filter cell after the magnetic separation step. The drain suspension is removed by backpumping before backwashing takes place.

Two theoretical models, namely the ideal displacement model (Ruslim 2008) and the ideal mixing-cell model from chemical process engineering (Levenspiel 1999), are suitable to compare with backwashing results of the HGM filter. The ideal displacement theory is based on an ideal plug flow and assumes that the washing liquid completely flushes out the magnetic particles. It defines that the relative residue is simply

$$r^*(W) = \frac{c}{c_0} = 1 - W. \tag{9.16}$$

The mixing-cell model considers the flow behavior inside the cell volume. It assumes ideal mixing in each cell, which involves homogeneous distribution/dilution of the residue. With growing number of cells N the flow pattern approaches an ideal plug flow. The relative residual concentration inside the filtration cell is

$$r^*(W) = \frac{1}{N} \cdot \sum_{j=1}^{N} \sum_{i=0}^{j-1} \frac{(N \cdot W)^i}{i!} \cdot \exp(-N \cdot W). \tag{9.17}$$

A typical wash curve subdivides into three regimes. The first part ($W \leq 1$) often approximates the ideal displacement curve. In the second section ($1 < W \leq 3$), mechanical dispersion (e.g., due to shear forces, turbulence) predominates and is best described by the mixing-cell model with the adjustment parameter N. The third region ($W > 3$) is characterized by diffusion, which is not considered by the two models and involves further declining of the wash curve slope.

9.4.2.2 Method

The filter loading takes place at 100 l/h with the same suspension as used for the separation efficiency tests. Before washing, the remaining mother liquor (drain suspension) is drained through the bottom of the HGMS cell, while the filter remains inside the magnetic field to avoid particle loss. Afterward, the washing process takes place in batches with the HGMS cell moved out of the Mandhala magnet as shown in Fig. 9.7.

The pressurized washing liquid (water at 2 bar, pH 7) is injected through an array of three spraying nozzles at the top of the HGMS cell (see Fig. 9.4). Simultaneously, the matrix and/or impellers rotate clockwise or counter clockwise. All experiments were executed with a fixed opening time $t_s = 0.35$ s and closing time $T = 0.1$ s (PFR of 2.2 Hz). Until the cell is filled the discharge valve at the bottom of the cell is closed. Then, the inflow stops while the matrices and/or impellers keep rotating for two more minutes. Afterward, the suspension discharges through the bottom of the cell to a sample container at the maximum volume flow of 200 l/h. This washing step is repeated several times.

9.4.2.3 Experimental Results

The analysis examines the backwashing behavior as a function of sole matrix or impeller rotation as well as the co-action of both, see Fig. 9.8. The results of sole matrix or impeller turning are shown in Fig. 9.8a. The diagram displays the wash curves of experiments with two different matrix rotational speeds (100 and 336 rpm) as well as with the maximum possible impeller velocity (171 rpm). The

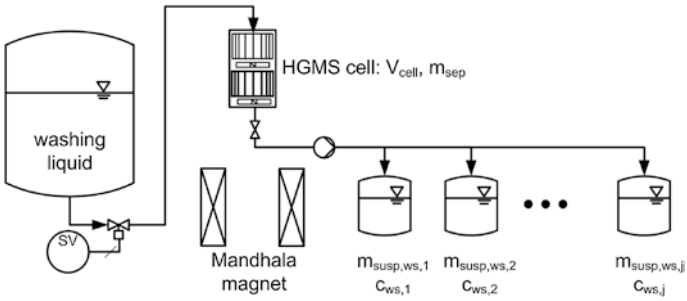

Fig. 9.7 Batchwise washing process with the HGMS cell moved out of the Mandhala magnet

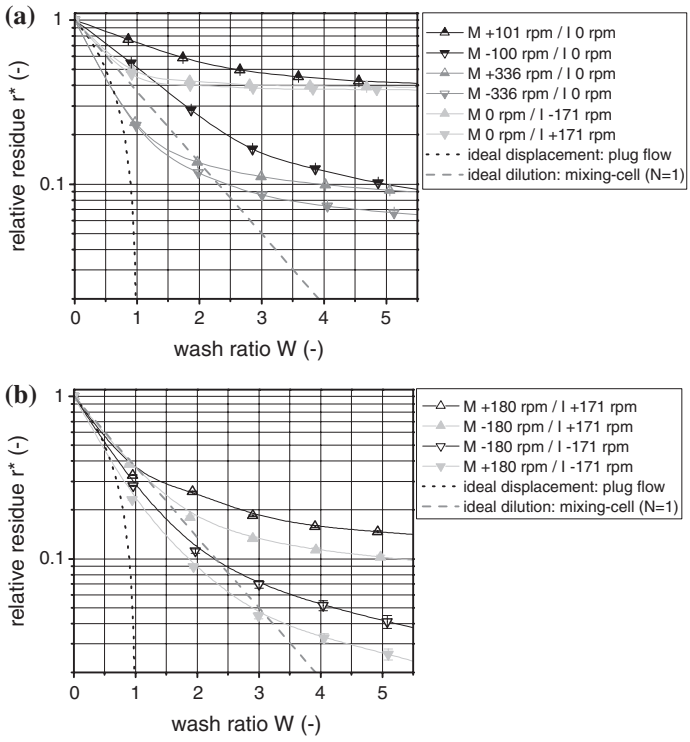

Fig. 9.8 Backwashing behavior as a function of rotational speed and sense of rotation of matrices (*M*) and/or impellers (*I*). The sense of rotation, considered from top view of the filter chamber, is indicated by + and –. It stand for clockwise and counter clockwise rotation, respectively. A comparison with ideal displacement and dilution models is given. **a** Solely using matrices (*M*) or impellers (*I*) rotation. **b** Simultaneously using matrix (*M*) and impeller (*I*) rotation

sense of rotation is indicated by + for clockwise and − for counter clockwise rotation considering the top view of the filter cell. The graph shows that solely operating the impellers, both counter clockwise and clockwise, results in a final

unsatisfactory relative residue of 0.4. Further, it can clearly be seen that the matrix revolution has a major impact residue than the impeller rotation on the decrease of the relative residue. The backwashing enhances with growing rotational speed. In addition, the sense of matrix rotation has an influence on the wash result, with clockwise rotation being better than counter clockwise rotation. The first two experiments presume that the influence of the sense of rotation is decreasing with growing rotational speed of the matrices.

The comparison of the wash diagrams in Fig. 9.8 reveals that an enhanced washing result can be achieved by simultaneous rotation of matrices and impellers. A clockwise rotation of the impellers (I+) is less effective than a counter clockwise rotation (I−). At the same time, the rotational sense of the matrices has no clear influence on the wash curve. The simultaneous revolution of impellers and matrices induces either concurrent or countercurrent flow. A concurrent flow occurs if both elements are turning in the same direction while opposite directions induce a countercurrent flow. Figure 9.8b reveals that negative rotation of the impellers is more efficient than positive one and a countercurrent flow outperforms a concurrent one.

The comparison of the experimental wash curves in Fig. 9.8 with the theoretical models illustrates two effects. Some wash curves lie above the ideal dilution and displacement curve, which indicates that there are stagnant zones with little turbulence in the filter cell and the wash result is insufficient. Other wash results resemble the ideal displacement curve in the first regime ($W \leq 1$) and are similar to the ideal dilution curve in the second region of the wash curve ($1 < W \leq 3$). This reveals good backwashing behavior. If the progression of the curve in the second regime ($1 < W \leq 3$) is steeper than that of the ideal dilution curve, the mixing-cell model can be adapted to a number greater than one. It indicates that considerable turbulence appears. With growing wash ratio ($W > 3$) the particle deposition layer on wall and separation matrices decreases. This involves that dispersion and diffusion limitations increasingly effect the wash result, which further declines the slope of the wash curve.

Concluding, the wash diagrams in Fig. 9.8 show the influence of rotational sense and speed of impellers and matrices. Their comparison with theoretical models indicates that the extent of raised turbulence is responsible for the quality of the wash result. The following analysis helps to elucidate the flow distribution and behavior in more detail.

9.4.2.4 Flow Analysis and Discussion

The filter apparatus has a glass wall and the flow pattern is visible by using glass beads suspended in water. The following section confines to schematic representation of the observed flow.

Figure 9.9 depicts the visual observations of the flow in case of either impeller or matrix rotation. The main difference is that the current is either directed axially upwards or downwards. The scheme illustrates that counter clockwise rotation of impellers (I−) in Fig. 9.9a (left) produces an upwards axial current, clockwise rotation of the impellers (I+) in Fig. 9.9b (left) causes a downwards axial

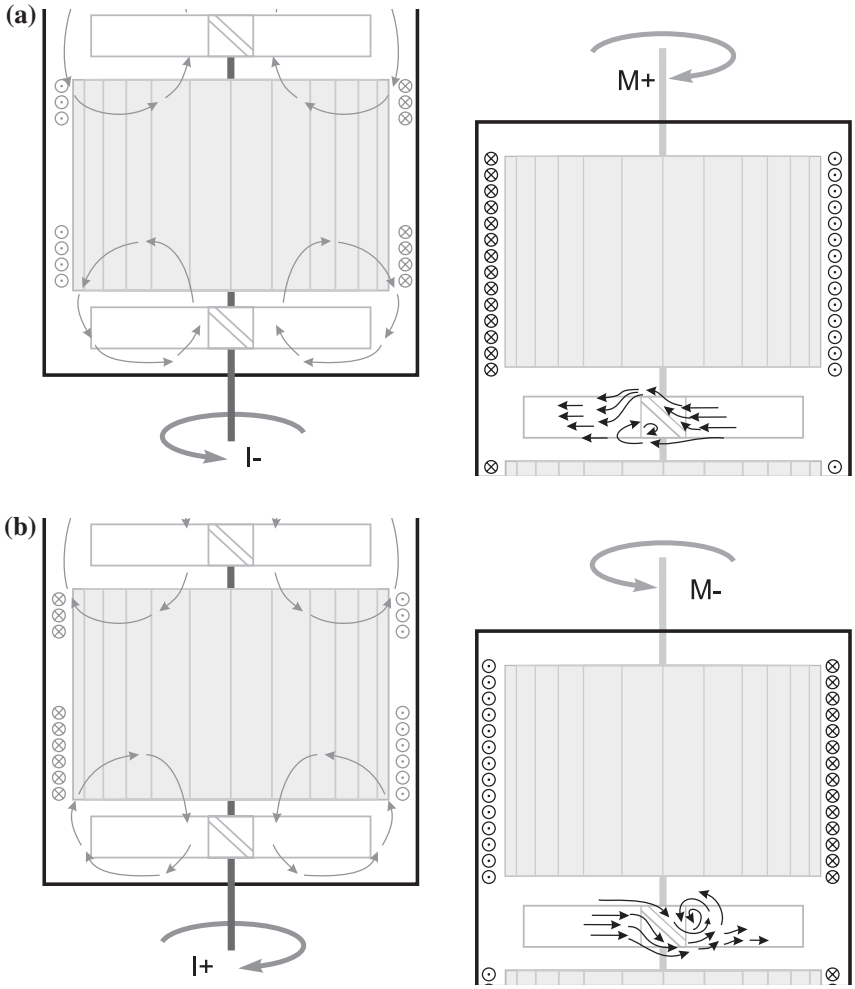

Fig. 9.9 Flow patterns of sole impeller or matrix rotation. The sense of rotation influences the axial flow direction. The inactive impellers serve as flow baffles, which induce turbulence. **a** Upwards axial current: counter clockwise impeller rotation ($I-$) or clockwise matrix rotation ($M+$). **b** Downwards axial current: clockwise impeller rotation ($I+$) or counter clockwise matrix rotation ($M-$)

current. Due to the presence of the matrix elements a tangential flow results, which is indicated by arrows pointing from and into the drawing layer. The sole matrix revolution generates mainly a tangential current. The fluid rotates and develops a spout in case of a sufficiently high rotational speed of the matrices. The inactive impellers act as baffles and induce turbulence. A clockwise rotation of the matrices (M+), see Fig. 9.9a (right)) induces that the main flow passes above the impellers, then it drops down, which induces eddies behind the blades. Hence, the axial flow points upwards. A rotation in opposite direction (counter clockwise rotation

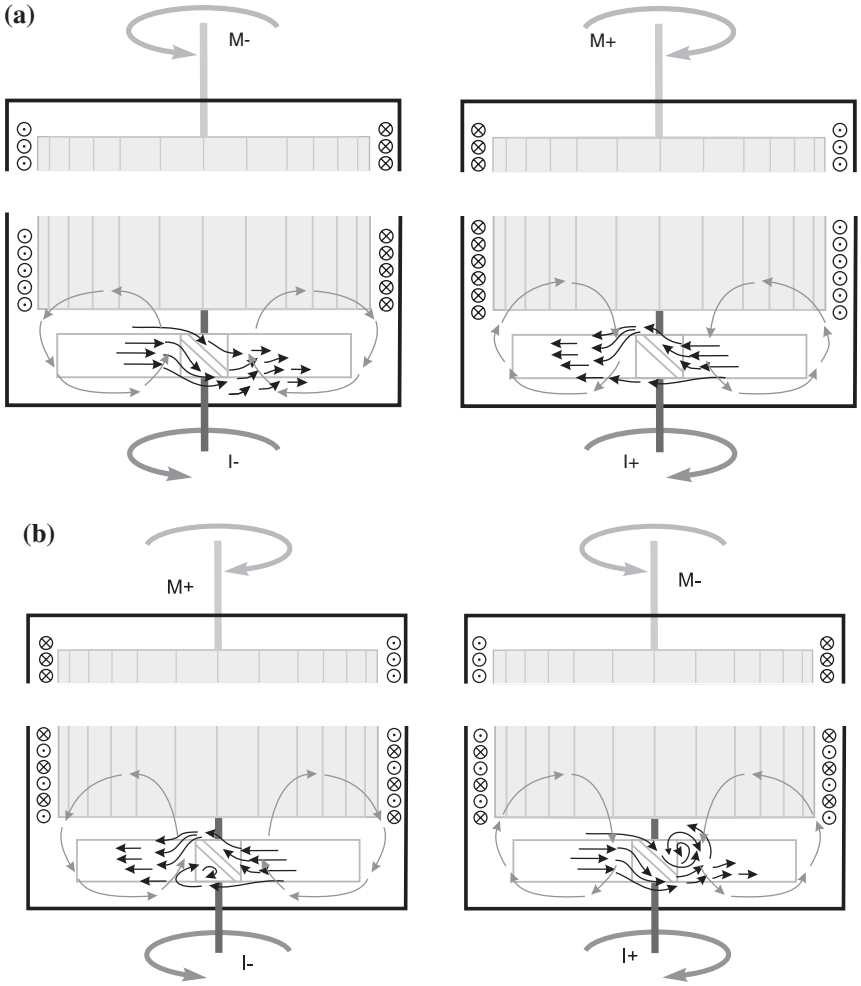

Fig. 9.10 Flow patterns of co-acting matrix and impeller rotation. **a** Concurrent rotation evokes that upwards axial flow superimposes downwards axial flow effects and vise-versa. **b** Countercurrent rotation enhances either upwards axial flow (M+/I−) or downwards axial flow (M−/I+)

of the matrices (M−), see Fig. 9.9b (right)) causes the main flow to traverse underneath the pitched blades. A turbulent reverse flow develops behind the impellers' blades and the flow pattern reveals that downwards axial current arises.

The appropriate axial flow direction depends on the particle/fluid density difference: upwards axial current (I− or M+, see Fig. 9.9a) promotes the distribution of floating particles, whereas downwards axial current (I+ or M−, see Fig. 9.9b) is most efficient for the resuspension of settling particles (Paul 2004).

Co-acting matrix and impeller rotation are subdividable into concurrent (see Fig. 9.10a) and countercurrent (see Fig. 9.10b) operation. Concurrent matrix and impeller rotation diminishes axial circulation and the fluid mainly moves radially

and tangentially. The extent of reduction depends on the relative velocity between the rotating element. If they have approximately the same rotational speed, the pitched blade impellers do not act as baffles, but accelerate the fluid spout rotation. The flow pattern exhibit less eddies which proves that the shear forces are small and the wash results are poor. In case of countercurrent rotation of impellers and matrices, see Fig. 9.10b, the baffle effect of the impellers is enhanced compared to sole matrix rotation. The increased turbulence evokes shear forces, which support the particle detachment from the matrices, and the backwashing is more successful. In both cases it applies that due to the pitched blades of the impellers, their rotational sense determines the axial current direction: Upwards axial flow arises, when impellers are turned counter clockwise whereas downwards axial flow occurs for clockwise impeller rotation.

The observations of the flow in Figs. 9.9 and 9.10 are in accordance with the experimental results in Fig. 9.8. The analysis shows that countercurrent rotation produces more turbulence than concurrent rotation and therefore is best suited for backwashing. The axial flow direction is also depicted in Fig. 9.8: The downwards directed triangle symbols stand for downwards axial flow and the upwards directed triangle symbol represents upwards axial flow. In this work, the density of the used particles exceed that of the fluid and, as expected for settling particles, downwards axial flow is more efficient that upwards axial flow.

9.5 Soy–Whey Protein Purification

Soy–whey is a side stream from soy processing that contains an important protease inhibitor, called BBI. The inhibitor is known as agent against cancer and multiples sclerosis (Fournier et al. 1998). It is a monomeric protein containing 71 amino acids in a single polypeptide chain with seven internal disulfide bonds and an isoelectric point at pH 4.2 (http://www.uniprot.org/uniprot/P01055). In SDS–PAGE[2] analysis, it appears at 12 kDa. The protein is highly stable against, e.g., high temperature and extreme pH and can be efficiently adsorbed from anion exchange resins above its isoelectric point. Conventional downstream processing is laborious and expensive as numerous process steps are required (Birk 1961) and is therefore not yet applied at large scale. This work presents the attempt to purify BBI from soy–whey with economic anion exchange magnetic particles. It proves if it is advantageous to additionally perform a treatment with washing buffer before elution in order remove residual sugar.

9.5.1 Methods

As stated in Sect. 9.4 only Orica Watercare MIEX® DOC resin were available in sufficient quantity for large-scale experiments. The Orica MIEX® DOC particles ($m_p = 110$ g) are stored in aqueous liquid that contains 20 % ethanol. SOLAE,

[2] Sodium dodecyl sulfate polyacrylamide gel electrophoresis.

Denmark kindly provided frozen natural and pretreated soy–whey (Charge: 20121022-001EE). The following section summarizes the used methods, which are applied for soy–whey protein purification.

9.5.1.1 Soy–Whey Pretreatment

The pretreatment facilitates the subsequent purification, which applies magnetic support with an anion exchange functionalization. It includes a heat conditioning at 80 °C and a removal of cationic protein components with 1 g/l LiChroprep® Si 60 resin from Merck (adsorption time is 15 min). The silica particles and precipitates are separated by decanter centrifugation. For further removal of fines and microorganisms, a subsequent filtration step (0.2 μm) is necessary. Finally, the pretreated soy–whey is preserved with Proclin®.

9.5.1.2 Process Description

The standard operating procedure (SOP) of the experiments is shown in Fig. 9.11. It depicts that at the beginning, possible residues that adhere on the particles' surface have to be eluted. Then the magnetic beads are washed and transferred to the soy–whey. In more detail, this requires the following steps:

(1) Transfer to elution buffer ($m_0 = 2$ l:20 mM Tris-HCl @pH 7.0 and 1 M NaCl).
(2) Transfer to washing buffer ($m_0 = 2$ l:20 mM Tris-HCl @pH 7.0).
(3) Transfer to pretreated soy–whey ($m_0 = 5.5$ l:$c_0 = 20$ g/l) pH adjusted to 7.0 by 2 M HCl or NaOH.

Each transfer comprises of removing the supernatant, draining of the separation cell, resuspension, and equilibration. The removal of the supernatant is done by magnetic separation. The volume flow through the magnetic filter cell is 50 l/h, which corresponds to 1.77 mm/s undisturbed flow rate. The resuspension with either washing liquid, elution buffer or soy–whey takes place within the backwashing step. Countercurrent matrix and impeller rotation (M+ 180 rpm/I− 171 rpm) is applied, which has proven to be most efficient (see Sect. 9.4.2). The wash ratio lies between 1.7 when applying 2 l of washing liquid or elution buffer and 4.5 if 5.5 l of soy–whey is used. Then, the relative residue is below 0.15 and 0.03, respectively. Afterwards, 10 min of equilibration allow the molecules to diffuse into or out of the porous Orica MIEX® DOC particle system.

The bound target protein is isolated by (multiple) elution. The chart in Fig. 9.11 depicts that it is possible to introduce a previously (multiple) treatment with washing buffer to remove residues. On completion of the purification, the particles are transferred to storage liquid and kept at 6 °C.

The system performance tests in Sect. 9.4 involved the measurement and evaluation of the values indicated as bold symbols in Fig. 9.11. In contrast, the purification experiments focus on the determination of the total protein c_{TP} and the sugar

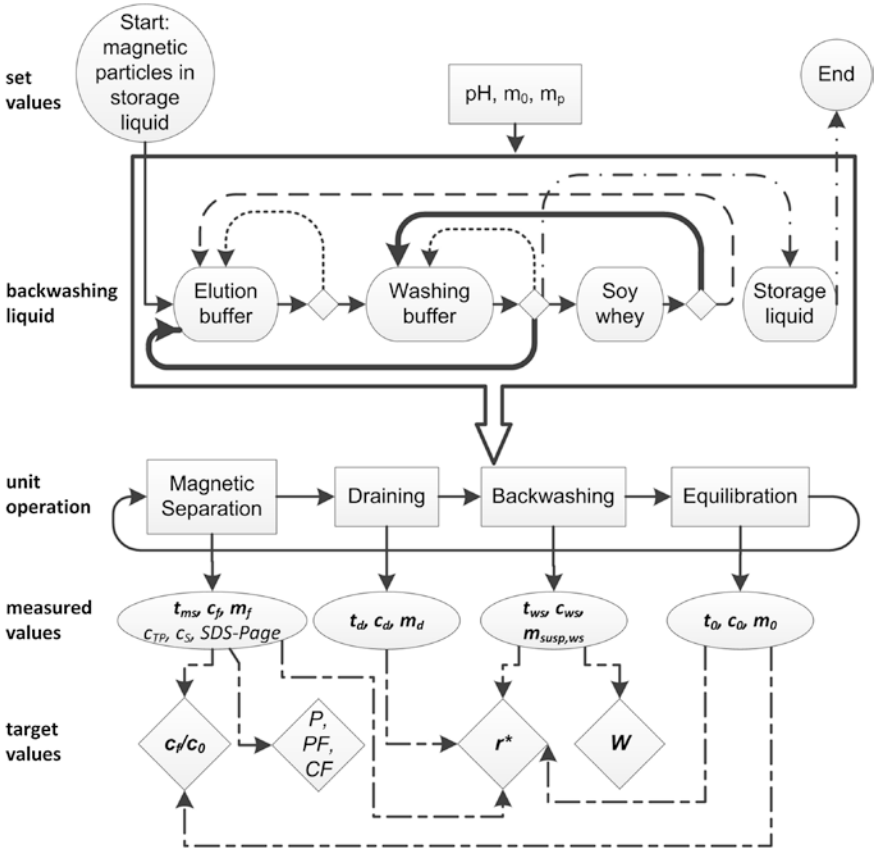

Fig. 9.11 Standard operating procedure of the experiments

content c_S as well as on target protein purity P, purification factor PF, and its concentration factor CF of the target protein SDS–PAGE. The determination of these data is described below.

9.5.1.3 Determination of Total Protein Content

The amount of total protein in each process stream is determined by a standard protein assay, namely bicinchoninic acid [2,2′-diquinolyl-4,4′-dicarboxylic acid (BCA)] assay using bovine serum albumin (BSA) (0–2 mg/mL) as a standard protein. Solved Cu(II) ions react with the proteins to Cu(I) ions, which again form a purple complex with BCA, a highly specific chromogenic reagent for Cu(I) (Biuret reaction) (Smith et al. 1985). Its absorbance maximum is at 562 nm (Ötleş 2012). The BCA kit for Protein Determination (BCA1) is supplied by Sigma-Aldrich Co. LLC.

9.5.1.4 Determination of Sugar Content

The enzymatic analysis based on photometry is appropriate to determine the amount of sugar in food with high specificity. If the sample is sufficiently diluted, the Lambert-Beer law is applicable. Soybean's sugar mainly consists of sucrose and stachyose (Hou et al. 2009). As stachyose is indigestible by humans and animals, the food and feed processing industry developed soybeans with high content of sucrose and low content of stachyose. Therefore, the analysis of stachyose is omitable and the sucrose/D-fructose/D-glucose kit (K-SUFRG) by Megazyme, Ireland is adequate. The principle is explained in the assay procedure of the manufacturer (http://secure.megazyme.com).

9.5.1.5 Monitoring the Purification Process by Sodium Dodecyl Sulfate Polyacrylamide Gel Electrophoresis (SDS–PAGE)

The analysis is performed with an electrophoresis cell unit, a precast gradient gel (4–20 %), modified Lämmli sample buffer (Roti-Load 1), prestrained 10–150 kDa marker, and analytic grade chemicals supplied by Roth GmbH, Karlsruhe, Germany. The principle is explained in the assay procedure of the manufacturer. The BBI standard, chymotrypsin-trypsin inhibitor (T9777), is supplied by Sigma-Aldrich Co. LLC.

The purity P of the target protein is determined by SDS–PAGE. The amount of a stain associated with the target band is referred to the amount of the stain associated with all the bands on the gel as proposed by Burgess (2009). The amount of stained protein equals the relevant peaks area within the densitogram. Hence, the purity is

$$P = \frac{A_{\mathrm{BBI}}}{A_t} \tag{9.18}$$

with the BBI peak area A_{BBI} and the total integral of the densitogram A_t. An ordinary office scanner captures the gel, then the image file is converted to gray scale and processed to get the densitograms. A calibration with the marker and background subtraction takes place.

The purification factor PF is given by the purity of the sample (unbound or eluate) in relation to the purity of the soy–whey (feed). If the PF is bigger than one, it expresses that purification has taken place.

The concentration factor CF describes the fraction of BBI content in the sample $c_{\mathrm{BBI},i}$ (i: unbound, washing or eluate) related to the BBI concentration of the original soy–whey $c_{\mathrm{BBI,sw}}$

$$\mathrm{CF} = \frac{c_{\mathrm{BBI},i}}{c_{\mathrm{BBI,sw}}}. \tag{9.19}$$

In order to evaluate the BBI concentration of the soy–whey, unbound and eluate samples, a calibration with the BBI standard concentration series takes place. It is

assumed that the standard is 100 % pure. The concentration of the standard solution is related to BBI target band area, which increases exponentially with the concentration. Afterwards, the content of the unknown samples (soy–whey, unbound, eluate) can be calculated.

9.5.2 Protein Purification Results and Discussion

The first purification experiment simply included adsorption and elution. The following experiments prove if it is advantageous to additionally wash the particles before the elution of the target molecules. It is investigated if a multistep washing and thereafter a multistep elution optimizes the purification result with respect to residual protein and sugar content.

9.5.2.1 Purification Without Washing

The experiment was executed according to the SOP in Fig. 9.11 using Orica MIEX® DOC particles and pretreated soy–whey. The determination of total protein concentration, sucrose content, and SDS–PAGE analysis characterizes the purification process. The results are summarized in the purification summary table (PST), see Table 9.1.

The pretreated soy–whey (5.5 l) contains 1.958 g/l of total protein, the supernatant (unbound, approx. 5.5 l) holds 0.952 g/l protein and the purified eluate (approx. 2 l) includes 1.405 g/l protein. As expected, the sugar assay showed that D-glucose and D-fructose content is below the detection limit and therefore both are omitted. The sucrose content in the pretreated soy–whey is 12.05 g/l. Although about 87 % of the sucrose content is separated with the unbound fraction, 7 % residual is measured in the eluate. The mass balance reveals that protein and sucrose are lost during the separation. It is assumed that this is due to unconsidered drained fraction and due to residue of protein and sucrose molecules, which still adhere to the magnetic particles' surface after elution.

The electrophoresis scan, see Fig. 9.12, monitors the purification process and enables the evaluation of the purity, the purification factor, and the concentration factor, which are presented in Table 9.1. It shows that the pretreated soy–whey (L1) still contains different impurities beside the target BBI at 12 kDa, e.g., the Kunitz inhibitor (KI) at 21 kDa. Due to the pretreatment, it exhibits a purity of 50 %. The unbound fraction (L2) depicts the loss of BBI and the separation of protein bigger than 30 kDa. The eluate in lane L3 still incorporates KI and residue of protein bigger than 30 kDa and its purity is 65 %, which is equivalent to a purification factor of 1.3. The eluate's concentration factor of 1.5 shows that the target protein has been concentrated. Additionally, the eluate is diluted with distilled water with ratios (1:1), (1:2), (1:4) (L4–L6). The concentration factor of L4 is halved to 0.7 and quartered to 0.4 for L5. The more the eluate is diluted, the

Table 9.1 Purification summary table with pretreated soy-whey

Step	Total protein[3] c_{TP} (g/l)	Sucrose[4] c_S (g/l)	Purity[5] P (%)	Purification factor[5] PF (-)	Concentration factor[5] CF (-)
L1: pretreated soy–whey	1.958	12.05	50	1	1
L2: unbound	0.952	10.51	30	0.6	0.5
L3: eluate	1.405	2.23	65	1.3	1.5
L4: eluate 1:1 dilution	n.d.	n.d.	64	1.3	0.7
L5: eluate 1:2 dilution	n.d.	n.d.	78	1.6	0.4
S1: BBI (0.2 g/l)	n.d.	n.d.	45	0.9	11.8
S2: BBI (0.1 g/l)	n.d.	n.d.	60	1.2	5.9
S3: BBI (0.05 g/l)	n.d.	n.d.	81	1.6	3
S4: BBI (0.025 g/l)	n.d.	n.d.	85	1.7	1.5

n.d. not determined

[3] Protein concentration determined by BCA assay using BSA (0–2 mg/ml) as a standard protein, see Sect. 9.5.1.3

[4] Sucrose content determined as described in Sect. 9.5.1.4

[5] Purity P, purification factor PF and concentration factor CF of target protein (BBI at approx. 12 kDa) measured as described in Sect. 9.5.1.5

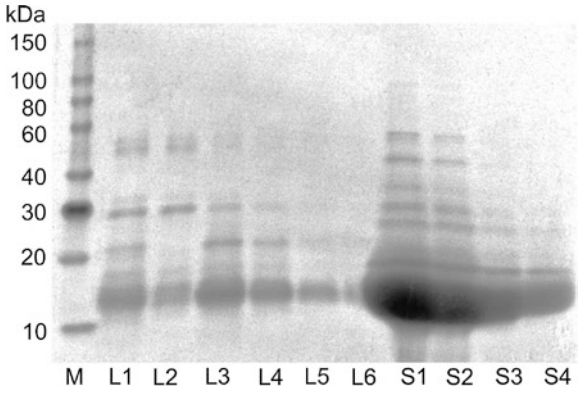

Fig. 9.12 Purification followed up by SDS–PAGE. *M* Marker, *L1* pretreated soy–whey (feed), *L2* unbound (filtrate), *L3* eluate, *L4* diluted eluate 1:1, *L5* diluted eluate 1:2, *L6* dilute eluate 1:4, *S1–S4* BBI standard in different concentrations *S1* 0.2 g/l, *S2* 0.1 g/l, *S3* 0.05 g/l, *S4* 0.025 g/l

more the apparent purity increases. It was impossible to evaluate L6 owing to the overlap of lane S1. The BBI standard exhibits residue of various other proteins, as shown in lanes S1 to S4, its purity is between 45 and 85 %. The lanes L3 and S4 both feature the same concentration factor, but the purity of the BBI standard is 20 % higher than that of the eluate.

The experiment shows that although some purification takes place, a selective separation of the protein is not possible due to the particle's nonselective surface modification. The lack of economic particles that selectively bind BBI is therefore the main obstacle of the process. Further, protein and sucrose that adhere to the particles was lost in the process.

9.5.2.2 Purification Optimization

The following experiments investigate the influence of repeatedly washing and elution. Untreated soy–whey is used as pretreated soy–whey stock had run out. The first experiment, labeled "w/o wash," is a repetition of the test in Sect. 9.5.2.1, which does not include washing and has only one elution step. The second trial "wash once" involves one washing step and three elution runs. Finally, in the third examination "wash twice" the particles are washed twice before they are eluted three times. Figure 9.13 collate the results of the three experiments. It presents the relative loss or gain of total protein and amount of sucrose of each process step in relation to the amount found in untreated soy–whey.

The unbound fraction (U) contains between 48.8 and 55.9 % of total protein and between 89.2 and 92.7 % sucrose compared to the untreated soy–whey, respectively. The eluate (E1) of the "w/o wash" experiment contains 8 % sucrose at maximum protein yield of (27.5 ± 3.1) %. Both values are in good accordance to the results in Sect. 9.5.2.1. In "wash once" and "wash twice", the total protein loss in washing step one (W1) is approx. 4 %. It further decreases in washing step two (W2) to 1.7 ± 0.04 %. At the same time, the sucrose content drops to 8 % (W1) and in case

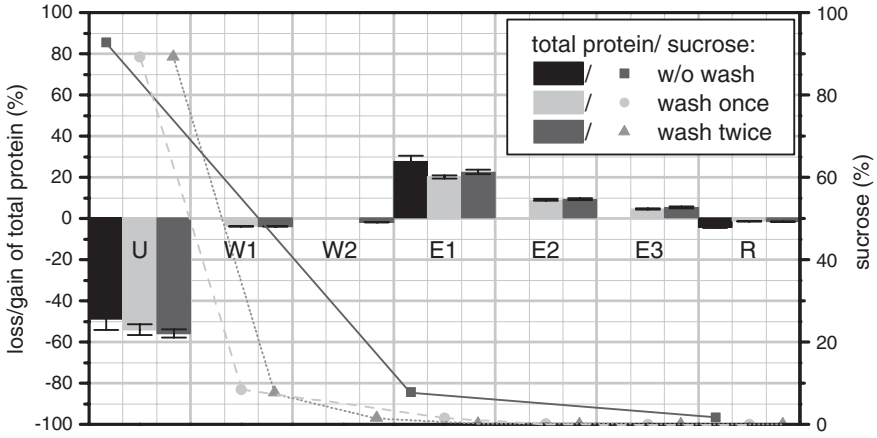

Fig. 9.13 Total protein loss or gain (BCA assay) and amount of sucrose in relation to the amount found in untreated soy–whey. *U* filtrate of magnetic separation (5.5 l unbound soy–whey), *W1/2* washing step 1 and 2 with 2 l of washing buffer each, *E1/2/3* elution step 1, 2 and 3 with 21 of elution buffer and *R* regeneration with 2 l washing buffer

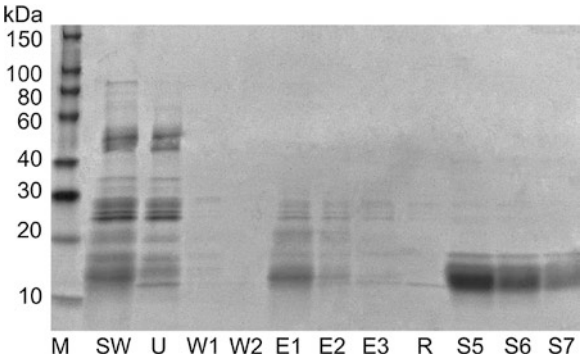

Fig. 9.14 Optimized purification, labeled as "wash twice" experiment, monitored by SDS–PAGE. *M* Marker, *SW* 5.51 untreated soy–whey (feed), *U* 5.51 of unbound soy–whey, *W1/2* washing step 1 and 2 with 21 of washing buffer each, *E1/2/3* elution step 1, 2, and 3 with 21 of elution buffer and *R* regeneration with 21 washing buffer. *S5–S7* BBI standard in different concentrations *S5* 0.02 g/l, *S6* 0.01 g/l, *S7* 0.005 g/l

of repeated washing runs to 1.5 % (W2). Thereafter, the protein content in eluate E1 exceeds 20 %, which is only slightly less than in case of the "w/o wash" experiment. The additional protein yield in elution step E2 (10 %) and E3 (5 %) compensate this initial loss, which is due to the additional washing. Moreover, the sucrose content in all eluate's fraction is minimized to less than 3 %. In the regeneration step (R) the particles are treated with washing buffer in order to charge their surface with anions and prepare them for the next binding step. The both assays showed that only marginal amount of protein and sucrose is found in the washing buffer supernatant (R). The highest total protein yield (approx. 35 %) with lowest sucrose content (less than 3 %) is achieved when the process includes two washing steps and three elution steps as in the "wash twice" experiment. The results show the positive effect of washing before the elution. The sugar is removed, however some protein is lost.

The "wash twice" experiment was analyzed in more detail performing a SDS–PAGE. Figure 9.14 shows the stained gel and the purification summary table in Table 9.2 condenses the results of total protein and sucrose analysis as well as the BBI purity and concentration evaluation. The natural soy–whey (SW) lane exhibits BBI at 12 kDa and a lot of stained protein peaks up to 100 kDa. Its BBI purity is 33 %, which is 17 % less than the pretreated soy–whey. The unbound (U) lane incorporates the proteins that did not adsorb to the Orica MIEX® DOC particles' surface. It contains most of the impurities of the soy–whey, therefore its purity is only 23 %. At the same time, the low intensity of the BBI band indicates that the target protein especially has been bound to the particles. The lanes W1 and W2 confirm that only a marginal amount of protein is lost due to the additionally performed washing runs. The analysis of the densitogram showed that the stained bands W1 and W2 vanish within the gel background intensity and they are therefore below the detection limit. The elution lane E1 indicates that the BBI peak almost has the same intensity than in the SW lane. The protein bands are

Table 9.2 Purification summary table (PST) with untreated soy–whey of the experiment "wash twice"

Step	Total protein[3] c_{TP} (g/l)	Sucrose[4] c_S (g/l)	Purity[5] P (%)	Purification factor[5] PF (−)	Concentration factor[5] CF (−)
SW: untreated soy–whey	2.7 ± 1.6 %	4.8	33	1	1
U: unbound	1.5 ± 3.3 %	4.4	23	0.7	0.5
W1: wash 1	0.3 ± 4.3 %	1	b.d.l.	–	–
W2: wash 2	0.1 ± 1.4 %	0.2	b.d.l.	–	–
E1: eluate 1	1.6 ± 4.3 %	0.02	55	1.7	0.8
E2: eluate 2	0.7 ± 4.3 %	b.d.l.	55	1.7	0.4
E3: eluate 3	0.4 ± 10.0 %	b.d.l.	33	1	0.3
R: regeneration	0.1 ± 0.9 %	b.d.l.	b.d.l.	–	–
S5: BBI (0.02 g/l)	n.d.	n.d.	81	2.5	1.7
S6: BBI (0.01 g/l)	n.d.	n.d.	95	2.9	1.3
S7: BBI (0.005 g/l)	n.d.	n.d.	95	2.9	0.8

n.d. not determined
b.d.l. below detection limit

visible up to 30 kDa, though less intense than in the natural soy–whey lane, and those larger than 30 kDa disappear completely. The eluate (E1) exhibits a purity of 55 %, which corresponds to 1.7 fold purification. The concentration factor is 0.8, which means that dilution takes place. This issue has to be addressed and optimized in further work. In E2 the intensity of the stained bands decreases, but BBI is still the most intensive band with same purity that E1, but the concentration factor is halved. Elution E3 and regeneration R only contain sparse stained protein bands. The BBI standard lines S5, S6, and S7 are a concentration series of 0.02, 0.01, and 0.005 g/l. The chosen dilutions are more appropriate than those in the first trial, see Fig. 9.12. The residual bands bigger than 20 kDa disappear almost completely and the apparent purity is larger 80 %. The intensity of the BBI band in S7 is in the same range than that in SW and E1 lanes, which proves that the concentration of BBI in those streams is about 0.005 g/l.

The untreated soy–whey shows 2.7 g/l of total protein and the sucrose concentration is 4.8 g/l. In the first cycle, the supernatant (unbound) holds 1.5 g/l protein and 4.4 g/l sucrose. The total protein analysis confirms the SDS–PAGE results, which stated that the protein loss due to washing is low. At the same time, the sucrose content is significantly reduced. The purified eluate (E1) contains 0.02 g/l sucrose, which is only 2 % of the amount that would be present if washing is omitted. In eluate E2 and E3 as well as in the regeneration supernatant (R) it is below the detection limit. Further, the total protein content in eluate E1 is 1.6 g/l and decreases to 0.7 g/l in E2 and 0.4 g/l in E3. The separated regeneration liquid hold 0.4 g/l total protein.

The process shows that a multistep elution increases the yield and the residual sucrose amount is removable before elution by additionally performing one or two washing steps. The results draw the conclusion that the pretreatment of soy–whey as proposed in Sect. 9.5.1.1 might be omitted. The application of ion-exchange magnetic particles (e.g., Orica MIEX® DOC) can serve as a pretreatment of the natural soy–whey. Thereafter, it is necessary to use more selective magnetic carrier particles (e.g., by a BBI-antibody functionalization) for further polishing of the target protein, which enhance the purity and the concentration factor.

9.6 Conclusion

The chapter analyzes the performance of the new pilot scale HGMS filter that is equipped with a rotatable matrices and impellers regarding its separation efficiency and backwashing characteristics. Its application for protein purification was successful. However, a selective separation of BBI is not possible with anion exchange magnetic particles. The lack of economic particles that selectively bind BBI is therefore the main obstacle of the process. Both the permanent magnet and the separation cell of the new design exhibit favorable characteristics to promote the principle for large-scale separation processes in industry. First, they both are easily scalable or parallelizable. Second, they exhibit a reasonable investment, and operational costs are low because no power supply is required for the magnet. The field corresponds to that of conventional magnet systems and more than sufficient for HGMS. Third, the separation unit is very compact and light as compared to conventional permanent magnets or electromagnet devices.

Acknowledgments This work has been carried out during the EU project "MagPro^{2}Life" at the Institute of Mechanical Process Engineering and Mechanics (MVM), Karlsruhe Institute of Technology (KIT). The authors owe special thanks for EU by Helmut Soltner (Forschungszentrum Jülich GmbH, Central Institute of Engineering, Electronics and Analytics (ZEA-1)) funding under contract FP7-NMP, 229335. We would like to acknowledge the helpful advises and material supply by Christian F. Nielson and Niels Daalgard (Solae LLC). Anja Pauls (Institute of Functional Interfaces, KIT), Johannes Lindner and Ellen Hildebrand (both MVM, KIT) supported the SDS–PAGE analysis. The design and construction of the magnet as well as the separation cell was mainly assisted by Hans Guigas and Thomas Reutter (MVM, KIT).

References

All FEM calculations were performed with the AC/DC module of the COMSOL Multiphysics. www.comsol.com (COMSOL 4.3 a)

Becker J, Thomas O, Franzreb M (2009) Protein Separation with magnetic adsorbents in micellar Aqueous Two-Phase Systems. Sep Purif Technol 65:46–53. doi:10.1016/j.seppur.2008.05.017

Birk Y (1961) Purification and some properties of a highly active inhibitor of trypsin and α-chymotrypsin from soybeans. Biochim Biophys Acta 54(2):378–381. doi:10.1016/0006-3002(61)90387-0

Burgess R (2009) Preparing a purification summary table. Methods Enzymol 463:29–34. doi:10.1016/S0076-6879(09)63004-4

Foster I, Millington R, Grew R (1992) The impact of particle size controls on stream turbidity measurement; some implications for suspended sediment yield estimation. In: Erosion and sediment transport monitoring programmes in river basins: proceedings of the Oslo symposium, vol 210, pp 51–62

Fournier D, Erdman J Jr, Gordon G (1998) Soy, its components, and cancer prevention: a review of the in vitro, animal, and human data. Cancer Epidemiol Biomarkers Prev 7(11):1055–1065

Gerber R, Birss R (1983) High gradient magnetic separation. Research Studies Press, chichester

Hou A, Chen P, Alloatti J, Li D, Mozzoni L, Zhang B, Shi A (2009) Genetic variability of seed sugar content in worldwide soybean germplasm collections. Crop Sci 49(3):903–912. doi:10.2135/cropsci2008.05.0256

Kaeppler T, Cerff M, Ottow K, Hobley T, Posten C (2009) In situ magnetic separation for extracellular protein production. Biotechnol Bioeng 102(2):535–545. doi:10.1002/bit.22064

Levenspiel O (1999) Chemical reaction engineering, 3rd edn. Wiley, New York

Lewis J (1996) Turbidity-controlled suspended sediment sampling for runoff-event load estimation. Water Resour Res 32(7):2299–2310. doi:10.1029/96WR00991

Lindner J, Wagner K, Eichholz C, Nirschl H (2010) Efficiency optimization and prediction in high-gradient magnetic centrifugation. Chem Eng Technol 33(8):1315–1320. doi:10.1002/ceat.201000112

Megazyme International Ireland (2012) Sucrose, D-fructose and D-glucose assay procedure (K-SUFRG). http://secure.megazyme.com. Accessed 29 Sep 2013 (Archived by Website at http://www.webcitation.org/6K010V8xJ)

Menzel K, Windt CW, Lindner JA, Michel A, Nirschl H (2013) Dipolar openable Halbach magnet design for High-Gradient Magnetic Filtration. Sep Purif Technol 105:114–120. doi:10.1016/j.seppur.2012.12.019

Menzel K, Lindner JA, Soltner H, Nirschl H (2014) Design and application of a longitudinal field Aubert magnet composed of identically shaped blocks for large-scale magnetic separation, submitted to Sep Purif Technol in June 2014 (to be published)

Ötleş S (ed) (2012) Methods of analysis of food components and additives, 2nd edn. Chemical & functional properties of food components. Taylor & Francis, Boca Raton

Paul EL (ed) (2004) Handbook of industrial mixing: science and practice. Wiley-Interscience, Hoboken

Raich H, Blümler P (2004) Design and construction of a dipolar Halbach array with a homogeneous field from identical bar magnets: NMR mandhalas. Concepts Magn Reson Part B Magn Reson Eng 23(1):16–25. doi:10.1002/cmr.b.20018

Ruslim F (2008) Flow phenomena in cake washing driven by mass forces. Ph.D. thesis, University of Karlsruhe, Germany, ISBN 978-3-86727-788-4

Ruslim F, Hoffner B, Nirschl H, Stahl W (2009) Evaluation of pathways for washing soluble solids. Chem Eng Res Des 87(8):1075–1084. doi:10.1016/j.cherd.2009.01.007

Smith P, Krohn R, Hermanson G, Mallia A, Gartner F, Provenzano M, Fujimoto E, Goeke N, Olson B, Klenk D (1985) Measurement of protein using bicinchoninic acid. Anal Biochem 150(1):76–85. doi:10.1016/0003-2697(85)90442-7

Soltner H, Blümler P (2010) Dipolar Halbach magnet stacks made from identically shaped permanent magnets for magnetic resonance. Concepts Magn Reson Part A Bridg Educ Res 36(4):211–222. doi:10.1002/cmr.a.20165

UniProt: the Universal Protein Resource (2013) Bowman-Birk type proteinase inhibitor. http://www.uniprot.org/uniprot/P01055. Accessed 12 Mar 2013 (Archived by WebCite at http://www.webcitation.org/6F3xoKJ7j)

Windt CW, Soltner H, Dusschoten DV, Blümler P (2011) A portable Halbach magnet that can be opened and closed without force: The NMR-CUFF. J Magn Reson 208(1):27–33. doi:10.1016/j.jmr.2010.09.020

Chapter 10
Continuous Magnetic Extraction for Protein Purification

Anja Paulus and Matthias Franzreb

Abstract Continuous Magnetic Extraction (CME) is a process for the separation and purification of proteins from crude feedstocks. Magnetic particles with functional surface groups, e.g., ion exchange ligands, serve as carriers for the target protein. Together with a mixture of thermoresponsive surfactants and binding buffer these carriers are added to the feed containing the target protein. After binding the target within minutes, the mixture is heated above the LCST of the surfactant and phase separation is induced. Through selective partitioning of the carrier particles to the top phase and partitioning of contaminants to the bottom phase of the system, purification is possible. The proof-of-concept of this bioseparation process has been recently released, and new devices for CME have been developed within the framework of the EU project MagPro^{2}Life and the respective results are reported in this chapter. Several particle types and feed streams, representing a broad field of potential applications, were tested with regard to their suitability for the CME process.

Abbreviations

AMTPS	Aqueous Micellar Two-Phase Systems
ATPS	Aqueous Two-Phase Systems
CME	Continuous Magnetic Extraction
DEAP	Diethylaminopropyl groups
LCST	Lower Critical Solution Temperature
MEP	Magnetic Extraction Phases

A. Paulus (✉) · M. Franzreb
Institute of Functional Interfaces (IFG), Karlsruhe Institute of Technology,
Hermann-Von-Helmholtz-Platz 1, 76344 Eggenstein-Leopoldshafen, Germany
e-mail: anja.paulus@kit.edu

H. Nirschl and K. Keller (eds.), *Upscaling of Bio-Nano-Processes*,
Lecture Notes in Bioengineering, DOI 10.1007/978-3-662-43899-2_10

10.1 Introduction to the Principle of CME

While the wide majority of magnetic separation processes are discontinuous or semi-continuous, it was our aim to design, characterize, and examine a continuous magnetic separation process for the purification of proteins. The method of choice was named Continuous Magnetic Extraction (CME) and makes use of a development known as magnetic extraction phases (MEP, Becker et al. 2009). MEP are the combination of Aqueous Micellar Two-Phase Systems (AMTPS) and functionalized magnetic (nano-) particles. AMTPS are formed by a mixture of thermoresponsive surfactant and water (usually added as feed stream or buffer) and form a single phase below a certain temperature (lower critical solution temperature, LCST). When the temperature is increased above the LCST, the system splits into two phases: a surfactant-rich phase and a surfactant-depleted phase. In an ideal CME system, all particles are drawn to the surfactant rich top phase where they serve as carriers for the target protein by offering specific binding sites (ion exchangers, affinity ligands, etc.). All proteins except for the target protein, which is attached to the magnetic particles, partition to the surfactant-depleted bottom phase.

The CME process is made up of three consecutive steps, namely adsorption, wash, and elution. A fourth step for the regeneration of the particles can be integrated after the elution. A schematic overview of these steps is given in Fig. 10.1.

In the first step, the pH-adjusted feed stream is mixed with the magnetic adsorbents and the surfactant at a temperature below the LCST. The adsorption of the target protein to the magnetic carrier takes place in this single phase

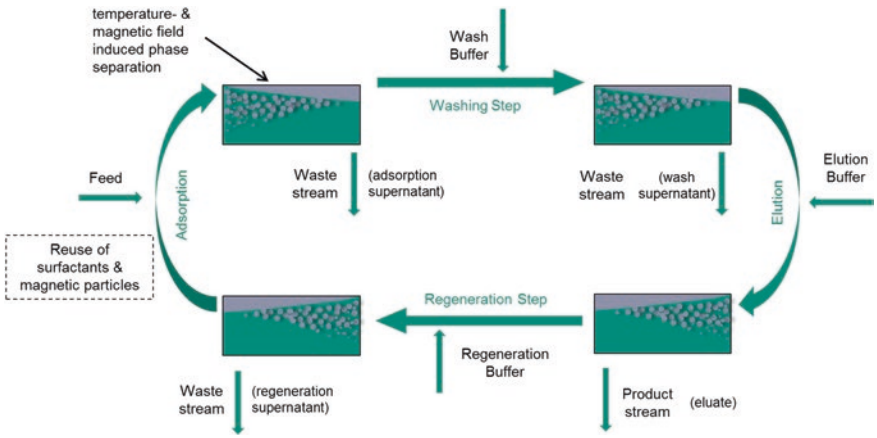

Fig. 10.1 Schematic illustration of a four-stage CME process with adsorption, wash, elution, and regeneration steps: Between the steps the temperature is lowered to allow adsorption/desorption processes in single phase state, while in the flow-through chambers temperature-and magnetic field-induced phase separation takes place

state. Afterwards, the stream is preheated and fed into the separation device. The device contains a large permanent magnet which accelerates phase separation by drawing particles to the top. It is insulated and heated to maintain a temperature above the LCST. Inside the separation device a simple flow-through chamber is located in which the system splits into two immiscible phases, which are collected through separate outlets. While the bottom phase contains the depleted feed stream together with little surfactant and no particles, the top phase has a high surfactant and particle concentration. The bottom phase is discarded, while the top phase is mixed with wash buffer at a low temperature to remove unwanted impurities from the particles. The suspension is heated again, and the phases separate. The bottom phase is discarded and the top phase is mixed with elution buffer at low temperature. The stream is heated, the system splits into two phases, and the eluted protein is withdrawn in the bottom phase. The top phase can be regenerated or equilibrated (e.g., with high/low salt buffers) and is reused in another cycle.

10.2 Theory of CME

The components forming the magnetic extraction phases are presented here, while process equipment necessary for continuous phase separation is introduced in Sect. 10.3. Aqueous Two Phase Systems (ATPS, Albertsson 1977, 1978) which consist of polymer/salt mixtures or two polymers in water are well-known in the field of biotechnology, where they are used for protein purification (Hatti-Kaul 2000). ATPS make use of the fact that one of the phases is more hydrophobic whereas the other is hydrophilic. This leads to a distribution of proteins depending on their hydrophobicity and enables the separation of hydrophilic proteins from hydrophobic proteins, such as membrane proteins. The partitioning of a protein is described by the partition coefficient K_p, with $c_{p,\,top}$ and $c_{p,\,bottom}$ being the concentration of the protein in the top and bottom phase, respectively:

$$K_p = \frac{c_{p,top}}{c_{p,bottom}} \tag{10.1}$$

Mild conditions (aqueous environment) and easy scale-up make ATPS fit for use as a purification technique for biological components. However, ATPS have several drawbacks, e.g., long phase separation times, high buffer consumption with no or little possibility for phase recycling, and dependency on partition coefficients of both the target molecule and impurities. In order to overcome these disadvantages, several variations have been proposed in the past. The effect of faster phase separation times through addition of magnetic particles was examined by Wikström et al. (1987). The so-called affinity partitioning was proposed in order to create systems with higher selectivity, without the limitation of separating only hydrophobic from hydrophilic proteins. The method involves modification of one phase forming polymer with ligands binding the target molecule, thus optimizing partitioning coefficients (Johansson and Tjerneld 1989; Johansson 1985; Walter and Johansson 1986).

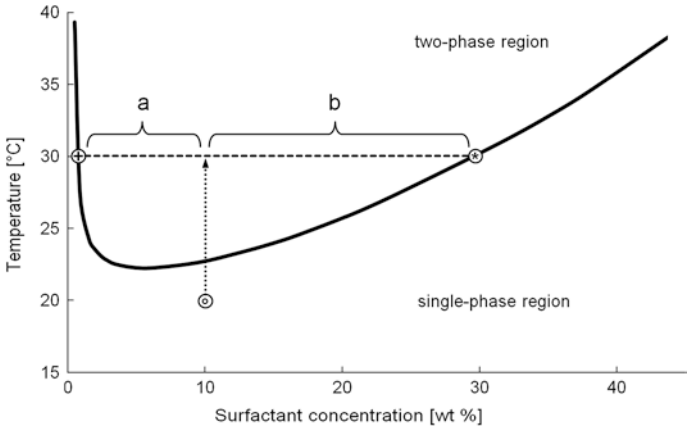

Fig. 10.2 Exemplary phase diagram with coexistence curve of the nonionic surfactant Eumulgin ES. A sample with a concentration of 10 % surfactant ('°') is heated so that the system splits into a surfactant rich ('*') and surfactant-depleted phase ('+')

Unlike ATPS, Aqueous Micellar Two Phase Systems (AMTPS) consist only of one thermoresponsive polymer and water /buffer (Fischer et al. 2012). Phase separation is induced by a temperature change and is fully reversible: Below a temperature known as the Lower Critical Solution Temperature (LCST) of the thermoresponsive polymer one homogenous phase exists. A temperature increase above the LCST will lead to a formation of two immiscible phases, the disperse phase containing a high polymer concentration and the continuous phase containing only about 1 % (wt) of polymer. The disperse phase is formed by small droplets (micelles) that coalesce into bigger droplets, which finally form the top phase of the system. Phase switching behavior of thermoresponsive polymers intended for bioseparation purposes occurs in a moderate temperature range between ~15 and 35 °C, where protein denaturation does not take place. The polymer used in the CME trials is a thermoresponsive surfactant (trade name Eumulgin ES) with a LCST of around 25 °C.

The phase behavior is best described by the coexistence curve in a temperature-surfactant concentration diagram (Fig. 10.2). The coexistence curve divides the area of the two-phase system from the single-phase region.

When an exemplary sample with a surfactant concentration of 10 % (marked with '°' in the graph) is heated from 20 to 30 °C, the sample will split into two phases: one surfactant rich phase ('*') and a surfactant-depleted, bottom phase ('+'). The phase volume ratio r_V of the two phases can be obtained by applying the lever rule. The volume of the top phase therefore is:

$$V_{top} = \frac{a}{a+b} * V_{total} \quad with \quad r_{V,t} = \frac{a}{a+b} \tag{10.2}$$

and a and b being the share of the tie line left and right of the intersection point, respectively. Accordingly, the volume of the bottom phase can be defined as:

$$V_{bottom} = \frac{b}{a+b} * V_{total} \quad with \quad r_{V,b} = \frac{b}{a+b} \tag{10.3}$$

The separation of phases is accelerated by magnetic (nano-) particles added to the AMTPS when a magnetic field is applied. In addition, magnetic particles offer binding sites or specific ligands to serve as carriers for target molecules. In the single phase state, the particles have to be dispersed completely, so that adsorption and desorption processes can take place unrestricted. This is given when the particles are superparamagnetic, which means that they have no remanent magnetization, i.e. they are no longer magnetized when no magnetic field is applied.

Apart from the requirements mentioned above (binding sites for interaction, superparamagnetic behavior for good redispersibility), the use of particles in the CME process depends on their partitioning behavior in AMTPS. Therefore, the combination of particles and AMTPS and its importance for the CME process is discussed in the following section.

10.2.1 Combination of Particles and AMTPS

The partitioning of both proteins and particles is crucial to the CME process. While protein partitioning is mostly dependent on the hydrophobicity and can be determined experimentally or theoretically using thermodynamic models (Nikas et al. 1992), particle partitioning behavior depends on a number of factors. It was recently found that the partitioning of micro- and nanoparticles in AMTPS can be pH-dependent (Fischer and Franzreb 2012). While some particles partition to the top phase at all pH-levels and others partition only to the bottom phase, there are certain particles where the partitioning behavior changes with pH. Figure 10.3 shows an example of micro particles that partition to the top phase at low pH-values and to the bottom phase at a higher pH. For these particles the transition between phases takes place between pH 4.5 and 4.6.

As can be seen in the pictures the particles partition completely in one phase at a given pH whereas a pH change of only 0.1 is enough to switch the phase partitioning behavior completely. In the CME process, it is necessary that particles partition to the top phase of the AMTPS in which they can be separated from the bottom phase, leading to a purification of the target protein. Therefore, particles and AMTPS systems have to be chosen carefully beforehand to find suitable conditions. A number of particles have been successfully tested in the CME devices (see Table 10.1).

10.2.1.1 Separation Efficiency

One of the main criteria for the determination of CME process quality is the particle separation efficiency of the used magnetic separator. In case of CME, it is

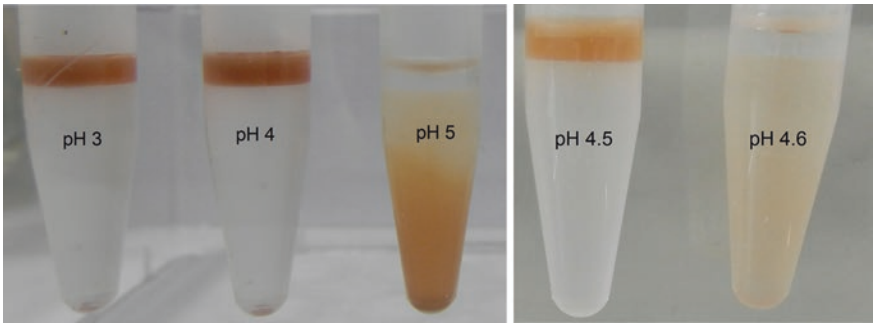

Fig. 10.3 pH-dependent partitioning behavior of magnetic particles (chemagen M-PVA C22) in AMTPS. Parameters: Surfactant concentration 10 % (wt), 30 °C (two-phase state) and varying pH values with a particle concentration of 0.5 g/l (*left*) and 0.2 g/l (*right*), respectively. Particles used have a mean size of 2 µm; no magnetic field was applied in this trial

Table 10.1 Particle types used in CME pilot trials, partial extract from (Fischer et al. 2013)

Particle type	Size (nm)	Functionalization	Flow rate (l/h)	Separation efficiency (%)
Mag Prep Silica (Merck)	25	–	5	>95 %
Mag Prep Silica (Merck)	100	SO_3	5	>99 %
p(NIPA-AAc) with embedded magnetite nanoparticles (NIIMT, Socoliuc et al. 2013)	200	Acrylic acid	9	>99 %
M-PVA 012 (Chemagen)	2,000	DEAP	9	>99 %
MIEX DOC (Orica)	200,000	Quaternary amine	72	98 %

defined by the particle concentration and flow rate in the feed stream and top outlet and is described by the following equation:

$$E = \frac{c_{top\,outlet} * \dot{V}_{top\,outlet}}{c_{feed} * \dot{V}_{feed}} * 100\% \tag{10.4}$$

As the particle concentration in the feed and the top outlet cannot easily be measured in-line, the mass of dried particles in the bottom outlet was determined gravimetrically. If the starting mass of particles in the feed of a given trial volume is known, the separation efficiency can be calculated as follows:

$$E = 100\% - \frac{m_{bottom\,outlet}}{m_{feed}} * 100\% \tag{10.5}$$

High separation efficiencies correspond to low particle loss and high product purity concerning contamination with particle traces. It is essential that only very few particles are lost in the bottom phase due to a number of reasons. Particles in the bottom phase are excluded from the recycling loop and have to be replaced,

which leads to an overall increase in costs. Furthermore, target protein attached to the particles in the bottom phase may be lost. Additional costs result from the removal of unwanted particle traces from product and/or waste streams.

Several particle kinds were tested in the CME setup, ranging from nanometer to micrometer scale. The separation efficiency results for the particles are shown in Table 10.1.

The separation efficiency trials were carried out in a 10 % surfactant system. The very large Orica particles were used without surfactant, to show that the CME device can also be used as a continuous magnetic separator without a two-phase system. The results of a simple magnetic separation trial using these particles can be found at the end of the next chapter.

10.3 CME-Setup and Operation

The Continuous Magnetic Extraction (CME) device is a simple arrangement, made up of a temperature-insulated case, a flow-through separator located below a permanent magnet, and a small fan heater (see Fig. 10.4). Peripheral devices include collection containers, a large-stirred double-jacketed reactor, a glass tube heat exchanger, and several peristaltic pumps for fluid transport. It is easily assembled and has low setup and maintenance costs. The process is energy saving and cheap due to the use of permanent magnets that do not need electricity or additional (water) cooling.

A first prototype of the CME separation chamber was made of glass and PVC and had a separation volume of 3 l. The glass reactor offered a view of the partitioning behavior and phase separation. Later, a stainless steel version (Fig. 10.5) was designed, with the advantage that it is easy to clean and assemble, due to a detachable cover.

The flow through the system is regulated by the peristaltic pumps of the inlet and bottom outlet, while the top outlet is merely drained into a collection container from which the liquid is pumped out. For the continuous process, the phase volume ratio r_V (see Eqs. 10.2 and 10.3) must be equal to the ratio of the volumetric flows in the top and bottom effluent. The optimum flow rate depends on the phase separation time of the AMTPS and is determined by the temperature, surfactant concentration, as well as the particle size and concentration. It is set in a way that the phases are separated to the largest extent possible, with complete collection of the top phase through the top outlet. This way no part of the top phase (particles and the majority of surfactant) is lost in the bottom outlet and only an insignificant amount of bottom phase is collected with the top phase.

Before real feed streams were processed, the setup was tested with regard to the capability for continuous operation. A trial with a flow rate of 9 l/h, a particle concentration of 2 g/l and surfactant concentration of 10 % in the feed was carried out at a constant temperature of 30 °C (Fischer et al. 2013). As particles, poly(NIPA-AAc) gels with embedded magnetite nanoparticles were used (Table 10.1). The phases were

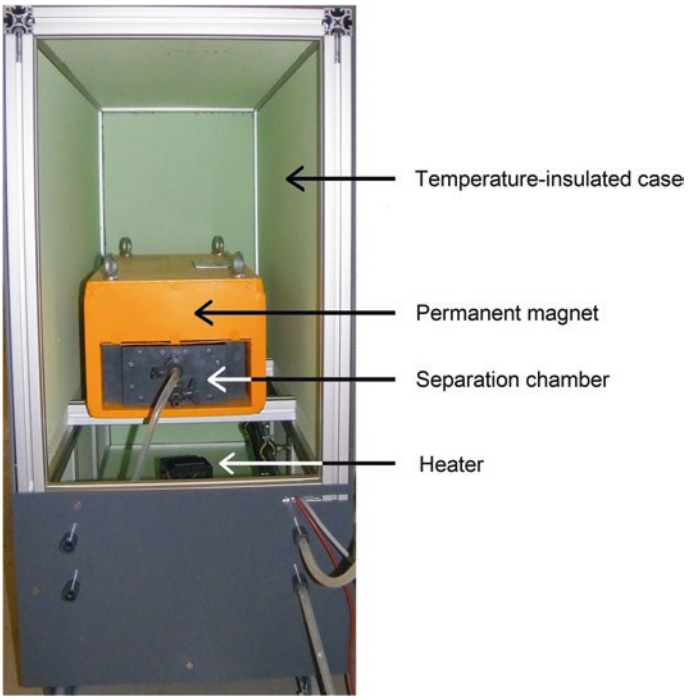

Fig. 10.4 Pilot plant separator setup with surrounding devices: separation chamber, permanent magnet, fan heater, and temperature-insulated case

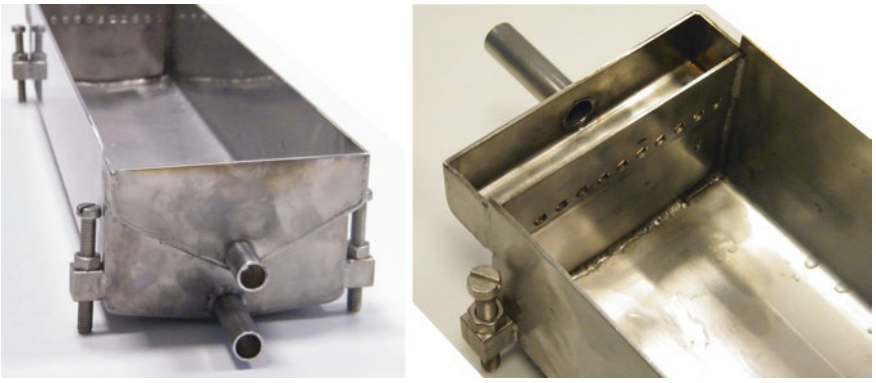

Fig. 10.5 Nonmagnetic stainless steel separation chamber with adjustable feet (*left*), inlet geometry (*right*) and outlet geometry with two outlets for *top* and *bottom* phase (*left*)

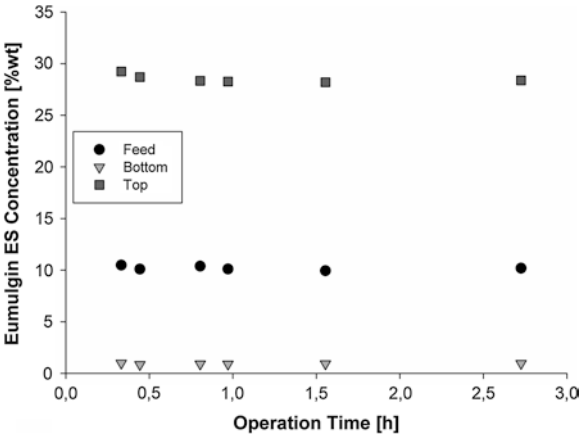

Fig. 10.6 Surfactant concentration in the feed stream, top and bottom outlet over time: Trial conducted with a flow rate of 9 l/h and an initial surfactant concentration of 10 % in the feed stream, particle type p(NIPA-AAc) with embedded magnetite nanoparticles at a concentration of 2 g/l, from (Fischer et al. 2013)

recycled to minimize material usage: the top and bottom phases were fed back into the stirred reactor from where the mixed suspension was reinjected into the separation chamber. As a measure for successful continuous operation, two important process parameters were monitored over the operation time of several hours.

Figure 10.6 shows the surfactant concentration in feed, and top and bottom outlet, determined by potentiometric titration as described in Fischer and Franzreb (2011). According to the phase diagram (Fig. 10.2), the concentration in the top phase of an AMTPS with a starting concentration of 10 % surfactant at 30 °C is around 30 %, while the bottom phase concentration decreases to about 1 %.

This is also true for the samples collected from the separation trial (as plotted above) where the top phase samples contain around 30 % of surfactant, and the bottom phase samples ~1 %. The concentrations are constant over the time interval.

Figure 10.7 shows the particle concentration in the feed, top and bottom outlet. The concentrations were determined gravimetrically, meaning magnetic particles in the sample volumes taken at different times were separated from the solution, washed, dried and weight.

As can be seen in the graph the particle concentration in the top phase is about three times higher than the feed concentration, with a relatively constant value of 6–7 g/l. The particle concentration in the bottom outlet is very low in all samples. The phase ratio of top phase to total volume at this surfactant concentration and temperature is around 1:3 (see Sect. 10.2, Fig. 10.2), leading to a concentration of particles in the top phase by a factor of about three. This proves that particles are continuously separated and accumulate in the top phase of the system where they serve as carriers for biomolecules. It can furthermore be assumed that the process parameters stay within the range they have been adjusted to. This demonstrates that particles do not accumulate in the CME, like in semi-continuous separators like HGMF (High Gradient Magnetic Separator), but that CME works as a truly continuous separator. Apart from the particle concentration determination above, this was proven by an additional set of trials that took place *without* surfactant. In these trials, large microparticles (Orica, see Table 10.1) were processed and the

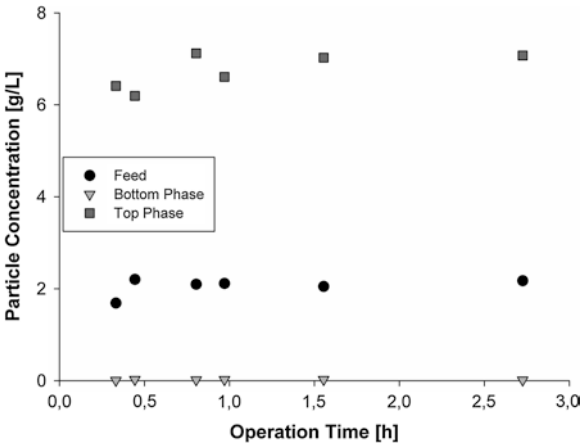

Fig. 10.7 Particle concentration in the feed stream, *top* and *bottom* outlet over time: Trial conducted with a flow rate of 9 l/h and an initial surfactant concentration of 10 % in the feed stream, particle type p(NIPA-AAc) with embedded magnetite nanoparticles at a concentration of 2 g/l, from (Fischer et al. 2013)

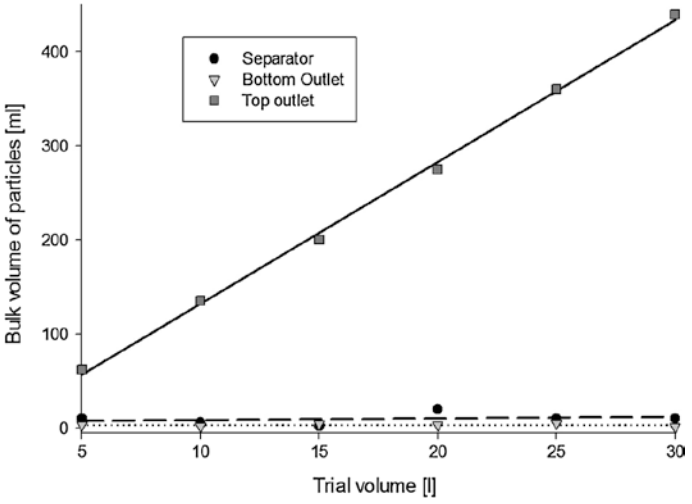

Fig. 10.8 CME trial to test accumulation of particles in the separation chamber: Comparison of six trial volumes. For each the particle, bulk volume in *top* and *bottom* phase and in the separator is given

CME device was used as a magnetic separator only. The particle concentration in the feed stream was kept constant at 2 g/l, while the trial volume was varied between 5 and 30 l. The bulk volume of particles in the top outlet, bottom outlet, and in the separator was recorded each time (Fig. 10.8).

The amount of particles lost in the bottom outlet stays approximately the same for all trials (dashed line), and is therefore independent of the processed volume.

The bulk volume of particles in the top outlet increases linearly (solid line, $R^2 = 99.8$ %) with the trial volume as expected.

After each run, the separation chamber was removed from the setup and the particles left inside were collected. The amount of particles that are not discharged is constant (dotted line) and results from the drainage during emptying of the separator after the run. This means that for large trial volumes and continuous operation only a very small, insignificant proportion of particles is lost in the bottom outlet and separation chamber.

10.4 Application of the CME Process

The CME process was used with a combination of various particles (Table 10.1) and different feed systems. *E.coli* fermentation broths have been processed to capture and purify a recombinant human antibody fragment (Fab), which binds a tumor-associated antigen on human colorectal carcinoma. In the Fab purification process, an adsorption, wash, and elution step was carried out and yielded a product purity of up to 98 % and a total yield of up to 67 % (Fischer et al. 2013).

In other trials, soy whey treated with heat and silica was processed to obtain a protein with potential cancer-prevention ability known as the Bowman–Birk protease inhibitor (BBI, Kennedy 1998) in pure, concentrated form. Two different modes of operation were applied: bind and elute and flow-through. The bind and elute mode is the standard procedure for applications with low product concentrations and an excess of contaminants. If the contaminant is present in low concentration, however the flow-through mode can be superior. A purity of 99 % and a yield of 46 % were reached for the bind and elute mode with Orica MIEX DOC particles at a flow rate of 72 l/h whereas the flow-through mode with chemagen DEAP particles at a flow rate of 5 l/h yielded 55 % of the target protein at a purity of 97 % (Paulus et al. 2014).

10.5 Conclusion and Outlook

Continuous Magnetic Extraction combines the advantages of ATPS, functionalized (nano-) carriers and magnetic separation processes and is able to overcome many disadvantages previously reported for ATPS systems. The advantages of CME include:

- easy scale-up with parallel separation devices
- inexpensive media components
- reuse of the phase forming component to a large extent
- increased selectivity and purity by use of magnetic adsorbents
- combined capture and purification process
- increased phase separation rates
- simple equipment with little maintenance
- low consumption of electricity

It was proven that the process is truly continuous, while reaching high separation efficiencies at the same time. It has potential applications over a wide range of particle types and feed systems.

Up until now, only ion exchange-based separations have been carried out. Other chromatography types are promising for use in CME as well. An affinity ligand for example, could greatly increase purity in one single run while at the same time still allowing the processing of raw bio-suspensions.

The application of CME is not limited to protein purification processes, but will be further examined for use in enzymatic catalysis. Reuse of enzymes has been a hot topic in recent years and a continuous separation process for large volumes of dilute product suspensions and enzyme-loaded particles is a promising perspective.

References

Albertsson P-Å (1977) Separation of particles and macromolecules by phase partition. Endeavour 1(2):69–74

Albertsson P-Å (1978) Partition between polymer phases. J Chromatogr A 159(1):111–122

Becker JS, Thomas ORT, Franzreb M (2009) Protein separation with magnetic adsorbents in micellar aqueous two-phase systems. Sep Purif Technol 65(1):46–53

Fischer I, Franzreb M (2011) Direct determination of the composition of aqueous micellar two-phase systems (AMTPS) using potentiometric titration—A rapid tool for detergent-based bioseparation. Colloids Surf A 377(1–3):97–102

Fischer I, Franzreb M (2012) Nanoparticle mediated protein separation in aqueous micellar two-phase systems. Solvent Extr Ion Exch 30(1):1–16

Fischer I et al (2012) Partitioning behavior of silica-coated nanoparticles in aqueous micellar two-phase systems: evidence for an adsorption-driven mechanism from QCM-D and ATR-FTIR measurements. Langmuir: ACS J surf colloids 28(45):15789–15796

Fischer I et al (2013) Continuous protein purification by combination of functional magnetic nanoparticles and aqueous micellar two-phase systems, Copyright (2013), with permission from Elsevier, Reprinted from Chromatography A, 1305(0), p 7–16

Hatti-Kaul R (ed) (2000) Aqueous two-phase systems. In: Walker JM (ed) Methods in biotechnology, Vol 11, Humana Press, Totowa, p 455

Johansson G (1985) Aqueous two-phase systems in protein purification. J Biotechnol 3(1–2):11–18

Johansson G, Tjerneld F (1989) Affinity partition between aqueous phases—a tool for large-scale purification of enzymes. J Biotechnol 11(2–3):135–141

Kennedy AR (1998) The Bowman-Birk inhibitor from soybeans as an anticarcinogenic agent. Am J clin nutr 68(6):1406S–1412S

Nikas YJ et al (1992) Protein partitioning in two-phase aqueous nonionic micellar solutions. Macromolecules 25(18):4797–4806

Paulus A et al (2014) Use of continuous magnetic extraction for removal of feedstock contaminants in flow-through mode. Sep Purif Technol 127(0):174–180

Socoliuc V, Vékás L, Turcu R (2013) Magnetically induced phase condensation in an aqueous dispersion of magnetic nanogels. Soft Matter 9(11):3098–3105

Walter H, Johansson G (1986) Partitioning in aqueous two-phase systems: an overview. Anal Biochem 155(2):215–242

Wikström P et al (1987) Magnetic aqueous two-phase separation: a new technique to increase rate of phase-separation, using dextran-ferrofluid or larger iron oxide particles. Anal Biochem 167(2):331–339

Part III
Process Examples

Chapter 11
In Situ Magnetic Separation on Pilot Scale: A Tool for Process Optimization

Alexander Scholz, Martin Cerff and Clemens Posten

Abstract This study describes the design and development of an in situ magnetic separation process (ISMS) based on the use of ion exchange functionalized magnetic particles. ISMS as a tool for in situ product removal (ISPR) has the potential to increase the performance of a biotechnological production process comprehensively by improving the bioprocess itself and the downstream processing simultaneously. The successful implementation of this concept requires the systematic examination and optimization of the different ISMS subsystem. Hence, this report presents detailed characterization data for the magnetic particle system, the magnetic separator, and the bioprocess. For each system, specific requirements were defined and subsequently applied to identify suitable process components. In this context always economic considerations were also accounted to enable the application of this new process as cost-efficiently as possible. Especially the selection and modification of a magnetic particle system and the development of a low-cost magnetic separator were subjected to these basic criteria. For the final verification of the ISMS effects, all components were brought together in a pilot scale system and used to perform cultivation with integrated ISPR. The results of this cultivation were compared to reference cultivations without ISMS to quantify the effects on the upstream processing. In addition, a detailed analysis of the efficiency of purification was performed to evaluate the consequences on the downstream processing.

11.1 Introduction

Modern biotechnological production processes, in contrast to classical (chemical) manufacturing techniques, have the potential to produce complex products in an economic and sustainable manner. In many cases those processes are the only alternative

A. Scholz (✉) · M. Cerff · C. Posten
Institute of Process Engineering in Life Sciences, Karlsruhe Institute of Technology, Karlsruhe, Germany
e-mail: alexander.scholz@kit.edu

H. Nirschl and K. Keller (eds.), *Upscaling of Bio-Nano-Processes*,
Lecture Notes in Bioengineering, DOI 10.1007/978-3-662-43899-2_11

for obtaining certain product classes (Gavrilescu and Chisti 2005), especially in the field of pharmaceutical ingredient or enzyme production. However, the fermentation-based production of valuable products is frequently also linked to low productivities and diluted product streams (Stark and Stockar 2003; Atkinson and Sainter 1982), thus reducing the efficiency of the whole process. Potential reasons for the limitations of the cultivation process are inhibitory or toxic effects of products or byproducts respectively (Takors 2004), as well as the reduction of product activity due to degradation (Schügerl 2000; Scholz et al. 2011; Maury et al. 2012). With respect to the downstream processing purity demands usually require multiple purification steps, each one associated with product losses and additional costs (Woodley et al. 2008; Fish and Lilly 1984). Thus, as starting point for a process intensification, upstream as well as downstream processing have to be considered simultaneously. In this context, the integration of several process steps into a single operation represents a promising starting point for an extensive process optimization. The approach of integrating product purification directly into the fermentation process is known as ISPR and includes a variety of different techniques. These techniques can be categorized according to the method of target product separation. According to Freeman et al. (1993) five different techniques can be distinguished: evaporation, extraction, permeation, complex formation and adsorptive immobilization. In general, each method has two different main objectives. On one hand, the preferably immediate removal of the target component out of the cultivation media aims to decrease inhibitory effects and to stabilize the target product. On the other hand, specific or at least semi-specific separation of the target product aims to reduce the number of purification steps necessary to achieve specified purities (Freeman et al. 1993).

In situ magnetic separation as an adsorptive ISPR technique has gained recent interest as a method for separating extracellular functional proteins (Käppler et al. 2009; Cerff et al. 2013a, b). The basic idea of this method is to use functionalized magnetic particles for the direct adsorption of target products in crude fermentation broths. After the adsorption step, the magnetic properties of the adsorbent phase are utilized to separate the product loaded particles and the biomass-containing medium. The selective and fast solid-solid-liquid separation enabled with this method represents a major advantage compared to other adsorptive ISPR techniques like expanded bed adsorption (Hubbuch et al. 2001). Furthermore, also the usual nonporous character of the magnetic particles makes this technique less sensitive against fouling, which is a prevalent problem in other ISPR methods (OBrien et al. 1996).

11.2 Process Definition

To facilitate a structured evaluation of the ISMS approach the whole method can be divided into the following three subsystems:

- Magnetic particle system
- Magnetic separator
- Bioprocess

By examining each of these subsystems separately, it is possible to identify critical parameters for the respective systems individually as well as their mutual interaction. The definition of specific requirements for each sub-system enables an optimal design of the whole ISMS process.

For the magnetic particle system those requirements are [partially adapted from Franzreb et al. (2006)]:

- Good magnetic separation properties (particle size $d_{P,\,50} = 0.5$–10 µm, saturation magnetization $M_S \geq 35$ Am^2/kg, preferably superparamagnetic behavior)
- High capacity for the target product
- Chemically inert behavior with respect to the bioprocess
- Fast adsorption and desorption kinetics
- High reusability, i.e., high particle stability
- Preferably low purchase costs

Especially the reusability and cost of purchase are major criteria influencing the economic performance of the ISMS concept. The ideal magnetic particle system for ISMS purposes would have a specific ligand for the respective product of interest (e.g., an immobilized reversible inhibitor if the target product is an enzyme), leading to high binding capacity and selectivity. Due to the fact that the ligand chemistry used in the production of these functionalized particles is usually connected to high production costs (Käppler et al. 2008), an economic application of such beads is limited. As a more economical alternative, semi-specific separation principles like ion exchange groups can be identified. The production costs for these kinds of ligands are linked to lower expenditures (Käppler et al. 2008; Heeboll-Nielsen et al. 2004), enabling the economically feasible implementation of ISMS into versatile cultivation processes. The drawbacks of using these ligand types are usually reduced selectivity and capacity for the desired target. However, the application as an integrated capture step to generate a purified product stream still has the potential to significantly improve the performance of the process (Käppler et al. 2008; Heeboll-Nielsen et al. 2004; Ditsch et al. 2006). Particular attention has to be paid to the adsorption conditions when ion exchange functionalized magnetic particles are applied as adsorbents during ISMS. In contrast to a non in situ downstream procedure, degrees of freedom regarding a manipulation of these conditions are very limited. Boundary conditions are strongly predetermined by the distinct physiological conditions of the respective production strains. These limitations, especially for ion exchange particles, are related to ionic strength, pH, and protein concentration in the cultivation medium. When it comes to the proper selection of a magnetic particle type in order to remove a certain target, it is essential to have knowledge on the type of ion exchange groups and properties of the target product itself (anionic, cationic character). However taking into account the requested inertial behavior, cation exchangers are preferable since cells usually have a negative zeta potential (Dickson and Koohmaraie 1989) and should not bind to negatively charged ionic groups.

Analogous to the magnetic particle system, a set of requirements can be also defined for the magnetic separation device. These requirements are [adapted from Franzreb et al. (2006)]:

- Efficient utilization of the magnetizable separator volume (high volume-specific particle capacities)
- Selective separation of magnetic particles and biomass-containing cultivation broth (solid-solid-liquid separation)
- High particle retention rates, desirably at high volume flow rates
- Complete particle resuspension after magnetic separation including good properties for cleaning in place (CIP) and sterilization in place (SIP)
- Low operating and investment costs (e.g., comparison and calculation for permanent versus electromagnet and thus magnetic field generation)

From an economic perspective, the operating and investment costs are decisive. A cost efficient utilization of electromagnetically-driven separators in large scale application is limited, due the high operational and investment costs of such units (Käppler et al. 2008; Hoffmann et al. 2002). Additional expense is caused not only by the energy consumed in order to produce and maintain the magnetic field, but also by the energy for cooling to dissipate the heat that is generated by the solenoid. When such devices are not equipped with an adequate cooling system the operating time is limited to short periods, making parallel operation of multiple systems a necessity. Both of these options cause additional costs compared to those of permanent magnetic separators. In addition to the facts named above also safety aspects are a further argument for the use of permanent magnets while working with large liquid volumes (Safarik et al. 2001). However, the source of magnetic field generation is not the only area of particular interest; the design of the separation device itself should meet the requirements listed above in the most efficient way. In the context of handling large particle-loaded liquid streams, a continuously or at least semi-continuously operating separator is preferable. A promising concept of a semi-continuously working carousel separator based on several high gradient magnetic filters (HGMF) is presented by Franzreb and Hoell (1999). The principle layout of a HGMF includes a separation chamber which is filled with magnetizable mesh wires and placed into a closed separation chamber. For magnetic separation, the particle suspension passes through the magnetized separation chamber and magnetic components settle on the wires due to the attractive magnetic force. This kind of separators already proved to be efficient in small-scale ISMS processes (Käppler et al. 2009). Although the construction of a HGMF in this layout is relatively simple, the device still offers the possibility to modify a variety of parameters (wire geometry, wire orientation, etc.) enabling the adjustment of the separator to specific feed conditions. A possible limitation of HGMFs is the inhomogeneous distribution of particles inside the separation chamber. If the whole separation chamber is homogeneously magnetized, more particles settle at the intake side. In the worst case this could lead to the formation of dense particle layers or even a massive filter cake making selective solid-solid-liquid separation impossible. To avoid this problem, appropriate separator magnetization and particle loading strategies have to be considered.

Finally, a set of specifications for the bioprocess can be defined as follows:

- The existence of an extracellular target product
- The presence of inhibitory effects on overall productivity (product degradation, feedback regulation, constraining medium properties, etc.)
- A certain market relevance of the produced product

Clearly, a basic prerequisite is the presence of an extracellular target product due to the aspired recycling of the cultivation medium during cultivation. For industrial applications, secretion of target products into the growth medium is often a double-edged sword. Although downstream processing is simplified due to the reduced protein background in the extracellular medium (Westers et al. 2004), the stability of the target might be reduced by extracellular proteases (Maury et al. 2012). By implementing ISMS, it is possible to overcome this restriction thus boosting the performance of these production organisms. Especially for industrial enzyme production, this might be interesting regarding the widespread use of the *Bacillus* species in this field. Special attention must be paid to the cultivation conditions. Focusing on ion exchange functionalized magnetic particles, the choice of the cultivation medium is of certain interest. Given the fact that complex media often contain proteins and peptides, the binding capacity of adsorbent particles would be reduced due to unspecific co-adsorption of these substances. As a result, the use of a chemically-defined medium is immanent. Although the majority of commercial cultivation processes uses inexpensive complex media, there are also examples of processes where defined media were successfully applied in accordance with economic criteria (Zhang and Greasham 1999).

11.3 Process Development

This chapter describes the detailed development of the particular ISMS subsystems on the basis of a model process. Here, critical characteristics of the respective systems and their potential interactions with the other subsystems will be mentioned. Phytase, a phosphatase used as feed additive, was chosen as model product with relevance for industrial applications (Greiner et al. 2013).

11.3.1 Bioprocess

The starting point of the development of the process was the identification of a suitable production strain fulfilling the requirements defined above. A native phytase-secreting strain [*Bacillus amyloliquefaciens* FZB45, (Idriss et al. 2002)] was identified as a potential candidate. To evaluate whether ISMS has the potential to increase the overall target yield of the process, the stability of the secreted

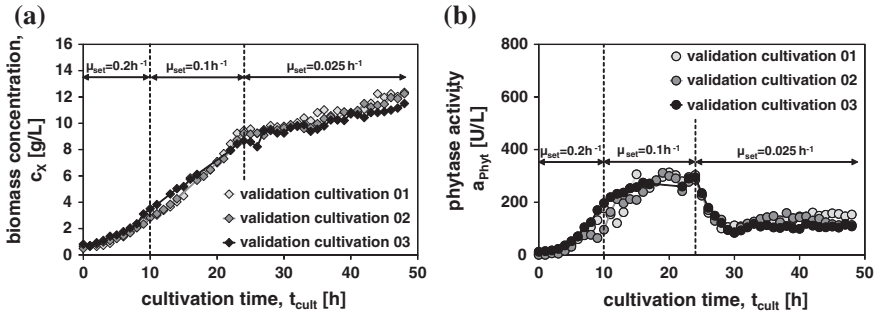

Fig. 11.1 **a** Biomass concentration curves of validation cultivations. **b** Phytase activity curves of validation cultivations

phytase was analyzed under cultivation conditions. For this purpose, cell-free cultivation supernatants (pH 6.5, cultivation media according to Zhang et al. (1983)) were incubated at 37 °C, and phytase activity was measured periodically. Based on the experimental data, the phytase half-life period was determined to be 4.2 h. Therefore, a significant loss of product activity has to be expected during cultivation, making this particular strain an ideal candidate for the implementation of ISMS. After selection of the production strain, it was necessary to set up a suitable process strategy to quantify the effects of ISMS on cell growth and overall phytase yield. Thus a process setup was required to obtain reproducible biomass and phytase formation during cultivation. A three stage exponential fed-batch profile with decreasing growth rates ($\mu_{set} = 0.2$, 0.1, 0.025 1/h) well below the maximum growth rate ($\mu_{max} = 0.55$ 1/h) was developed as the processing strategy. According to Jenzsch et al. (2006), this strategy should assure reproducible growth and product formation. Glucose and phosphate, as well as ammonium (provided as glucose monohydrate and ammonium sulfate), were used as feed components. A process validation was performed using this cultivation strategy. Figure 11.1 presents the phytase activity and biomass concentration curves of three validation cultivations.

The results of the validation cultivations confirm that the selected process strategy ensures a reproducible mode of operation. Both biomass concentration as well as phytase activity graphs show similar curve progressions. Therefore, the achieved product formation rates can serve as reference for the respective cultivations with ISMS.

11.3.2 Magnetic Particle System

As the next step after characterization of the product and design of the bioprocess, a suitable magnetic particle system was identified for the separation of the *Bacillus amyloliquefaciens* phytase produced. Several anion exchange-(AEX) and cation

Table 11.1 Langmuir parameters of different ion exchange functionalized magnetic particles determined by adsorption experiments

Producer	Type	Ligand type	Q_{max} (U/g)	Q_{max}/K_D (L/g)
Merck KGaA	MagPrep® Silica HS	(CEX)	455.9	10
Merck KGaA	MagPrep® SO_3	CEX	202.3	8.6
TU Bergakademie Freiberg	AEX	AEX	6.2	7.8
Merck KGaA	MagPrep® COOH	CEX	24.1	2.4
Merck KGaA	MagPrep® TMAP	AEX	1	1.2
PerkinElmer Inc.	M-PVA C22	CEX	81	0.6
ICDTIM Cluj Napoca	PNIPAm ACC	CEX	8	0.2
TU Bergakademie Freiberg	CEX	CEX	8.5	0.1

Media properties pH = 6.0 ionic strength I ≪ 115 mM

exchange-(CEX) functionalized magnetic particle systems were tested for this purpose (Table 11.1). Adsorption experiments using cell-free cultivation supernatants containing different concentrations of phytase were performed. The determined capacity data was used to calculate the Langmuir parameters (Langmuir 1918) for each of the analyzed particle systems. In agreement with Franzreb et al. (2006), the ratio of the maximum binding capacity Q_{max} over the dissociation constant K_D was chosen as the primary evaluation criteria for this screening procedure. In Table 11.1 summarizes the screening results for eight different particle systems. The MagPrep® Silica particles are in an exceptional position with respect to the fact that they are actually unfunctionalized core particles. However, the silica coated beads could act as a cation exchanger due to their hydroxide groups.

On the basis of the determined Q_{max}/K_D-values it is evident that the MagPrep® Silica as well as the MagPrep® SO_3 particles are adequate for phytase adsorption, with results of 10 and 8.6 L/g respectively. Both particle systems were examined in more detail.

The complete characterization of each particle system comprises the following process conditions and particle properties:

- Adsorption and elution conditions
- Reusability
- Adsorption and elution kinetics

Characterization of the adsorption conditions was accomplished by comparative adsorption experiments in dependency of the ionic strength and the pH-value of the adsorption medium. For variation of the pH-value, phytase-containing media were dialyzed against buffers with different pH-values, but constant ionic strength. Variation of the ionic strength was achieved by mixing cultivation media with equal volumes of saline solutions of defined concentrations (0–2 M NaCl). For both experiments, cell-free cultivation media with a pH of 6.0 and a base ionic strength of I < 115 mM were used as the reference medium. The adsorption time for each experiment was chosen to be 20 min. Figure 11.2a, b presents the particle phytase capacity results, dependent on pH and ionic strength.

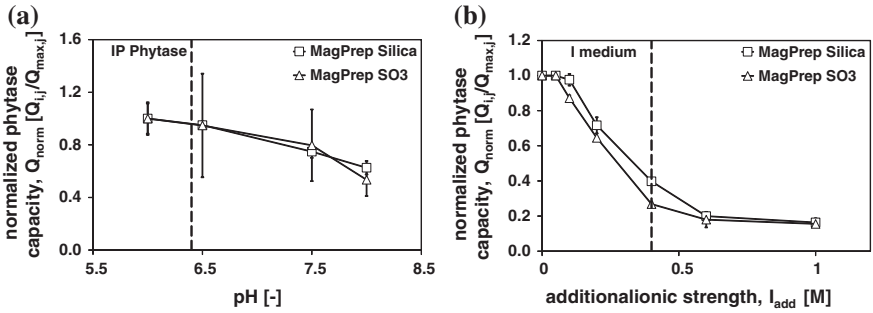

Fig. 11.2 **a** Normalized phytase capacity over the medium pH. The *vertical dashed line* represents the isoelectric point (IP) of the Bacillus phytase species according to Kerovuo et al. (1998). **b** Normalized phytase capacity over additional ionic strength in the medium. The *vertical dashed line* represents the typical ionic strength of a cultivation medium according to Ditsch et al. (2006)

Upon examination of the results of the pH dependent phytase adsorption, it becomes apparent that at the chosen cultivation pH of 6.5 for both particle systems sufficient relative capacities are attainable (Fig. 11.2a). Furthermore, the data reveals that selection of ion exchange functionalized magnetic particles based on the global charge theorem is not possible. According to the theory, the macroscopic charge characteristic of a protein is decisive for its interaction with ion exchange surfaces. The main criterion for characterization in this context is the isoelectric point (IP), at which a protein is considered uncharged in global terms, thus giving no reason for binding on ion exchange matrices to occur. In contrast to this, the results of the analyses demonstrate that phytase capacities close to the maximum load are possible, even at the IP of the phytase. Furthermore also above the IP, where the global charge of the protein becomes more negative, adsorption to the negatively charged CEX particles is still observable. Both of these effects might be explained by the existence of positive local charge distributions which are accessible for the small-sized magnetic particles even if the macroscopic net charge of the protein is zero or negative (Ditsch et al. 2006; Kopaciewicz et al. 1983). With respect to the influence of ionic strength, a decreasing capacity with increasing ion concentration can be observed. This confirms the electrostatic nature of phytase adsorption. Through metabolic activity as well as through the addition of pH-adjusting agents and feed media, an increase of ionic strength is expected during the cultivation. As a consequence, the effective binding capacity of the particles is reduced over the cultivation time. Nevertheless, relative capacities of 27–40 % are available for an ion concentration of 0.4 M, which corresponds to the ionic strength of a typical cultivation medium. For the layout of the final ISMS it is desirable, however, to perform the separation as early as possible to preserve the particles' capacities at the relatively low ionic strength of the medium.

To identify suitable compositions for the washing and elution buffers in order to optimize elution efficiencies (E_{eff}) and purification factors (PF), desorption

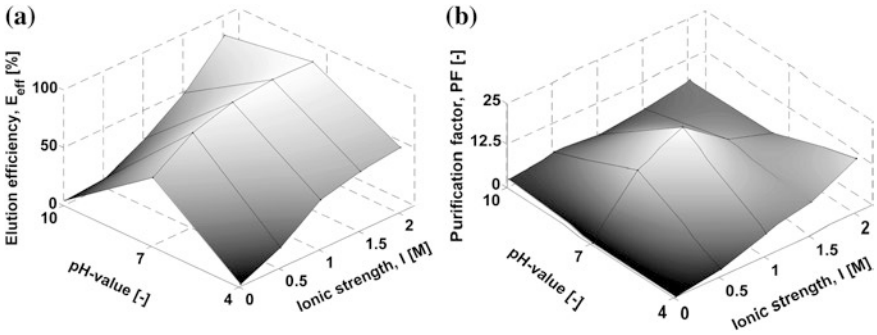

Fig. 11.3 **a** Normalized phytase capacity over the medium pH. The *vertical dashed line* represents the isoelectric point (IP) of the Bacillus phytase species according to Kerovuo et al. (1998). **b** Normalized phytase capacity over additional ionic strength in the medium. The *vertical dashed line* represents the typical ionic strength of a cultivation medium according to Ditsch et al. (2006)

experiments with different buffer systems were performed. For this purpose phytase-loaded particles (MagPrep® Silica HS, MagPrep® SO_3 and M-PVA C22) were eluted (for at least 20 min) using buffers with differing ionic strength and pH (Fig. 11.3a and b, exemplary results for the MagPrep® Silica particles).

From an economical point of view both aspects, product recovery and product purification, are essential. With respect to elution efficiency, the MagPrep® Silica achieved high recovery rates of up to 95 % (Fig. 11.3a). In contrast, the MagPrep® SO_3 particles (data not shown) reached only incomplete recovery rates with a maximum elution efficiency of 73 %. For the MagPrep® Silica an optimal elution buffer for maximum elution efficiency has to have an ionic strength of 1.5 M and a pH of 7 (Fig. 11.3b). The composition of an appropriate washing buffer (minimal phytase leakage) could also be obtained from these experiments. In case of the MagPrep® Silica those properties are an ionic strength of 0 M and a pH of 4. With respect to product purification, both particle systems enriched the phytase content in the elution stream, and maximum purification factors of 21.4 and 13.3 were obtained for the MagPrep® Silica and MagPrep® SO_3 (data not shown) respectively. The lower purification factors of the MagPrep® SO_3 beads might be partially caused by the reduced phytase elution efficiency. An elution buffer for maximum product purification for the MagPrep® Silica has to have a pH-value of 7 and an ionic strength of 1 M. The elution efficiency for this buffer composition equates to 91.8 %, meaning that maximum product purification is attainable at the expense of only minor product losses.

In addition to these basic process properties, further analyses were performed with respect to other critical process parameters such as long-term stability of particle systems. Therefore, repeated adsorption experiments with a constant particle mass were undertaken. Including particle pre- and post-treatment, each of these adsorption experiments consisted of five magnetic separation steps (i.e., washing and elution steps). From a practical perspective, the time-dependent adsorption behavior of the magnetic particle systems is also essential. To minimize the

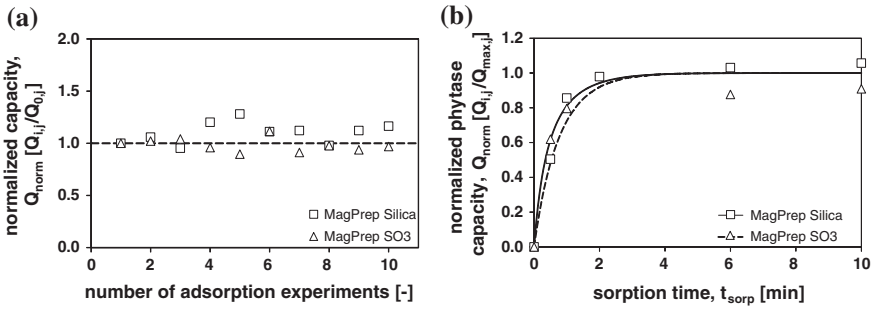

Fig. 11.4 **a** Results of the stability analyses, presented as capacity in dependency of the number of adsorption steps. **b** Adsorption behavior in dependency of the sorption time. Symbols are representing experimental data and lines the respective calculated adsorption kinetics according to the model of Norde et al. (2005). Experimental conditions: particle concentration 1 g/L, phytase activity in adsorption medium 35 U/L

retention time of the fermentation broth outside the regulated environment of the bioreactor, the ISMS step, and in this setup the adsorption kinetic as well, should take the least amount of time possible. To determine the rate of phytase adsorption, defined particle masses were incubated for different periods of time in phytase-containing media. That experimental data was used to determine the parameters of the kinetic adsorption model according to Norde et al. (2005) Results from the long-term stability as well as the adsorption kinetics experiments are presented in Fig. 11.4a, b.

With respect to particle reusability, each of the analyzed particle systems showed good results over ten consecutive adsorption experiments (Fig. 11.4a). Although the measurements had high variation limits, no major drop in capacity was detectable. Thus, the obtained results indicate that reusability of the respective particle systems is ensured making the concept of ISMS more economically feasible. The characterization of the time-dependent adsorption behavior (Fig. 11.4b) showed that the equilibrium load is reached within seconds or a few minutes in any case. This is consistent with the literature, which generally states that adsorption onto nonporous magnetic particles is rather quick (Ditsch et al. 2006; Käppler 2008). On this basis, ISMS performed in an external vessel apart from the bioreactor seems to be feasible and beneficial. In addition to the adsorption kinetics also the time-dependent elution behavior was analyzed (data not shown). As was observed for adsorption, desorption of phytase from the beads occurred within at most 5 min and is thus not time consuming.

Based on this detailed particle characterization, the most promising particle system for ISMS purposes turned out to be the MagPrep® Silica. The superior particle capacity and the good adsorption behavior under cultivation conditions (pH, ionic strength), as well as the fast adsorption kinetics qualify those beads for in situ applications. Their good elution behavior and high grade of reusability are further criteria in favor of these magnetic beads. In addition, the potentially lower

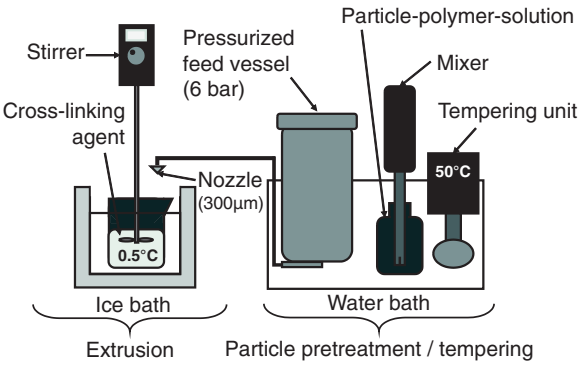

Fig. 11.5 Scheme of the polymer-suspension-extrusion setup

production costs of the unfunctionalized MagPrep® Silica beads are an economic benefit. Due to these facts, MagPrep® Silica particles were used in all further experiments.

Use of ion exchange functionalized magnetic beads during ISMS in a biomass-containing cultivation medium revealed unwanted, specific adsorption of biomass to the beads. In contrast to the assumption that globally negatively charged *B. amyloliquefaciens* will not bind to cation-functionalized adsorbent particles, substantial amounts of biomass were specifically adsorbed onto the magnetic beads (maximum capacities of up to 12 g/g). The explanation might be the same as for phytase, where local positive charges on the cell surface could trigger adsorption to negatively charged small-sized magnetic particles (Käppler et al. 2008). There are numerous negative consequences due to this phenomenon, such as reduced binding capacity and selectivity for phytase. Additionally, the productivity of the cultivation process decreases, due to the loss of phytase-producing cells. In this situation the most practical approach to solve the problem seemed to coat the magnetic beads with a porous polymer. This technique has already been established for expanded bed adsorption media (Viloria-Cols et al. 2004; Jahanshahi et al. 2008; Arpanaei et al. 2010), which must overcome similar limitations. By surface coating with a porous polymer, a second functionalization is put on top of the IEX layer of the core particles. The pores of the polymer act as size exclusion media, allowing small molecules to pass while bigger particles (cells, cell debris, etc.) are retained. A temperature-controlled procedure based on polymer-suspension-extrusion was developed as the coating process. This approach includes the pre-mixing of a defined mass of magnetic particles with a pre-heated polymer solution, followed by the pressurized extrusion through a nozzle ($d = 300$ µm) into a cooled and gently stirred cross-linking agent (Fig. 11.5). Agarose was identified as the polymer with the best handling and shielding properties and was thus used to modify MagPrep® Silica particles for ISMS applications.

By varying critical process parameters it was possible to set up a coating procedure enabling the production of magnetic particles with a drastically reduced biomass adsorption and almost unaffected phytase binding capacities. Those critical parameters were: polymer pre-tempering as well as particle pre-treatment at

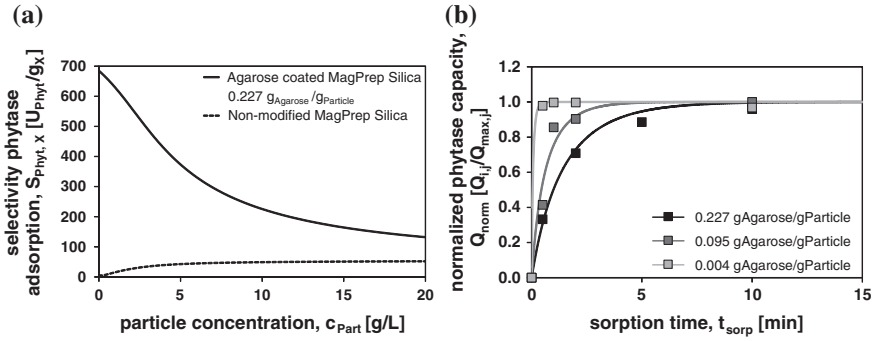

Fig. 11.6 **a** Calculated biomass specific selectivities of phytase adsorption for modified and nonmodified MagPrep® Silica particles as a function of the particle concentration. The following conditions of the adsorption medium were used as basis of comparison: phytase activity 273 U/L, biomass concentration 5 g/L. **b** Adsorption kinetics for MagPrep® Silica particles with different agarose polymer loads. Symbols represent experimental data and lines the respective calculated adsorption kinetics according to the model of Norde et al. (2005). Experimental conditions: particle concentration 3 g/L, phytase activity in adsorption medium 103 U/L

50 °C, 13.3 mL 3 % w/v agarose solution per gram of magnetic particles, cold (at least 0.5 °C) water as cross-linking agent, and low mechanical shear forces during extrusion. The production of coated MagPrep® Silica particles based on these process parameters resulted in a specific polymer load (dry weight) of 0.227 g agarose per gram of magnetic particles. The success of the particle shielding was validated by determining phytase and biomass specific adsorption isotherms for the modified and nonmodified particles respectively. After approximation of the corresponding Langmuir parameters for both components it was possible to calculate the selectivity S of phytase adsorption in reference to the adsorbed biomass amounts for different particle concentrations according to Eqs. 11.1 and 11.2 (Fig. 11.6a).

$$S = \frac{Q_{\mathrm{Phy}}}{Q_X} \tag{11.1}$$

$$Q_i = \left(\frac{p}{2} - \sqrt{\frac{p^2}{4} - q} \right) \quad \text{with} \; p = \frac{K_{D,i} + c_{\mathrm{Med},i} + c_{\mathrm{Part}} \cdot Q\mathrm{max},i}{c_{\mathrm{Med},i}} \; q = \frac{c_{\mathrm{Part}} \cdot Q\mathrm{max},i}{c_{\mathrm{med},i}} \tag{11.2}$$

Given the fact that the deposition of an additional polymer layer on top of the functionalization ligands also represents a diffusional barrier, it was expected that the adsorption kinetics would slow down. To characterize the impact of particle coating in this context, adsorption kinetics for particle systems with different polymer loads were determined (Fig. 11.6b).

With regard to selectivity the modified and nonmodified magnetic particles showed inverse behavior. While nonmodified MagPrep® Silica exhibited growing selectivities (saturation value of 54.6 U_{Phyt}/g_X) with increasing particle concentration, modified ones (0.227 $g_{agarose}/g_{particle}$) showed a decreasing behavior (Fig. 11.6a). From these results it can be concluded that it is preferable to use only the essential amount of modified beads to reduce the overall biomass loss. Considering the actually required phytase capacities, realistic particle concentrations are 0.75–5.5 g/L. Within this concentration range, the modified MagPrep® Silica particles had an increased selectivity by factor 8–53 compared to the nonmodified ones. However, higher polymer loads slow down adsorption kinetics due to pore diffusion (Fig. 11.6b). For the highest polymer load (0.227 $g_{agarose}/g_{particle}$) an increase of the saturation time by a factor of 60 was detectable. Nevertheless, this period of time (10 min) was still considered to be acceptable for ISMS purposes. But not only protein binding properties are affected: particle handling specific characteristics are also influenced by the surface coating. The increased total particle mass due to the agarose coating causes a descent of the (mass specific) magnetization, leading to a reduced separability. Furthermore, the increased specific particle volume leads to a decreased retaining capacity for a magnetic separator. However, all of these worsened characteristics were expected to be acceptable for the final ISMS setup, bearing in mind that inert (in reference to the biomass) magnetic particles are essential for the whole process concept.

11.3.3 Separator

The third and last subsystem to be characterized was the magnetic separation device. Development of this unit included the characterization of two already available small-scale HGMFs (HGMF 1 and 2) and the construction of a new upscaled device (HGMF 3). The HGMF 1 was developed at the Institute of Process Engineering in Life Sciences, Karlsruhe Institute of Technology (KIT) and the HGFM 2 was obtained from the Institute of Biochemical Engineering, University of Stuttgart. Knowledge gained through the characterization of these two small-scale separators served as the basis for the layout of the pilot scale HGMF 3 device based on a design introduced by Franzreb and Hoell (1999).

A comparison of important geometric dimensions and properties for each separator is presented in Table 11.2.

For all separators used, the initial challenge was to determine the maximum particle capacity by loading trial runs. This approach included pumping a particle suspension (10 g/L MagPrep® Silica suspended in ultrapure water) through the magnetized separator with defined flow rates (mean residence time 1 min). During these experiments the flow-through at the separator outlet was analyzed with respect to particle concentration. The optical density was continuously monitored with a flow-through photometer and validated by periodic particle dry mass estimations. In agreement with (Ebner et al. 2007) a breakthrough concentration

Table 11.2 Overview about the geometric dimensions and properties of the analyzed HGMFs

		HGMF 1	HGMF 2	HGMF 3
Separator	Type of magnet	Solenoid	Permanent	Permanent
	Magnetic flux density (maximum)	0.42 T	0.45 T	0.45 T
	Structural shape	Barrel	Canister	Canister
	Total free volume	369 mL	666 mL	2072 mL
Grid geometry	Mesh width	3.15 mm	0.8 mm	3.15 mm
	Wire cross section	0.5 mm	0.2 mm	0.5 mm
	Dimension	Ø 5.5 cm	13.9 × 9 cm	15.7 × 6 cm
	Grid number	25	18	30
	Total area	594 cm^2	2627 cm^2	2826 cm^2
	Material	1.4016	1.4016	1.4016
	Orientation relative to magnetic flux and volume flow	longitudinal	transversal, axial	Transversal
Spacer	Height	3 mm	1 mm	3 mm
	Type	PMMA frame	1.4301 grid	PMMA frame
	Number	50	15	66
	Formation[a]	0/2/0	0/1/0	3/2/3

[a]The arrangement shown relates to the number of spacers before the first, between the subsequent and after the last separation grid

of 5 % relative to the loading concentration was chosen as a reference criterion. Although the hereby ascertained particle loads are not representative for a practical ISMS application (filter cake formation), the obtained capacities can still be used as a criterion for a relative comparison. Based on the procedure described above, maximum volume specific capacities of 211 and 86 g/L were determined for HGMF 1 and HGMF 2 respectively. The main reason for the low capacity of HGMF 2 is most probably the significantly narrower mesh width of the separation grids, as well as the unfavorable orientation of the spacer and the separation grids axial to the liquid perfusion direction. Based on these results, the principle spacer and grid design for HGMF 3 was adapted from HGMF 1. To effectively use the complete magnetizable volume, a closed separation canister with maximum dimensions in relation to the yoke of a permanent magnet (derived from the HGMF 2) was constructed (Fig. 11.7a, b). Using this setup a maximum volume specific capacity of 126 g/L was accomplished. To evaluate this result against the performance of HGMF 1 and 2, it is necessary to note that, due to a lack of MagPrep® Silica particles, no particle breakthrough was achieved for HGMF 3. On this basis it can be assumed that the actual volume specific capacity is probably larger than predicted by this experiment.

Because of the great importance of complete particle resuspension, investigations into particle recovery were also conducted. For this purpose each device was loaded with a comparable volume specific amount of magnetic particles

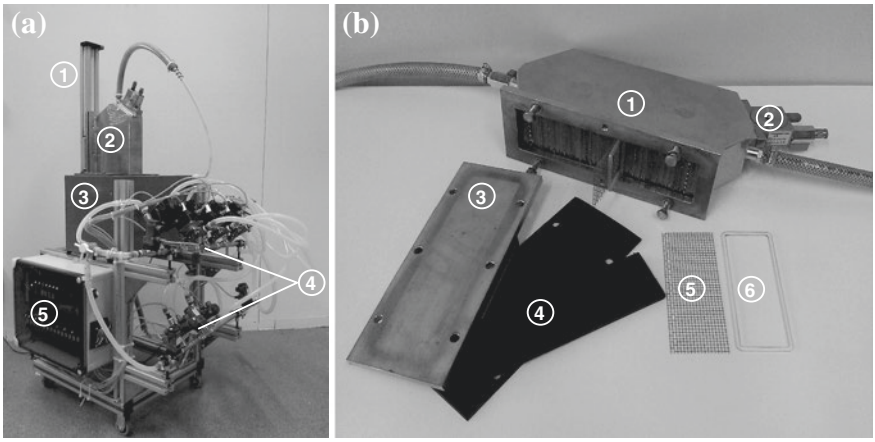

Fig. 11.7 **a** ISMS system consisting of the *1* vertical displacement, the *2* separation chamber, the *3* permanent horse shoe magnet. Further components which can be seen are the *4* valve blocks and the *5* control box. **b** Dismantled filter canister of the HGMF 3. The following components can be seen: *1* canister housing, *2* pneumatic roller vibrator, *3* case cover, *4* cover flat gaskets, *5* separation grid, *6* spacer

(110 ± 25 g/L), and the nonmagnetic supernatant was rinsed out of the separator. Afterwards the separator was demagnetized and filled with a defined amount of ultrapure water (1/3 of the separation volume). To improve particle resuspension HGMF 1 and 2 were manually shaken for 10 min. In case of HGMF 3, a pneumatic roller vibrator mounted on the filter canister was switched on for the same period of time. Finally, the particle-loaded wash fraction was rinsed out of the separator and the particle concentration was determined by dry mass measurements. This washing procedure was repeated twice (the wash volume being 3/4 of the separator volume each time). The ascertained particle dry masses were added up and balanced against the initially loaded mass. In doing so, recovery rates of 99.91 ± 0.86 %, 79.11 ± 2.38 %, and 99.89 ± 0.79 % were achieved for HGMF 1, 2 and 3 respectively. The remaining particles had to be cleaned off manually after disassembling the separation chambers. Analyses of the results reveal that the overall cleaning efficiency of HGMF 2 was less effective compared to the other two filters. This might be due to the narrow mesh width and the orientation of the spacer and separation grids.

Taking into account the results of the capacity and resuspension analyses, both HGMF 1 and HGMF 3 were qualified for ISMS applications. However, HGMF 3 was favored over HGMF 1due to its higher absolute particle capacity (261.1 g) and the cost efficient magnetic field generation by permanent magnet. Thus, all cultivations implying ISMS were performed using this device. For a better handling, the magnet as well as the separation chamber were installed into a frame which included a vertical displacement mechanism to move the filter canister continuously into or out of the magnetic field, thus “switching” the magnetic field on or off (Fig. 11.7a).

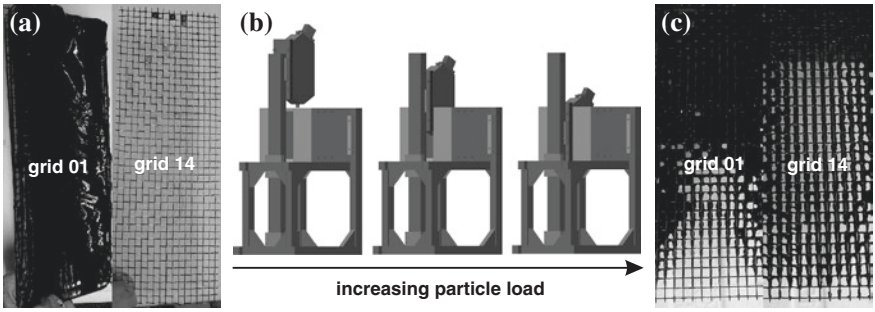

Fig. 11.8 **a** Particle deposition on separation grid 1 and 14 of the HGMF 3 using instantaneous magnetization of the whole separation chamber. **b** Scheme of the HGMF 3 during particle separation using the gradual magnetization strategy. **c** Particle deposition on different separation grids of the HGMF 3 using the gradual magnetization strategy. Numbering of the grids starts at the separator intake side

As mentioned earlier, a homogeneous particle distribution inside the separator is desired in order to achieve maximum particle capacities without the formation of a dense particle filter cake on the deposition matrices, especially at the inlet of the HGMS. To characterize the particle deposition on the separation matrices, loading trial runs at a constant feed rate (30 L/h) were performed with the HGMF 3. Each time, 50 g of MagPrep® Silica particles were magnetically settled inside the separation chamber. Analysis using the conventional particle loading strategy revealed that instantaneous magnetization of the whole separator leads to the heavy accumulation of magnetic beads at the inlet of the separator with decreased filter cake formation further inside the separator (Fig. 11.8a). To achieve a more homogeneous particle distribution along the flow direction, a continuous lowering of the separation chamber into the yoke of the permanent magnet was accomplished using a vertical displacement unit (Fig. 11.8b).

The gradual magnetization beginning at the separator outtake side enables the initial loading of the lower separation elements, thus distributing the particles more homogeneously along the flow direction (Fig. 11.8c). Using this loading strategy a maximization of the separator capacity is accomplished without a loss in separation selectivity.

11.4 Process Integration of ISMS

For the consolidation of the different ISMS subsystems, the bioreactor and HGMF 3 were assembled into a sterilizable separation circuit (Fig. 11.9). The general structure of this circuit was inspired by the system developed by Cerff et al. (2013b). Silicone tubing in combination with a peristaltic pump was used to handle the liquid within the separation circuit. Flow path control between the

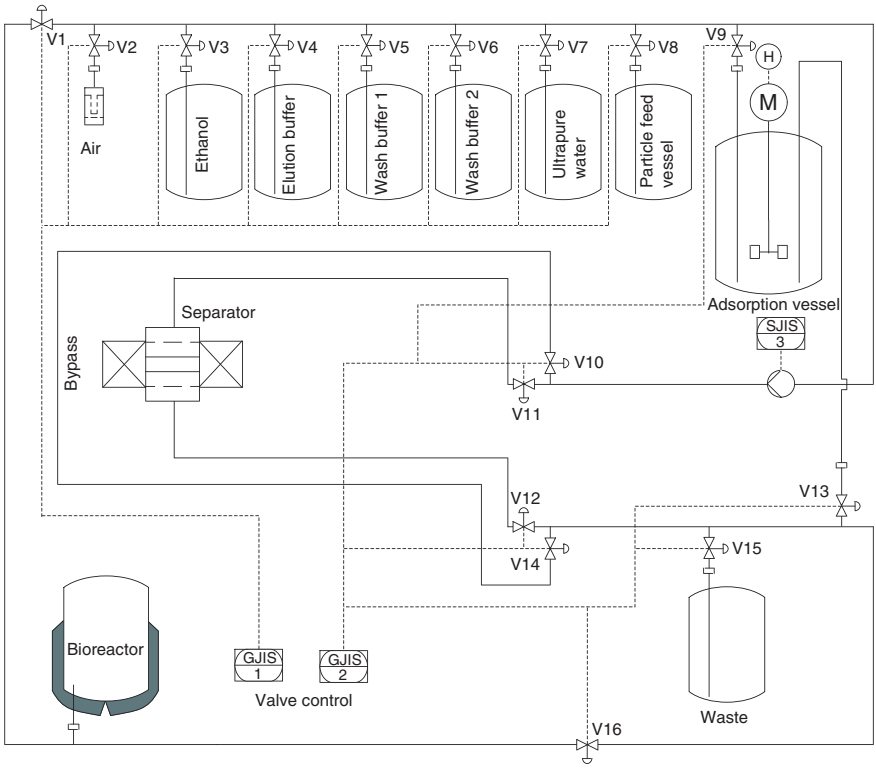

Fig. 11.9 Schematic piping and instrumentation diagram of the separation circuit

separator, the bioreactor and the several receiver tanks (necessary for particle pre- and post-treatment) was achieved by a pneumatic valve system. For the layout of this system particular attention was paid to minimum liquid losses. For this purpose the valves as well as the manifolds were arranged in self draining positions. The procedure for sterilization of the separation circuit included filling it completely with 30 % (v/v) ethanol and incubating for 60 min. Then the system was evacuated and purged with autoclaved ultrapure water. All buffers and media connected to the system were autoclaved separately before usage.

Prior to each ISMS, magnetic particles were incubated for at least 60 min in 76 % (v/v) ethanol to ensure aseptic handling. After this sterilization the particle feed vessel was connected to the separation circuit and the suspension was pumped through the magnetized separator. Particle free supernatant was discarded and particles were washed twice with washing buffer. For this purpose the separator was demagnetized and the particles were resuspended with the respective buffer. The particle suspension was collected in the adsorption vessel before a new magnetic separation was performed. All further buffer or media exchanges were done in the same manner. For separation, the cultivation broth containing the biomass was

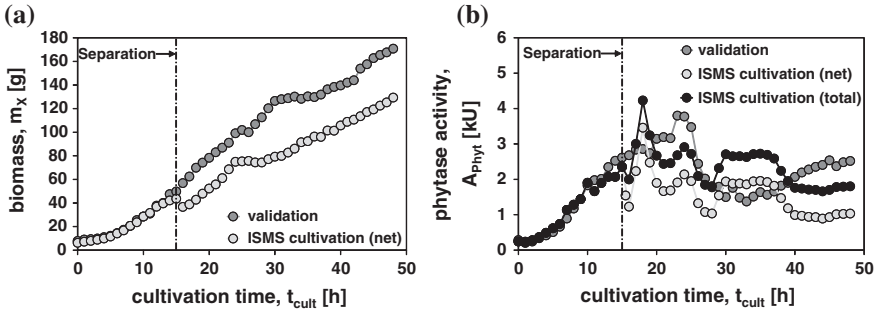

Fig. 11.10 **a** Biomass profiles of the ISMS and the validation cultivation. **b** Phytase profiles of the ISMS and the validation cultivation. The total values are representing the particular net phytase activities including the amount separated via ISMS (4.8 % elution loss considered)

pumped from the 19 L standard bioreactor through the demagnetized, particle filled separator. After a brief incubation period and subsequent magnetic separation, the particle free supernatant was recycled into the bioreactor and cultivation was continued. The results of ISMS during cultivation for enhanced phytase production are presented together with the respective validation cultivation in Fig. 11.10.

Figure 11.10 shows that after a cultivation time of 15 h a significant amount of the phytase (34.4 %) was separated from the medium by the ISMS step. Following the separation step, phytase was reproduced quickly and exceeded the reference value of the validation cultivation after a cultivation time of 18 h. If the separated phytase amount under consideration of the characterized elution efficiency (95.2 %) is added to this value, a total phytase activity of 4228 U is achieved. In relation to the validation cultivation (3800 U after 23 h) this equates to an increase of 11.2 %. With regard to phytase productivity, the rate of increase is even higher at a value of 38.3 % due to the shortened process time of the ISMS cultivation. With respect to the biomass profiles it is noticeable that although the modified MagPrep® Silica beads were used, a significant loss of biomass was still observable (12.7 %). However, this value is still significantly lower than for ISMS cultivations with nonmodified MagPrep® Silica beads, where up to 70 % of biomass was separated. Table 11.3 shows a summary of important data for both cultivations.

The presented data indicates that, in principle, the ISMS had a positive impact on both maximum phytase productivity and maximum phytase amount. However, in addition to the already mentioned biomass loss, the weight loss induced by the ISMS step further reduces this benefit. In detail, this loss is caused by medium remaining inside the separation circuit and to a certain extent also by the interrupted feed supply during the ISMS step. A reduction of these losses might be possible by further optimizing the separation system and reducing the separation time.

Equivalent to the upstream processing, a detailed analysis of the ISMS effects was performed for the downstream processing as well. For post-treatment of particles the buffers identified by the particle characterization experiments were used. Overall, three washing steps were conducted with the optimal washing buffer and

Table 11.3 Comparison of the performance data for the cultivation with and without ISMS

	Validation cultivations	ISMS cultivation
Particle mass	–	13.2 g (≙1.5 g/L)
Separated phytase amount	–	808.7 U
Selectivity	–	139.2 U/g_X
Period of time needed for ISMS	–	30.1 min
Biomass loss	–	5.5 g (≙12.7 %)
Weight loss (ISMS + feed)	–	323.2 g (≙3.8 %)
Maximum phytase productivity	160.1 U/h[a]	221.4 U/h[b] (≙ + 38.3 %)
Maximum phytase amount	3800.6 U[a]	4228.1 U[a] (≙ + 11.2 %)

Phytase losses due to incomplete elution (as determined during the particle characterization) are considered for the ISMS values
[a]Referred to a cultivation time of 24 h
[b]Referred to a cultivation time of 18 h

Table 11.4 Purification table ISMS cultivation (fractions without any phytase activities are not listed)

	Protein specific phytase activity $A_{Phyt,\ spec}$ (U/mg)	Phytase recovery R (%)	Purification factor PF (−)
Medium (t_{cult} = 15 h)	2.3	–	–
ISMS supernatant	1.7	–	–
Wash fraction 1	1.1	3.3	0.5
Elution fraction 1	12.8	23.9	5.6
Elution fraction 2	13.7	12.4	6.1
Elution fraction 3	57.4	4.9	25.3

three elution steps with the optimal elution buffer (maximum elution efficiency). The main evaluation criterion for the assessment of the downstream efficiency was the purification table (Table 11.4) validated by the results of the SDS-PAGE (Fig. 11.11).

With respect to phytase purification, a mean purification factor of 5.8 was achieved by the first two elutions. This is a significant increase of the specific activity compared to the cultivation medium. The specific activity of the third elution fraction was even higher, but has to be evaluated critically given the fact that the measured protein concentration was close to the detection limit of the Bradford protein assay (Bradford 1976) used. Compared to the particle characterization experiments, (PF = 11.3) the realized mean purification factor was quite low. This might be due to a loss of active phytase caused by the prolonged handling time in comparison to the lab scale characterization experiments. Furthermore, it is also conceivable that the mixing of the particle suspension inside the separation circuit during particle resuspension was insufficient. Both aspects also could explain the relatively low recovery rates obtained in the elution fractions. The eluted phytase content is 41.2 % in total and lower than predicted by the particle

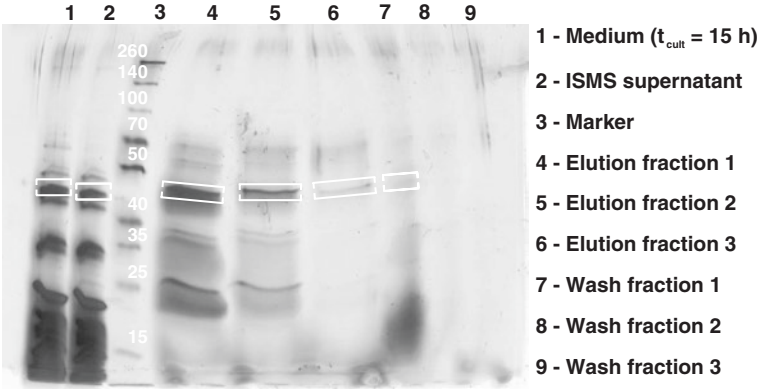

Fig. 11.11 SDS-PAGE medium-scale ISMS cultivation. The phytase bands (45 kDa) are marked with white frames

characterization experiments (95.2 %). Still, it can be assumed that a particle performance comparable to the particle characterization experiments could also be attained at the reactor scale. Starting points for an optimization in this context might be an improved buffer composition (containing phytase stabilizing components like calcium) as well as an improvement of the particle mixing behavior inside the separation circuit (static mixers). In addition to the quantity based purification considerations Fig. 11.11 presents the results of the SDS-PAGE analyses.

In reference to the sample of the cultivation medium all three elution fractions showed significantly less impurities, especially in the lower molecular weight range (<25 kDa), thus validating the results of the activity measurements. Regarding the particle washing procedure it is obvious that only the first washing steps caused a substantial purification effect.

11.5 Conclusion

This paper presents the development of a bioprocess for extracellular phytase with integrated ISMS based on ion exchange functionalized magnetic particles. For the design of the procedure the whole process was structured into the subsystems bioprocess, magnetic particle system, and magnetic separator. Initially, specific requirements were determined for each subsystem. In this context critical parameters were highlighted and comprehensively discussed. Based on the defined catalog of requirements a screening for each subsystem was performed. *Bacillus amyloliquefaciens* secreting a highly instable phytase was identified as suitable production organism for the bioprocess. Out of 8 different analyzed ion exchange functionalized magnetic particle systems, two principally suitable for adsorption of the target product. Both of these particle systems were included

into a detailed characterization procedure. In addition to adsorption and elution conditions, reusability and selectivity of product adsorption were also characteristics which were determined during these analyses. As a result, MagPrep® Silica particles were identified to have the best performance data. To increase the particles' selectivity for phytase adsorption a polymer coating procedure was successfully developed. Initially, two different small-scale HGMFs were examined as magnetic separation devices with respect to particle capacity and resuspension. Based on this data, a larger-scale device combining the positive characteristics of the two small-scale units was constructed.

After characterizing each subsystem, the final process was assembled. For this purpose, a sterilizable separation circuit consolidating the different systems was constructed. The process integration of ISMS prove to be efficient in terms of increasing the process performance compared to an identical process without ISPR. In this context the potential positive impact on both process sections (up- and downstream processing) could be proven. Compared to the validation process phytase productivity was increased by 38.8 %, and the elution fractions of the ISMS step yielded a partially purified product stream ($PF = 5.8$).

As a starting point for a further improvement of the ISMS concept, clearly the magnetic particle system needs to be improved. Basic requirements for the comprehensive revelation of the ISMS concept are cheap, inertial, and high capacity magnetic particles. Thus the further development of the introduced coating procedure should be in focus.

References

Arpanaei A et al (2010) Surface modification of chromatography adsorbents by low temperature low pressure plasma. J Chromatogr A 1217(44):6905–6916

Atkinson B, Sainter P (1982) Development of downstream processing. J Chem Technol Biotechnol 32(1):100–108

Bradford MM (1976) A rapid and sensitive method for the quantitation of microgram quantities of protein utilizing the principle of protein-dye binding. Anal Biochem 72(1):248–254

Cerff M et al (2013a) Semi—continuous in situ magnetic separation for enhanced extracellular protease production–modeling and experimental validation. Biotechnol Bioeng 110(8):2161–2172

Cerff M et al (2013b) In situ magnetic separation of antibody fragments from Escherichia coli in complex media. BMC biotechnol 13(1):44

Dickson JS, Koohmaraie M (1989) Cell-Surface Charge Characteristics and Their Relationship to Bacterial Attachment to Meat Surfaces. Appl Environ Microbiol 55(4):832–836

Ditsch A et al (2006) Ion-exchange purification of proteins using magnetic nanoclusters. Biotechnol Prog 22(4):1153–1162

Ebner NA et al (2007) Filter capacity predictions for the capture of magnetic microparticles by high-gradient magnetic separation. IEEE Trans Magn 43(5):1941–1949

Fish NM, Lilly MD (1984) The Interactions between Fermentation and Protein Recovery. Bio-Technology 2(7):623–627

Franzreb D, Hoell D (1999) High gradient magnetic separator. EP Patent 0,920,916

Franzreb M et al (2006) Protein purification using magnetic adsorbent particles. Appl Microbiol Biotechnol 70(5):505–516

Freeman A, Woodley JM, Lilly MD (1993) In situ product removal as a tool for bioprocessing. Bio-Technology 11(9):1007–1012
Gavrilescu M, Chisti Y (2005) Biotechnology—a sustainable alternative for chemical industry. Biotechnol Adv 23(7–8):471–499
Greiner R et al (2013) Production of partially phosphorylated myo-inositol phosphates using phytases immobilised on magnetic nanoparticles. Bioresour Technol 142:375–383
Heeboll-Nielsen A et al (2004) Superparamagnetic cation-exchange adsorbents for bioproduct recovery from crude process liquors by high-gradient magnetic fishing. Sep Sci Technol 39(12):2891–2914
Hoffmann C, Franzreb M, Hoell WH (2002) A novel high-gradient magnetic separator (HGMS) design for biotech applications. IEEE Trans Appl Supercond 12(1):963–966
Hubbuch JJ et al (2001) High gradient magnetic separation versus expanded bed adsorption: a first principle comparison. Bioseparation 10(1–3):99–112
Idriss EE et al (2002) Extracellular phytase activity of Bacillus amyloliquefaciens FZB45 contributes to its plant-growth-promoting effect. Microbiology-Sgm 148:2097–2109
Jahanshahi M, Partida-Martinez L, Hajizadeh S (2008) Preparation and evaluation of polymer-coated adsorbents for the expanded bed recovery of protein products from particulate feedstocks. J Chromatogr A 1203(1):13–20
Jenzsch M et al (2006) Open-loop control of the biomass concentration within the growth phase of recombinant protein production processes. J Biotechnol 127(1):84–94
Käppler T (2008) In: Prozessintensivierung durch feldunterstützte Bioseparation: Elektrofiltration und in situ Magnetseparation, in Faculty of chemical engineering and process engineering. Universitiy Karlsruhe, Karlsruhe
Käppler TE et al (2008) Characterization of magnetic ion-exchange composites for protein separation from biosuspensions. J Biosci Bioeng 105(6):579–585
Käppler T et al (2009) In situ magnetic separation for extracellular protein production. Biotechnol Bioeng 102(2):535–545
Kerovuo J et al (1998) Isolation, characterization, molecular gene cloning, and sequencing of a novel phytase from Bacillus subtilis. Appl Environ Microbiol 64(6):2079–2085
Kopaciewicz W et al (1983) Retention model for high-performance ion-exchange chromatography. J Chromatogr 266:3–21
Langmuir I (1918) The adsorption of gases on plane surfaces of glass, mica and platinum. J Am Chem Soc 40(9):1361–1403
Maury TL et al (2012) Use of high-gradient magnetic fishing for reducing proteolysis during fermentation. Biotechnol J 7(7):909–918
Norde W, Buijs J, Lyklema H (2005) 3 Adsorption of globular proteins. Fundam Interface Colloid Sci 5:1–59
OBrien SM, Thomas ORT, Dunnill P (1996) Non-porous magnetic chelator supports for protein recovery by immobilised metal affinity adsorption. J Biotechnol 50(1):13–25
Safarik I, Ptackova L, Safarikova M (2001) Large-scale separation of magnetic bioaffinity adsorbents. Biotechnol Lett 23(23):1953–1956
Scholz A, Cerff M, Posten C (2011) In situ product removal (ISPR) of functional proteins from prokaryotic cultivations by high specific magnetic separation. In: AFS 24th Annual conference. AFS Society, Louisville
Schügerl K (2000) Integrated processing of biotechnology products. Biotechnol Adv 18(7):581–599
Stark D, Stockar U (2003) In situ product removal (ISPR) in whole cell biotechnology during the last twenty years. In: Stockar U et al (eds) Process integration in biochemical engineering. Springer, Heidelberg, pp 149–175
Takors R (2004) Ganzzell-ISPR-Prozessentwicklung: Chancen und Risiken. Chem Ing Tech 76(12):1857–1864
Viloria-Cols ME, Hatti-Kaul R, Mattiasson B (2004) Agarose-coated anion exchanger prevents cell-adsorbent interactions. J Chromatogr A 1043(2):195–200

Westers L, Westers H, Quax WJ (2004) Bacillus subtilis as cell factory for pharmaceutical proteins: a biotechnological approach to optimize the host organism. Biochim Biophys Acta-Mol Cell Res 1694(1–3):299–310

Woodley JM et al (2008) Future directions for in situ product removal (ISPR). J Chem Technol Biotechnol 83(2):121–123

Zhang J, Greasham R (1999) Chemically defined media for commercial fermentations. Appl Microbiol Biotechnol 51(4):407–421

Zhang QX et al (1983) Increased production of alpha-amylase by bacillus-amyloliquefaciens in the presence of glycine. Appl Environ Microbiol 46(1):293–295

Chapter 12
An Industrial Approach to High Gradient Magnetic Fishing in the Food Industry

Christian Fiil Nielsen, Karsten Keller, Susanne Rasmussen, Niels Dalgaard, Timothy John Hobley, Wickie Sondergaard, Hermann Nirschl and Johannes Lindner

Abstract High-gradient magnetic filtration bases on the separation of target media by synthetic particles with magnetic core and an adsorbent immobilized on the surface. The process was used in a pilot line at liter-scale for the separation of a protein Bowman-Birk protease Inhibitor (BBI) out of an industrial coproduct stream in the soy industry. The target protein has potential applications as pharmaceutical or food additive. The starting medium is challenging as the product cost is low, its concentration is low and its purity needs to be high. The main method tested was magnetically

C.F. Nielsen (✉) · S. Rasmussen · N. Dalgaard
DuPont Nutritional Biosciences Aps, Edwin Rahrs Vej 38, 8220 Brabrand, Denmark
e-mail: Christian.Fiil.Nielsen@dupont.com

S. Rasmussen
e-mail: Susanne.Rasmussen@dupont.com

N. Dalgaard
e-mail: Niels.Dalgaard@dupont.com

K. Keller
DuPont, Wilmington, DE 19980, USA
e-mail: Karsten.Keller@dupont.com

T.J. Hobley · W. Sondergaard
Technical University of Denmark, Søltofts Plads Building 221,
2800 Kongens Lyngby, Denmark
e-mail: tjho@food.dtu.dk

W. Sondergaard
e-mail: wics@food.dtu.dk

H. Nirschl
Institute of Mechanical Process Engineering and Mechanics, Karlsruhe Institute of Technology, 76131 Karlsruhe, Germany
e-mail: hermann.nirschl@kit.edu

J. Lindner
Karlsruher Institut für Technologie (KIT), Institut fuer Mechanische Verfahrenstechnik und Mechanik, Geb. 30.70, Straße am Forum 8, D-76131 Karlsruhe, Germany
e-mail: johannes.lindner@kit.edu

H. Nirschl and K. Keller (eds.), *Upscaling of Bio-Nano-Processes*,
Lecture Notes in Bioengineering, DOI 10.1007/978-3-662-43899-2_12

enhanced centrifugation in a batch-wise mode with anion exchange ligands. The separation of the target protein at large scale was successful and economical. The efficiency was low due to the low ligand selectivity and the batch-wise processing. For commercialization, high ligand selectivity and continuous processing would make this new magnetic separation process very attractive. An economic study was performed to determine the influence of different parameters on prices. Competing technologies were evaluated. A risk analysis of nanoparticles used in the pilot line was performed.

12.1 Introduction

In the food industry, an increased effort is done on the further use of coproduct streams from the production, partly for sustainability reasons, partly because the disposal costs of aqueous wastes increase. Instead side-streams containing biological material are increasingly transformed into useful products or feed stocks for other processes. A large amount of water is used in the processing of food, leading to very dilute side-streams. More sustainable processing becomes increasingly important, and is hence a goal of the current project. Traditional separation processes are costly, resulting in a need for new approaches.

The current chapter covers the process development and optimization in lab and pilot scale. Considering the target purity and the market price, an ion-exchange ligand-based multistage process was selected. Anion exchange resins were chosen as a consequence of the isoelectric point of the BBI. Substantial pretreatment steps showed to be necessary for the final process due to the low selectivity of ion-exchange functionalization. BBI-specific ligands are technically possible, such as antibodies and phage display of peptides, but for the specific system not available. If available they would be excessively expensive, as discussed below.

Out of the particle systems developed, two systems were produced at a scale sufficient for the pilot line, the Merck MagPrep TMAP, introduced in Chap. 7, and SolPro from Chap. 6. Additionally, commercial particles thankfully provided by Orica Watercare were tested.

Three magnetic separation devices were introduced in part II. The Halbach magnet arrangement from Chap. 8 was tested on the system, the results were presented in the respective chapter. Results on the CME from Chap. 10 on the separation of proteins are presented elsewhere. The most promising separation principle for this project seemed to be magnetically enhanced centrifugation (MEC, US patent 8012357) presented in Chap. 9. It was chosen for its high volume flow up to 1 m^3/h in a 6 L chamber (not counting dead times in the batch-wise machine) and the option for continuous use. As only one machine was available, the process was realized batch-wise. The separation steps adsorption, washing, elution, and another washing step were performed subsequently in one MEC. In a continuous process, four machines would be necessary (two in case of omission of the washing steps). The performance was already shown in Chap. 9.

An important aspect of the evaluation of a new technology is its feasibility in an industrial setting. Target is the evaluation of economic aspects and of the

process safety for operators, environment, and the consumer. Additionally, an overview over the footprint in terms of sustainability is necessary. Finally, the technology needs to be competitive with other technologies applied to the same task, both from a process footprint and economical point of view.

12.2 The Raw System and Pretreatment

One example of a complex food production side-stream containing a desirable product is soy whey from the production of soy protein isolates. The soy whey contains suspended solids and a range of dissolved components, e.g., carbohydrates, salts, and proteins. One of these proteins, Bowman-Birk protease Inhibitor (BBI), has attracted attention lately, most notably due to alleged cancer prevention properties. The BBI in soy whey is difficult to separate by traditional downstream processing as the stream contains only low concentrations but significant amounts of other proteins.

In Table 12.1, important process variables of the food pilot line are presented. Raw material of this process is the non-pretreated soy whey.

The soy whey for all lab and pilot scale experiments was obtained from one of Solae's soy protein isolate plants. To ensure constant sample quality the soy whey went through a rigor pretreatment process. The soy whey from the production line was transported cooled, heat treated using steam, stirred and neutralized from the acid pH of the soy whey by concentrated NaOH. Then 1 % of the silica gel Geduran SI60 from Merck was added and stirred for 15 min to adsorb unwanted proteins. The target protein bound as well to Silica, but to a much lower extent compared to other proteins. The Silica was removed from the suspension, by sedimentation and the centrate and overphase is filtered through 40, 10, and 0.2 μm filters to completely remove silica, suspended solids, and microbial contamination. The soy whey was then preserved with 0.05 % Proclin 300 from Sigma Aldrich.

Table 12.1 Important process variables for the layout of the food pilot line

Process variable	Value
Total protein concentration in the raw material	0.1–1 %
Ionic strength/conductivity of the raw material	5–15 mS/cm
pH value of the raw material	4.5 ± 0.2
Solid content of the raw material	Low
Concentration of other critical components in the raw material	0.5–2.0 % dissolved sugar
Separation relevant target product properties	IP $\approx$ 4.2
Stability of the target product in the raw material	Stable (especially with respect to temperature)
Target product concentration in the raw material	100–500 mg/L
Aspired target purity end product	>90 % (>1,000 units/g)
Aspired market price of the end product	>250 €/kg

Table 12.2 Composition of pretreated soy whey batches

Batch number	Protein via BCA (mg/g)	Ci activity (U/kg)	Specific activity (U/g)	Conductivity (mS/cm)	Sugar (mg/g)	Ash (mg/g)
Raw	2.6	373	146	10.12	11.5	6.8
Heat treated 1	1.74	389	223	9.02	n/a	n/a
Heat treated 2	2.0	243	121	7.90	9.6	5.5
Heat treated 3	1.8	471	265	6.28	9.71	n/a

Four batches of soy whey were produced in different stages of the project, one from raw whey and three from industrially heat treated streams. Table 12.2 shows the composition of soy whey and the batch to batch variation. The differences also affect variation between trials. To eliminate these variations, all trials run in pilot scale, both in the food pilot line and in the academic MEC, CME, and HGMS use the same batch 3, as well as a single batch of Orica MIEX DOC and Magprep TMAP particles.

12.3 Lab Scale Process Development

First operating conditions were investigated in lab scale on different bead system and on parameters like pH, conductivity, and bead concentration. Samples were analyzed by reducing SDS-PAGE, which showed changes in the product composition due to different affinities of each protein species. A pH-value of 7 showed to give good adsorption.

Purification of BBI from pretreated soy whey by adsorption to MagPrep TMAP particles of different concentrations is shown exemplary in Fig. 12.1 left. The proportion of separated product to contaminating proteins showed to be higher at high

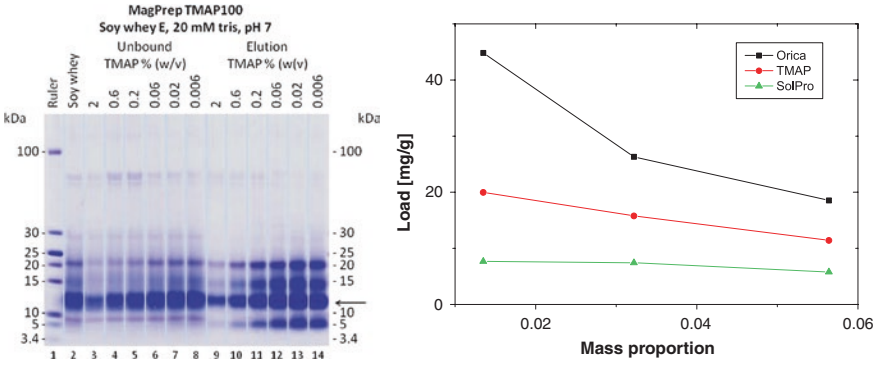

Fig. 12.1 *Left* SDS-PAGE gel of purification in soy whey at pH 7 using different concentrations of TMAP particles; *right* protein binding capacity Q of Orica, TMAP and SolPro adsorbents at three different particle concentrations in pretreated soy whey at pH 7

TMAP particle concentrations of 2 %. Purification of BBI from pretreated soy whey was tested by the anion exchange magnetic particle systems Orica MIEX DOC, SolPro, and Magprep TMAP. Three different particle concentrations (1.5, 3 and 6 %) were examined. The highest binding capacity was achieved at a particle concentration of 1.5 % for all particle systems. While the maximum adsorbed amount of the model protein BSA as a pure substance was 1,150 mg/g, nonprotein contamination reduced the adsorption significantly. Orica and Merck TMAP particles bound up to 22 and 15 mg/g, and SolPro bound 7–8 mg protein/g (see Fig. 12.1 right).

The unbound fractions and the eluded protein were analyzed by SDS-PAGE in Fig. 12.2. The first elution showed to be sufficient for most of the protein, while

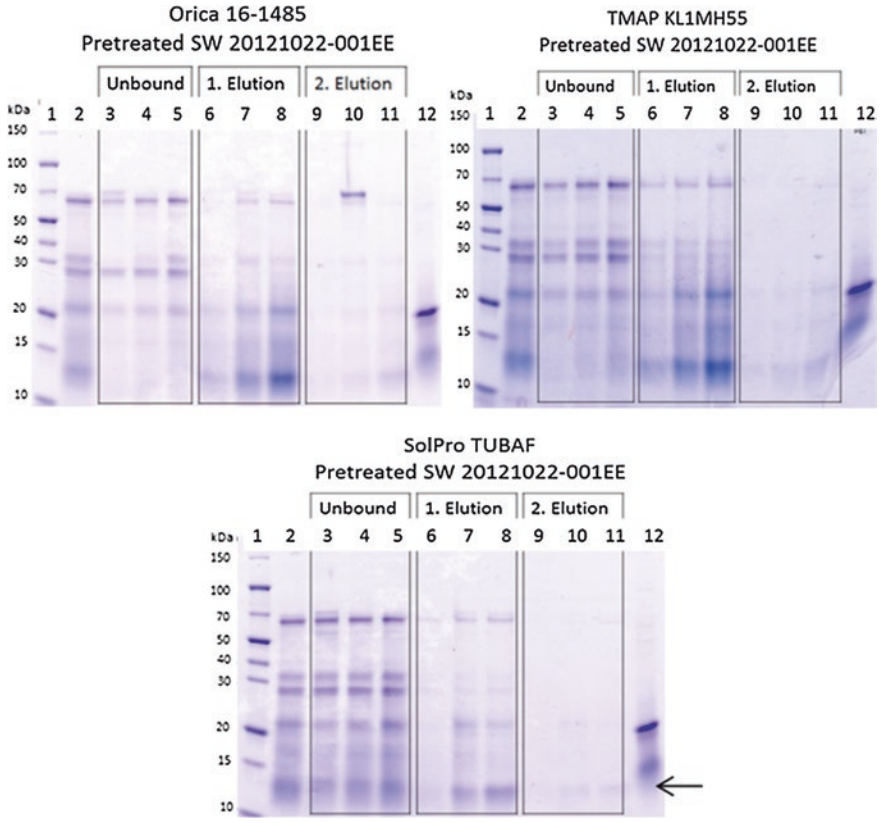

Fig. 12.2 SDS-PAGE gels of purification with the anion exchange magnetic adsorbents (*Orica, TMAP and SolPro*) used for pilot trials at 3 different particle concentrations. Elution was conducted using 0.5 M Na_2SO_4, 20 mM Na_2HPO_4, pH 7 buffer. The *arrow* shows the position of the BBI target; lane *1* molecular weight markers; *2* soy whey before addition of magnetic particles; *3–5* unbound proteins after purification with magnetic particles with *6*, *3* and 1.5 % *Orica*, TMAP or SolPro particles; *6–8* first elution at *6*, *3* and 1.5 % Orica, *TMAP or SolPro particles 9–11* second elution at *6*, *3* and 1.5 % Orica, *TMAP* or *SolPro* particles; *12* 14 µg BBI from Sigma

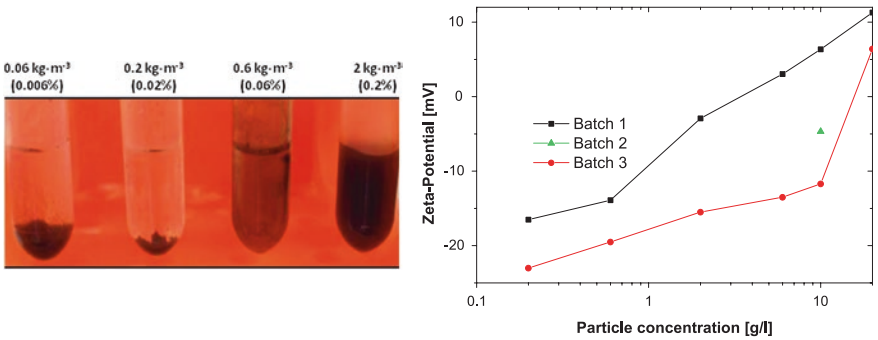

Fig. 12.3 *Left* TMAP particles exhibit different physical behavior at different particle concentrations in soy whey; *right* zeta potential of different Merck TMAP batches at different concentrations in soy whey

a second elution was necessary to elute virtually all of the protein bound to the adsorbents. Due to the low yield, in the final process, 2 % particle concentration was used.

The optimization aimed to replace chemicals not suitable for large-scale processes as well as identifying a process with a minimum consumption, acceptable yield, and robust conditions for upscaling. Magnetic particles were washed after binding to remove unbound contaminant protein. One washing cycle showed to be sufficient for this purpose. Washing was done for 10 min in 1 mL 20 mM Tris-HCl at pH 7.

Figure 12.3 left shows different concentrations of Merck TMAP particles in the same product. The particles precipitated to a highly porous deposit at a particle concentration of 0.006 %, a lowly porous deposit at 0.02 % and formed a colloidal suspension as the particle concentration was increased to 0.06 and 0.2 %. Ionic strength and pH needs hence to be controlled to keep the binding capacity, the porosity, and the separation efficiency in a magnetic separator constant.

The zeta potential of the different TMAP particle charges (Fig. 12.3 right) ranged from slightly negative at 0.006 % in whey to highly positive at concentrations above 0.2 %. TMAP particles showed to be unstable and difficult to resolve from walls at a neutral charge, while an amount of 2 % (20 g/l) of particles could be handled easily. A similar behavior was not identified on different particle systems due to the particle size of nonporous 100 nm Merck particles to 150–180 μm macro-porous Orica particles.

12.4 The Large Scale BBI Production

The system was tested in two approaches. A small batch-wise MEC of 1 L filter chamber volume showed the feasibility of the process. Subsequently separation in a MEC of 6 L volume, produced by Andritz KMPT, was performed to show

the pilot line scale of 1 m^3/h. Both devices and their performance were already presented in Chap. 9, the smaller as well with a permanent magnet.

12.4.1 High Gradient Magnetic Fishing in a Small Pilot Line

The BBI separation was tested in a batch-wise magnetically enhanced centrifuge on the two different particle systems Orica MIEX DOC and Magprep TMAP. In the test, 1.25 L of soy whey were adjusted to pH 9 with NaOH and mixed for 10 min with 25 g of Merck TMAP particles, respectively 2.5 L of soy whey with 50 g of Orica MIEX DOC. 0.7 L of washing water for each washing step was set to 20 mM sodium phosphate buffer at pH 7, and 0.7 L of elution buffer was set to 20 mM Na_2HPO_4 at pH 8 and 1 M sodium chloride. After 20 min adsorption, the suspension was fed in the machine. The magnetic particle separation was performed at 1,500 rpm, 0.2 T and 40 l/h. The centrifuge was drained with magnetic particles left in the machine at applied magnetic field without centrifugal velocity. To remove the remaining particles in the centrifuge, the centrifuge and magnet was switched off and washing liquid was fed in the machine. To resuspend, 3 min washing with stirring at 180 rpm was performed. After 5 min sedimentation at 600 rpm and 0.2 T, the machine was drained. This step was repeated with elution buffer and washing buffer. At the end of the run, the machine was discharged. The result for the protein content in each process step is shown in Fig. 12.4, with Orica MIEX DOC particles (left) and Merck TMAP particles (right). Both particle systems separated effectively BBI. The process was hence effectively transferred from the lab scale to magnetically enhanced centrifugation without large deviation in the separation, as results from lab scale are similar. The scale was only limited by the available amount of magnetic particles.

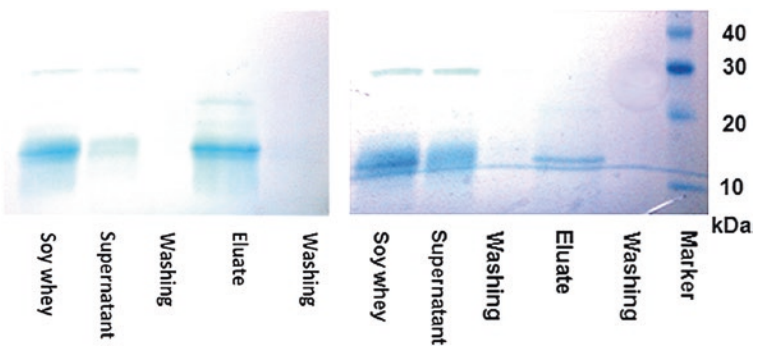

Fig. 12.4 *Left* SDS-Page gel for Orica MIEX DOC particles shows selective separation with the last contamination disappearing, a large part of the BBI is adsorbed and a part eluted; *right* TMAP shows as well adsorption and desorption of BBI

12.4.2 High Gradient Magnetic Fishing in a Large Pilot Line

For the final scale of the process, the pilot line was based on the large centrifuge of 6 L filter cell volume with 20 wire stages and a water cooled electromagnet of 400 mT flux density. Chemicals were changed to transfer the process to a pilot line. Tris-HCl was used at lab scale but cannot be used in the food industry. It was therefore replaced by 20 mM NaH_2PO_4. Similarly, 1 M NaCl was used for elution, which causes corrosion on the equipment. It was replaced by 0.5 M Na_2SO_4. The change in buffer and elution did not have a significant impact on the purification results.

For an exchange of the liquids, a displacement was performed from top to bottom. The elution liquid was displaced bottom to top to avoid mixing of the less dense salt suspension. The resuspension was done at a volume flow of 240 l/h, while stirring in both directions with the matrix for 5 min. A valve system was used to feed the centrifuge forward or backward. An amount of 300 g particles were used to process 15 L of soy whey, corresponding to a concentration of 20 g/l. Before starting the process, the particles were trapped in the centrifuge, washed, eluded, and washed again.

- First the adsorption was done. For this purpose, the magnetic field was applied and the liquid in the centrifuge displaced with soy whey from bottom to top at a volume flow of 60 l/h. Then the liquid was pumped at 240 l/h in a cycle for 5 min, while the matrix was used as a stirrer at 120 rpm to redisperse the magnetic particles. No centrifugal velocity was applied in this step.
- The washing liquid in the centrifuge was replaced by soy whey and the particles were redispersed for 5 min similar to step 1.
- An elution step was performed, again doing the displacement. This was performed from top to bottom. Subsequently, the redispersion was performed again from bottom to top at 240 l/h.
- Finally, a washing step was done while the elution liquid containing the protein was collected. To make sure displacement was efficient, the conductivity was measured and displacement was continued until the conductivity of the effluent undercut 3 mS/cm.

SolPro and MIEX DOC were easily transferred from the MEC by reversing the flow and flushing with water. Draining was not possible because of the design of the centrifuge. Displacement by an elution buffer was performed from bottom to top, while the elution buffer itself was displaced in opposite direction to take profit of the density difference. Conductivity measurement showed efficient displacement. The complete process is shown in Fig. 12.5.

The particle loss during separation was below the detection limit during the separation for all three particle kinds tested. The only significant particle loss appeared hence at cleaning after the process. Merck TMAP particles showed to form a stable cake in the center of the centrifuge which seemed to be lost for the process. This reduced the amount of separated protein significantly, the effect

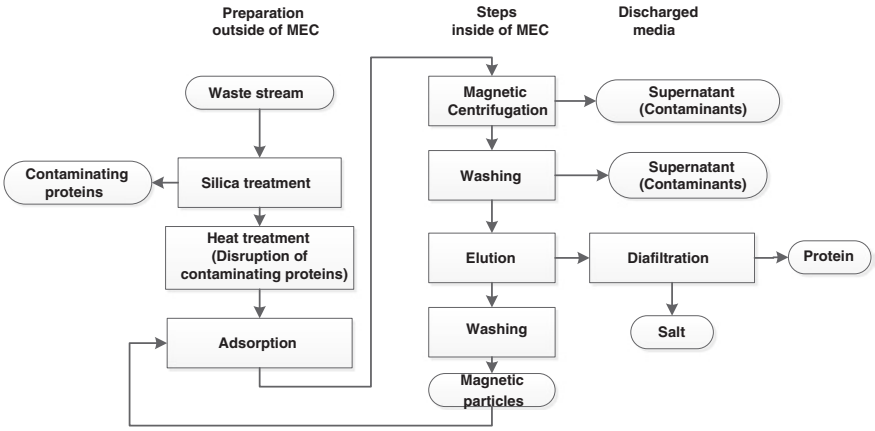

Fig. 12.5 The flow scheme of the BBI separation process shows the preparation steps outside of the MEC, the steps inside of the batch-wise MEC and lists the discharged media

Table 12.3 Separation efficiency of MEC with two batches of TMAP determined from particles in the eluates; trials on 300 g particles; Cycle 4 and 5 based on draining

Cycle number	BBI Mass (mg)	Separation efficiency (%)
1	18.5	99.994
2	64.8	99.98
3	63.5	99.98
4	11.7	99.996
5	33.9	99.98
6	63.2	99.97
7	84.6	99.97
8	96.5	99.97
9	80.1	99.97

was not observed in other particle systems. The BBI production trials comprised the use of Magprep TMAP in five cycles, Orica MIEX DOC in five cycles and SolPro PAAm in two cycles. Before cold storage, the eluates were preserved with 0.050 % Proclin. The separation efficiency of MagPrep TMAP is shown in Table 12.3.

12.4.3 Postprocessing: Purification and Drying

The eluate is dilute and contains a significant amount of salt. It was collected and filtered through a 0.2 µm filter. An iron content of 1.3 ppm was determined (4.7 ppm before filtration). As this is the same level as the original soy whey, magnetic particles seem not left in the eluate. Subsequently, the eluate was concentrated on a M20 membrane filtration rig using UFX10-pHt crossflow flat

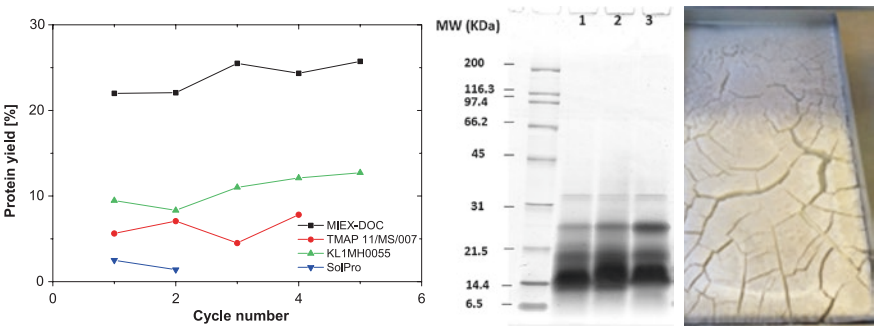

Fig. 12.6 *Left* the yield from all the binding-elution cycles run in the *food pilot line*, intended to identify if the particles show decreasing binding capacity; *middle* SDS gel of the three products from the *food pilot line*. The numbers refer to *1* TMAP, *2* MIEX DOC, *3* SolPro; *right* the product after freeze drying

Table 12.4 The stepwise protein and BBI yield is given, as well as the mass of protein in each step and the amount of BBI (Chymotrypsin inhibitor units (U))

	TMAP		MIEX DOC		SolPro	
	Protein (g)	BBI (u)	Protein (g)	BBI (u)	Protein (g)	BBI (u)
Soy whey content	243	63585	110	35325	49	7065
Eluate content	21 (8.7 %)	4745 (7.5 %)	26 (24 %)	8,870 (25 %)	1.0 (2.0 %)	132 (1.9 %)
Concentrate content	12 (57 %)	3435 (72 %)	13 (51 %)	6,930 (78 %)	0.6 (63 %)	25 (19 %)
Diawashed concentrate (g) or (U)	10 (86 %)	2,521 (73 %)	10 (77 %)	4,805 (69 %)	0.5 (83 %)	27 (108 %)
Dried powder content	11 (4.3 %)	2,280 (3.6 %)	11 (10 %)	4,325 (12 %)	0.4 (0.9 %)	20 (0.3 %)

sheet membranes from Alfa Laval at 50 °C. The eluate was concentrated to 3.5 L and diafiltered to less than 0.5 mS/cm. The seven times diawashing resulted hence in more than 1,000 times dilution. The diawashed concentrate was stored. Figure 12.6 C shows the result. The stepwise and total yields for all cycles of each of the three particle types are given in Table 12.4. There were protein losses in the order of 50 % in ultrafiltration and diawashing, reducing the overall yield.

To estimate the success of the purifications, the soy whey and the eluted fractions were analyzed by a chymotrypsin inhibition assay to determine the amount of BBI in units (CI/l). The amount of total protein was analyzed by a BCA assay and the specific activity (CI/g) and a fold purification of BBI could thus be calculated. Purification of BBI using magnetic adsorbents (Orica MIEX DOC and MagPrep TMAP) in pretreated soy whey was conducted in pilot scale (15 L soy whey, 300 g particles, 5 cycles) at using a MEC for separation (built by ANDRITZ

Table 12.5 Amount of product, protein content, activity and specific activity of each product

Particle	Amount of product (g)	BCA protein (%)	CI activity (U/g)	Specific activity (U/g protein)	Sugar (%)	Ash (%)	Kjeldahl protein (%)	ELIZA BBI (mg/g)
TMAP	22.2	47.3	108.5	229	14.1	14.5	61.5	72
MIEX DOC	19.3	56.6	224.1	396	8.7	12	66.8	159
SolPro	1.11	37.4	18.2	49	5.8	n/a	n/a	14

Contents of products, sugar determined by phenol-sulfuric acid method, ash by heating to 600 °C, Kjeldahl protein from nitrogen(*6,25) and BBI contents measured by FZMB

Table 12.6 Sugars found in the three dried products

Sugar	Stachyose	Glucose	Xylose	Sucrose	Galacturonic	Total (ppm)
TMAP	221.4	22.4	11.3	120.2	85.9	461.1
MIEX DOC	72.6	0.0	7.0	110.4	132.5	322.5
SolPro	60.5	0.0	3.5	74.3	83.6	221.8

KMPT GmbH). The BBI purifications in pilot trials reached a fold purification of 1.05 and 0.79 and a BBI yield of 25.1 and 8.5 % for Orica MIEX DOC and MagPrep TMAP, respectively.

In the lab MagPrep TMAP and MIEX DOC particles have shown to maintain their binding capacity through 50 cycles. Figure 12.6 left shows the yield per cycle of several particles in the process. As the yield is not reduced, the ligands stay active. Figure 12.6 middle shows protein contaminants in the powdered products. Figure 12.6 right shows the dried BBI product.

The amount of product produced varies, which is shown in Table 12.5.

Table 12.6 gives an overview over content of sugar. The sugars and ash numbers are high considering that excessive diafiltration was done. The samples have been filtered, and are precipitate-free, even though the color of the liquid sample is dark brown. The ash may be a result of chemical elements in the proteins not evaporating after burning, e.g., sulfur. The table shows the 200–500 ppm mono-di- and trimeric sugars, with the total content of 60,000–140,000 ppm carbohydrates. MS analysis has identified a small amount of glycoproteins and lectins.

There is a dense band on the gel for each product in Fig. 12.7, above the 180 kDa marker. This hints to soluble, negatively charged polysaccharides. These are known to be extracted from the soy bean during processing. The pectin-like molecules are negatively charged and might well be the contaminant competing contaminant reducing the amount of BBI separated in the process. Polysaccharides are also concentrated with the protein on UF, explaining the high sugar concentration.

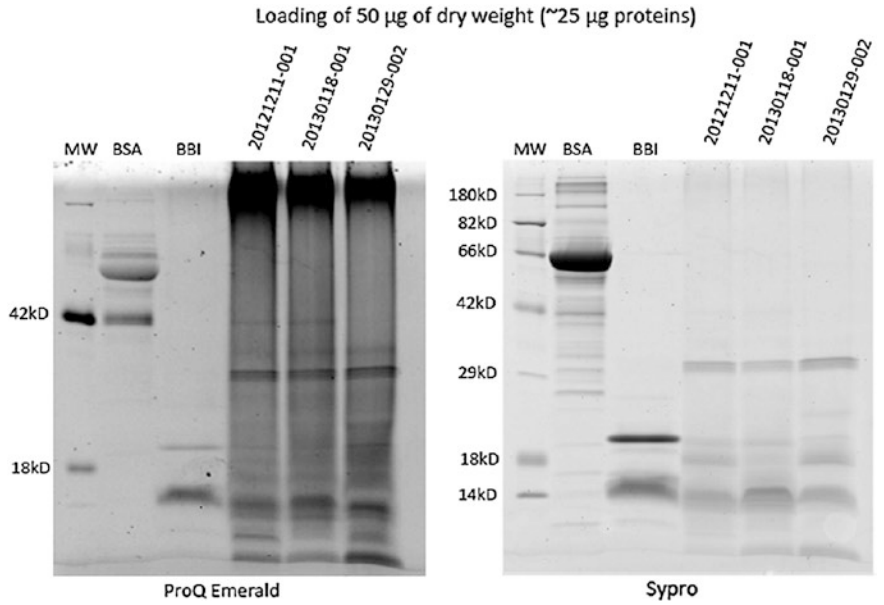

Fig. 12.7 *Left* gel stained targeting carbohydrates on glycoproteins; *right* gel stained targeting all proteins

12.5 Economic Evaluation

The main target of this chapter is the economic perspective of an industrial process. Therefore based on the separation experiments, a model calculation is performed to determine the economics.

12.5.1 Economic Process Modeling

The economic evaluation of the food pilot line was set up in the software SuperPro Designer®. The model was a direct implementation of the data of the batch-wise pilot trials of the food pilot line-based Orica MIEX DOC test runs. The materials, labor, and equipment costs, as well as utilities used in the trials were included to show the actual costs of the pilot scale process. These models serve as initial mass balance for the production scale models of the two processes. Three major assumptions are taken: .

1. All operations are continuous, running 300 days/year, 24 h a day, with a 1 week CIP interval.
2. The particles path in the process is changed into a continuous cycle of two continuous MEC units, one for separation after binding, the other after elution. These two units are extrapolated in cost, capabilities, and consumption from the pilot MEC200 from AKMPT.

3. Spray drying replaces freeze drying, because this batch-wise, laborious process is rarely scaled to production size.

Besides these changes, two additional assumptions are taken.

1. A membrane with insignificant loss of protein is identified and used for the purification.
2. Some form of separation aid is added, improving the separation during pretreatment and allowing for easier filtration.

The prices and utility requirements of all process units, including depreciation and prices of utilities and materials were identified and an industrially feasible process scheme created to enable a realistic evaluation of the process in production scale. A cost factor of 4.0 was used to find the total investment cost based on the equipment purchase price. The purchase prices of the equipment are scaled using the six-tenths rule, i.e., the approximate equipment cost C_B is estimated from the equipment cost at lower scale C_A, the size at lower scale S_A and the size at final scale S_B.

$$C_B = C_A \left(\frac{S_b}{S_A} \right)^{0.6} \tag{12.1}$$

The scale of the model is defined by the feed rate of 24 m^3/h of soy whey. A sensitivity analysis of the changing of key parameters in the production model is given below.

12.5.2 Process Economy

An economical model was created based on the test production runs of Orica particles, because this system achieved in comparison high separation rates at a low particle price. Technically an upscale of the other particle systems would result as well in lower market prices. Calculations were performed with the assumption of avoiding further losses during washing and drying, resulting in 25 % separation actually achieved in the pilot plant. Current losses result in doubling the production cost given below. The BBI yield of Orica particles of 25 % resulted in a production rate of 73.5 ton of spray dried product per year. The product contained a BBI activity of 270 U/g. The calculation resulted in costs of 344 €/kg in a large scale production line. The same scenario for TMAP yields 8.5 % BBI, with a production of 30.7 ton per year at an activity of 220 U/g. The costs of this product are higher, reaching 5,910 €/kg.

In the sensitivity analysis, a separation of 25 % of the protein was assumed (which comes at no cost in a waste stream) at 24 m^3/h with particles at 2 mass % concentration of 254 €/kg price with particles used for 100 cycles (i.e., low loss and no deterioration at these 100 cycles).

Figure 12.8 left shows the cost distribution of the Orica production process. The largest expense is the replacement of particles, followed by investment depreciation (over a 10 year period) and facility costs. The pretreatment of the soy whey

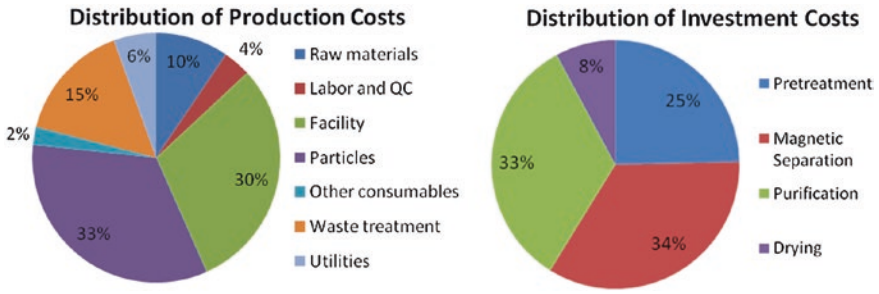

Fig. 12.8 *Left* distribution of production costs for a plant based on Orica particles(25 million €/yr); *right* distribution of investment costs for a plant based on Orica particles (25 million €)

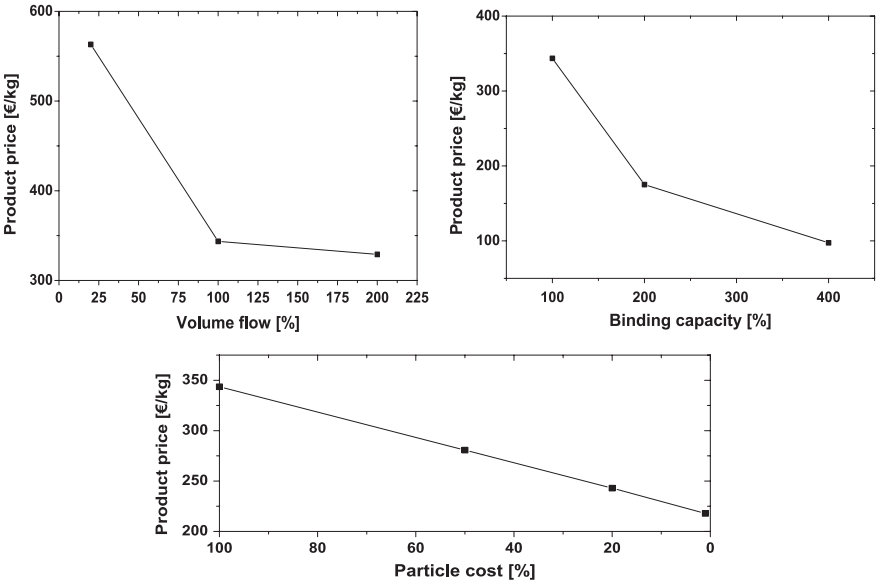

Fig. 12.9 *Top left* the effect of process capacity on product price, relative to the reference process model. *Top right* the effect of binding capacity on product price, relative to the binding capacity identified in the pilot trials. The models assume that higher binding capacity results in higher process yield, as the process parameters remains constant. *Bottom* The effect of particle cost on the product price, relative to the price indicated by Orica for MIEX DOC particles

for the process accounted for the third largest costs proportion in the calculation, as both the purchase and disposal of the solid waste showed to be significant in a process. Utilities, consumables, and chemicals represent only minor expenses compared to the factors aforementioned. Figure 12.8 right shows that the equipment costs are dominated by the first steps of the process handling a large volume. In the pretreatment, the decanter centrifuge and in the magnetic separation the MEC and UF showed to be important, while spray drying is cheap due to low volume.

Figure 12.9 bottom shows the influence of the particle cost and the consequence of a theoretic reduction. Figure 12.9 top right shows a theoretic increase of

the process yield by a higher binding capacity, which would reduce the cost even more with a theoretic 90 €/kg at a protein yield of 100 %. A theoretic evaluation of a further increase of the process scale in Fig. 12.9 top left does not improve the process significantly due to its already very high scale in the calculation. Omitting the Silica pretreatment step has been shown in the lab to have minor impact on the yield but reduced the production costs to 276 €/kg.

In this study, even with further developments and optimizations the limit of a production cost of BBI proteins can be seen at 50 €/kg.

12.5.3 Theoretic Calculation on Selective Ligands

A theoretic study was as well run on the production model by highly selective MagPrep Antibody particles at 49 €/g functionalized particle and 100 cycle times. The result was a price of 180,000 €/kg product, while Orica product resulted in 340 €/kg. A consequence is that the nonparticle related cost sum to only 0.33 %, which is neglectable. Orica reach about 270 U/g(~150–200 mg/g), while antibody functionalized particles might in theory achieve above 1,000 U/g including a washing step. In a pure product, the price would be 270,000 €/kg. A high yield and a selective process are in the calculation essential to product purity. The price of the magnetic fishing technology using antibodies is estimated exclusively by the antibody particle cost C in €/g, the binding capacity B in (g/g) and lifetime L in cycles which includes as well particle losses in the separation. The particle cost constitutes more than 90 %, for specific particles more than 99 %, of the total costs in industrial scale systems. To give an example, the cost of 1 kg BBI produced by particles at 49,000 €/kg at a binding capacity of 2 mg/g and a lifetime of 100 cycles results in 245 €/g.

$$C = \frac{P}{B * L} \tag{2}$$

In conclusion, the process yield and fold purification is highly dependent on the binding and elution technology in the process. The binding capacity, and thereby process yield, together with the lifetime and cost of the resin/magnetic particles, are important cost drivers. Further optimization is possible both resin- and process-wise, but magnetic adsorbent-based purification using a MEC is competitive to other adsorption technologies and can be expected to show additional benefit by a reduction of pretreatment of the feedstocks. In the model ultrafiltration seems to be the most cost-efficient process, while not being highly selective. In comparison to conventional adsorption technologies, magnetic fishing seems to be a commercially viable option.

12.6 Technology Benchmarking

A theoretic benchmark against established competing technologies for the production of specific proteins from coproduct streams allows estimating the commercial perspectives of the process. Relevant competing technologies are

packed bed adsorption (PBA), expanded bed adsorption (EBA), and ultrafiltration (UF). The benchmarking is based on lab experiments at the assumption that separation achieved in lab experiments is scalable (EBA, PBA, UF, HGMF).

PBA bases on adsorbents immobilized in a packed bed, which is passed by the target liquid. EBA is a variant of PBA, in this case the packed bed is passed from bottom to top at flow velocity sufficient to equalize gravity and resistance force of the packing to create a fluidized bed. This results in a lower necessary pretreatment, as larger contamination passes unhindered. PBA has several of the advantages of HGMF, but is not possible in a continuous way. UF is a common semipermeable membrane-based separation selective for molecular weight instead of surface properties. This is rather different compared to HGMF, PBA, and EBA, which are adsorption-based separation methods.

The benchmark of performance and costs of the technology is based on ion-exchange resins. In this comparison, two magnetic adsorbent carrier systems (Orica DOC and MagPrep TMAP) are compared to three established separation technologies (EBA, PBA, and UF) for the purification of the target protein BBI from soy whey. The modeling of the five benchmark processes included the feedstock pretreatment and the downstream processing in the software SuperPro Designer®. The mass was balanced and the equipment sized according to the process scale. The economic consequences of various manufacturing scenarios were evaluated, and prices for materials (equipment, utilities, and chemicals), energy, and labor were incorporated into the process models to calculate costs based on pilot scale trials.

12.6.1 Experimental Test Runs on Competing Technologies

The purification of BBI in soy whey was developed in both EBA and PBA with approximately 300 mL of pretreated soy whey. The activity of the pretreated whey and the eluted samples containing protein were analyzed with the chymotrypsin inhibition assay to quantify BBI and BCA assay. The purification of PBA and EBA resulted in a fold purification of 1.2 and 0.97 and a BBI yield of 18 and 11 %, respectively (Table 12.7). The UF membrane used in the benchmarking study had a cut-off of 3 kDa and can be expected to retain the BBI in the retentate as BBI has a molecular weight of 8 kDa. UF of pretreated soy whey resulted in a fold purification of 1.61 (Table 12.7) which is higher compared to both EBA and PBA. The yield of BBI was 81 %. The fold concentration of BBI in the retentate from UF is 5.28 which shows that most of the proteins present in the soy whey were retained in the retentate. EBA was chosen as a promising technology to benchmark against magnetic adsorbents as both EBA and magnetic adsorbents can handle purification in unclarified feed stocks which neither packed bed adsorption (PBA), chromatography nor ultrafiltration

Table 12.7 PBA, EBA, UF and HGMF purification of BBI from pretreated whey

PBA	Vol. mL	CI/L	CI/g	% BBI yield	Fold conc.	Fold purification
SW load	304	324	181	100	1.00	1.00
Elution	20	894	217	18	2.76	1.20
EBA						
SW load	302	324	141	100	1.00	1.00
Elution	36	297	135	11	0.92	0.97
SW load	110	348	229	100	1.00	1.00
Elution	27	943	597	66	2.71	2.60
UF						
SW load	100	448	201	100	1.00	1.00
Retentate	15.4	2367	324	81	5.28	1.61
HGMF (Orica)						
SW load	15,000	471	320	100	1.00	1.00
Retentate	16,042	111	337	25.1	0.24	1.05

(UF) do. A fold purification of 2.6 at 110 mL soy whey load was obtained. It was possible to use food compatible buffers in the process without affecting the results. While 300 mL soy whey in an EBA column did not deliver good results, an optimal amount of pretreated soy whey (110 mL) was identified. This corresponds to 7 times the column volume to reach a high yield and amount of purified BBI.

12.6.2 Benchmarking Results

The models comprise all steps of the process, from pretreatment of the soy whey to drying of the purified and concentrated product. The mass balances were scaled linearly. In addition the pretreatment, purification, and drying processes were adjusted to yield products of similar purity. This allows for the cost differences in the investigated processes.

EBA was in our calculation efficient in yield and thereby utilization of the equipment and resources, giving a good cost optimization potential. The influence might as well be down to a better optimization. The magnetic fishing process based on Orica particles showed to be highly cost efficient. The costs of BBI production shown in Fig. 12.10 can be compared to the price of the currently commercially available BBI from the Sigma Aldrich catalogue (3000 €/g). The project purity goal of more than 1,000 U/g was not reached in the experiments. While the current cost estimate appears low at less than 20 €/g, the result is rather theoretic as long as no particles for a purity increase are found.

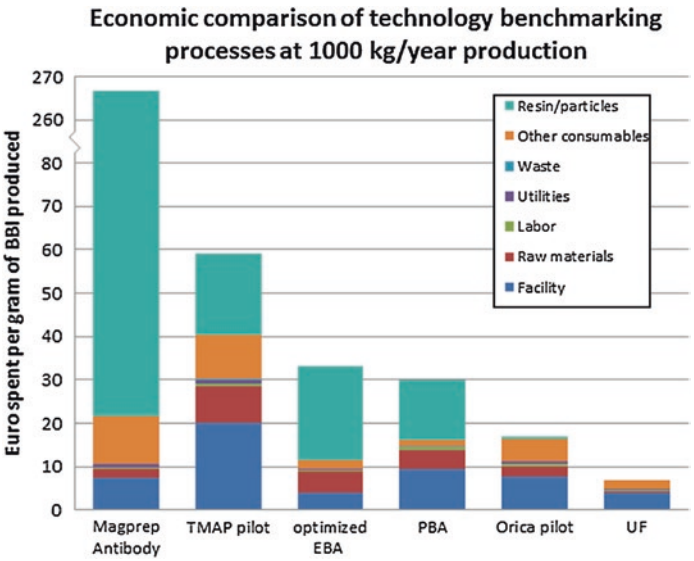

Fig. 12.10 Comparison of the costs of 1 g BBI distributed on major cost items for the five key models in the technology benchmarking

12.6.3 Carbon Footprint

The life cycle assessment investigates the environmental implications of BBI separation. The Life Cycle Assessment (LCA) is done according to ISO 14040 and ISO 14044. The assessment compares BBI separation by EBA with BBI separation by the novel magnetic separation process. Two magnetic separation scenarios were investigated. The first magnetic separation scenario is based on lower yields than currently obtained in pilot scale experiments, while the second scenario assumes similar BBI separation yields compared to the expanded bed adsorption reference case. Due to the high specific energy and material consumption of the separation processes, the separation of BBI by either EBA or magnetic separation has a significant environmental burden. Assuming comparable BBI separation yields, the magnetic separation process seems to be superior to the expanded bed adsorption process with respect to the environmental categories studied in the assessment (MEC+TMAP I in Fig. 12.11). At low yields, currently observed in the experiments, expanded bed adsorption would be the more sustainable BBI separation process choice with respect to the environmental impact categories assessed in this study (MEC+TMAP II in Fig. 12.11).

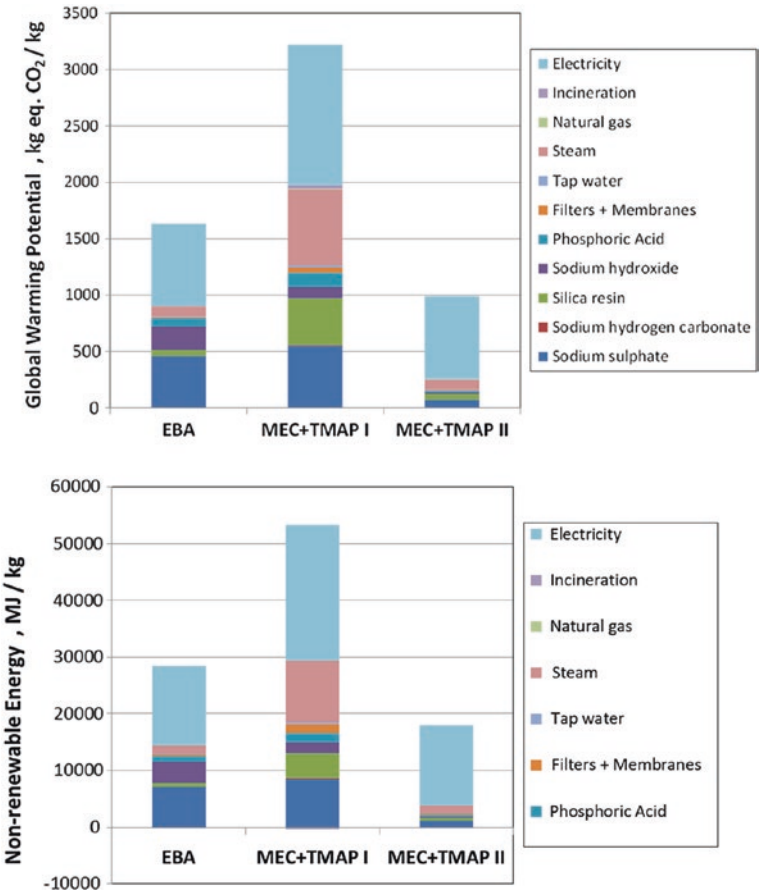

Fig. 12.11 *Top* benchmark comparison on the climate change; *bottom* benchmark Comparison on nonrenewable energy consumption

12.7 Safety, Health and Environment and Legal Considerations

On October 18th 2011, the European Commission adopted the Recommendation on the definition of a nanomaterial. According to this recommendation a "Nanomaterial" means:

> A natural, incidental, or manufactured material containing particles, in an unbound state or as an aggregate or as an agglomerate and where, for 50 % or more of the particles in the number size distribution, one or more external dimensions is in the size range 1–100 nm.

Nanomaterials are not intrinsically hazardous per se but there may be a need to take into account specific considerations in their risk assessment. The chosen Orica particle system was not considered as nanomaterial.

12.7.1 Nanomaterials in REACH and CLP

REACH is the over-arching legislation applicable to the manufacture, placing on the market and use of substances on their own, in preparations or in articles. Nanomaterials are covered by the definition of a "substance" in REACH, even though there is no explicit reference to nanomaterials.

In the European Commission the definition of a nanoparticle, the determination of the percentage of particles in the number size distribution is required. Currently, the exact determination of the size distribution is difficult because of methodological limitations. **B**runauer-**E**mmett-**T**eller (BET) allows the determination of the specific surface, and a deduced average particle size, but not a number size distribution. **D**ynamic **L**ight **S**cattering (DLS) results in a size distribution, but cannot distinguish between individual particles and aggregates. The most precise method would be the evaluation of electron micrographs (SEM, TEM) by directly measuring the diameter of a large number of particles. Manual screening of hundreds or thousands of particles would be too time-consuming and expensive.

12.7.2 Potential Risks/Negatives of the Nanomaterial

Dermal irritation and dermal sensitization studies were conducted with MagPrep TMAP test materials. In those studies, the test substance was a skin irritant (OECD 404) or a dermal sensitizer (OECD 429). Acute oral toxicity studies were also conducted with a group of female rats (OECD 423). Under the conditions of the study, single oral applications (2 g/kg body weight) of the MagPrep TMAP test substance produced no mortality and were associated with minor signs of toxicity, which were fully reversible within 1 day postexposure. Because all of the exposed female rats survived the single dose through a 14 day postexposure period, the median lethal dose (LD_{50} cut-off rat) of particles is potentially at 5 g/kg. The magnetic particles, which go to the municipal wastewater treatment plant are expected to partition to washed grit/sand.

In conformity with the criteria given in Annex VI to Commission Directive 2001/59/EC, the test item has no obligatory labeling requirement for toxicity. According to Annex I of Regulation (EC) 1272/2008, the test item MagPrep TMAP has no obligatory labeling requirement for toxicity and is not classified. According to Globally Harmonized Classification System (GHS) the test item has obligatory labeling requirement for toxicity and is classified into Category 5: "LD50 >2,000 mg/kg <5,000 mg/kg. WARNING. No symbol. May be harmful if swallowed."

12.8 Conclusion

A pilot line was set up, processing magnetic particles at losses of less than 1 ‰ particles. The Achilles heel of the process is the lack of selective ligands, which resulted in competing adsorption of contamination and in a less efficient process. The specific activity did not excel 400 U/g protein, or 159 mg/g product. Additional development is specifically necessary to achieve commercially interesting concentrations of BBI.

Combining actual pilot scale measurements with detailed modeling showed that a product holding BBI equal to 270 U/g could probably be produced at a cost in the range of 344 €/kg. The cost is sensitive to the magnetic fishing step in particular. Different particle kinds are available, with price being a major criterion. The separation device as the core of a pilot line showed to be necessary in a continuous version for large scale use. A realization of the simulated process scale is tempting for performance. It depends on the availability of selective ligands at large scale.

The risk assessment characterizes the human health risk and environmental risk as low when handling the investigated materials.

In conclusion, there are several apparatuses available or in development which allow HGMF at a scale from µl-batches to continuous production at a scale of 1 m^3/h. Systems for magnetic particles are in development and on the market, with a wide spread in price and properties. Particle systems as cheap as 250 €/kg were found and protein production costs of below 50 €/kg were reported. Both particle and separation device seem to be in an evolved state for use. The comparison of different separation technologies shows a large commercial potential for magnetic separation in comparison to standard separation technologies.

Critical for the process is the specific system and the ligands. In the system, the contaminations and the target product influences the choice of the ligand. The identification of a ligand, which separates the target selectively, can be eluded and recycled and is available at reasonable costs is the main challenge. It needs to be fitted to the system, so there is not general approach. Despite major effort in the current project, a selective ligand for the particle system could not be brought to large scale. Less selective ligands showed competing adsorption, which reduced the efficiency of the whole process.

Part IV
Conclusion

Chapter 13
Conclusion

Johannes Lindner, Karsten Keller and Hermann Nirschl

The separation of proteins by High Gradient Magnetic Filtration is a promising process for the purification of media. Its success depends on four different elements: the *synthesis* of coated particles with magnetic core, a selective *functionalization* which needs to be adapted to adsorb the target matter and exclude contamination, the *separation devices* which need to fit for the process in scale, budget and separation characteristics, and the *process design*. All of these elements need to fit together and to be available at a reasonable price.

Competing technologies comprise expanded and packed bed adsorption. The core advantage of magnetic separation is the fast kinetics, similar to expanded bed adsorption, but in a continuous process combined with an easier process control and a high flow rate. The recovery rate of the adsorbent achieves, depending on the particle magnetization, is more than 99.9 %.

13.1 Particle Synthesis

For particle synthesis, different methods were presented. The core may be produced, e.g., by laser pyrolysis, which is expensive but allows an exact adjustment of properties. The particle size and the chemical content can be influenced by this method. The size variation is very narrow, allowing the production of highly defined particles.

J. Lindner (✉)
Institute of Mechanical Process Engineering and Mechanics, Karlsruhe Institute of Technology, Strasse am Forum 8, 76131 Karlsruhe, Germany
e-mail: johannes.lindner@kit.edu

K. Keller
DuPont, Wilmington, DE 19980, USA
e-mail: Karsten.Keller@dupont.com

H. Nirschl
Institute of Mechanical Process Engineering and Mechanics, Karlsruhe Institute of Technology, 76131 Karlsruhe, Germany
e-mail: hermann.nirschl@kit.edu

H. Nirschl and K. Keller (eds.), *Upscaling of Bio-Nano-Processes*,
Lecture Notes in Bioengineering, DOI 10.1007/978-3-662-43899-2_13

Another possibility is co-precipitation which showed to be versatile for the production in the range of 6–10 nm with particle clusters without any remanence. The synthesis of microgels allows as well a precise design. Microgels were obtained by achieving colloidal stability of a magnetic fluid. Dynamic membrane pore extrusion allowed the formation of vesicles; in this case, the magnetic core is encapsulated in a fatty acid for a specific coating. Spray drying results in a low-cost and an easy scalable process. It is well suited for cheap, large-scale synthesis of particles for industrial use in the 100 g scale. Mixing aqueous solutions of iron salts under alkaline conditions is possible in a continuous process and was performed in the project for the synthesis of magnetic particles in kilogram scale. The system is now on the market commercially and seems from a comparison to the other synthesis approaches to be a viable option. There are as well commercial particles available from numerous producers.

13.2 Functionalization

Synthesized particles were functionalized with an unselective silica, low selective ion exchange, and high selective antibody adsorbent. Cheap and low selective functionalization showed to work well in several, but not in all applications. Notably in the in-situ pilot-line presented, particles with a silica functionalization could be additionally shielded to prevent bacteriae from adsorbing, which resulted in an interesting process. In the food side stream, low selective functionalization did not show to be efficient though, with a nonprotein contaminant strongly reducing the activity. Antibody functionalization was developed and tested successfully. An economic analysis showed this adsorbent to be too expensive though for an implementation in the industrial pilot line.

In general, for most target systems the particle functionalization needs to be custom-made. A consequence is that in a HGMF process, the development should start with the pairing of product system and adsorbent. This is crucial and needs to be finished before the line development starts, as it directly impacts on the necessary pretreatment and further purification steps. The adsorbent hence influences the overall process design and performance.

13.3 Separation Devices

Three different separation approaches were presented, additionally a Rotor-Stator called device is on the market. They are summarized in Table 13.1. The modeling and simulation by the Discrete Element Method of particle agglomeration, deposition and detachment from magnetic wires showed the formation of needle-shaped agglomeration as expected in High Gradient Magnetic Separation. One variant is Magnetically Enhanced Centrifugation, which allows the continuous separation of particles by cleaning a magnetic wire filter by low centrifugal forces.

Table 13.1 Comparison of devices

Device	Investment cost scale (€)	Tested scale
Rotor-stator HGMS	50 000	Batch-wise 200 g particles
Halbach-based HGMS	10 000	Batch-wise 200 g particles
Continuous magnetic extraction	10 000	Continuously 10 l/h
Magnetically enhanced centrifugation	100 000	Continuously 50 l/h (to 1 m^3/h in a batch test)

It is specifically designed for large volume flows. Despite it is possible to design the device based on a permanent magnet arrangement, it is in investment more expensive than the "static" Halbach-based High Gradient Magnetic Separation and Continuous Magnetic Extraction. It allows continuous processing of high volume flows, in a significantly larger scale than the competing processes.

A Halbach-magnet-based High Gradient Magnetic Separation reactor is robust and cheap, based on permanent magnets, which allows batch-wise separation. It is easily scalable and usable in parallel. Additionally, it has a cylindrical cell including a stirrer and can therefore be used as reactor for consecutive washing and elution steps without further tank-to-tank transfer.

Continuous Magnetic Extraction allows the chemical separation of particles and adsorbed media. It is cheap investment-wise, based on a permanent magnet. It is slower compared to High Gradient Magnetic Separation variants such as Halbach-based High Gradient Magnetic Separation and Magnetically Enhanced Centrifugation in terms of the necessary residence time but allows the separation of small, colloidal particles. It needs the addition of tensides, but performs the extraction step not just as a magnetic separation but simultaneously a chemical separation step.

Two continuous approaches were developed within the project. With some optimization and refinement for industrial use, Magnetically Enhanced Centrifugation and Continuous Magnetic Extraction present an interesting option for the processing of large volumes.

13.4 The Processes

The particles synthesized as well as the devices set up were tested with industrial suspensions. Two different processes were presented, one being the separation of Phytase out of fermentation broth by In Situ-Separation to enhance the fermentation. The particles used were coated with nonselective Silica, combined with a coating excluding bacteriae. It showed to be possible to separate proteins in situ. The process was continued after separation, resulting in an increase of the process yield.

The separation of a protein as a pharmaceutical and food additive from a waste stream of the soy industry was an attempt to move to a large scale and set up an industrial process. Anion exchanger functionalized particles were used in combination with a pretreatment eliminating contaminating proteins. The process design

and separation was possible, and several grams of protein could be separated by processing a significant amount of magnetic particles per batch. The economic perspective was reduced through the low selectivity of the particles and the activity reduction of the particles by nonprotein contaminants. A more sophisticated and more selective ligand was not available at process scale and would strongly increase the process cost. A ligand fitting to the system at a reasonable price would be the key to an economically viable process.

Recycling of particles showed to be effective in small-scale tests, and particles did not show to change behavior in repeated large-scale environments. Loss of particles in dead zones and walls of tubes, valves, and devices showed to be significant. This depends as well on the functionalization, which made specific particles adhere to walls. Elution is critical, as incomplete elution reduces the overall processes efficiency. Especially on selective particles, elution is nontrivial. The separation of the target protein from the elution medium is another challenge. Excessive washing showed in the current process to reduce the amount of the salt used for the elution, which resulted in a much higher concentrations compared to the target protein. The process advantages are the possibility for continuous use and the low number of process steps.

13.5 Outlook

The technology is in an evolved state with several different approaches available for the synthesis of particles. While some of the approaches allow an exact structuring of the particle sizes such as laser pyrolysis, some approaches can be scaled economically to a large scale, specifically taking the economic perspective into account. Particle prices for diagnostics do not apply, as the large scale results in a significant reduction of costs. Nonspecific functionalization is available at an acceptable price. Silica-coated and ion-exchange particles were produced and used effectively. Silica-coated particles delivered good results in the in situ phytase separation, after modifying the particles to exclude the adsorption of bacteriae. Cation-exchange SO_3 particles showed to be efficient as well. Anion exchange TMAP-functionalized particles were used in the industrial line for separation.

Specific functionalization showed to be nonrealistic for the current production lines. While antigen functionalization works, it was not available at process scale and exceeded the financial scope of the project. A consequence is that the choice of the process depends on the availability of cheap functionalization. A theoretic comparison showed that magnetic fishing in the current process, while not economic, is competitive with different processes like packed bed adsorption. For an economic perspective, the market price of the product and the costs of the functionalization decide on the potential of the process. In different processes it might make sense to take profit of the fast and continuous magnetic separation instead of conventional packed bed adsorption. In theory this allows much lower cycle times, an easy exchange and storing of functionalization.

Several magnetic separation devices are available at different process scales. The choice depends amongst other things on the scale and the regime of the process—batch-wise or continuous. A continuous large-scale process is possible based on Magnetic Enhanced Centrifugation. In the pharmaceutical industry, batch processes are more common, which is possible by a Halbach-based High Gradient Magnetic Separation reactor with the advantage of higher volume flow and easy exchange of functionalization compared to a packed bed. Magnetic extraction allows simultaneous magnetic and chemical separation.

The integration of these technologies in pilot lines was successful. While not every element worked out perfectly, there is no major obstacle left for a complete process integrating the developed separation devices and core particles.

Overall it could be shown that a continuous magnetic separation process can be realized in a production scale. There are still some limitations, which have to be explored for an efficient and economic use. It is now the challenge of interested companies to implement this technology into their manufacturing sites for the production of innovative, new products.

Index

H. Nirschl and K. Keller (eds.), *Upscaling of Bio-Nano-Processes*,
Lecture Notes in Bioengineering, DOI 10.1007/978-3-662-43899-2